ISAS - INTERNATIONAL SCHOOL
FOR ADVANCED STUDIES

The Broad-Band Energy Distribution of Ultraviolet-Bright Blazars

Thesis submitted for the degree of
Doctor Philosophiae

Astrophysics Sector

Candidate:
Elena Pian

Supervisor:
Prof. Aldo Treves

October 1994

TRIESTE

SISSA - SCUOLA
INTERNAZIONALE
SUPERIORE
STUDI AVANZATI
TRIESTE
Strada Costiera 11

The Broad-Band Energy Distribution of Ultraviolet-Bright Blazars

Thesis submitted for the degree of
Doctor Philosophiae

Astrophysics Sector

Candidate:
Elena Pian

Supervisor:
Prof. Aldo Treves

October 1994

Acknowledgements

I deeply thank Aldo Treves, who directed my work with constant support and advice. I would like to thank Prof. Dennis W. Sciama, Head of the Astrophysics Sector of SISSA. I am very grateful to Lucio Chiappetti, Rick Edelson, Renato Falomo, Gabriele Ghisellini, Laura Maraschi, Joe Pesce, Rita Sambruna, Riccardo Scarpa, Meg Urry, and to the staff of the IUE Observatory, particularly to Domitilla De Martino and Willem Wamsteker. Finally, I thank all the colleagues of the Astrophysics Sector and my friends in SISSA. I would like to dedicate this thesis to my parents.

Table of Contents

Introduction

Active Galactic Nuclei (AGN) are extragalactic objects exhibiting an anomalous energy output, compared to that expected from a "normal" mixture of stars and gas. Their activity appears to be non-stellar in origin and confined to the inner few parsec of an otherwise normal galaxy. A wide range of phenomena are associated with non-stellar activity, including: broad-band spectra, from radio frequencies to γ-rays; rapid variability, indicating an extremely compact source; luminosities that may exceed the stellar luminosity of the host galaxy; strong broad emission lines, apparently due to photoionization, and implying gas random motions velocities of even 2000 km s^{-1}; and relativistic jets, observed to emanate from regions less than a parsec across. It is generally accepted that this activity results from the gravitational interaction of matter with a central black hole of mass $\sim 10^3 \div 10^{10} M_\odot$ (Rees 1984; Shlosman et al. 1990).

I.a Blazars

AGN can be divided into two broad classes, where the emitted continuum power is dominated either by thermal emission (likely due to the presence of an accretion disk and/or of a dusty torus; radio-quiet AGN), or by non-thermal emission (radio-loud quasars and blazars). The blazar continuum is characterized by strong optical polarization ($\gtrsim$ 3%), rapid variability at all frequencies, flat radio spectra ($-0.5 < \alpha < 0.5$, where $F_\nu \propto \nu^{-\alpha}$), continuous downward curvature which generally gives them a convex shape across the overall electromagnetic spectrum.

According to whether strong optical emission lines (EW $\gtrsim$ 5 Å) are present or lacking, they are classified as Optically Violently Variable, or Highly Polarized Quasars (OVV or HPQ), and BL Lacertae Objects (BL Lacs) respectively. The identification of OVV with HPQ was established by

Moore & Stockman (1981; 1984) on the basis of the optical variability and radio properties.

The unreasonably high inferred radio brightness temperatures ($T \gg 10^{12}$ K; Quirrenbach et al. 1989) suggest a coherent emission mechanism and the flux polarization observed at radio (Gabuzda et al. 1992), infrared (IR, Jannuzi 1994), optical (Angel & Stockman 1980; Impey & Tapia 1988; 1990; Impey et al. 1991; Takalo 1992; Cimatti et al. 1993) and recently investigated also at ultraviolet (UV) wavelengths (Allen et al. 1993; Smith et al. 1993) is a strong signature of synchrotron radiation, which is believed to be the dominant process responsible for low frequency (up to soft-X-rays) blazar emission. The radio-to-X-ray average blazar spectrum is of smoother appearance than in radio-quiet or radio-loud quasars, which confirms the dominance of a unique emission component (see Fig. I.1).

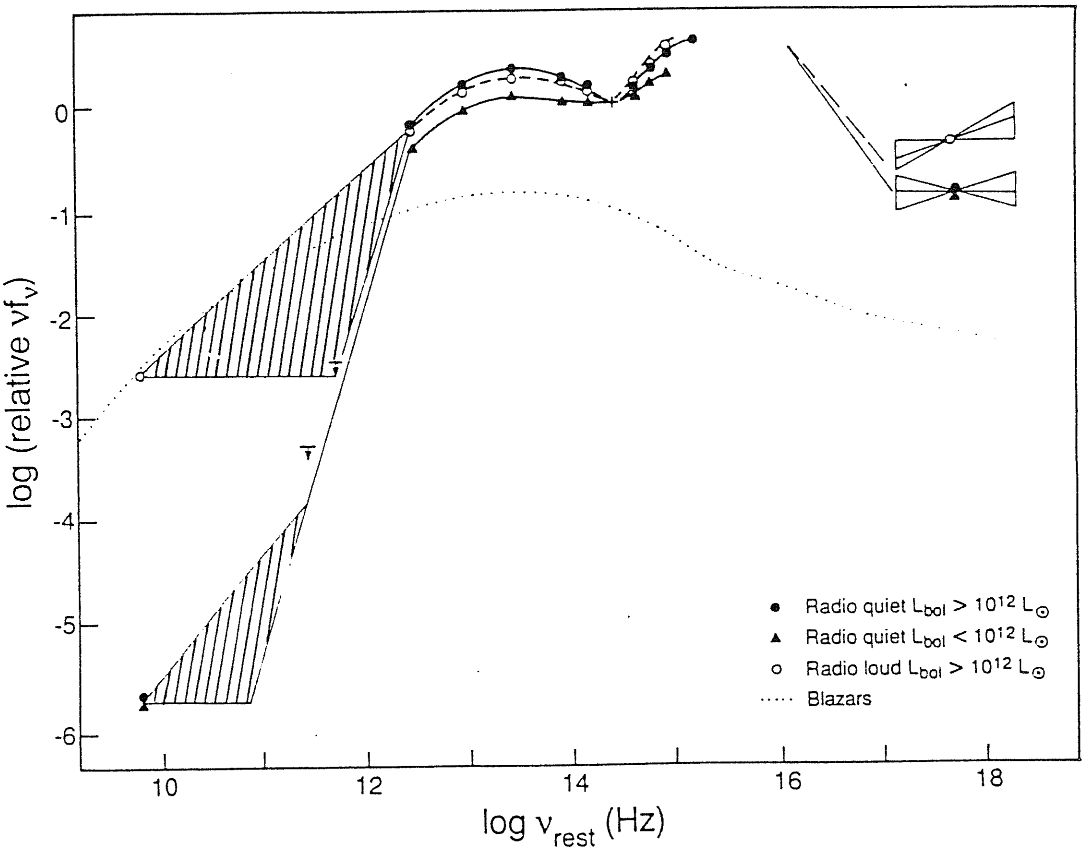

FIG. I.1 — Average continuum energy distributions of AGN (from Sanders et al. 1989).

At higher energies, the inverse Compton (IC) process is often invoked to explain the appearance of a second emission component. Upscattering of relativistic electrons off synchrotron photons or off external photons (accretion disk) produces radiation by synchrotron self-Compton (SSC, Maraschi et al. 1992; Maraschi et al. 1994a, hereafter MCG) or external Compton (Sikora et al. 1993; 1994) respectively, and gives rise to a spectral component located at very high energies (from 1 keV up to even 1 TeV).

The most exciting new development at high energies comes from the EGRET instrument on the *Compton Gamma-Ray Observatory* (CGRO), which can measure fluxes in the 30 MeV–20 GeV photon range (Kurfess 1994, and references therein). So far, EGRET has detected 38 AGN, every one is a radio-loud object (at least 0.5 Jy at 5 GHz) and many of them exhibit blazar characteristics (one of these sources, Mkn 421, was detected in the TeV range by the Whipple telescope; Punch et al. 1992); not a single radio-quiet object is detected in the GeV range (Kurfess 1994; Thompson et al. 1994).

The power output of blazars in the 100–1000 MeV range is comparable to, and in several cases exceeds, that in the rest of the electromagnetic spectrum (see Sections 1.4 and 2.3). Thus, the discovery of γ-ray emission represents a fundamental advance in the observational knowledge about these objects and its explanation is of key importance for a theoretical understanding of their properties.

I.b Variability

Blazars are characterized by remarkable emission variability at all wavelengths, which is generally of larger amplitude at higher energies (see e.g. Impey & Neugebauer 1988, and Sections 2.2 and 2.3). Flux variations, which are either recurrent or occasional (isolated flares), can occur over a variety of timescales. Rapid fluctuations are the most likely to contain information about the size of the source, while slower variations are likely to be dominated by radiative cooling or heating, or slow changes in the structure of the system. As reviewed by Bregman (1990, and references therein), the characteristic timescale of flux variation decreases with wavelength, being of the order of months-years in the radio; weeks-months in the millimeter (mm); days in the near-IR region (1–10 μm); hours-days in the optical and hours or even minutes in the soft-X-rays (0.1–2 keV). The medium- and hard-X-ray emission is varying with high amplitude (factors of 2 to even 30, Giommi et al. 1990) and with typical timescale of hours or less (Treves et al. 1989; Ohashi 1989). The timescale of variability at γ-ray energies is few days (Thompson et al. 1994), although it would be impossible to detect very rapid variations in this domain because of the extremely low count rates.

Spectral changes are usually smaller than flux variations in all bands, as deduced from observations in the radio-mm (Gear et al. 1994), near-IR (Massaro et al. 1994), optical (Falomo et al. 1994b) and X-ray bands (Sambruna et al. 1994; Brunner et al. 1994); moreover they are not obviously correlated with flux (see to this regard Section 2.1).

UV variability, which is an important issue of Chapter 2 of this thesis, was studied by Treves & Girardi (1990), Edelson (1992) and Paltani & Courvoisier (1994), who based their analyses on blazars with a substantial number of IUE observations in both cameras. All of these authors find a significantly larger variability at shorter UV wavelengths ($\sim$1500 Å) than at longer ones ($\sim$2500 Å), which is in agreement with the overall variability-energy correlation seen in broad-band blazar spectra. Unlike in Seyfert galaxies (Edelson et al. 1990), weak and no clear anticorrelation is seen between UV flux and spectral index, which is attributed by Edelson (1994) to the presence of a unique emission component in blazars which causes flux variations without colour changes; whereas in Seyferts a hard, more variable component and a softer, more stable one produce large spectral shape flattening during flux enhancement. Conflicting conclusions are reached by the above authors as for the correlation of UV variability with UV luminosity. Particularly, Treves & Girardi and Edelson find two opposite results, which however depend on the difference in the selected samples. If only the common objects are considered, a general trend of correlation is found for both analyses, though the statistical significance is poor (5 objects). Edelson finds that the shape of a typical burst may be a slow rise followed by a rapid decline (see however the regular shape of the flares in UV and X-rays exhibited by PKS 2155–304, Section 2.1 and Brinkmann et al. 1994). Finally, Edelson finds a significant correlation of UV variability with optical polarization, which is considered a strong evidence of synchrotron radiation.

I.c Relativistic Beaming

The most puzzling aspect of AGN has always been their high power output coupled with the small emission region inferred from rapid variability. The high (and variable) polarization, the compact radio structure, the smooth continuum spectrum from radio through soft-X-ray wavelengths, and superluminal motion, may owe their origin to a relativistic jet (Blandford & Rees 1978). The absence of the *Compton catastrophe* (Marscher et al. 1979), the high luminosities ($L \gtrsim 10^{12} L_\odot$) and flare quotients in excess of the Eddington-limited value assuming accretion efficiency η (Fabian 1979), $\Delta L/\Delta t > 2 \times 10^{42}\ \eta$ erg s^{-2} (e.g., Feigelson et al. 1986; Morini et al. 1986), often exhibited by blazars, can most easily be explained by relativistic effects.

The jet model is supported by direct radio and optical observations of extended structures of kpc sizes (e.g. M87, PKS 0521–365), by radio observations of superluminal motion on parsec scales (e.g. Cohen & Unwin 1981; Zensus 1989; Krichbaum et al. 1994), in which VLBI emission components appear to separate at speeds well in excess of the speed of light, and by the transparency to γ-ray photons despite the high observed compactness (Maraschi et al. 1992), which implies anisotropic, relativistically enhanced radiation.

Due to the point-like appearance of blazars at radio frequencies also on VLBI scales, there is general agreement that if their energy production takes place in an elongated structure such as a jet, this should be aligned with the observing direction.

The quantity $\Delta L/\Delta t$ is proportional to δ^5, where $\delta = (\Gamma[1-\beta\cos\theta])^{-1}$ is the kinematic Doppler factor describing relativistic motion with bulk Lorentz factor Γ (velocity β) at an angle θ to the line of sight, and measuring the relativistic modification of the intrinsic source parameters, such as luminosity and variability timescale. The observed power is related to that emitted in the rest frame of the jet by $L_{obs} = L_{int}\delta^p$, where $p = 4$ for a moving blob and $p = 3$ for a continuous jet of plasma.

I.d Inhomogeneous Jet Model

The jet-like geometry for blazars gave rise to several theoretical models for the emission (see review of Bregman 1990). The simplest one, which postulates a homogeneous region and a power-law energy spectrum for the electrons ($N(E) \propto E^{-s}$), cannot explain the full spectral energy distributions of BL Lac objects, which show an overall downward curvature when νF_ν is plotted as a function of ν. Either multiple components, an inhomogeneous or non-axisymmetric region, or non-power-law particle spectra are required (e.g. Königl 1989).

Since the size of an emitting region can be directly inferred from the light crossing time, the shorter flux variation timescales observed at shorter wavelengths (see § I.b) provide evidence for the inhomogeneity of the emission within the jet: the energy output at higher frequencies comes from progressively smaller regions, the X-rays being produced closest to the nucleus.

In the last decade, considerable progress has been made interpreting the broad-band spectra of blazars in terms of models of inhomogeneous relativistic jets (Marscher 1980; Königl 1981; Ghisellini et al. 1985, hereafter GMT; Worrall et al. 1986; Hutter & Mufson 1986; George et al. 1988). These models have been very successful in reproducing the radio through UV spectral energy distributions, in the sense that with a minimal number of parameters they usually fit the continuum spectrum over nearly 10 decades in wavelength. Unfortunately, the parameters of the model are rarely well-determined because a variety of assumptions can produce acceptable fits for a large volume of parameter space. The degeneracy of multiple model solutions vanishes or is greatly reduced when variability information is added because the change in spectrum with intensity is a strong diagnostic of the emission process (e.g. George et al. 1988; Mufson et al. 1990).

One of the most accredited pictures is the inhomogeneous relativistic jet model described in GMT, where the emitting region is made up of a paraboloid ending up in a cone. The plasma flow, described by the bulk motion Lorentz factor Γ, is relativistic and it accelerates outwards in the parabolic part of the jet (Ghisellini & Maraschi 1989). The electron density, maximum electron energy, magnetic field within the jet and the bulk acceleration are simple functions (power-laws) of the radial distance.

In this model the overall spectrum is the sum of the local contributions which have different spectra. Energetically, the dominant emission region is the outer part of the paraboloid, which radiates at 10^{13}–10^{14} Hz by synchrotron and in γ-rays by self-Compton, while the conical region, smoothly connected to the internal one, is necessary to account for the radio emission. Although the model is rather simplified, it contains a large number of free parameters, which often cannot be rigorously and uniquely determined by the data (see applications of the model to broad-band data of blazars in Sections 1.4 and 2.1.3).

Finally, alternatives to the relativistic jet model have been advanced. For instance, it has been proposed that gravitational micro-lensing of quasars by intervening galaxies could explain the high apparent luminosities and lack of line emission (Ostriker & Vietri 1985; 1990; Stickel et al. 1988; Schneider & Weiss 1987); this picture is however affected by several problems and inconsistencies (see Urry & Padovani 1993). It has also been suggested that the optical-UV emission could be thermal radiation from an accretion flow (Wandel & Urry 1991).

I.e The "Shock-in-jet" Model

Radio flux monitoring observations of the entire core/jet region have been also interpreted in terms of a jet model (see Bregman 1990, and references therein). These studies show flux density outbursts with corresponding variations in the angle and degree of polarization that can be understood in a model where a shock propagates down a jet of plasma, compressing high density parcels of plasma and altering their emission properties. The shock compresses the plasma, preferentially raising the component of the magnetic filed parallel to the shock front, and imparts a velocity to the plasma that results in significant relativistic boosting. Since one expects the mean velocity of the shock to be along the jet axis, the magnetic field will be oriented approximately perpendicular to the jet axis, a result seen directly in the VLBI observations (e.g. Gabuzda et al. 1992). A shock wave passing through an adiabatic, conical, relativistic jet not only reproduces this broad-band variability, but also naturally leads to relatively flat radio spectra. Optical polarization measurements further support this model. Although the position angle of polarization can vary considerably, it often has a preferred value, a mean or most frequently observed angle. This preferred position angle is well correlated with the VLBI structural axis, again implying a magnetic field perpendicular to the jet axis for the much smaller optical region. Several lines of evidence support a "shock-in-jet" model, which appears to be valid in the whole radio through X-ray region (e.g. Celotti et al. 1991; Marscher et al. 1992).

I.f Unifying Schemes

The presence of an extended structure in AGN such as a jet determined the formulation of a unifying scheme in which intrinsically similar objects appear different mainly due to effects of orientation of the jet with respect to the observer. Within this scenario, blazars could be radio galaxies with jets directed at small angles with the line of sight, so that they are seen perfectly face-on, their radio spectra are extremely flat and their radio luminosities relativistically enhanced.

The absence of lines in BL Lacs was explained as due to a more intense beaming than in OVV so that the boosted continuum swamps out the emission features. This would imply that BL Lacs are objects similar to OVV, but their jets are seen at smaller angles. The observation of higher Doppler factors and larger core-dominance parameters (Madau et al. 1987; Ghisellini et al. 1993) and of higher luminosities in OVV (Section 1.1) rules out this picture and leads to consider the two classes as distinct. Thus emission lines are *intrinsically* more luminous in OVV than in BL Lacs. Netzer et al. (1994) suggest that a highly boosted ionizing continuum such as present in OVV can affect the line radiation, enhancing its intensity as well. Nonetheless, it may happen that some very distant objects have so largely boosted continua (otherwise they would not be visible due to their great distance) that their lines are washed out during the continuum outbursts, so that their classification can be matter of controversy (e.g. 3C 279, 3C 446, Browne 1989; see also Moore & Stockman 1981).

There is now definite agreement that BL Lacs and OVV constitute intrinsically different classes. Urry & Padovani (1993) conclude from comparison of X-ray slopes, [O III] line luminosities and polarization structure that BL Lacs and OVV are not compatible with a same parent population. For different orientations of the nonthermal jet, relativistic Doppler boosting can produce BL Lac objects or FR I radio galaxies, or at higher jet luminosities, flat-spectrum high-polarization quasars or FR II radio galaxies (Bregman 1990; Urry & Padovani 1993). Observations at radio, mm and sub-mm wavelengths of Gear et al. (1994) support such distinction in terms of different orientations of the magnetic fields, particularly during the quiescent states of the examined sources.

The distinction between radio-selected and X-ray-selected BL Lacs, which received recently further observational support (Giommi et al. 1994), is based on their discovery and is related to the jet orientation (see however Chapter 1 for a classification criterion independent from the source selection). The plasma is moving at relativistic velocities within the jet (see above) with outwardly increasing bulk motion Lorentz factor (typically 2÷10). This causes a progressively decreasing opening angle and increasing collimation with distance along the jet. Since X-ray emission is likely produced close to the nucleus, it is isotropic (i.e. not beamed), while lower frequencies radiation is relativistically beamed. Radio-loud BL Lacs should be those with the beam pointing toward the observer or misaligned by no more than $\sim 15^\circ$, for which the radio emission is enhanced and the high energy radiation consequently depressed. For larger viewing angles (up to $\lesssim 30^\circ$), the radio frequency output is less boosted toward the observer and then weakly affected by relativistic beaming. This explanation is supported by the dominance of radio-weak BL Lacs in terms of space density and by the wide range of radio luminosities seen in blazars (more than two decades) compared with the more restricted range of X-ray luminosities (Maraschi et al. 1986b; Padovani & Urry 1990; Celotti et al. 1993; MCG).

I.g Environment and Evolution

Blazars are known to generally reside in giant elliptical galaxies, the only exception being probably the object A 1415+25, which lies in a spiral. The host galaxies of BL Lacs exhibit an average absolute magnitude of ~ -23, which puts them at the bright end of the luminosity function of normal ellipticals (Ulrich 1989).

The environments of BL Lacs have been poorly investigated with respect to those of quasars, since in the former case the faintness of the spectral lines with respect to the continuum hinders the derivation of the redshift and thus the proof of the physical association with nearby galaxies. Imaging and spectroscopy of blazar host galaxies are presented by Falomo et al. (1993b,c; 1994c), who found that BL Lacs may be often found in rich environments, i.e. in galaxy clusters or groups. In some cases (see e.g. Falomo 1991; Falomo et al. 1993b) the detection of absorption features in the spectrum of the nebulosity which surrounds the BL Lac nucleus allows the determination of the object redshift.

Studies of the host galaxies and environment of BL Lacs offered a powerful diagnostic for AGN unification. For instance, the BL Lac H 0414+009 is found in an environment consistent with those in which FR I radio galaxies, the proposed parent population of BL Lacs, are often found (Falomo et al. 1993c). Based on the comparison of the absolute magnitudes of 15 low redshift BL Lacs ($z \lesssim 0.2$) with those of the B2 catalog of medium bright radio galaxies, Ulrich (1989) concluded that the latter form the parent population of the BL Lacs with nebulosity. BL Lacs are those radio galaxies whose jet is nearly along the line of sight. It is deduced that the cosmic evolution and other properties such as cluster or group membership should be the same for the nearby BL Lacs and for medium bright radio galaxies. Weak evolution in number and luminosity with cosmic time is found in the B2 radio galaxies, and the same is therefore expected also for BL Lacs. In fact, it has been shown by Woltjer & Setti (1982) that the nearby BL Lac objects form a population which does not evolve with cosmic time.

I.h Outline of the Present Work

The two main issues of the thesis work are the study of multi-frequency spectral flux distributions and the analysis of flux and spectral variability of blazars. To this regard, the far-UV band (1000–3000 Å) covered by the satellite *International Ultraviolet Explorer* (IUE, see Boggess et al. 1978 for details about the spacecraft and scientific instrumentation) has in AGN the important advantage, with respect to the optical and near-IR, of a lesser contamination by the stellar light of the host galaxy. This enables a reliable determination of the nonthermal continuum.

The thesis is divided as follows: Chapter 1 is devoted to the first part of the research program, consisting of the study of the near-IR, optical, UV spectral properties of blazars. In Section 1.1 are reconsidered the IUE archives, with the aim of determining the average UV spectral properties of a rather large sample of blazars. In Section 1.2 are presented the near-IR, optical, UV spectra of BL Lacs based on simultaneous observations. One of these sources is a γ-ray emitter, so its overall radio-to-γ-ray energy distribution is constructed and discussed in Section 1.4. The results of multi-frequency monitoring campaigns on the three blazars PKS 2155–304 (Section 2.1), OJ 287 (Section 2.2) and 3C 279 (Section 2.3) will be presented in Chapter 2. Particular enphasis will be put on the UV light curves, which represent my direct contribution to the wide international collaboration engaged for these multi-wavelength observing projects. The correlation of light curves at different wavelengths is also discussed in the case of PKS 2155–304 (§ 2.1.2). In Appendix A are reported the fit parameters for the 201 IUE spectra of PKS 2155–304. Appendices B and C contain the IUE extracted spectra of OJ 287 and 3C 279 respectively.

The work presented in this thesis is partially published or in progress. Part of the material included in Chapter 1 is presented in Pian & Treves (1993); Pian, Falomo, Scarpa & Treves (1994a) and Pian, Falomo, Ghisellini, Maraschi, Sambruna, Scarpa & Treves (1994c; Sections 1.1, 1.2 and 1.4 respectively). In Chapter 2 are collected the results presented in the papers by Urry et al. (1993), Edelson et al. (1994a), Pian et al. (1994b) and Maraschi et al. (1994b), corresponding respectively to Sections 2.1.1, 2.1.2, 2.2, 2.3.

Chapter 1

Spectral Properties of Blazars

The spectral properties of blazars are widely studied at all frequencies from radio to γ-rays (see reviews of Bregman 1990; 1994; Kollgaard 1994).

Single epoch multi-frequency observations allow to construct spectral flux distributions of blazars over an extended energy range and to evaluate the overall spectral slope. It is crucial that monochromatic fluxes, measured by different instruments, are taken strictly close in time; otherwise, possible temporal flux variations can result in unreal colour changes and then cause spurious spectral breaks or features. The variability timescales in blazar AGN range from few hours (X-rays) to months or years (radio and IR wavelengths, see Introduction, § I.b), thus the simultaneity requirement depends on the observing energy band: time separations of $\lesssim 1$ day between observations at different wavelengths are needed to avoid variability effects of unphysical nature in the IR-to-UV spectral region.

If several repeated multi-frequency observations are available for a blazar, the additional issue of variability can be investigated, which adds temporal information to the spectral and flux characteristics. It is very important to this regard to perform, at all the studied energies, a continuous and regular monitoring (i.e. without time gaps in the total observing duration) with frequent sampling still to avoid a "mismatch" between fluxes in different bands due to short-term variations ($\lesssim 1$ day) and to resolve small flares due to extremely short-term variability (microvariability). Repeated observations moreover provide information on the correlation between the monochromatic light curves and allow to test the models of energy production at different frequencies (see § 2.1.2). Single epoch multi-frequency observations will be a crucial item in this Chapter (Sections 1.2 and 1.4), while multi-frequency monitoring campaigns on blazars will be illustrated in Chapter 2.

As explained in the Introduction section, the UV data presented in this thesis come from IUE observations. The IUE satellite did not perform a systematic survey of the UV sky, but during its long life it detected many extragalactic sources, allowing the compilation of many catalogs and lists of UV bright AGN (Kinney et al. 1991a; Edelson et al. 1992, hereafter E92; Lanzetta et al. 1993; Courvoisier & Paltani 1992) and statistical studies of the UV properties of the blazar class.

From knowledge of the average spectral properties of blazars in the UV, a typical UV blazar spectrum arises directly comparable with the models and with characteristic behaviours at other frequencies. The first part of this Chapter (Section 1.1) contains a study of the UV spectral properties of blazars. This work is based on IUE archival data analysed in a homogeneous way and properly corrected for the galactic extinction.

Section 1.2 is devoted to the presentation of simultaneous near-IR-optical-UV observations of a list of 11 BL Lacs included in the sample studied in the previous Section. These selected objects belong to a 10 years research program aimed at determining the physical processes responsible for the large luminosities and smooth spectral continua of BL Lacs. The continuum emission in AGN is thought to arise closer to the center than the line emission, and since BL Lacs are the AGN for which the continuum is most dominant, their behavior may yield clues about the physical conditions nearest the center. Unlike the less active AGN (normal quasars and Seyfert galaxies), BL Lacs have highly polarized optical-IR continua, which are generally devoid of strong, broad emission lines. This suggests that with BL Lacs, we may be seeing as close as possible to the central engine, without complications such as emission or obscuration from surrounding regions.

The spectral shape is analysed in the frequency range from $8{\cdot}10^{13}$ to $2{\cdot}10^{15}$ Hz. This energy band is particularly important since, according to the inhomogeneous jet model, it is far from the maximum emitted frequency within the paraboloid region, occurring around $\sim 3 \cdot 10^{13}$ Hz, and, on the other hand, the IC scattering in unlikely to take place at far-UV energies. Thus the IR-to-UV radiation is likely produced via pure synchrotron process within the paraboloid region. Therefore, the observation of active galaxies at those frequencies carries information on an emitting zone which is supposedly very close to the power house and dominated by the synchrotron mechanism.

Among the selected objects, PKS 0521–365 and PKS 2005–489 were detected with marginal significance by the EGRET experiment (4.4 and 4.3σ respectively, Fichtel et al. 1994). An overall spectrum of PKS 0521–365 exhibiting clear nonthermal nature from radio to γ-ray frequencies is shown in Section 1.4, where we particularly focus on IUE and EXOSAT simultaneous observations for this object. Rosat and *Einstein* observations of the source at different epochs are discussed as well.

1.1 The Ultraviolet Continua of Blazars

The UV region of the spectrum is of particular interest because, unlike the optical and IR, it is practically unaffected by the contribution of the host galaxy, and it is close to the region where the energy distribution νF_ν apparently peaks (extreme-UV (EUV)/soft-X-ray band).

The potentiality of IUE archives for exploring the average properties of the UV continuum of blazars were first appreciated by Ghisellini et al. (1986, hereafter GMTT) who considered the IUE spectra up to 1984. Similar data were examined also by Bregman et al. (1987). Since that time, IUE observations of blazars have expanded substantially, and the IUE archives have been explored systematically. Kinney et al. (1991a) retrieved all the good signal-to-noise ratio (S/N) IUE spectra of AGN archived before 1988 and produced an atlas of extracted spectra using the rather advanced Slit-Weighted Extraction Technique (SWET, Kinney et al. 1991b). Lanzetta et al. (1993)

analysed those IUE archival spectra which did not satisfy the selection criteria of Kinney et al. (1991a), in search of strong absorption features. E92 concentrated on the subsample of BL Lac objects, studying in particular their variability (Edelson 1992). An independent analysis of the IUE archives of AGN observed up to 1988 was performed by Courvoisier & Paltani (1992) using the IUESIPS extraction procedure. Based on this systematic analysis, these authors studied the variability properties of active galaxies, including 18 BL Lacs (Paltani & Courvoisier 1994).

Of importance is the extraction procedure of the spectrum, which implies a number of steps like filtering, background correction, error evaluation, calibration and conversion into physical units. Several procedures have been adopted to this goal. The current standard software is IUESIPS, which uses a boxcar extraction. In the SWET procedure developed by Kinney et al. (1991b), empirical spline fits are made to the cross-dispersion point spread function (PSF) along the spectrum, which constrains the PSF to vary smoothly in the dispersion direction. This imposition of information contributes to an improvement in the S/N of the extracted spectrum relative to IUESIPS, while flux is still conserved. The flux at each wavelength is then determined by fitting the empirically determined profile, sample by sample, weighted according to a noise model determined from studies of hundreds of unrelated IUE images. Discrepant points are eliminated, which automatically removes most of the cosmic rays, with the exception of those that fall exactly at the center of the cross-dispersion profile. An uncertainty is associated with each flux value based on the noise model. Extensive comparisons of SWET-extracted and boxcar-extracted spectra show no systematic disagreement between the two. Note that SWET-extracted spectra are the standard output for low-dispersion images in the Final IUE Archive that is now being created jointly by NASA, ESA, and SERC. There is another slit-weighted technique, the Gaussian extraction or GEX method (Urry & Reichert 1988), which assumes the cross-dispersion profile is a Gaussian. Because of this additional constraint, GEX gives a somewhat better S/N than SWET for very low S/N data, but for well-exposed spectra, systematic problems at the level of a few percent can occur because the true PSF is not precisely Gaussian. GEX consists of two passes on the line-by-line file, one coarse and one fine. The first pass, GEX1, fits a linear background plus a Gaussian to a series of cross-cuts (signal perpendicular to the dispersion direction). All fit parameters are stored in a table. In an intermediate step, the Gaussian widths are fitted to a quadratic, allowing for a smoothly changing focus along the spectrum. The second pass, GEX2, uses the same Gaussian-plus-linear-background model, but calculates only the height of the Gaussian for each cross-cut, taking the appropriate linear background coefficients and Gaussian centers from the table and imposing Gaussian widths determined from the quadratic fit. The width and height of the Gaussian determine its area and thus the flux at that particular cross-cut. The automatic GEX algorithms currently available do not produce an error vector.

Here we reconsider the UV spectral properties of the set of blazars defined in the § 1.1.1. The sample (47 objects observed with IUE, see Table 1.1) increased by $\sim$ 50% with respect to that examined in GMTT, allowing a more detailed comparison of the various subclasses of blazars (radio-strong, radio-weak BL Lacs, OVV). A key consideration in this kind of study is the reddening correction, which in this study is performed using the galactic neutral hydrogen columns obtained from radio surveys at 21 cm.

The present study is based on the atlases of reduced spectra mentioned above. From such atlases we also retrieved the spectra of a substantial fraction of *Palomar Green* bright quasars, which allows a direct comparison of the two classes of AGN (§ 1.1.2).

TABLE 1.1
IUE DATA OF ULTRAVIOLET-BRIGHT BLAZARS

Coordinates (1)	Name (2)	(3)	z^a (4)	F_{1400} (mJy) (5)	σ_F^b (6)	α_{SWP} (7)	σ_α (8)	N^c (9)	F_{2800} (mJy) (10)	σ_F (11)	$\alpha_{LWP/R}$ (12)	σ_α (13)	N (14)	F_C^d (mJy) (15)	σ_F (16)	α_C^e (17)	σ_α (18)	N (19)	A_V (mag) (20)
0048−097	OB 80	R^f	...	0.78	0.48	1.19	0.40	2	1.98		0.84		1	1.49		0.82		1	0.22
0118−272	OC 230.4	R	0.559	...	...	...	...	...	0.74		2.60		1	...	...	...	...	...	0.09
0215+015	OD 26	R	1.715	...	...	...	...	...	1.11	0.33	3.17	0.97	5	...	...	...	...	...	0.21
0219+428	3C 66A	R	0.444	1.38	0.10	0.77	0.20	5	3.14	0.24	0.19	0.24	2	2.04		1.08		1	0.46
0235+164	AO	R	0.940	...	...	...	...	...	0.64		1.12		1	...	...	...	...	...	0.57
0301−243	PKS	R	...	0.41		1.15		1	0.73		0.11		1	0.55		0.81		1	0.11
0323+022	H	X	0.147	0.67	0.15	0.03	0.08	4	0.83	0.27	−0.72	0.43	3	0.74	0.19	0.30	0.47	3	0.51
0414+009	H	X	0.287	0.72	0.05	0.13	0.07	2	0.56	0.25	1.18	1.35	3	0.80		0.16		1	0.51
0422+004	OF 38	R	...	0.54	0.19	1.50	1.01	3	0.92	0.22	1.90	1.60	3	0.66	0.04	1.26	0.36	2	0.44
0521−365	PKS	R	0.055	0.36	0.06	0.52	0.94	8	0.74	0.20	2.66	2.02	5	0.65		0.93		1	0.22
0537−441	PKS	R	0.894	...	...	...	...	...	1.33	0.24	1.71	0.48	3	...	...	...	...	...	0.20
0548−323	A	X	0.069	0.45	0.04	0.40	0.42	2	...	...	...	...	...	...	...	...	...	...	0.14
0637−752	PKS	R	0.656	1.20	0.15	0.96	0.13	3	1.86	0.28	−0.90	0.16	4	1.29		0.63		1	0.38
0716+714	...	R	...	0.14		0.72		1	...	...	...	...	...	...	...	...	...	...	0.23
0735+178	OI 158	R	0.424	0.89	0.59	2.47	0.46	6	2.87	1.61	1.07	0.47	7	1.39	1.22	1.63	0.54	3	0.29
0736+017	OI 061	R,E	0.191	0.89	0.22	2.82	1.77	3	1.23		0.95		1	...	...	...	...	...	0.63
0754+100	OI 90.4	R	...	0.60	0.24	1.07	0.33	4	1.60	0.65	1.41	0.54	4	0.98	0.40	1.40	0.09	4	0.17
0829+046	OJ 49	R	0.180	0.74	0.33	1.24	0.12	3	3.28		0.98		1	1.80		1.74		1	0.19
0851+202	OJ 287	R	0.306	1.57	1.06	1.12	0.29	25	3.16	2.10	1.21	0.47	21	2.15	1.44	1.20	0.28	18	0.18
0912+297	Ton 396	R	...	0.63		1.43		1	1.58		1.14		1	0.99		1.33		1	0.13
1101−232	H	X	0.180	0.33		0.03		1	...	...	...	...	...	...	...	...	...	...	0.35
1101+384	Mkn 421	X	0.031	4.70	2.65	0.67	0.25	37	7.85	3.78	0.75	0.21	41	5.98	3.19	0.72	0.13	39	0.11
1133+704	Mkn 180	X	0.046	0.71	0.33	0.82	0.18	2	1.21	0.10	1.76	1.12	4	...	...	...	...	...	0.09
1156+295	Ton 599	R,E	0.729	0.69	0.67	1.45	1.21	8	3.88	2.67	0.99	0.63	3	2.21	1.51	1.60	0.08	3	0.10
1215+303	Ton 605	X	...	0.95	0.23	0.95	0.09	2	...	...	...	...	...	...	...	...	...	...	0.10
1219+285	W COMA	R	0.102	0.46		1.15		1	1.07		1.07		1	0.70		1.22		1	0.11

TABLE 1.1 (continued)

Coordinates (1)	Name (2)	(3)	z (4)	F_{1400} (mJy) (5)	σ_F (6)	α_{SWP} (7)	σ_α (8)	N (9)	F_{2800} (mJy) (10)	σ_F (11)	$\alpha_{LWP/R}$ (12)	σ_α (13)	N (14)	F_C (mJy) (15)	σ_F (16)	α_C (17)	σ_α (18)	N (19)	A_V (mag) (20)
1219+305	2A	X	0.130^g	0.64	0.01	0.60	0.30	2	0.93		0.54		1	0.78		0.52		1	0.10
1253−053	3C 279	R,E	0.538	1.61	0.62	1.55	0.22	5	4.33	1.84	1.84	0.43	7	2.87	0.98	1.45	0.16	6	0.13
1308+326	OP 313	R	0.997	0.28		2.22		1	0.53	0.04	2.55	2.38	3	…	…	…	…	…	0.07
1415+259	A	X	>0.237	0.24		0.85		1	…	…	…	…	…	…	…	…	…	…	0.10
1418+543	OQ 530	R	0.152	0.28	0.14	1.42	0.36	3	1.15	0.51	1.96	0.16	2	0.64	0.18	1.61	0.49	2	0.08
1510−089	PKS	R,E	0.360	0.61	0.13	0.24	1.42	2	1.06		0.73		1	…	…	…	…	…	0.46
1514−241	AP Lib	R	0.049	…	…	…	…	…	2.62	1.45	0.79	0.50	2	…	…	…	…	…	0.54
1538+149	4C 14.6	R	0.605	…	…	…	…	…	0.22		1.80		1	…	…	…	…	…	0.20
1553+113	PG	X	…	1.67	0.88	1.21	0.28	4	3.36	1.81	0.65	0.31	4	2.36	1.26	0.99	0.19	4	0.22
1641+399	3C 345	R,E	0.594	0.52	0.22	1.88	0.22	5	1.47	0.48	−0.95	1.23	2	1.26		1.04		1	0.06
1652+398	Mkn 501	X	0.034	1.67	0.14	0.62	0.19	11	2.93	0.13	0.90	0.41	6	2.18	0.08	0.77	0.13	3	0.10
1722+118	A	X	>0.100	0.87	0.17	0.59	0.49	3	1.86	0.41	1.96	0.96	4	1.29	0.21	1.17	0.44	3	0.51
1727+502	ZW 187	X	0.055	0.44	0.14	0.97	0.75	6	0.62	0.06	1.00	0.40	3	0.51	0.10	0.61	0.42	3	0.17
1807+698	3C 371	R	0.051	1.06	0.33	0.92	0.19	9	2.07	0.39	1.29	0.60	9	1.42	0.22	1.11	0.16	7	0.30
1845+797	3C 390	X,E	0.057	0.52	0.16	−0.22	0.87	20	0.83	0.13	1.23	1.39	9	0.72	0.12	0.44	0.26	7	0.26
1921−293	PKS	R	0.352	…	…	…	…	…	1.82		1.47		1	…	…	…	…	…	0.49
2005−489	PKS	X	0.071	5.44	1.59	0.62	0.15	13	9.14	2.32	0.08	0.11	13	7.25	2.13	0.74	0.12	10	0.33
2155−304	PKS	X	0.116	11.35	2.68	0.62	0.12	174	17.44	4.05	0.68	0.22	162	14.23	3.26	0.60	0.11	168	0.10
2200+420	BL Lac	R	0.070	…	…	…	…	…	2.93	1.36	−0.54	1.06	9	…	…	…	…	…	1.19
2223−052	3C 446	R,E	1.400	0.21		0.35		1	0.61	0.61	3.92	1.77	16	0.49		2.39		1	0.34
2251+158	4C 11	R,E	0.859	0.32		1.51		1	…	…	…	…	…	…	…	…	…	…	0.39

[a] Redshift (a superscript ^{g}, means that the value is based on the host galaxy photometry)

[b] The reported errors represent standard deviations

[c] Number of used spectra

[d] Effective flux at 1980 Å

[e] Combined energy spectral index in the IUE-wide range (1200–3000 Å)

[f] R, radio-strong objects; X, radio-weak objects; E, strong emission-line sources (OVV)

1.1.1 Blazars Observed with IUE

1.1.1.1 Selection Criteria

The IUE archives include a classification of different types of targets, one of which corresponds to BL Lac objects. This classification, which is responsibility of the observing team, is the starting point for the build up of the list of blazars observed with IUE, but it is not free of ambiguities. We therefore integrated and amended this list from a number of compilations of blazars available in the literature and compared with the IUE log. For BL Lac objects, we used in particular Veron-Cetty & Veron (1989), Hewitt & Burbidge (1987; 1989), Impey & Tapia (1988), while for OVV we used Moore & Stockman (1981; 1984), Ledden & O'Dell (1985), Ghisellini et al. (1993).

The distinction between radio-strong (RSBL) and radio-weak (RWBL) BL Lacs (which essentially corresponds to the somewhat ambiguous denomination "radio-selected" and "X-ray-selected") follows the criteria proposed by Ledden & O'Dell (1985). One object (Ton 396) is so far not revealed in X-rays, so we have considered it as radio-strong emitter. Some uncertainty remains. For instance, we did not consider 3C 273 and NGC 1275 as blazars. The distinction between BL Lacs and OVV may also be ambiguous, especially when large variations of the line equivalent widths are present (see § I.f).

Our list of blazars is given in Table 1.1, where we report the UV properties of 24 RSBL, 15 RWBL, and 8 OVV. Obviously the list does not represent in any sense a well defined sample, but only the result of retrieval from IUE archives.

1.1.1.2 Analysis and Dereddening Procedure

For a large part of the sources contained in Table 1.1, spectral indices and fluxes at fixed wavelengths (1400 Å and 2800 Å) have been derived by E92 separately fitting the spectral flux distributions obtained with the three cameras of IUE, i.e. the Short Wavelength Primary (SWP, range: 1200–1950 Å) and the Long Wavelength Primary and Redundant (LWP/R, range: 2000–

3000 Å). When more than one observation was available for an object, the average spectral index was calculated as well as the mean flux.

For the few objects which do not appear in the E92 list, we reproduced an analysis similar to that of E92 using the IUESIPS extracted spectra available from the ULDA archive. In particular, for each spectrum, the average fluxes were calculated in bands of 50 or 100 Å and fitted to a single power-law ($F_\nu \propto \nu^{-\alpha_\nu}$). In order to evaluate the difference which may be introduced by the use of the two extraction methods we examined a number of sources with both procedures. We found that the monochromatic fluxes were in agreement within 10% and the spectral indices within ± 0.2. This point is further discussed in § 1.1.2. The quoted uncertainties cover also the systematic errors in the calibration of IUE cameras.

The correction for the galactic extinction is taken into account by first obtaining the column density $N_{\rm H}$ in the direction of each source as measured with the 2° × 3°-beam 21-cm survey of Stark et al. (1992). Assuming $N_{\rm H}/E(B-V) = 5.2 \times 10^{21}$ (Shull & Van Steenberg 1985), $A_V/E(B-V) = 3.1$ (Rieke & Lebofsky 1985) the extinction A_V is deduced. The data are dereddened using the average Galactic curve given by Seaton (1979). The dereddening procedure acts on the power-law trasforming it into a spectral flux distribution which we again best fitted to a power-law, eventually obtaining the dereddened indices and fluxes as fitting parameters.

For each source, the average dereddened flux and slope are given in Table 1.1 together with the standard deviation with respect to the mean and the numbers of used spectra. Values of A_V are given as well.

For the 29 objects for which IUE spectra are available in both bands (SWP and LWP/R), an effective spectral index in the 1200–3000 Å band was calculated with the following formula (E92):

$$\alpha_C = \frac{log(F_{2800}/F_{1400})}{log2} \quad . \tag{1.1}$$

One can also define an effective flux at ∼ 1980 Å:

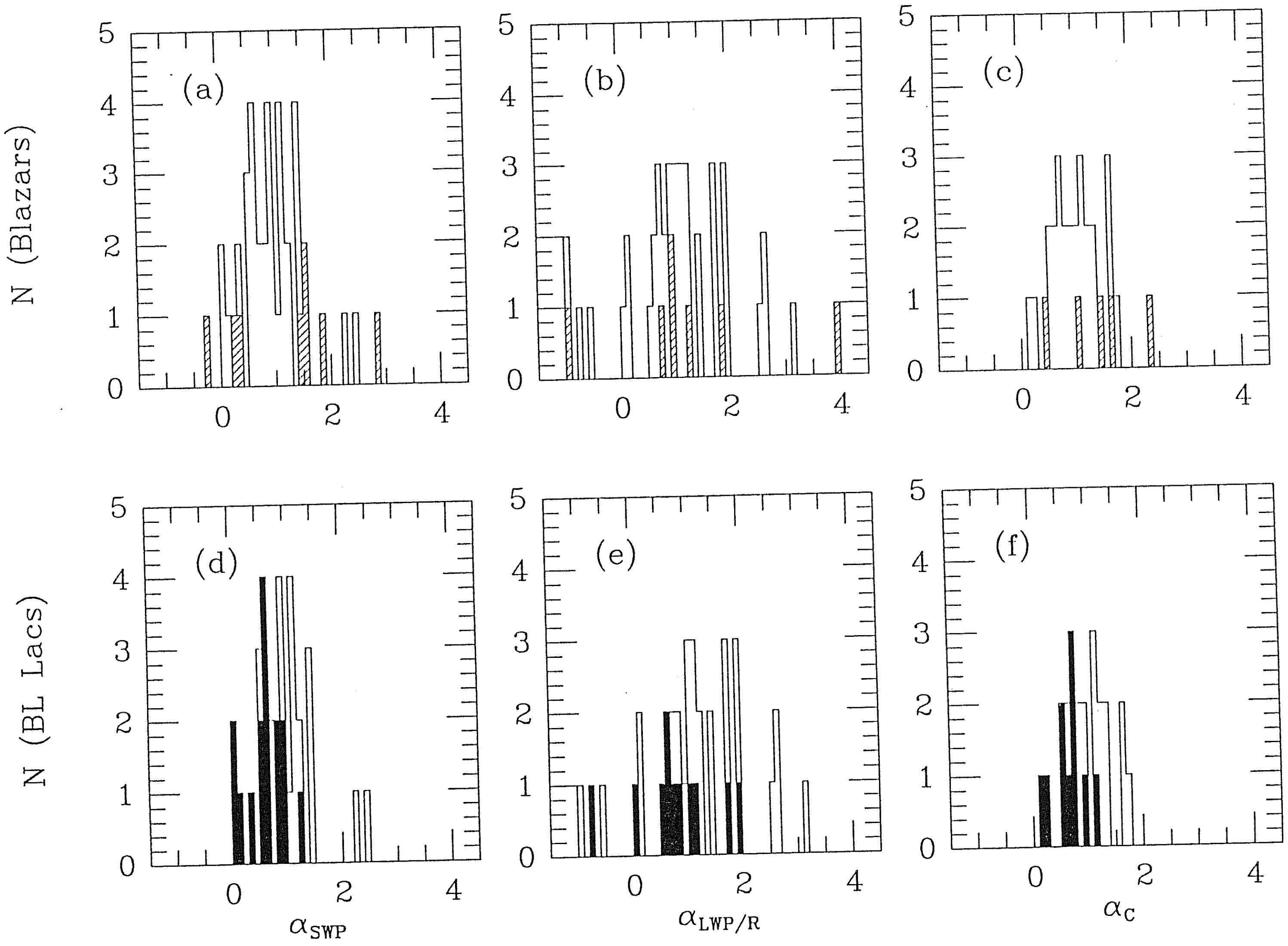

FIG. 1.1 – Distribution of UV spectral indices. *(a)* SWP spectral indices of blazars. The hatched area corresponds to OVV objects. *(b)* Same as (a) with LWP indices. *(c)* Same as (a) with combined indices. *(d)* SWP spectral indices of BL Lac objects. The shaded area corresponds to radio-weak sources. *(e)* Same as (d) with LWP indices. *(f)* Same as (d) with combined indices.

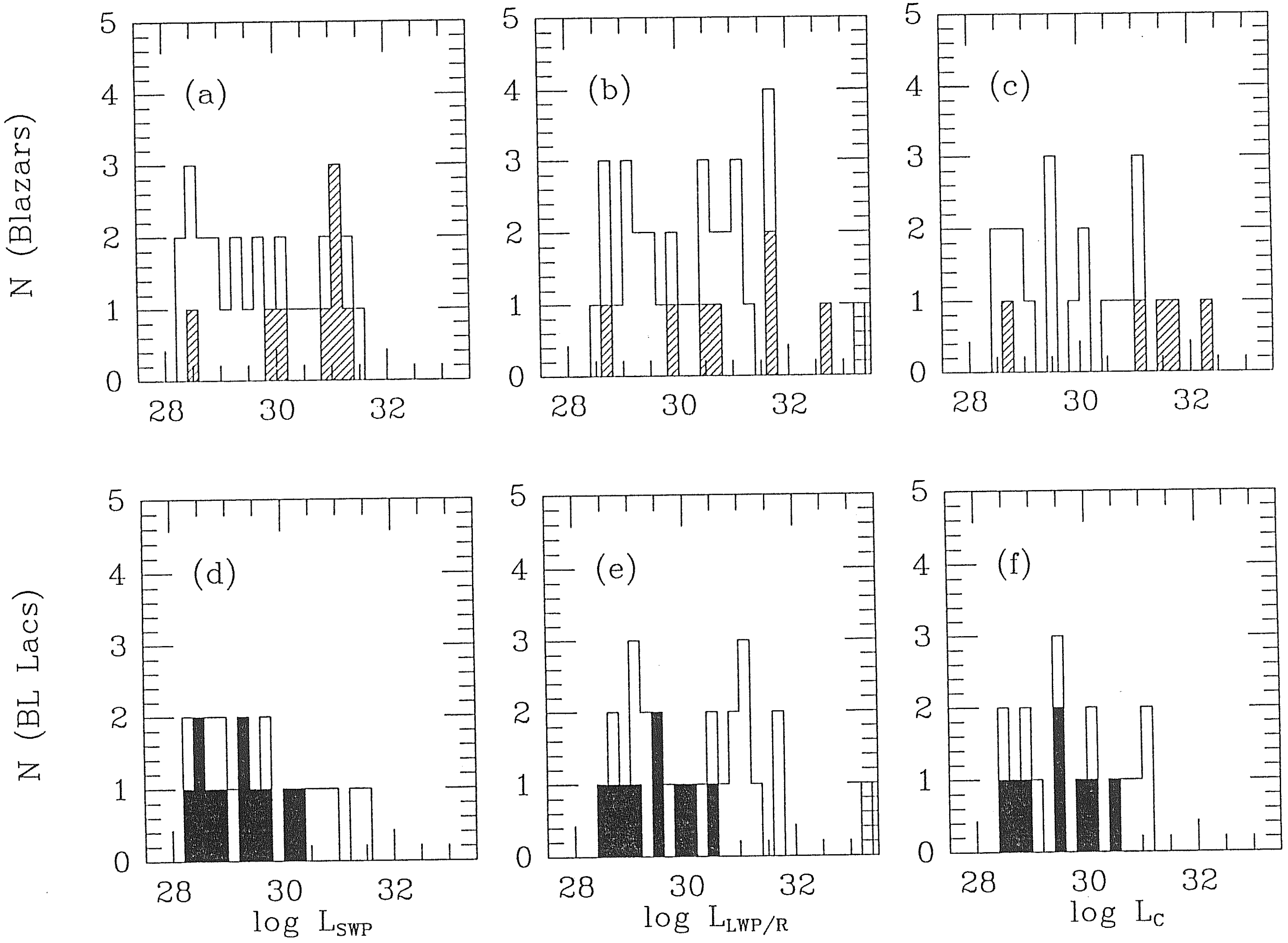

FIG. 1.2 — Distribution of monochromatic UV luminosities. *(a)* Luminosities of blazars at 1400 Å in units of erg s^{-1} Hz^{-1}. The hatched area corresponds to OVV objects. *(b)* Same as (a) with luminosities at 2800 Å. *(c)* Same as (a) with luminosities at 1980 Å. *(d)* Luminosities of BL Lac objects at 1400 Å. The shaded area corresponds to radio-weak sources. *(e)* Same as (d) with luminosities at 2800 Å. *(f)* Same as (d) with luminosities at 1980 Å.

$$F_C = \sqrt{F_{1400} \times F_{2800}} \quad , \tag{1.2}$$

where F_{1400} and F_{2800} are in units of erg s^{-1} cm^{-2} Hz^{-1}.

Due to the variability of blazars, computation of the composite spectral index was made only between SWP and LWP/R observations not too far separated in time ($\lesssim$ 1 day).

1.1.1.3 *Spectral Shape and Energy Distribution*

In order to calculate the UV luminosities, the k-correction was performed on the IUE fluxes for the objects with known redshift z (see GMTT),

$$F = F^{obs}(1+z)^{\alpha-1} \quad . \tag{1.3}$$

Distances are evaluated assuming $H_0 = 75$ km s^{-1} Mpc^{-1} and $q_0 = 0$.

The spectral indices and UV luminosities (in units of erg s^{-1} Hz^{-1}) for the short, long and total IUE wavelength ranges averaged over the whole set of objects are given in Table 1.2 with associated standard deviations.

The sample is divided in RSBL, RWBL and OVV, and the relevant parameters for each subset are given in Table 1.2. Distributions are shown in Figs. 1.1 and 1.2. Notice that the distribution of indices α_C in the entire band (1200–3000 Å) is narrower than those in the single bands. In our opinion this is because the combined indices α_C derived through eq. (1.1) are less uncertain than α_{SWP} and $\alpha_{LWP/R}$.

1.1.2 Bright Quasars

In order to compare the UV properties of blazars with those of quasars, we have considered the set of the *Palomar Green* Bright Quasars (BQS) observed in both IUE bands. Out of the 114 objects which constitute the BQS sample (Schmidt & Green 1983), 37 were retrieved from the ULDA IUE archives (Courvoisier & Paltani 1992), exhibiting well exposed spectra and good signal in both IUE energy ranges.

TABLE 1.2
MEAN SPECTRAL INDICES AND LUMINOSITIES

Parameter	Blazars	Strong Emission Lines Objects	BL Lac Objects	Radio-weak BL Lacs	Radio-strong BL Lacs	Palomar Green Bright Quasars
	(47)	(8)	(39)	(15)	(24)	(35)
α_{SWP}	0.99 ± 0.65 (39)[a]	1.20 ± 1.00 (8)	0.93 ± 0.54 (31)	0.61 ± 0.34 (15)	1.24 ± 0.51 (16)	...
$\alpha_{LWP/R}$	1.15 ± 1.02 (41)	1.24 ± 1.46 (7)	1.13 ± 0.93 (34)	0.80 ± 0.73 (11)	1.29 ± 0.99 (23)	...
α_C	1.04 ± 0.49 (29)	1.38 ± 0.72 (5)	0.97 ± 0.41 (24)	0.66 ± 0.30 (10)	1.20 ± 0.33 (14)	0.84 ± 0.52 (37)
log L^b_{SWP}	29.81 ± 1.04 (29)	30.50 ± 0.94 (8)	29.54 ± 0.98 (21)	29.18 ± 0.67 (11)	29.95 ± 1.13 (10)	...
log $L_{LWP/R}$	30.32 ± 1.22 (34)	30.88 ± 1.32 (7)	30.18 ± 1.17 (27)	29.40 ± 0.67 (9)	30.57 ± 1.19 (18)	...
log L_C	30.01 ± 1.13 (22)	31.02 ± 1.39 (5)	29.72 ± 0.89 (17)	29.42 ± 0.69 (8)	29.99 ± 0.99 (9)	30.24 ± 0.80 (37)

[a] Parentheses enclose number of objects used for each entry

[b] Monochromatic luminosities are in units of erg s^{-1} Hz^{-1}

TABLE 1.3

ARCHIVAL IUE DATA OF *PALOMAR GREEN* BRIGHT QUASARS

R.A. (1)		Dec. (2)		z (3)	F_{1400} (mJy) (4)	F_{2800} (mJy) (5)	α_C[a] (6)	F_C[b] (mJy) (7)	A_V (mag) (8)
00	07	10	41	0.090	1.23	3.61	1.55	2.11	0.35
00	26	12	59	0.142	1.62	2.13	0.40	1.86	0.28
00	44	03	03	0.624	0.65	1.42	1.12	0.96	0.18
00	50	12	25	0.061	1.69	4.97	1.56	2.90	0.31
00	52	25	09	0.154	2.29	2.14	−0.09	2.22	0.28
01	57	00	09	0.163	1.20	1.67	0.48	1.41	0.14
08	04	76	11	0.100	3.11	5.45	0.81	4.12	0.19
10	48	−09	02	0.345	0.37	0.55	0.58	0.45	0.20
10	49	−00	35	0.357	0.47	0.99	1.08	0.68	0.24
11	03	−00	36	0.426	0.47	1.39	1.56	0.81	0.24
11	15	08	02	1.722	0.34	0.77	1.19	0.51	0.22
11	16	21	35	0.177	4.27	4.49	0.07	4.38	0.08
11	48	54	54	0.969	0.73	0.86	0.25	0.79	0.07
11	51	11	45	0.176	1.05	0.86	−0.30	0.95	0.16
12	02	28	10	0.165	0.68	0.79	0.21	0.73	0.11
12	11	14	19	0.085	2.93	6.97	1.25	4.52	0.17
12	16	06	55	0.334	0.91	1.24	0.44	1.06	0.10
12	26	02	19	0.158	16.32	23.83	0.55	19.72	0.11
12	59	59	18	0.472	0.80	1.66	1.05	1.16	0.08
13	07	08	35	0.155	1.43	2.28	0.68	1.80	0.13
13	33	17	40	0.554	0.51	1.42	1.47	0.85	0.11
13	51	64	00	0.088	1.26	3.61	1.52	2.13	0.13
14	07	26	32	0.944	0.49	1.22	1.32	0.77	0.09
14	11	44	14	0.089	0.93	1.78	0.93	1.29	0.07
14	16	−12	56	0.129	1.08	1.27	0.24	1.17	0.38
14	25	26	45	0.366	0.29	0.41	0.51	0.34	0.10
14	26	01	30	0.086	4.06	7.03	0.79	5.34	0.17
14	40	35	38	0.079	2.13	2.91	0.45	2.49	0.06
15	12	37	01	0.370	0.51	0.91	0.82	0.68	0.08
15	22	10	09	1.321	0.45	1.42	1.65	0.80	0.18
15	52	08	31	0.119	0.33	0.75	1.21	0.49	0.21
16	13	65	50	0.129	1.31	1.78	0.44	1.53	0.18
17	04	60	48	0.371	0.74	1.11	0.58	0.91	0.14
21	12	05	55	0.457	0.66	1.57	1.25	1.02	0.40
21	30	09	56	0.063	3.25	5.13	0.66	4.08	0.28
22	14	13	59	0.067	1.10	2.22	1.01	1.57	0.31
23	02	02	55	1.044	0.46	1.37	1.58	0.79	0.32

---

[a] Combined energy spectral index in the IUE-wide range (1200–3000 Å)

[b] Effective flux at 1980 Å

Fluxes at 1400 and 2800 Å were derived from the average spectra by fitting them to a single power-law, after rejecting the broad emission lines, which strongly affect the continua. The spectra were then dereddened and the combined spectral index was deduced as described in the previous section. Results are summarized in Table 1.3 and Figs. 1.3 and 1.4.

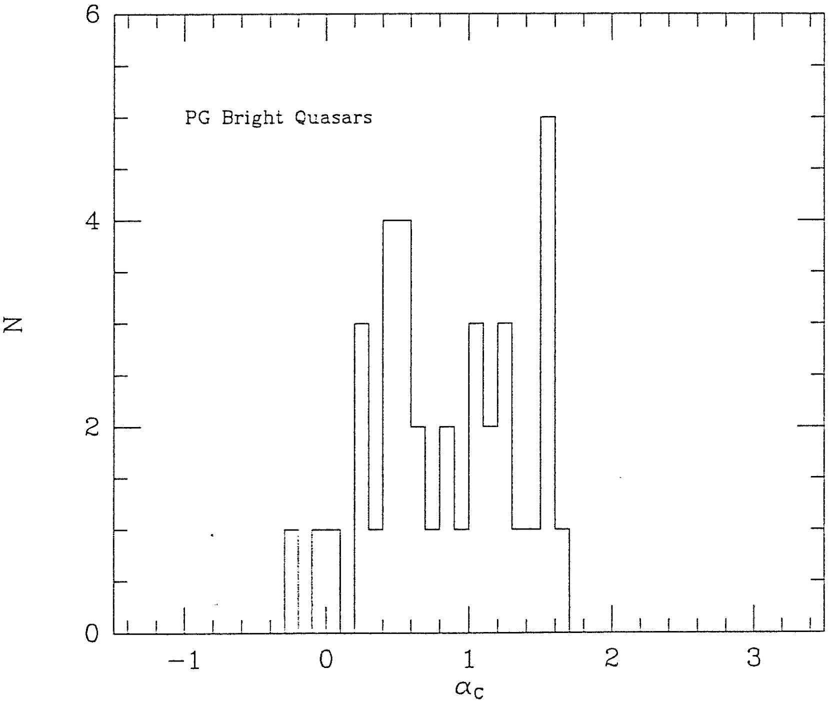

FIG. 1.3 — Distribution of UV spectral indices of *Palomar Green* Bright Quasars.

The mean spectral index of BQS is $<\alpha_\nu> = 0.84 \pm 0.52$. We also used the fluxes listed in Table 1.3 to derive the monochromatic luminosities, and obtained the total mean value $logL = 30.2 \pm 0.8$. This is comparable with the average UV luminosity of blazars.

In the Kinney et al. (1991a) atlas there are 11 BQS quasars with spectra in both IUE energy ranges. The average dereddened spectral index is $<\alpha_\nu>$ $= 0.85 \pm 0.37$, while for the corresponding Courvoisier & Paltani objects we find $<\alpha_\nu> = 0.86 \pm 0.41$, confirming the substantial equivalence of the two extraction procedures of IUE spectra.

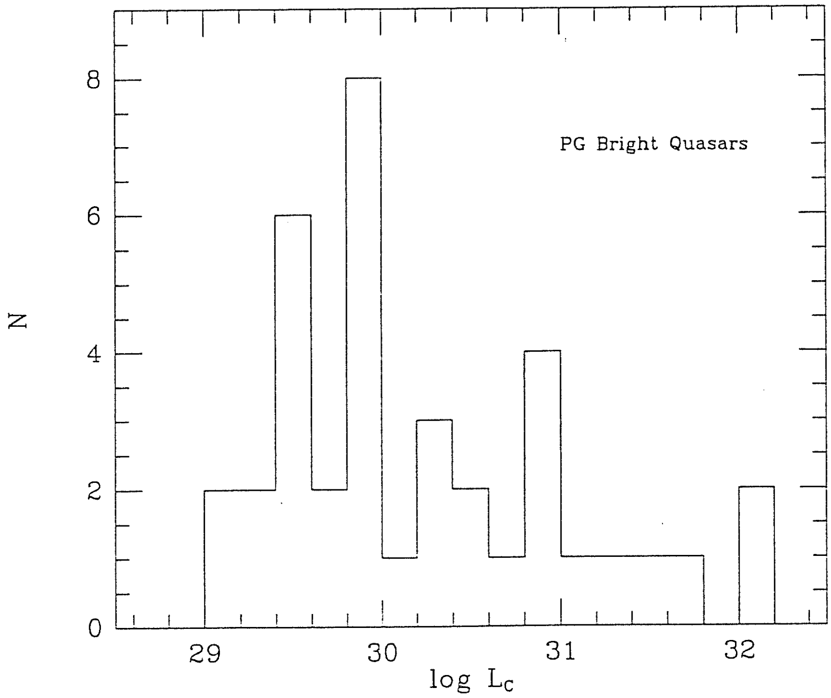

FIG. 1.4 — Distribution of monochromatic UV luminosities of *Palomar Green* Bright Quasars at 1980 Å.

1.1.3 Discussion

As shown in the first column of Table 1.2, the spectral indices in the two bands for the overall blazar sample are both close to 1, with a Kolmogorov-Smirnov (KS) test probability of deriving from a same population of $\sim$ 50%. Considering only RSBL, the KS probability increases to $\sim$ 75%. We interpret that as an indication of the substantial correctness of the dereddening procedure. There is some indication that for RWBL the average spectrum is steeper at longer wavelengths, but the KS probability that the indices in the two bands derive from the same distribution is still 50%. OVV are averagely more luminous than the BL Lacs, and with regard to spectral indices, they appear very close to RSBL.

The average values of the indices reported here correspond to a harder mean spectrum than those reported by GMTT ($\Delta\alpha \simeq 0.4$). We consider this to be due mainly to the fact that GMTT used an unsystematic reddening correction, a different analysis procedure, and a different sample than this study.

A clear difference appears when comparing RSBL and RWBL. The KS probability that the spectral indices derive from a same distribution is $\lesssim 1\%$. RWBL are flatter than RSBL ($\Delta\alpha_C \simeq 0.5$). This point was already noticed by GMTT.

In Fig. 1.5 we plot the composite UV index versus the radio-to-X-ray index calculated as

$$\alpha_{rx} = \frac{log(F_r/F_X)}{log(\nu_X/\nu_r)} \quad , \tag{1.4}$$

where F_r and F_X are the radio and X-ray fluxes respectively, and ν_r and ν_X

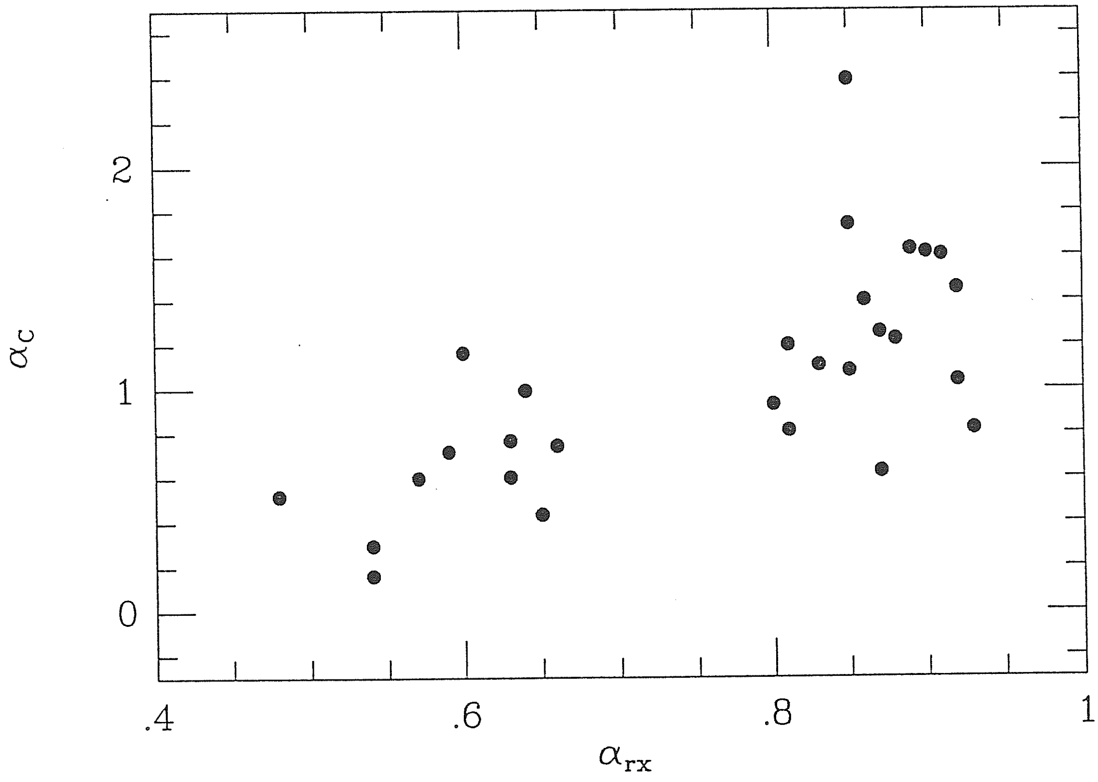

FIG. 1.5 — Combined UV spectral index versus the radio-to-X-ray spectral index α_{rx}.

As from Table 1.1, the typical errors on α_{UV} are $\lesssim 0.5$. Following Ledden & O'Dell (1985), the discriminant between RSBL and RWBL is $\alpha_{rx} = 0.8$. From the figure it is apparent that the objects considered here cluster at $\alpha_{rx} = 0.60$ and $\alpha_{rx} = 0.85$, with no objects with $0.7 \leq \alpha_{rx} \leq 0.8$. Even taking into account the poor statistical properties of our sample, this confirms the reality of the clustering (e.g. Stocke et al. 1990). On the same time, if radio-weak and radio-strong sources are considered together there is an indication of some positive correlation between the two indices consistent with a smooth transition between the two classes of blazars.

The distribution of the Rosat spectral slopes of 6 BL Lacs (Maraschi et al. 1994d) seems to confirm that the distinction between RSBL and RWBL is not sharp. However, a harder UV spectrum for RWBL with respect to RSBL is just the opposite of what is found in the X-ray band, where RWBL are steeper than RSBL (Worrall & Wilkes 1990; Sambruna et al. 1994). While the results in both bands are only indicative, because of the non statistical properties of the considered samples, the different behaviour may be considered as an important constraint in emission models, like the ones based on inhomogeneous jets (see Introduction, § I.d). Qualitatively, one can argue that in RSBL, which are the objects beamed toward us, the synchrotron radiation is depressed, which explains the softer UV, but at the same time the Compton component starts to contribute, yielding a harder X-ray spectrum.

There is an indication that in the UV domain, blazars are somewhat steeper than BQS quasars ($\Delta\alpha \simeq 0.2$). This was already noticed by GMTT, who however used the optical indices of BQS, and may be due to some contribution of the thermal component (blue bump) which is present in quasars but not in BL Lac objects. The difference between the UV spectral shape of BQS quasars and OVV and RSBL ($\Delta\alpha \sim 0.5$) is more marked, with a KS probability for the RSBL slopes of deriving from the same population as BQS less than 4%. This may suggest a possible contribution of relativistic beaming in softening the UV spectrum, consistently with the arguments reported above.

Considerations on the luminosity are strongly affected by the fact that the distributions in redshift are different for the different subclasses. Still two points seem noticeable. RSBL and RWBL have similar UV luminosities, as apparent from Table 1.2. Instead, the BQS quasars are brighter than BL Lacs (the probability that they derive from a population of same luminosity objects is P $\lesssim$ 9%), which is possibly another manifestation of the UV bump.

The present data allow also to explore the correlation between slope and luminosity. This is illustrated in the case of blazars in Fig. 1.6. It is apparent that no strict correlation is present, but there is an indication of a steeper spectrum in more luminous objects, although dividing the blazars in subsamples the general trend becomes uncertain. The absence of a strong spectral slope-luminosity correlation (see however Paltani & Courvoisier 1994) seems consistent with the poor slope-intensity correlation found in the few single BL Lacs intensively monitored (e.g. Maraschi et al. 1986a; Urry et al. 1988; Edelson 1992, see also Section 2.1).

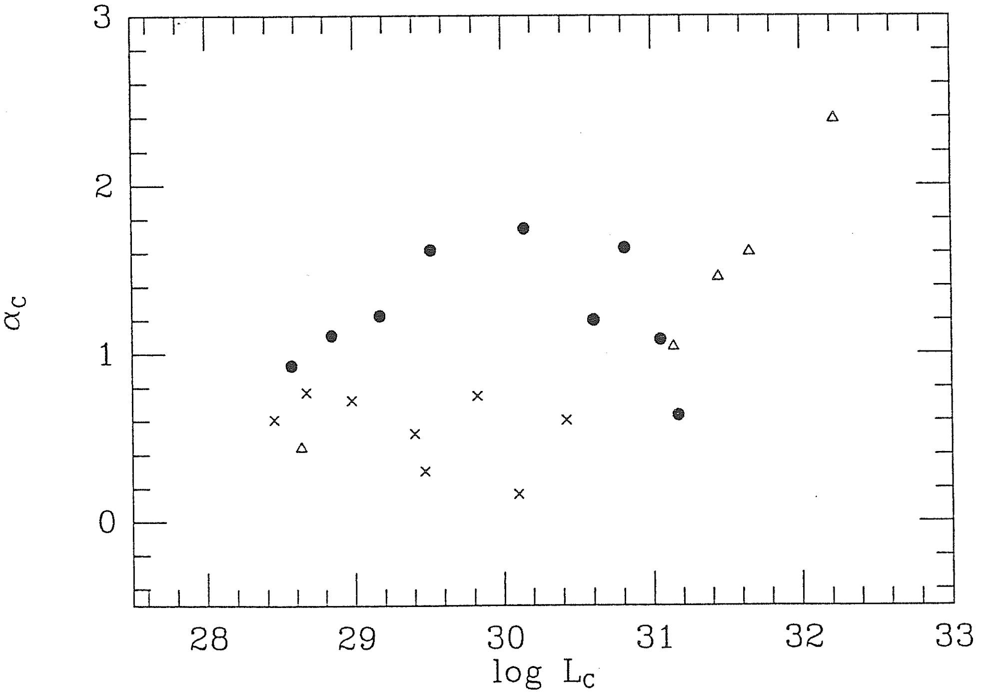

FIG. 1.6 — Combined UV spectral index versus luminosities of blazars at 1980 Å in units of erg s^{-1} Hz^{-1}. *Filled dots*: RSBL; *crosses*: RWBL; *open triangles*: OVV.

1.2 The Near-IR-Optical-UV Emission of BL Lacertae Objects

The spectral flux distribution of BL Lacs from the far-IR to X-ray range is supposedly dominated by nonthermal emission due to synchrotron radiation with possible contribution, at the higher frequencies, of the IC mechanism. The existence of breaks or of spectral curvature is important for constructing models for acceleration and radiation of electrons, and for constraining the emitting region, in particular to ascertain if it has an anisotropic structure where relativistic beaming possibly takes place.

The overall spectral flux distribution is generally described either by broken power-laws or by continuous steepening (see e.g. Cruz-Gonzalez & Huchra 1984; Landau et al. 1986; GMTT; Brown et al. 1989; Ballard et al. 1990). Many of the previous studies refer to non simultaneous observations, not systematically corrected for extinction due to dust inside our Galaxy and for the thermal contribution produced by the host galaxy starlight. The stellar contribution, if non negligible with respect to the nonthermal emission, produces a steepening of the energy distribution in the optical and a flattening in the near-IR, while reddening extinction introduces a steepening of the continuum mainly at optical-UV frequencies. For instance, the spectral break observed in some objects between near-IR and optical is completely removed when proper reddening corrections are applied (see e.g. Falomo et al. 1993d).

We report here on quasi-simultaneous ($\Delta t \lesssim 1$ day) near-IR, optical and UV ($8 \cdot 10^{13} - 2 \cdot 10^{15}$ Hz) observations of 11 BL Lacs (Table 1.4) obtained in the course of a 10 years systematic multi-frequency study of blazars (see Falomo et al. 1993a,d and references therein). Some of these objects have been selected for being among the most optically bright sources of the catalog of Impey & Tapia (1988; 1990), and therefore observable from IUE. The catalog includes a complete sample of radio-selected objects for which optical polarimetry is available. Within this program, half of the sources (0048–097, 0118–272, 0301–243, 0422+004, and 1538+149) were observed by IUE for the first time.

TABLE 1.4
BLAZARS OBSERVED IN NEAR-IR-OPTICAL-UV

Object (1)	Date (2)	z^a (3)	A_V^b (4)	RS/RW (5)	α^c (6)	P_g^d (7)	χ^2 (8)	M_V^e (9)
$0048-097$	87 Jan 8	…	0.22	RS	0.93 ± 0.06	…	0.87	…
	88 Aug 3				1.20 ± 0.06	…	1.39	…
$0118-272$	89 Aug 10	0.559	0.09	RS	1.20 ± 0.03	…	0.40	…
$0301-243$	89 Aug 9	(0.2)	0.11	RS	0.79 ± 0.06	11	0.90	-22.2
$0323+022$	89 Aug 10	0.147	0.50	RW	0.23 ± 0.12	30	1.92	-22.2
$0414+009$	89 Feb 15	0.287	0.51	RW	0.54 ± 0.15	3	0.06	-21.3
$0422+004$	88 Jan 10	(0.1)	0.42	RS	1.20 ± 0.15	10	1.88	-21.5
	89 Feb 13				1.19 ± 0.15	15	0.70	-21.5
$0521-365$	87 Jan 8	0.055	0.21	RS	1.43 ± 0.09	51	1.39	-21.7
$1538+149$	88 Aug 2	0.605	0.20	RS	1.34 ± 0.06	…	0.23	…
$1553+113^f$	88 Aug 2	…	0.22	RW		…		…
$2005-489$	86 Sep/89 Aug	0.071	0.33	RW	0.57 ± 0.06	12	3.21	-22.2
$2155-304$	84 Nov/89 Aug	0.116	0.10	RW	0.47 ± 0.06	3	0.94	-22.2

[a] Values in parentheses are from the best fit optimization procedure
[b] Extinction value (in magnitudes)
[c] Errors correspond to 3σ uncertainties
[d] Percentage of host galaxy contribution at 5500 Å (observer frame)
[e] Values are not *k*-corrected and computed assuming H_0=50 km s^{-1} Mpc^{-1}, q_0=0
[f] IR-optical region: $\alpha = 0.78 \pm 0.06$ ($\chi^2 = 0.38$); UV region: $\alpha = 1.56 \pm 0.12$ ($\chi^2 = 0.21$)

Col. 5 of Table 1.4 labels whether the source is radio-strong (RS) or radio-weak (RW), following the criterion of Ledden & O'Dell (1985). RS objects substantially correspond to radio-selected ones, and RW to X-ray-selected ones.

The data are here reconsidered and analysed using a homogeneous procedure which takes into account the galactic extinction and the host galaxy contribution. Based on a relatively extended sample, though not complete from the statistical point of view, the intrinsic shape of the nonthermal emission from near-IR to UV frequencies is derived. After a brief description of the target sources, the modes of observation and of data analysis are illustrated. Later on (§ 1.2.3), the general characteristics of the near-IR-optical-UV spectral flux distributions are outlined and their extrapolations are compared with non simultaneous far-IR (IRAS) and soft-X-ray (*Einstein*) data.

1.2.1 Target Objects

PKS 0048–097

This flat-spectrum radio-source is strongly variable at radio and optical wavelengths (Stull 1972; Pica & Smith 1983) and it was confirmed as blazar by Angel & Stockman (1980). Impey & Tapia (1990) report a maximum polarization of 27%. The first IUE observations of PKS 0048–097 were obtained on 1987 January 7 and 8 (Falomo et al. 1988), when the object was in a moderately high optical state ($m_V \approx 15.5$).

PKS 0118–272

The optical magnitude ranges between $m_V = 15.5$ and $m_V = 17.0$ (Condon et al. 1977; Thompson et al. 1990). The polarization has been measured by Impey & Tapia (1988; 1990) who report the value of 17.4%. An absorption redshift $z = 0.559$ was recently determined by Falomo (1991) from an intervening absorption feature attributed to the Mg*II* doublet.

PKS 0301–243

The optical magnitude ranges between 16.0 and 17.0 (Condon et al. 1977; Pica et al. 1980; 1988). Optical polarimetry by Impey & Tapia (1988; 1990) gave an average polarization of 10.6%. The object has been recently detected in the X-rays by Rosat ($F_{1keV} = 0.26$ μJy, Maraschi et al. 1994c).

H 0323+022

The flaring X-ray source H 0323+022 was independently noted by Doxsey et al. (1981) and Piccinotti et al. (1982) because of its dramatic variability and is well studied at all frequencies (Feigelson et al. 1986, and references therein). The redshift $z = 0.147$ has been measured by Filippenko et al. (1986). The visual magnitude ranges from 15.5 to 17.5 (Doxsey et al. 1983; Feigelson et al. 1986, and Pica et al. 1988) with short-term fluctuations.

GINGA observations by Ohashi (1989) in the range 2–30 keV yielded a dramatic variation of the flux in 5 hours from 1.1 μJy to 0.4 μJy.

H 0414–009

This BL Lac object was first detected by *HEAO 1*, and identified in *Einstein* X-ray images. The polarization of Impey & Tapia (1988, $\sim 3\%$) confirmed the BL Lac classification. Halpern et al. (1991) report a redshift $z = 0.287$, which makes H 0414–009 one of the most luminous X-ray emitters. The UV flux is very weak (Halpern et al. 1991; George 1988).

PKS 0422+004

The strongly variable radio-source PKS 0422+004 was identified by Bolton et al. (1968) with a starlike counterpart ($m_V \approx 17$), whose featureless optical spectrum (Wills & Wills 1976) and variable optical polarization revealed its BL Lac nature.

PKS 0521–365

This source was discovered in the NRL LASS *HEAO 1* experiment and identified as a BL Lac object by Schwartz et al. (1979). The bright BL Lac nucleus ($m_V = 16$) is hosted by a relatively isolated elliptical radio galaxy at a redshift $z = 0.055$, characterized by a prominent radio and optical jet (e.g. Macchetto et al. 1991). The first IUE observations of the object was made by Danziger et al. (1983). The source, which shows broad and variable optical and UV emission lines (Scarpa et al. 1994), is described in more detail in Section 1.4, where the radio-to-γ-ray continuum is studied.

PKS 1538+149

The optical identification ($m_V = 15.5$) and the confirmation of this strong and variable radio source as a BL Lac are due to Wills & Wills (1974). Optical monitoring of the source by Kinman (1976) and Pica et al. (1988) evidenced a variability in the visual band of almost 2 mag ($17.2 \leq m_V \leq 19$) and a weaker one in the blue band (Kidger 1988). The maximum optical polarization measured by Impey & Tapia (1990) was of 20%. The redshift $z = 0.605$ is reported by Stickel et al. (1991).

PG 1553+113

This is a bright BL Lac object discovered by the PG survey (Green et al. 1986). The $m_V \simeq 15$ source is pointlike and no redshift determination is yet available (Falomo & Treves 1990). A range of variability of ~2 magnitudes is seen in the optical band as reported by Miller et al. (1988).

PKS 2005-489

This is a bright X-ray BL Lac, originally classified as an N galaxy (Savage et al. 1977). The source has been studied in detail by Wall et al. (1986). The redshift derived from weak emission lines is 0.071 (Falomo et al. 1987).

PKS 2155-304

The brightest BL Lac object in the UV sky was discovered as a counterpart of a *HEAO 1* X-ray source (Griffiths et al. 1979). It is one of the few BL Lacs detected by the OSSE instrument onboard CGRO (Kurfess 1994). More details on this well studied source are given in Section 2.1.

TABLE 1.5
JOURNAL OF OBSERVATIONS

Name	MJD[a]	F_K^b	Δt[c]	F_V^d	F_{LWP}^e	Δt[c]	F_{SWP}^f	Δt[c]	Refs.[g]
0048 − 097	46804.074	10.38	-0.016	2.31	1.23	0.986	0.59	-0.046	1
	47377.336	6.98	0.012	1.51			0.25	1.092	2,3
0118 − 272	47748.289	6.71	0.078	1.25	0.50	-0.120			4
0301 − 243	47749.277	4.32	0.066	1.16	0.53	-1.985	0.31	-1.062	4
0323 + 022	47749.367	2.65	-0.012	0.67	0.26	-1.011	0.15	0.906	4
0414 + 009	47570.000	2.31	4.100	0.64	0.26	4.917	0.19	3.856	5
0422 + 004	47171.078	16.41	-0.020	2.38			0.24	0.898	6
	47571.031	12.79	0.012	1.66	0.33	1.899	0.19	0.827	2,3
0521 − 365	46803.152	18.20	0.043	2.38			0.17	1.754	2,3
1538 + 149	47377.035	2.93	-0.031	0.39	0.12	0.384			4
1553 + 113	47376.969	28.31	0.023	8.43	3.44	0.348	1.37	-0.552	7
2005 − 489	46683.102			8.93	4.11	0.291	1.97	0.171	2,3,8
	47748.105	26.79	0.000	8.32					2,3,8
2155 − 304	46017.051			24.49	1.18	-0.047	0.98	0.107	2,3,8
	47749.156	26.55	-0.008	12.33					2,3,8

[a] Modified Julian Day of the optical observation
[b] Flux at 2.19 μm in mJy
[c] Time lag with respect to the optical observation (days)
[d] Flux at ~ 5500 Å in mJy
[e] Flux at ~ 2800 Å in mJy
[f] Flux at ~ 1400 Å in mJy
[g] References to papers where some of the data have been presented:
(1) Falomo et al. 1988; (2) Falomo et al. 1993d; (3) this thesis;
(4) Falomo et al. 1993a; (5) Falomo & Tanzi 1991; (6) Falomo et al. 1989
(7) Falomo & Treves 1990; (8) Falomo et al. 1994b

1.2.2 Observations and Data Analysis

A journal of observations is given in Table 1.5, where fluxes in selected bands are reported. All observations were obtained with the same instrumentation and analysed using a uniform procedure. For most objects, observations in the near-IR, optical and UV bands were taken within ~1 day. In two cases (2005–489 and 2155–304) we combined simultaneous IR-optical and optical-UV observations taken at different epochs to study the IR-optical-UV emission (see § 1.2.3). For two sources (0048–097 and 0422+004), more than one overall spectrum has been obtained, allowing a comparison of the spectral shape at different states.

1.2.2.1 Near-IR Photometry

J,H,K and L photometry was obtained at the European Southern Observatory (ESO) 2.2m telescope (+ InSb photometer). A 15 arcsec circular aperture with chopper throw of 20 arcsec in the E-W direction was used. Statistical 1σ errors are less than 0.1 mag in all bands. Conversion to flux units is made according to the zero-magnitude fluxes given in Bersanelli et al. (1991).

1.2.2.2 Optical Spectrophotometry

Optical spectrophotometry of the sources was gathered at the ESO 1.5m telescope equipped with a Boller and Chivens spectrograph and CCD detector. Spectra were taken at a resolution of $\approx$ 15 Å (FWHM) through a long slit of 8 arcsec width. Standard reduction procedures were applied to obtain flux calibrated spectra. From repeated observations of standard stars (Stone 1977; Baldwin & Stone 1984) during each night, we derived a photometric accuracy better than 10%. To increase the S/N, we averaged the fluxes binning the spectra over bands of 100 Å.

1.2.2.3 Ultraviolet Spectra

UV spectra derive from the SWP and the LWP cameras onboard of IUE. The sources were centered in the blind offset mode in the large aperture ($10'' \times 20''$

oval) at coordinates measured on a blue POSS paper copy or on ESO plates. IUE line-by-line images were flux calibrated using curves provided by Bohlin & Holm (1980) and Bohlin et al. (1990) for the SWP camera and Cassatella et al. (1988) for the LWP camera. Net spectra were extracted using the GEX procedure locally implemented within the *MIDAS* interactive analysis system (Chiappetti 1992).

For some very faint but still visible spectra (e.g. 1538+149 and 0521–365) the extraction criteria of GEX have been relaxed: the default procedure first makes a fit of the background and computes the r.m.s. of the residuals around this fit in the region where signal is expected, then proceeds to signal extraction only if the average signal is > r.m.s./2. In our case we have loosened this constraints to be > r.m.s./3 to give evidence to the very faint signal.

For the purpose of fitting, the fluxes were binned in wavelength intervals of 50 Å or 100 Å, after some spectral regions, heavily affected by camera artifacts and cosmic rays hits, had been excluded. The associated errors are the standard deviations in the considered wavelength intervals divided by $\sqrt{N/3}$, where N is the number of pixels contained in each wavelength interval. This follows from the finding of a correlation length of $\simeq 3$ pixels in the cameras response (see Kinney et al. 1991b and E92). We added a 10% photometric error to the statistical flux errors.

The UV spectra of 2005–489 and 2155–304 were retrieved from the ULDA archive. We note that IUE spectra extracted with the IUESIPS procedure, show systematic flux differences by 5–10% with respect to extraction with the SWET method of Kinney et al. (1991b). In order to avoid such flux distortion due to different extraction methods, we have applied correction on IUESIPS extraction based on comparison with the UV data reported by E92.

The IR-to-UV data were corrected for galactic interstellar reddening using the extinction values listed in Table 1.4 (see § 1.1.1.2). The interstellar extinction curve of Cardelli et al. (1989) was used.

1.2.3 Spectral Flux Distributions

A composite spectral flux distribution was constructed for each object from

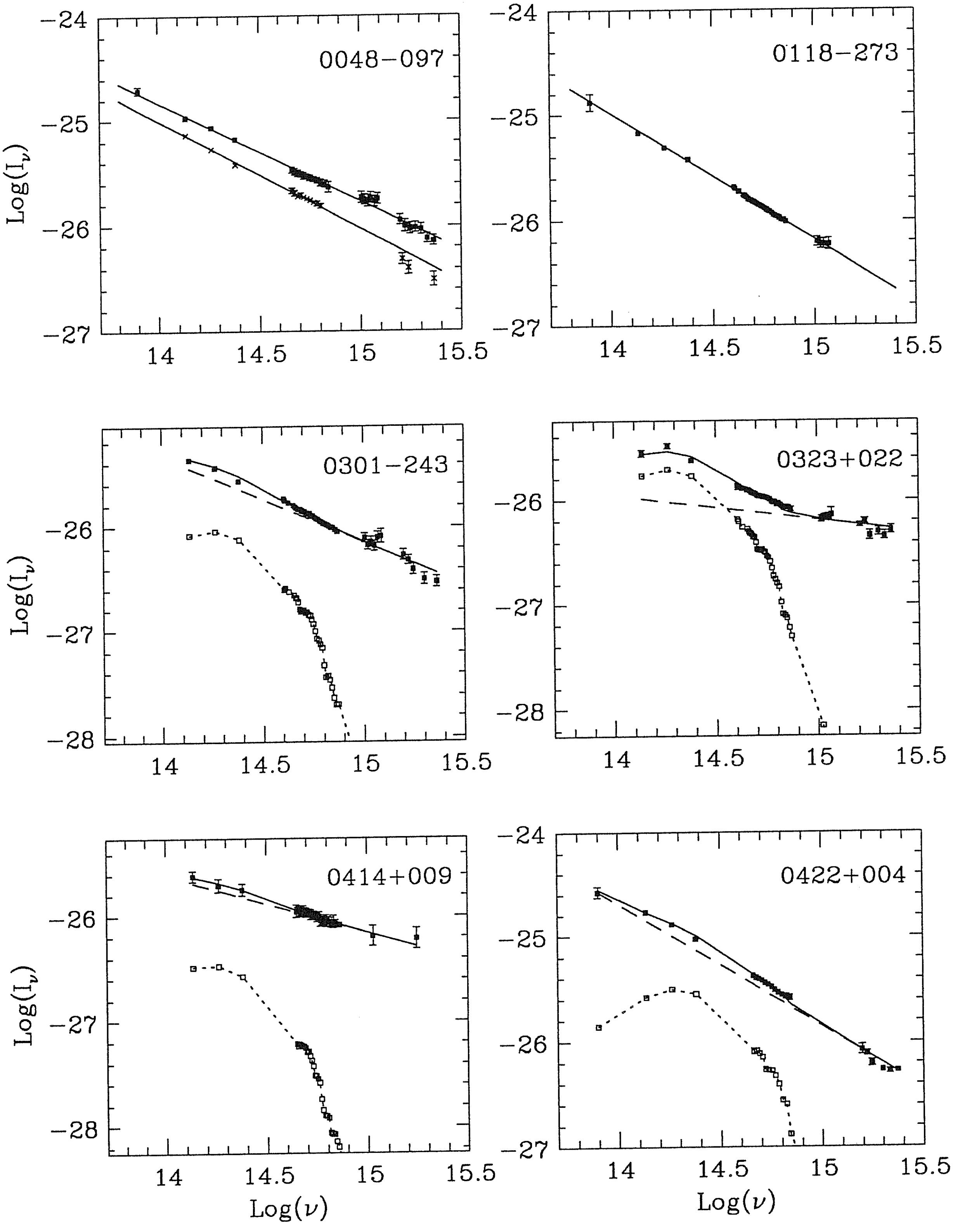
0048−097
0118−273
0301−243
0323+022
0414+009
0422+004
Log(I_ν)
Log(ν)
−24
−25
−26
−27
−28
14
14.5
15
15.5

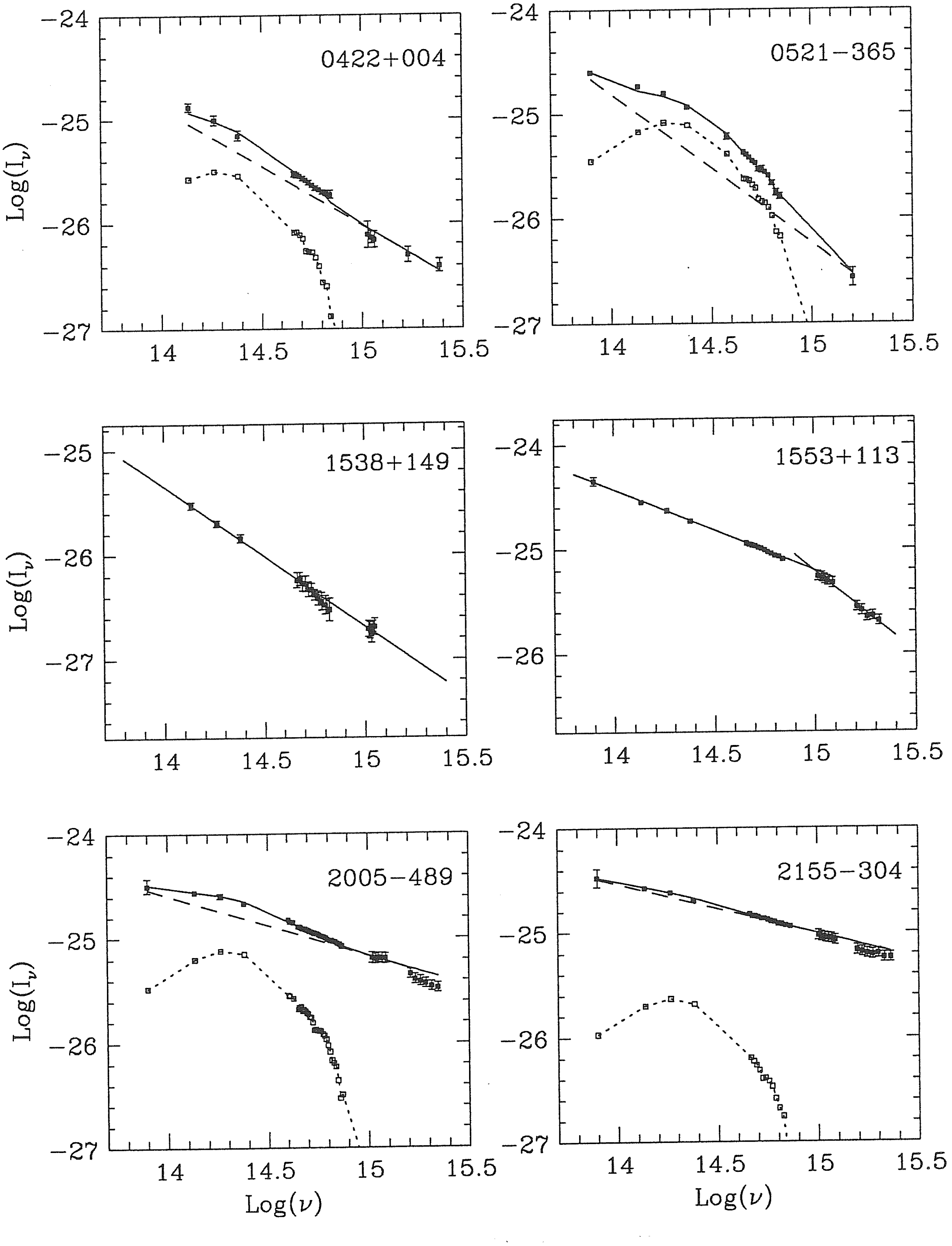

0422+004
0521−365
1538+149
1553+113
2005−489
2155−304
Log(I$_\nu$)
Log(ν)
−24
−25
−26
−27
14
14.5
15
15.5

quasi-simultaneous IR, optical and UV observations. For many objects, we have some additional optical observations, spaced by ~1 day from the one presented here for a given epoch (see Falomo et al. 1994b). Because no significant flux variations during day timescales are found, we do not expect that intra-day variability substantially affects our results.

For all sources we attempted a decomposition of the spectral flux distribution in terms of a power-law plus the contribution of a host galaxy through a χ^2 minimization procedure (see Fig. 1.7). As a model for the starlight contribution we assumed the energy distribution of a standard giant elliptical galaxy (Yee & Oke 1978) for the optical region, extended to the near-IR using the colors for ellipticals given by Arimoto & Yoshii (1987). To subtract the host galaxy component, the redshift of the object is needed. This is not available for 2 objects, therefore we assumed a rough estimate of z based on fit optimization. Parameters of the decomposition are: the spectral index α of the power-law component and the percentage P_g of starlight contribution at 5500 Å. We performed a least squares fit of the spectral flux distributions and report in Table 1.4 the best fit values. Col. 9 gives the estimated absolute magnitude of the host galaxy.

On the previous pages:

FIG. 1.7 — Spectral flux distributions of BL Lac objects observed simultaneously at near-IR, optical and UV frequencies. Data (filled squares) are corrected for galactic interstellar extinction. The solid line is the best fit model, which is either a single power law or the combination of a host galaxy (dotted line) and a power law component (dashed line). Open squares represent the spectrum of the standard elliptical after rebinning in conformity to the observed data points.

For most sources, after proper correction for the galactic extinction and subtraction of the starlight component, the IR-optical-UV nonthermal emission is adequately well fitted by a single power-law. In four objects (0048–097, 0118–272, 1538+149, 1553+113) the host galaxy is not detectable, thus no decomposition of the spectral flux distribution was performed. The spectral flux distributions of the first three objects are well described by a single power-law (see Fig. 1.7 and Table 1.4). For 1553+113 a single power-law does not account for the spectral flux distribution but a considerable discontinuity is apparent ($\Delta\alpha \sim 0.8$) at ~3000 Å, which makes this source the only case where a marked spectral change is observed (see also Falomo & Treves 1990). For seven objects we observe a bending of the spectral flux distribution, which we ascribe to the host galaxy. After decomposition of the thermal component, the data are satisfactorily represented by a single power-law. In two cases (0323+022 and the high state of 0422+004), however, the fit is poor ($\chi^2 \sim 2$).

For two sources (0048–097 and 0422+004) we obtained spectral flux distributions at two different epochs. As for 0048–097, the two spectral flux distributions differ by a factor 1.5 in the optical range and a slightly steeper spectrum ($\Delta\alpha \sim 0.3$) is exhibited in the lower state (August 1988, see Fig. 1.7). In the low state the UV data appear systematically below the power-law fit, suggesting a possible further steepening of the spectral flux distribution in the UV. However, due to the low flux level of this IUE spectrum, its steepening must be regarded with caution. The higher state (January 1987), was previously analyzed also by Falomo et al. (1988), who found an IR-to-UV spectral slope larger than, though consistent with, that reported here, probably due to the absence of reddening correction. Similarly, 0422+004 shows an optical flux variability of a factor ~1.5. After subtraction of the host galaxy, the nonthermal component is described at both epochs by a single power-law. No significant changes of spectral index are found here (see Table 1.4). The source had been observed also in a previous occasion (January/August 1987, Falomo et al. 1989), but the lack of a correction for reddening and for the host galaxy contribution led to the interpretation of the 1987 and 1988 spectral flux distributions in terms of broken power-laws or of logarithmic parabolas.

For 2005–489 and 2155–304 we do not have IR, optical and UV simultaneous observations, therefore we combined simultaneous IR-optical observations (Falomo et al. 1993d) with simultaneous optical-UV observations obtained at different epochs. Optical-UV observations were scaled to match near-IR-optical data in the optical range. This is justified by the property that the optical spectral index remains rather constant, even if the flux level changes sizeably with time (Falomo et al. 1994b). The combined spectral flux distribution of 2005–489 (see Table 1.4 and Fig. 1.7) exhibits a clear bending in the near-IR due to the host galaxy. The decomposition of the spectral flux distribution in terms of power-law plus host galaxy is not very satisfactory ($\chi^2 \sim 3$), because far-UV data appear to be systematically below the fit. A similar situation occurs in the case of 2155–304, although the bending is here less evident. Also in this case, far-UV fluxes lie systematically below the overall fit. This, similarly to the case of 1553+113, might be due to an intrinsic spectral break of the power-law component at $\log(\nu) \sim 15.1$. Although an intrinsic spectral steepening in the UV band of these two sources appears an acceptable explanation, we believe that other causes as IUE flux extraction and calibration, proper reddening correction and the lack of a single epoch observation may build up a similar effect. Based only on these data, we cannot draw a firm conclusion on this point.

In order to extend our spectral flux distributions to adjacent bands (far-IR and X-rays) we collected from the literature IRAS data (Impey & Neugebauer 1988) and soft-X-ray fluxes gathered by the *Einstein Observatory* (Owen et al. 1981; Madejski & Schwartz 1983; Ulmer et al. 1983; Ledden & O'Dell 1985; Worrall & Wilkes 1990; Elvis et al. 1992) and, in one case (0301–243), by the Rosat satellite (Maraschi et al. 1994c). The IRAS fluxes represent in four cases only upper limit values. The overall (non simultaneous) spectral flux distributions from far-IR to X-rays of our target objects are reported in Fig. 1.8. We note that the extrapolation of our IR-to-UV power-law fit to far-IR is consistent with IRAS fluxes (and upper limits) taking into account the variability regime of the objects. On the other hand, in all cases but 0521–365 the observed X-ray flux lies on or below our extrapolations.

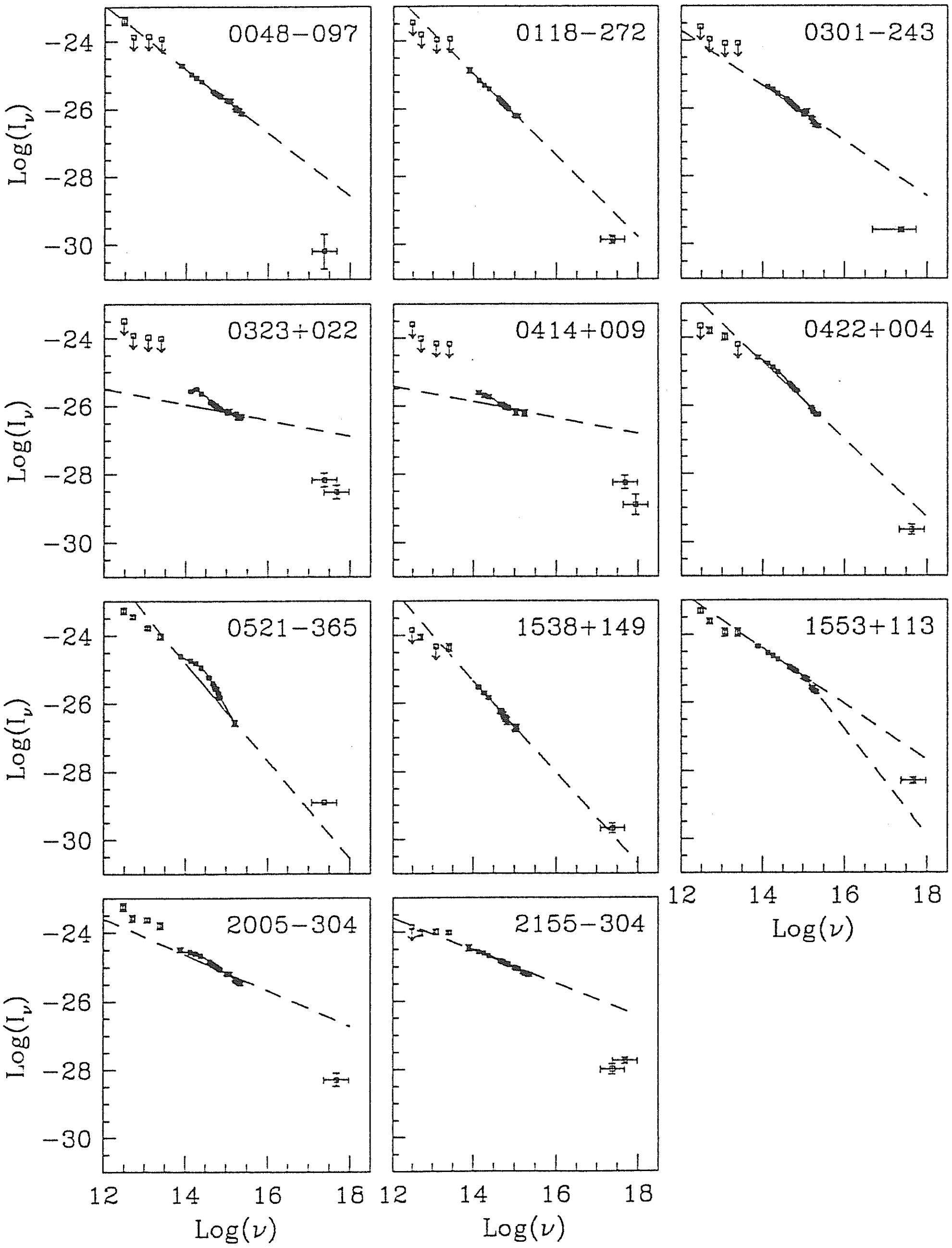

FIG. 1.8 — Overall spectra from far-IR to soft-X-rays. Comparison of the non thermal component (dashed line) with non simultaneous far-IR and X-ray data (open squares). Near-IR-optical-UV data from our dereddened observations are also reported (filled squares).

1.2.4 Discussion

The main result of this study is that in all of the examined objects but 1553+113 the spectral flux distribution in the IR-optical-UV band is properly represented by a unique power-law, when corrections for reddening and host galaxy are taken into account. This is at variance with previous results, which found a turnover in blazar spectra between IR and UV wavelengths (e.g. Cruz-Gonzalez & Huchra 1984; GMTT) or a smooth curvature from the radio to the UV domain (e.g. Landau et al. 1986; Brown et al. 1989). We believe that most of the difference is due to the use of simultaneous observations and proper corrections for extinction and for the stellar contribution. This is illustrated by the case of 0422+004, for which the proper account of the severe galactic extinction and of the host galaxy contribution, determines a radical change in the description of the emission components. Due to the higher, and more reliable, value of the extinction coefficient adopted here for 0323+022, the fit decomposition parameters for this object are slightly different from those previously obtained (Falomo et al. 1993a).

Our decomposition of the spectral flux distribution allows to estimate also the starlight contribution of program objects. The derived absolute magnitudes correspond to an 8×8 arcsec^2 effective aperture. They are in general good agreement with those obtained from direct imaging studies, considering the aperture correction, which is crucial for low redshift objects (see e.g. the cases of 0323+022 studied by Filippenko et al. 1986; 0521–365, Keel 1986; 0414+009, Falomo & Tanzi 1991; 2155–304, Falomo et al. 1993b). Furthermore, recent optical imaging of 0301–243 confirmed the presence of a diffuse nebulosity surrounding the object (Falomo 1994).

The average spectral index of the power-law component in our sample is $< \alpha > = 0.88 \pm 0.42$ (standard deviation), with a marked tendency for RW objects to be flatter than RS ones at the $\sim 3\sigma$ confidence level; the average spectral slopes are in fact, respectively, $< \alpha > = 0.45 \pm 0.15$ (s.d.) and $< \alpha > = 1.17 \pm 0.22$ (s.d.). Such difference is related to a different beaming angle in the two classes (see Introduction, § I.f, and Section 1.3).

The absence of breaks or curvature in the spectral shape in the $8 \cdot 10^{13}$ to $2 \cdot 10^{15}$ Hz frequency interval suggests that a single mechanism is responsible for the radiation in the whole range. The obvious candidate is thin synchrotron radiation.

1.3 Remarks

The analysis and interpretation of near-IR-optical-UV observations of 11 BL Lacs showed that their dereddened spectral flux distributions in the $8 \cdot 10^{13} - 2 \cdot 10^{15}$ Hz frequency range can be described in almost all cases by a single power-law with average spectral index $< \alpha >= 0.88 \pm 0.42$ plus, where relevant, the contribution of the host galaxy.

We have compared this finding, based on observations of a limited number of objects, with the average spectral properties of BL Lacs in the separate IR-optical and UV bands. On one hand we considered the 24 BL Lacs simultaneously observed in the two IUE bands belonging to the sample examined in Section 1.1, on the other we referred to a list of 33 objects (Falomo et al. 1993d), whose simultaneous IR-optical data were properly corrected for reddening and host galaxy contribution. In Table 1.6, which summarizes the results of the comparison, we report the average spectral indices of the different samples, which appear very similar and support our claim that the average spectral slope in the IR-optical-UV band has no discontinuities. It is noticeable that also in the broader samples RW objects have average harder spectra than RS ones, regardless of luminosity, which is interpreted in terms of the inhomogeneous jet scenario as due to a different viewing angle and therefore to a different beaming. We tested this subdivision for the sample studied in the UV with the KS method at the 99% significance level.

Although the unique slope $\alpha \sim 1$ refers to the overall population of blazars, it may be indicative that νF_{ν} is essentially constant, which may point to a homogeneous model of emission in the given energy interval. At the same time one should take into account that the inhomogeneous jet model in its simplest form requires that the dimension of the emitting region should increase with the considered wavelength.

TABLE 1.6
AVERAGE SPECTRAL INDICES[a]

	$< \alpha_{IROP} >$ Falomo et al. 1993d	$< \alpha_{UV} >$ Section 1.1	$< \alpha_{IROPUV} >$ Section 1.2
All	1.08 ± 0.34 (33)	0.97 ± 0.41 (24)	0.88 ± 0.42 (10)
Radio-weak	0.68 ± 0.28 (8)	0.66 ± 0.30 (10)	0.45 ± 0.15 (4)
Radio-strong	1.20 ± 0.30 (25)	1.20 ± 0.33 (14)	1.17 ± 0.22 (6)

[a] The quoted errors represent the standard deviations from the mean quantities and values in parentheses refer to the number of objects

The average slope ($\alpha_\nu = 1$) found for the 11 BL Lacs observed from IR to UV may be compared with the average UV to X-ray slope reported by GMTT, $\alpha_{UX} = 1.1$. The indication is therefore that if a steepening is present above UV frequencies, it could be rather modest. In fact, in most cases the non simultaneous soft-X-ray fluxes obtained by *Einstein* lie on or below the extrapolation of the power-law (Fig. 1.8). Although the X-ray data were not taken simultaneously, this is indicative that no component in addition to the synchrotron one is present in the soft-X-rays, and in particular the SSC process is probably negligible. Instead, the data suggest a steepening of the spectrum toward soft-X-ray frequencies. This means that the electron acceleration mechanism at the higher energies has a typical timescale longer than the electron lifetimes, so that injection of high energy particles is less efficient than radiative losses.

The only exception to this steepening behaviour toward soft-X-rays is represented by PKS 0521–365, for which flux at 1 keV exceeds that extrapolated from the IR-to-UV power-law (Fig. 1.8). Simultaneous UV and X-ray observations at a previous epoch (1983) display an appreciable difference between the UV and X-ray slopes ($\Delta\alpha \simeq 0.5$) indicating that the energy distribution hardens at the higher frequencies, as suggested by the detection of the source at > 100 MeV.

In Section 1.4 we will construct the radio-to-γ-ray flux distribution of this object, including the simultaneous UV and X-ray data, and will show that the SSC mechanism is dominant in this source.

Finally, we note that both IR-optical and UV observations of BL Lacs indicate that the spectral slope changes only modestly with the flux level (Falomo et al. 1993d; Falomo et al. 1994b; Edelson 1992; Urry et al. 1993 and Section 2.1). This fact, together with our results, suggests that the whole IR-optical-UV slope is unique and constant even when the intensity varies by large factors, which is likely to happen if the flux is dominated by a unique component (Edelson 1994). Such lack of spectral variability however does not arise in a natural way in any of the proposed models for BL Lacs, apart from those implying gravitational lensing (see Introduction, § I.d). The constant shape of the continuum spectral energy suggests that only the number of electrons whose emission is beamed towards the observer changes, rather than the arrival of fresh electrons that are being accelerated (Blecha et al. 1994). This very constancy seems to us a key constraint in a theoretical progress of our understanding of BL Lac emission.

1.4 The Broad-Band Energy Distribution of the Gamma-Ray Blazar PKS 0521–365

The flat spectrum radio source PKS 0521–365 is strongly polarized (6%, Angel & Stockman 1980), variable (Eggen 1970; Shen et al. 1972; Ulrich et al. 1984; Edelson 1992; Falomo et al. 1994b) and exhibits strong emission lines (Scarpa et al. 1994, and references therein). Its proximity ($z = 0.055$) allows the detection of the host galaxy and of a bright optical jet (Danziger et al. 1979; Cayatte & Sol 1987; Macchetto et al. 1991). Thus it cannot be classified neither as a BL Lac object nor as a HPQ. The term blazar, intended to include essentially all flat spectrum radio sources, is particularly useful for this source.

During the 1992 May 14–June 4 viewing period, the EGRET instrument onboard CGRO detected the source in γ-rays at a significance level of 4.4σ (Fichtel et al. 1994).

Here we study the broad-band energy distribution of the source using simultaneous UV and X-ray observations taken on 1983 November and combining them with radio, mm and simultaneous near-IR-optical data at different epochs and with the recently measured γ-ray flux. Part of these data have been already published separately (see § 1.4.1 for references), but the UV and X-ray observations were never jointly studied, while the circumstance of their simultaneity is crucial in modelling the spectral energy distribution.

Several arguments indicate that the emitting jet in this source is not closely aligned with the line of sight and therefore the continuum cannot be strongly boosted by relativistic bulk motion. This fact, together with the direct observation of broad emission lines, allows to discuss the relative importance of synchrotron and external photons for the production of γ-rays via the IC process. The physical and geometrical parameters of the jet are estimated applying an inhomogeneous relativistic jet model which radiates through the SSC process.

TABLE 1.7

Journal of Observations[a]

Date	Instrument	Range	Energy Index	F^b (2650 Å)	F (1750 Å)	F (1 keV)
1979 Oct 06	*Einstein*[c] (IPC)	0.2–3.5 keV	$0.58^{+0.35}_{-0.38}$	–	–	1.03 ± 0.17
1983 Nov 02	EXOSAT[d] (LE+ME)	0.2–7 keV	0.52 ± 0.09	–	–	1.47 ± 0.17
	IUE (SWP)	1300–1900 Å	...	–	202 ± 43	–
1983 Nov 30	EXOSAT[d] (LE+ME)	0.2–7 keV	0.68 ± 0.12	–	–	1.78 ± 0.24
	IUE (SWP+LWP)	1300–2840 Å	1.1 ± 0.5	421 ± 91	242 ± 37	–
1992 Aug 29	Rosat[e] (PSPC)	0.2–2.4	$0.97^{+0.05}_{-0.07}$	–	–	2.06 ± 0.09

[a] Errors represent 90% uncertainties

[b] Fluxes are in μJy

[c] A power law fit at free $N_{\rm H}$ yielded an energy index $\alpha = 1.14^{+2.4}_{-0.9}$ (Worrall & Wilkes 1990)

[d] The reported results are in good agreement with those obtained by Garilli & Maccagni (1990)

[e] 3869 ± 63 net counts for a total exposure of 4845 s

1.4.1 Observations and Data Analysis

Simultaneous observations of the object with IUE (1200–3000 Å) and EXOSAT (0.2–7 keV) were performed on 1983 November 2 and 30 (see Table 1.7). During the first IUE observation only the SWP camera was exposed, whereas on November 30 both SWP and LWP spectra were recorded. The UV spectra were extracted with the GEX procedure, flux calibrated after Bohlin et al. (1990) and Cassatella et al. (1988). The spectral fluxes were binned and averaged in intervals of ~100 Å. These data, dereddened with $A_V = 0.2$, were best-fitted with a power-law model. The results are reported in Table 1.7.

The X-ray data obtained at both epochs with the LE and ME instruments onboard of EXOSAT were analysed by Sambruna et al. (1994). No significant flux variations are present between the two epochs. The results of a power-law fit with absorption fixed at the Galactic value, $N_{\rm H} = 3.37 \cdot 10^{20}$ cm^{-2} (Elvis et al. 1989), are reported in Table 1.7.

X-ray data obtained with *Einstein* (1979) and Rosat (1992) were retrieved from the archives and analysed again under the hypothesis of a simple power-law with a fixed column density. The results are also reported in Table 1.7.

Near-IR-optical spectrophotometry was obtained in January 1988 at ESO (see Falomo et al. 1993d). Simultaneously with our IR-optical observation, we recorded an IUE spectrum, at the same flux level of those of 1983. On the basis of this agreement, we combined the 1983 November 30 and 1988 January data to obtain the spectral flux distribution from the near-IR to the X-ray range shown in Fig. 1.9, together with archival IRAS data (Impey & Neugebauer 1988). The near-IR and optical data were dereddened and the stellar contribution of the host galaxy, which is rather strong in this object ($\simeq$ 50%, Pian et al. 1994a), was subtracted.

It is clear from Fig. 1.9 that the spectral flux distribution steepens around 10^{14} Hz. Above this frequency, the data are consistent with a single power-law. A best fit to the combined near-IR, optical and UV data yields $\alpha = 1.4 \pm 0.1$ ($\chi^2 \simeq 1.3$). An extrapolation of the optical-UV continuum to the X-ray band falls below the simultaneously observed 1 keV flux by almost a factor 10 and the X-ray slope ($\alpha_X = 0.68 \pm 0.12$), is definitely flatter than that in the IR-optical-UV range, suggesting that a different emission mechanism operates in the X-ray band.

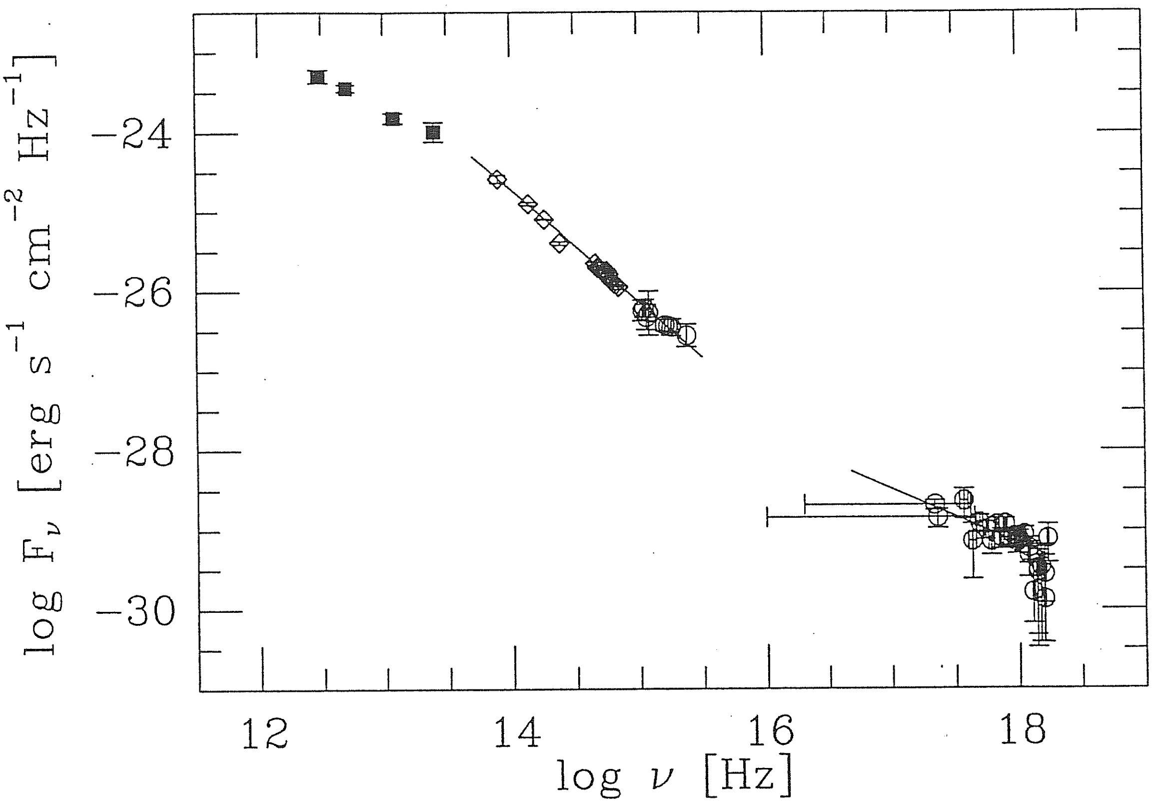

FIG. 1.9 — Spectral flux distribution of PKS 0521–365 from far-IR to X-rays. Equal symbols are used for simultaneous data. UV and X-ray data (open dots) refer to 1983 November 30. Near-IR-optical data (open diamonds) refer to January 1988. Far-IR data (filled squares) are taken from the IRAS archive. Error bars represent 1σ uncertainties. The overimposed solid lines represent the power law best fit curves to the near-IR-to-UV and to the X-ray data.

1.4.2 The Broad-Band Energy Distribution

To the near-IR-to-X-ray spectral flux distribution we added the VLBI radio flux measured by Preston et al. (1989); fluxes at mm wavelengths (Knapp & Patten 1991); far-IR data from the IRAS satellite (Impey & Neugebauer

1988), and the γ-ray flux measured by EGRET (Fichtel et al. 1994), thus obtaining an overall spectral flux distribution extending over 14.5 decades in frequency. We do not expect that non simultaneity of the far-IR and radio data can largely affect the overall spectral flux distribution, since at long wavelengths the variability amplitude is usually not large (see e.g. Edelson & Malkan 1987; Valtaoja 1994). On the other hand, as apparent from observations of other blazars, the γ-ray emission can undergo significant variability (see e.g. Thompson et al. 1994; Maraschi et al. 1994b). The flux used here ($(2.0 \pm 0.5) \cdot 10^{-7}$ ph s^{-1} cm^{-2} at energy > 100 MeV) is the only one reported thus far for this source.

The overall spectral energy distribution is shown in Fig. 1.10 in the νF_ν representation. The X-ray data obtained with *Einstein* and Rosat are also shown in the form of best fit power-laws (absorption was fixed at the Galactic value; see Table 1.7 for our best fit parameters). The source intensity at 1 keV varied by a factor 2. The spectral indices derived from EXOSAT are consistent with that from *Einstein* (which has rather large errors). The Rosat spectrum is softer than measured either with EXOSAT or *Einstein*. This could be due to spectral variability of the source, ($\Delta\alpha \simeq 0.3$ is not uncommon for blazars; see e.g. Sambruna et al. 1994), but it may also be related to the softer range of the Rosat instrument (Table 1.7). In fact an extension of the steep UV component to the soft-X-ray band is not unlikely. A similar situation was found in the case of the BL Lac object PKS 0537–441 (Treves et al. 1993).

The broad-band energy distribution clearly shows two spectral regions where the observed energy output is maximum (see Fig. 1.10). One component peaks in the far-IR ($\simeq 10^{13}$–10^{14} Hz), the other component shows up between 1 keV and 100 MeV; due to the lack of data at higher or intermediate frequencies the peak of the power of the second component cannot be further constrained. To this end, a determination of the spectral shape in the γ-ray band would be extremely valuable. In any case, we note that the power in the observed γ-ray band is already comparable to the bolometric power at all other frequencies. The two components apparently join in the

EUV-soft-X-ray range. This "double humped" energy distribution is similar to that of other blazars (see e.g. MCG).

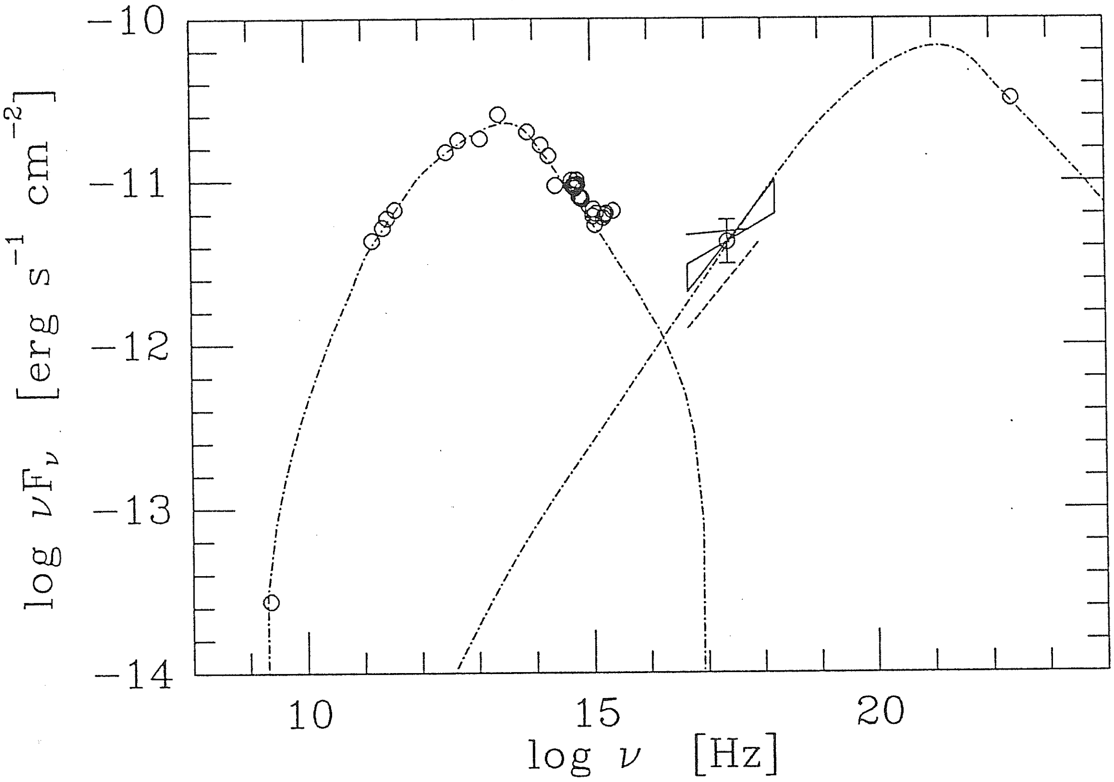

FIG. 1.10 — Spectral energy distribution of PKS 0521–365. IUE and EXOSAT data refer to 1983 November 30. The EXOSAT power law spectral fit is reported along with the 1.6σ (90%) confidence range. For comparison, the power laws representing the Rosat spectrum best fit (solid line) and the *Einstein* best fit (dashed line) are reported. The dashed-dotted line represents the synchrotron and self-Compton contributions within the adopted jet model. Error bars on the data points are omitted.

1.4.3 Theoretical Considerations

1.4.3.1 General Remarks

Within the jet model scenario, the case of PKS 0521–365 is of special interest in that there is evidence that relativistic boosting *is not large* in this source:

1) PKS 0521–365 is not a core dominated radio source: the ratio of the core to extended radio emission at 1.4 GHz is ~ 0.3 (Antonucci & Ulvestad 1985);

2) a well defined optical jet is visible with an angular size of $6''.5$ (7 kpc, Keel 1986; Macchetto et al. 1991; Sparks et al. 1994) and well aligned with the nucleus, suggesting that the jet is not closely aligned with the line of sight;

3) the luminosity of the [O III] emission line (5007 Å) is low compared to the distribution for BL Lac objects and Flat Spectrum Radio Quasars obtained by Stickel et al. (1991), yet the equivalent width is rather large ($\sim$3 Å, Scarpa et al. 1994) implying a low continuum-to-line ratio;

4) applying the SSC model to the VLBI core of this source (requiring that the radio core does not overproduce the X-ray emission) Ghisellini et al. (1993) found $\delta \sim 1$ for the radio emission;

5) requiring the source to be transparent to 1 GeV γ-rays, estimating the size from variability and assuming that the X-rays (which are targets of the γ-rays for the photon-photon process) are cospatial with the γ-rays, Dondi & Ghisellini (1994) found $\delta \sim 1.3$ for the high energy emission. Note that a Doppler boosting factor $\delta \sim 1$ means that we are measuring the *"intrinsic"* continuum of this source.

It is natural to interpret the double humped energy distribution of blazars as due to synchrotron and IC emission (see Introduction, § I.a). The first mechanism can account for the self-absorbed radio emission and for the mm, far- and near-IR, optical and UV continuum of PKS 0521–365, assuming a suitably curved spectral shape of the relativistic electrons or an inhomogeneous jet.

The high energy emission (X- and γ-rays) can then be produced via IC scattering of the relativistic (synchrotron emitting) electrons off photons produced in the same region (SSC, e.g. Maraschi et al. 1992); or alternatively off photons emitted by an accretion disk (e.g. Dermer & Schlickeiser 1993) or the broad-line region, and/or scattered by some surrounding material (e.g.

Sikora et al. 1993; 1994).

We can estimate the relative importance of different sources of photons for IC scattering by relativistic electrons in the jet. Approximating the emission region within the jet as a sphere of radius R_{blob} moving with bulk Lorentz factor Γ at an angle θ with the line of sight and defining the Doppler factor $\delta = [\Gamma - (\Gamma^2 - 1)^{1/2}\cos\theta]^{-1}$, the intrinsic (primed) energy density of the internally produced radiation is

$$U'_{int} = \frac{L_{syn}}{4\pi R^2_{blob} c \delta^4} = 2.6 \frac{L_{syn,44}}{\delta^4 R^2_{blob,16}} \quad \text{erg cm}^{-3} \tag{1.5}$$

since the *observed* synchrotron luminosity L_{syn} corresponds to an intrinsically emitted luminosity $L'_{syn} = \delta^{-4} L_{syn}$. Here $L_{syn,44}$ and $R_{blob,16}$ are in units of 10^{44} erg s^{-1} and 10^{16} cm, respectively.

From the luminosity in the broad lines L_{BLR} (which is of the order of 6×10^{42} erg s^{-1}, Scarpa et al. 1994) we can evaluate the energy density of the external radiation, in the rest frame of the blob, where it is enhanced by a factor Γ^2. Assuming a spherical broad-line region with radius R_{BLR}, we have

$$U'_{BLR} \sim \frac{L_{BLR}\Gamma^2}{4\pi R^2_{BLR} c} \frac{(1+\beta)^3}{3\beta} \sim 7.1 \times 10^{-4} \frac{L_{BLR,42}\Gamma^2}{R^2_{BLR,17}} \quad \text{erg cm}^{-3} \tag{1.6}$$

where $L_{BLR,42}$ and $R_{BLR,17}$ are in units of 10^{42} erg s^{-1} and 10^{17} cm, respectively.

Another contribution to the radiation energy density may come from photons emitted directly by a disk (see far-UV points in Fig. 1.10). This contribution is very important close to the disk, but decreases rapidly for larger distance. Assuming that a luminosity L_d is emitted by the inner accretion disk, within a radius R_d, we have

$$\begin{aligned} U'_d &\sim \frac{L_d \Gamma^2}{3\pi R_d^2 \beta c} \left\{ \left[1 - \beta \left(1 + R_d^2/R_\gamma^2 \right)^{-1/2} \right]^3 - [1-\beta]^3 \right\} \\ &\sim 3.5 \times 10^2 \frac{L_{d,44}\Gamma^2}{R^2_{d,15}} \left\{ \left[1 - \beta \left(1 + R_d^2/R_\gamma^2 \right)^{-1/2} \right]^3 - [1-\beta]^3 \right\} \quad \text{erg cm}^{-3} \end{aligned} \tag{1.7}$$

where R_γ is the distance of the emitting blob to the accretion disk.

We can see that if δ is of order unity and $\Gamma \simeq 10$, the external radiation density is unlikely to dominate. In this case, assuming a blob radius $R_{blob} = 10^{16}$ cm, and deriving from the overall energy distribution (Fig. 1.10) $L_{syn} \simeq 10^{44}$ erg s^{-1} and $L_d < 7 \times 10^{43}$ erg s^{-1}, we have that the internal radiation energy density always dominates the contribution from the broad-line region, and dominates the radiation energy density produced directly by the accretion disk if $R_\gamma > 3 \times 10^{15}$ cm.

As a consequence, equations 1.5–1.7 suggest that the main mechanism for the production of γ-rays is SSC, unless Γ is uncommonly large or the size of the blob is of the same order of the size of the broad-line region. In this respect, note that in the case of a relativistic jet, R_{blob} should correspond to the cross-sectional radius of the jet.

1.4.3.2 Inhomogeneous Jet Model

In order to be more quantitative, we apply specifically the inhomogeneous jet model of GMT and Ghisellini & Maraschi (1989, see Introduction, § I.d). Although the model is rather simplified, it contains a large number of free parameters. We therefore searched for a solution which appears consistent with the data rather than for a best fit to the data. The result is shown in Fig. 1.10 and the corresponding parameters are given in Table 1.8.

The bulk Lorentz factor of the plasma in the paraboloid is constant, $\Gamma \simeq 4$ (see Table 1.8), and the viewing angle is $\theta \simeq 30°$, implying a Doppler beaming factor $\delta \sim 1.5$ and a $\beta_{app} \simeq 3$ for the superluminal motion. The small value of the beaming factor is in agreement with the other independent estimates discussed in § 1.4.3.1. The presence of only marginally relativistic conditions and of modest beaming is consistent with the observation of the radio and optical jet, which would not be visible if it were strictly aligned with the line of sight, and with the modest value of the core dominance parameter.

The model reproduces rather well the data from radio to γ-rays. In particular, it fits well to the slope of the EXOSAT and the *Einstein* X-ray data, and accounts for the X- and γ-ray fluxes within the uncertainties. Note that in the soft-X-ray band the synchrotron and the self-Compton contributions, which have very different spectra, overlap. Therefore a relatively small relative flux variation may yield a significant spectral variation, which may account for the softer Rosat spectrum. A similar behaviour was found in the case of the radio bright BL Lac object PKS 0537–441 (Treves et al. 1993).

TABLE 1.8

INPUT PARAMETERS FOR AN INHOMOGENEOUS JET MODEL[a]

	Paraboloid	Cone
Synchrotron Spectral Index α_0	0.5	0.5
Magnetic Field Power Law Index m	1	1
Electron Density Power Law Index n	0.5	1.5
Emission Region Profile ϵ	0.5	1
Inner Radius R_0 (cm)	10^{15}	$10^3 R_0$
Outer Radius	$10^3 R_0$	$10^5 R_0$
Initial Magnetic Field B_0 (Gauss)	20	0.02
Initial Electron Density K_0 (cm^{-3})	$7.5 \cdot 10^4$	$2.4 \cdot 10^3$
Initial Maximum Synch. Frequency $\nu^s_{max}(R_0)$ (Hz)	$6 \cdot 10^{16}$	$6 \cdot 10^{13}$
Bulk Lorentz Factor Γ	4	4

[a] Symbols for the relevant parameters are those adopted in GMT

In this model, X-rays are coming from SSC scattering of relativistic electrons off the radio and mm photons, while the GeV γ-ray emission is produced by SSC off optical-UV photons.

This allows to predict for PKS 0521–365 a γ-ray spectral slope of $\simeq 1.3$, slightly harder than the near-IR-optical-UV one ($\alpha = 1.4$). The observed peak at $\sim 3 \cdot 10^{13}$ Hz corresponds to the thin synchrotron emission of the intermediate region of the jet (outer paraboloid). The same region is responsible for the self-Compton peak in the MeV band.

1.4.4 Discussion

PKS 0521–365 is one of the three relatively nearby sources detected by EGRET (the other two objects with $z < 0.1$ are Mkn 421 and PKS 2005–489). The proximity of these objects allows their detection above 100 MeV even if their γ-ray luminosity does not largely dominate their power output, and even if the entire radiation is not greatly Doppler boosted. It may be that the dominance of the γ-ray luminosity in other blazars observed by EGRET so far is the result of a selection effect, due to the limited EGRET sensitivity which prevents detection of far away objects unless they are in "exceptional" flaring state in γ-rays.

The proximity of PKS 0521–365 allows in principle its detectability at TeV energies, like Mkn 421 (Punch et al. 1992), since photon-photon interactions with the IR background radiation should be modest (Stecker et al. 1992; De Jager et al. 1994). However, in our model, the IC component at TeV energies falls much below the threshold sensitivity of present detectors, so that the actual detection is not expected, unless the object undergoes an extraordinarily large γ-ray outburst.

We have shown that the origin of the high energy emission in PKS 0521–365 is likely SSC process, rather than IC on externally produced radiation. This result is based on the small value of the beaming factor, resulting in a large intrinsic (and internally produced) synchrotron energy density.

The similar output in synchrotron and self-Compton luminosities thus indicates an approximate equipartition between the magnetic and synchrotron energy density in the relativistic jet. This of course does not exclude the possibility that in other sources the dominant cooling mechanism is IC on external radiation, as proposed by Sikora et al. (1994).

If SSC is the dominant cooling mechanism in PKS 0521–365, then we can predict a general pattern of variability at different frequencies (see also MCG; Maraschi et al. 1994b). Assume in fact that the variation in flux is produced by a variation in the density of the relativistic electrons N. Then the synchrotron luminosity varies linearly with N, while the self-Compton flux should be proportional to N^2. If, instead, external radiation is important for the IC mechanism, then both the synchrotron and the Compton components are proportional to N, and should thus vary with similar amplitudes.

1.4.5 Conclusion

Emission at IR, optical and UV frequencies in this object is ascribed to synchrotron radiation from the inner part of a jet misaligned with respect to the line of sight ($\theta \sim 30°$), implying a weakly beamed energy outflow. The higher energy emission is due to IC of relativistic particles on the synchrotron photons themselves.

The interpretation of the broad-band energy distribution through an inhomogeneous jet model for blazar radiation is proposed (§ 1.4.3.2) which satisfactorily reproduces the two observed emission maxima at IR and GeV energies as due to synchrotron and SSC processes respectively. According to that view, a good correlation might generally be expected between the scattered X-rays and the seed IR-mm photons, which is seen (see e.g. Owen et al. 1981); moreover, variability has been seen at γ-ray energies in 3C 279 (Kniffen et al. 1993), and the timescale of variation (a few days) is characteristic of the optical-UV region.

The comparison of the EXOSAT spectrum with data from other X-ray experiments shows that the slope of the former is significantly harder, and the application of the inhomogeneous model suggests that this is related to the presence of a remarkable γ-ray emission (a factor of $\sim$100 larger than the radio luminosity at 1 GHz).

If the direction of the jet had a much smaller angular distance with respect to the Earth ($\sim 5°$) the object's luminosity would appear relativistically enhanced. Simulating such behaviour (with the remaining parameters unchanged) we note that the broad-band energy distribution of another blazar, PKS 0735+178, is moderately well reproduced (Fig. 1.11). There is firm independent evidence that this object (at $z > 0.424$) is strongly beamed ($\delta = 7.3$). This yields an indication that the parent population of the objects could be the same, the differences being due only to orientation effects and to the presence of beaming.

Our study enphasizes the importance of multi-frequency observations of blazars particularly stressing the need of very high energy observing campaigns.

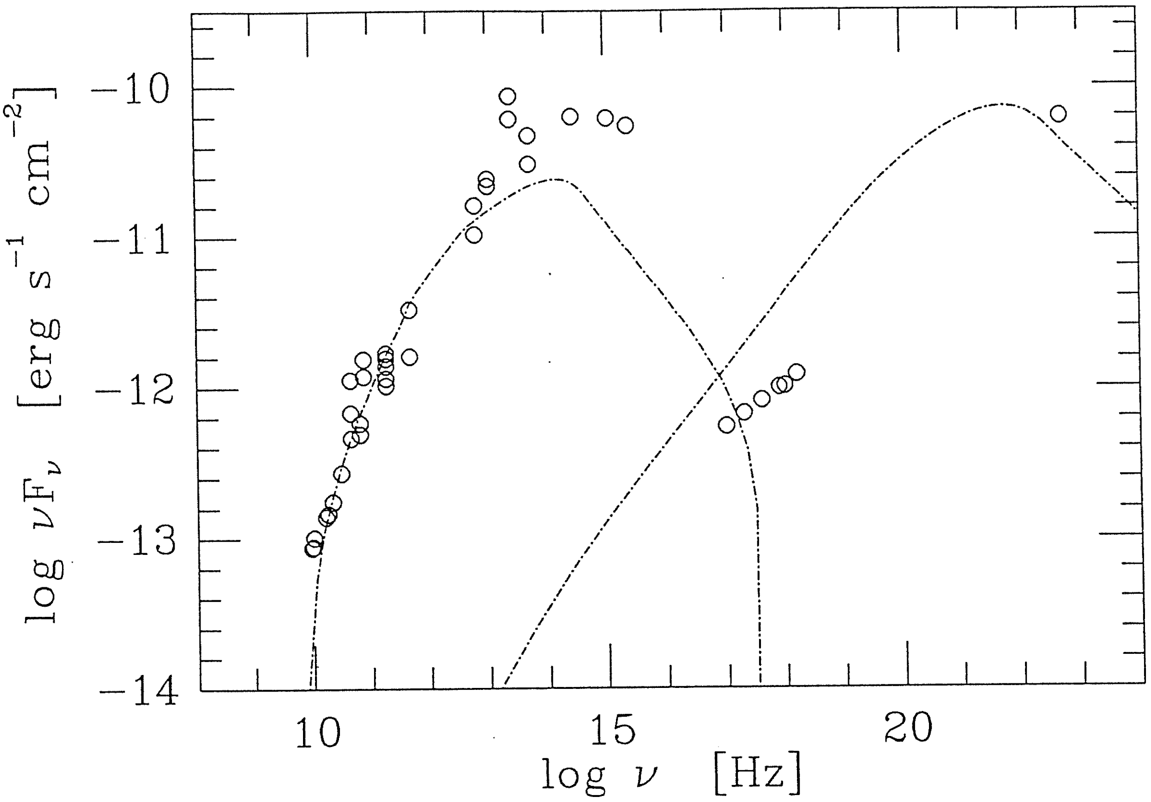

FIG. 1.11 — Emitted power per unit frequency of PKS 0735+178. Overimposed is the theoretical curve derived for PKS 0521–365 in a beamed scenario. Error bars on the data points are omitted.

Chapter 2

Variability of Blazars

Because they emit copiously over almost 15 decades in frequency, AGN cannot be understood without the help of multi-wavelength observations. On the other hand, variability monitoring has also proven to be invaluable in understanding the continuum and line emission processes as well as the geometry of the innermost regions in these objects. Although sizes can be determined directly from VLBI observations in the radio region, the central engine is much too small to image from Earth, thus the only tool for probing the source structure is temporal evolution of its spectrum. The equivalent resolution which can be achieved in this way is of the order of 1 microarcsec (at $z \simeq 0.1$ and with a typical variability timescale of $\sim$1 day), far beyond the capability of any UV or optical telescope.

Correlated variability strongly suggests, and is often taken as a proof, of a causal link between the components. For example, Compton upscattering of synchrotron photons off relativistic electrons in the same region could not vary more rapidly than or lead the direct synchrotron emission (e.g. Maraschi 1992). Likewise, in an accretion disk model, the lower temperature (lower frequency) radiation comes from farther out in the disk, so the UV variations should be much stronger and lead those at optical wavelengths.

Inhomogeneous jet models are strongly supported by radio and optical observations of blazars, but the situation at higher frequencies is less clear. Alternatives include a two-temperature accretion disk model and gravitational micro-lensing of background quasars (see Introduction, § I.d). The disk and jet models differ most at UV through X-ray wavelengths, where the spectral curvature is greatest; among jet models there are differences in how the UV and X-ray emission are related (e.g. GMT). Since the amplitude and rapidity of variability in most blazars increases with decreasing wavelength, the chances of successfully observing significant variations at UV and soft-X-ray wavelengths are high.

Multi-frequency observing campaigns on AGN of non-blazar type (mostly Seyferts, see review in Clavel 1994, and radio-quiet quasars, Ulrich 1990; Treves et al. 1994) were organized in the last few years with the simultaneous scheduling of space- and ground-based instruments. These monitoring programs have demonstrated that the IUE observatory is very well suited to regular monitoring of AGN because of its ease of scheduling, efficient geosynchronous orbit, precise photometric calibration and stability, and broad wavelength coverage.

Simultaneous, frequently and regularly sampled multi-wavelength light curves are particularly important for blazars, since the variability timescales, at least at high energies are very short. Previous multi-wavelength studies on blazars have tried to investigate if the broad-band spectral energy distributions evolve in a consistent and reasonable fashion (e.g. George et al. 1988; Treves et al. 1989; Mufson et al. 1990). Unfortunately, their temporal sampling and multi-wavelength coordination were insufficient to allow determination of the temporal correlations and lags between the bands.

Recently, the IUE satellite has been employed for intensive blazar monitoring campaigns with nearly complete time coverage, often in conjunction with other satellites such as EXOSAT, Rosat, EUVE and ASCA, as well as with ground-based optical and radio telescopes. Monitoring programs for three well known blazars (PKS 2155–304, OJ 287 and 3C 279) were designed and realized by a large consortium of observers.

The BL Lac object PKS 2155–304 was intensively monitored during the month of November 1991 at radio through soft-X-ray energies. In 1993 March, the radio-strong BL Lac OJ 287 was observed simultaneously at radio, optical and UV wavelengths. Radio through γ-ray observations were obtained in 1992

December/1993 January for the OVV 3C 279 and are here compared to those of 1991: an additional constraint on very high energy variability is present for this source, which is not available for the other two.

Various models have been proposed to explain the γ-ray emission, the majority favoring the IC mechanism for γ-ray production (see Section 1.4 and, for reviews, Sikora 1994; MCG; Marscher & Bloom 1994). In fact, if the spectrum from radio to UV frequencies is interpreted as synchrotron radiation from high energy electrons in a jet with relativistic bulk flow, the same electrons can produce γ-rays by upscattering either the synchrotron photons (see case of PKS 0521–365, Section 1.4) or other photons external to the jet. In both cases a strong correlation between the synchrotron and IC emission is predicted, since they derive from the same relativistic electrons. The exact quantitative relation depends on the specific model, and the study of the simultaneous variations of the synchrotron (mm, UV, soft-X-rays) and IC (hard-X- and γ-rays) components offers a unique opportunity to test and constrain the models.

The results of the observations of the three selected blazars are described in this Chapter, devoting particular attention to the UV data. In Section 2.1.1 are reported in shortened form the results, presented by Urry et al. (1993), of the IUE campaign on PKS 2155–304; the multi-wavelength analysis based on the simultaneous multi-frequency data of the source was coordinated by Edelson (Edelson et al. 1994a) and is summarized in Section 2.1.2. The results of the 1993 March radio-to-UV campaign on OJ 287 were collected in Pian et al. (1994b) and are reported in Section 2.2. The radio-to-γ-ray energy distribution from the multi-wavelength observing campaign on 3C 279 was reported and discussed by Maraschi et al. (1994b). A summary of those results is given in Section 2.3, where also some unpublished UV data are presented.

2.1 Multi-Wavelength Monitoring of the BL Lac PKS 2155–304

PKS 2155–304 was chosen for an intensive multi-wavelength monitoring campaign because it is one of the brightest BL Lacs in the sky at X-ray through optical wavelengths, and has a history of strong, rapid multi-wavelength variability. Like most BL Lac objects, PKS 2155–304 has no strong emission features; overimposed on the UV spectrum are several absorption lines (Maraschi et al. 1988; Bruhweiler et al. 1993). A redshift $z = 0.116$ can be inferred from optical spectroscopy of the surrounding nebulosity (Falomo et al. 1993b). The object has previously been observed to be highly variable at both UV (Maraschi et al. 1986a; Urry et al. 1988; Tagliaferri et al. 1991; Edelson et al. 1991) and X-ray (Snyder et al. 1980; Sembay et al. 1992) wavelengths, with some evidence of quasi-simultaneous variability in those bands, albeit with smaller amplitudes and longer timescales at the longer wavelengths (Treves et al. 1989). The soft-X-ray spectrum is steep, and can be connected smoothly to the UV spectrum, implying that the UV and X-ray emission mechanisms may be related. This motivated the first application of relativistic jet (Urry & Mushotzky 1982) and accretion disk (Wandel & Urry 1991) models to the continuum emission from PKS 2155–304.

A monitoring program was designed with the aim of producing high-quality light curves in several bands, including unprecedented spectral coverage in the UV, EUV and soft-X-ray from the combination of IUE, the Rosat Wide Field Camera (WFC), and the Rosat Position Sensitive Proportional Counter (PSPC).

Observations were made in 1991 November at X-ray, UV, optical, near-IR, and radio wavelengths. Typically, each available instrument observed PKS 2155–304 about once per day during the period 1991 November 1–30. Furthermore, an intensive campaign of observations once every 96 min was undertaken with IUE during the period November 10.7–15.2, and with Rosat during the period November 12.2–15.3 (excluding time lost to Earth occultations and scheduling problems).

The result was the largest and most comprehensive database of multiwavelength observations ever gathered on an AGN in such a short time period. A data set containing over 200 IUE spectra, 10^6 Rosat PSPC photons, and 500 ground-based photometric observations were obtained in this period. The X-ray data and the ground-based optical and radio data are presented in three papers that discuss the data collection and reduction and the single-band analyses. The 24 Å soft-X-ray light curve resulting from the quasi-continuous four-day Rosat monitoring was presented by Brinkmann et al. (1994), and all of the month-long ground-based optical, IR, and radio data by Smith et al. (1992) and Courvoisier et al. (1994). The 1400 Å IUE-SWP, 2800 Å IUE-LWP and 5000 Å Fine Error Sensor (FES) data were taken directly from Urry et al. (1993, see Section 2.1.1).

In Section 2.1.1 the IUE data set, which is of unprecedented quality, is described. There will be presented the auto- and cross-correlations of the IUE light curves as well as the correlation between UV flux and spectral index. Multi-wavelength cross-correlations among the light curves at radio through X-ray frequencies are studied by the application of four different methods and discussed in Section 2.1.2. The implications of the results for models of variability are discussed in Section 2.1.3.

2.1.1 THE IUE CAMPAIGN

2.1.1.1 Observations and Data Analysis

2.1.1.1.a Observing Strategy

PKS 2155–304 is bright enough to be observed easily in a half IUE shift (four hours) or once per Rosat orbit (roughly 2000 seconds). The Rosat spacecraft constraints restricted observing to a 32-day period from 27 October 1991 to 28 November 1991, so the monitoring campaign was planned for that time (in the end, Rosat monitored the source only for a few days in the middle of the month; Brinkmann et al. 1994.) The variability timescales of BL Lac objects in general, and even this best-studied source in particular, were not well measured previously, so the observing plan bracketed a range of timescales. In order to measure moderate timescale variations (days to a week) we scheduled at least one half IUE shift daily from 1 to 29 November (except on November 8, due to a scheduling conflict). In order to study short-term variability, 4.6 days in the middle of the campaign (10.7–15.3 November) were devoted to nearly continuous coverage using ~3 shifts per day. The journal of the 201 IUE observations is given in Appendix A (Table A.1).

The SWP and LWP IUE cameras were exposed alternately, with nominal integration times of 55 and 25 minutes, respectively. This allowed us to get two pairs of spectra during each half IUE shift, in the absence of any operational problems. Just before each SWP or LWP exposure, counts from the FES, the optical monitor on IUE, were measured on target and on background. During the continuous observing period, the SWP/LWP/FES observing cycle was slaved to the 95.8-minute Rosat orbital period so that the IUE and Rosat observations would be locked in phase, thus greatly simplifying the cross-correlation between UV and X-ray light curves. As a result of this rigid schedule, some IUE exposures had to be longer or shorter than the nominal exposure times, typically by a few minutes. Only four SWP spectra (see Table A.1) are definitely underexposed ($t_{int} < 30$ min), and have been excluded from the correlation analysis, since short IUE exposures have been shown to give systematically low fluxes (Walter & Courvoisier 1991). The errors on quantities measured from these SWP exposures are almost certainly underestimated.

2.1.1.1.b Optical Calibration

The FES counts were converted to optical magnitudes using the algorithm of Perez & Loomis (1991), which takes into account the background due to scattered light. PKS 2155–304 was assumed to have color $B - V = 0.26$ mag throughout the month, which is the mean value measured contemporaneously with ground-based optical telescopes (it did not change much during the monitoring period; Smith et al. 1992). In any case, the conversion from FES counts to V magnitude is not terribly sensitive to the color; for example, using $B - V = 0.5$ mag would increase V by about 0.06 mag. Reddening corrections are minimal at these wavelengths (well within the FES accuracy), and so were ignored. The optical light curve is discussed in § 2.1.1.2.a.

2.1.1.1.c Ultraviolet Spectral Extraction

Spectra were extracted from each of the 201 IUE images using the SWET technique of Kinney et al. (1991b). These spectra are generally well-exposed, so that the SWET method is slightly preferred with respect to the GEX procedure (see Section 1.1). Nonetheless, we have also extracted all the spectra using GEX (the complete analysis is reported in Pian 1992), and compared this to the SWET results. Although there are small systematic differences between spectra extracted with the two methods, the results (which depend on fitted fluxes; see § 2.1.1.1.e) are not affected significantly.

2.1.1.1.d Ultraviolet Spectral Corrections

The extracted net fluxes were converted to absolute flux using the IUE calibration of Bohlin et al. (1990). A correction was made for degradation in the SWP sensitivity (Bohlin & Grillmair 1988, as updated through 1989.36 by Bohlin, private communication). The extrapolation to 1992 introduces some noise on the 5 Å scale but should not cause absolute flux errors of more than 1% in broad bands. No sensitivity correction was made to the LWP net flux.

The IUE spectra were dereddened using $A_V = 0.1$ mag (see Sections 1.1 and 1.2) and the average Galactic curve from Seaton (1979). The dereddening correction has often been ignored by previous IUE observers of PKS 2155–304, but it makes a significant difference. The dereddened flux is 31% greater at 1400 Å and 21% greater at 2800 Å than the observed flux, and the fitted energy spectral index is typically 0.07 flatter in the SWP and 0.32 flatter in the LWP. The soft-X-ray spectrum of PKS 2155–304 is consistent with the adopted column density of absorbing cool gas (e.g. Canizares & Kruper 1984; Madejski 1985), as are results from the Hopkins Ultraviolet Telescope, which is sensitive down to 912 Å (J. Kruk, private communication). These results all indicate there is little or no internal reddening in PKS 2155–304.

2.1.1.1.e Ultraviolet Spectral Fitting

Using an iterative, chi-squared minimization fitting routine, the dereddened IUE spectra were fitted to a simple power-law model of the form $F_\lambda = F_0(\lambda/\lambda_0)^{-\alpha_\lambda}$. The results are given here in terms of the energy index α_ν, which is related to α_λ by $\alpha_\nu = 2 - \alpha_\lambda$, but the fitting was done in wavelength space, with no resampling to frequency space.

Two sample fits to the data, chosen to be representative of the median intensities and the mean χ^2_ν-values for the SWP and LWP samples as a whole, are shown in Fig. 2.1; the SWET error vectors are plotted below each spectrum (in order to show the raw extracted spectra, the data and fits in Fig. 2.1 are not dereddened). The wavelength ranges over which the data were fitted were 1230–1950 Å for the SWP camera (which excludes the geocoronal Lyman-α region) and 2100–3100 for the LWP camera.

On the next page:

FIG. 2.1 — Representative spectra from among the 201 spectra in the data set. In both cases the source intensities are approximately the median values for the month-long monitoring campaign, and the exposure times are typical. Regions excluded from the power-law fitting are shown as dotted lines. Best-fit power law models, weighted according to the SWET error vector plotted in the panel at bottom, are shown as smooth curves; the spectra have not been de-reddened, so the fits shown differ from those presented in Table A.1. *(a)* An SWP spectrum obtained on 14 November 1991, with $\chi^2_\nu = 3.44$ for the best-fit power-law model. *(b)* An LWP spectrum obtained on 10 November 1991, with $\chi^2_\nu = 2.25$ for the best-fit power law.

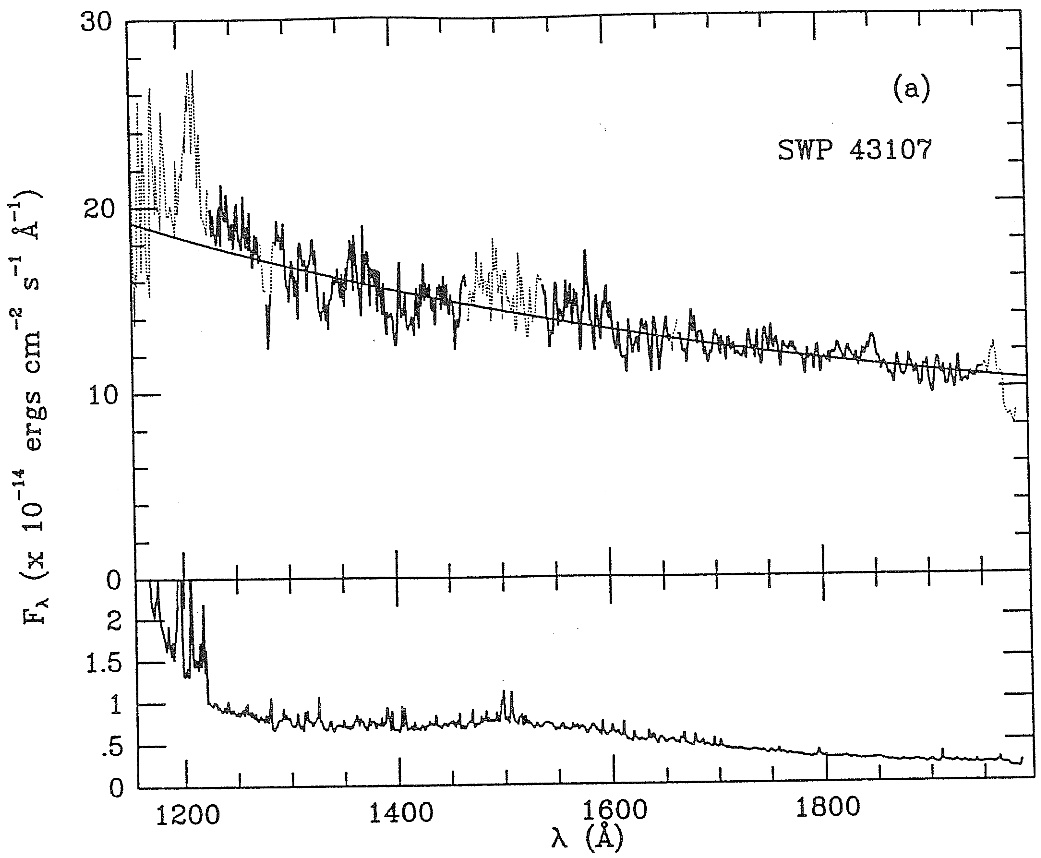
(a)
SWP 43107
F_λ (x 10^{-14} ergs cm^{-2} s^{-1} Å^{-1})
30
20
10
0
2
1.5
1
.5
0
1200
1400
1600
1800
λ (Å)

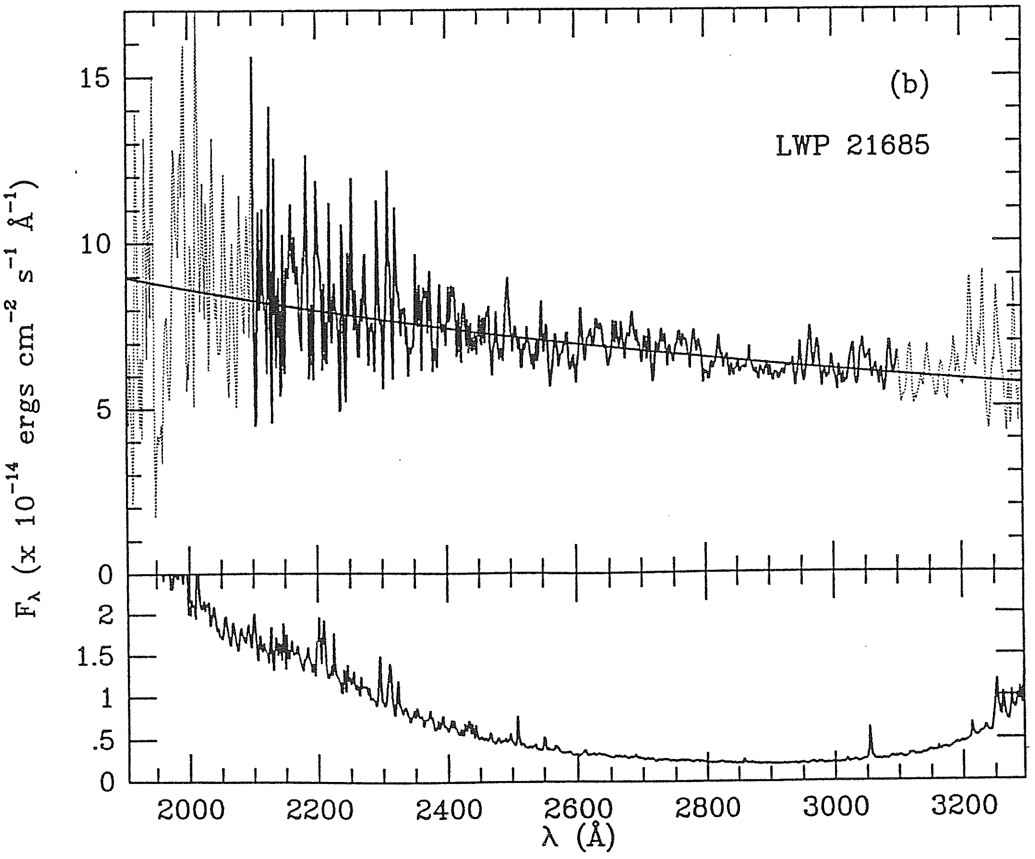
(b)
LWP 21685
F_λ (x 10^{-14} ergs cm^{-2} s^{-1} Å^{-1})
15
10
5
0
2
1.5
1
.5
0
2000
2200
2400
2600
2800
3000
3200
λ (Å)

Wavelength regions affected by SWP camera artifacts (Crenshaw et al. 1990), at 1277–1281 Å, 1286–1290 Å, and 1660–1666 Å, were excluded, as was the region 1470–1540 Å, in which unusual features were apparent in many of the spectra. These excluded regions are shown as light dotted lines in Fig. 2.1a. Since the artifacts in the LWP camera are of low contrast, no spectral regions were excluded in those fits. The power-law fit is clearly good, as is generally true for all the spectra.

Results of the fits to dereddened spectra are given in Table A.1. The normalization is at 1400 Å for SWP spectra and 2800 Å for LWP spectra. These wavelengths are close to the flux-weighted means of each band ($\sim$ 1560 Å and $\sim$ 2568 Å, respectively, for $\alpha = 1$), so that the uncertainty in the derived flux is small; they are in regions of the cameras where the S/N is good; and they were chosen to be relatively far away from one another, increasing the independence of the SWP and LWP flux measurements. The reduced chi-squared values in Table A.1 were calculated using the raw SWET errors, prior to the correction procedure described in § 2.1.1.1.f.

We also fitted combined spectra, i.e. pairs of SWP and LWP spectra taken close together in time, spliced together at 1978 Å. Power-laws were fitted to the wavelength range 1230–3100 Å, excluding the same regions as in the SWP analysis above, as well as 1900–2150 Å (which has relatively large errors anyway). The results are given in Table A.2. The advantage of fitting combined SWP-LWP spectra is that the longer baseline in wavelength gives smaller uncertainties on the fitted flux and spectral index; however, the mismatch between SWP and LWP spectra seen in previous work (e.g. Urry et al. 1988; George et al. 1988) and again here (see § 2.1.1.2.c) illustrates how the absolute values of fitted flux and spectral index depend on the uncertain intercalibration of the two cameras. Therefore, for absolute values of the flux and spectral index, the estimates from fits to the individual spectra (F_{1400}, F_{2800}, α_{SWP}, and α_{LWP}, in Table A.1) are better than those from the combined fits (α_C and F_C, in Table A.2). We consider the latter quantities when evaluating *changes* in spectral shape and intensity because of the larger bandwidth for the power-law fits (the combined spectral index is an effective hardness ratio between the SWP and LWP cameras).

2.1.1.1.f Error Analysis

Estimating the error bars reliably is the key to the detection and evaluation of variability. IUE spectra are dominated by systematic noise, including well-known features at the wavelengths mentioned above. The flux calculated from a fitted power-law gives a much smaller error bar than direct measurement because information from the full band is used.

The initial estimate of the uncertainty in the flux measurement comes directly from propagated uncertainties on fit parameters. The latter are derived from the error matrix calculated in the least-squares fitting procedure (e.g. Bevington 1969), which in turn depends linearly on the SWET errors used to weight the input data points. Thus, the estimated uncertainty in the flux measurement scales linearly with any modification to the SWET error.

While the relative sizes of the SWET errors make sense, the chi-squared distribution for the 201 spectral fits is far from acceptable. The mean reduced chi-squared values for the SWP and LWP fits are $\langle\chi^2_\nu\rangle = 3.76$ and $\langle\chi^2_\nu\rangle = 2.42$, respectively, where the number of degrees of freedom is taken as the number of points fitted in the spectrum (539 and 535, respectively) minus the number of fit parameters (2). The probability of exceeding either of these values given the number of degrees of freedom is vanishingly small. The power-law model appears to be a good fit to the data, and there are no systematic trends in the residuals that would indicate a different model might be preferred, so either the SWET errors are underestimated or the number of degrees of freedom (the number of independent points in each spectrum) is overestimated.

Previous authors (e.g. Clavel et al. 1991) have suggested normalizing the error vector for a given spectrum by the square-root of the reduced chi-squared value for that fit. In our view this is not the best approach, as it makes the χ^2_ν-distribution for all the fits look like a delta-function when in fact the χ^2_ν values should be distributed as chi-squared (it might be the best approach in the case of a single measurement.) Here we have a large number of measurements (201), so we imposed the condition that the mean of the reduced-chi-squared distribution be 1, as is expected for this many degrees of freedom (the 102 SWP spectra and 99 LWP spectra were handled separately; characteristics of the cameras such as graininess and fixed-pattern noise are quite different, so there is no reason to expect the corrections to the error vectors to be the same in the two cases.)

Scaling the SWET errors by 1.94 for the SWP spectra and 1.56 for the LWP spectra gave normal chi-squared distributions. Not only were the mean values 1, by definition, but a KS test showed no difference between the observed distributions and the expected $P(\chi^2_\nu)$. The uncertainties in the fitted fluxes were thus increased by those factors. A similar procedure was followed for the combined fits, where the mean reduced chi-squared value using the uncorrected sigmas was $\langle\chi^2_\nu\rangle = 3.42$. In this case, however, although the mean of the corrected distribution was adjusted to be 1, a KS test gave a low probability (4.7×10^{-4}) that the observed distribution was drawn from a normal chi-squared distribution. Thinking this might be related to the different camera characteristics, we re-fit the combined spectra normalizing SWP errors by 1.94 and LWP errors by 1.56. The resulting reduced-chi-squared distribution had a mean of 1.11, so we renormalized the errors by $1.05 = \sqrt{1.11}$. The final χ^2_ν-distribution, with mean equal to 1, was still incompatible with the expected distribution ($P < 3.9 \times 10^{-5}$ according to a KS test), probably because of the mismatch between SWP and LWP spectra. This reinforces our belief that the individual fits are better for measuring fluxes or spectral indices, while the combined fits may be more sensitive (due to the broader bandwidth) to trends in either flux or spectral index.

There can still be residual errors in measured quantities, such as spectral index or normalization, associated with the reproducibility from one spectrum to the next. These must be included when evaluating light curves. IUE fluxes of standard stars are reproducible at the ~ 1.25 % level (Bohlin 1988), so errors of this magnitude were added in quadrature to the internal flux errors estimated above (as in Edelson et al. 1991). In general, the internal photometric error is considerably smaller than 1.25%, unless the exposure time is unusually short. Estimating the repeatability of the spectral index measurements was more complicated. In their study, Clavel et al. (1991) estimated residual errors in measured quantities by comparing close pairs of spectra and assuming no variability on short timescales. If the estimated errors were really 1σ errors, the difference in measured values divided by the estimated error (the quadrature sum of the two individual error estimates) should be normally distributed, i.e., a Gaussian with zero mean and unit dispersion. A variance larger than one, Clavel et al. argued, meant the uncertainties on that measured quantity should be increased by just that factor. Since PKS 2155–304 is much more rapidly variable than their target, the Seyfert galaxy NGC 5548, this procedure was not appropriate for our flux measurement, hence the 1.25% photometric correction adopted as described above. However, it was the best alternative for evaluating the uncertainty on spectral index, particularly as the spectral index is certainly less variable than the flux (see § 2.1.1.2.b). Adjacent spectra taken closer in time than 5 hours were compared; this included 75 pairs of SWP and 69 pairs of LWP spectra. The variances in the distributions of normalized errors for short- and long-wavelength spectral indices were 1.94 and 2.41, respectively, so the error estimates in α_{SWP} and α_{LWP} were increased by those factors. The distributions of normalized, scaled errors were then consistent ($\gtrsim 50\%$ probability according to a KS test) with the normal Gaussian distribution expected. This procedure was repeated for combined spectra, comparing 78 pairs of adjacent, combined SWP-LWP spectra, taken within 5 hours of one another. Here, the scale factor for the combined spectral index was 2.18, and the final distribution was consistent with a Gaussian ($\sim 59\%$ probability, according to a KS test).

The estimation of errors in the flux and spectral index, in summary, involves several steps. First, the SWET error vector is propagated through the fitting procedure to get initial uncertainties for the parameters of the power-law fit. Next, uncertainties in both F_0 and α_λ are increased by a factor equal to the square root of the mean of the reduced chi-squared distribution, $\sqrt{\langle\chi^2_\nu\rangle}$, where $\langle\chi^2_\nu\rangle = 3.76$ for the SWP and $\langle\chi^2_\nu\rangle = 2.42$ for the LWP. This is effectively scaling up the SWET error vector so that $\langle\chi^2_\nu\rangle = 1$ in both cases. The final error estimate on the flux at λ_0 is equal to the quadrature sum of the scaled error on F_0 and 1.25% of F_0. The final error estimate on the spectral index was derived by increasing the scaled error on α_λ by 1.94 for the SWP, 2.41 for the LWP, and 2.18 for the combined SWP-LWP fits, so that it represents the 1σ error for the observed differences between adjacent measurements of α_λ. Since this assumes no intrinsic variation between adjacent measurements, it is if anything an overestimate of the error on the spectral index.

As a check, we did look at the distribution of normalized errors in the fluxes, using the uncertainties calculated as described above. In all three cases (SWP, LWP, and combined SWP-LWP values), the distributions were consistent with the expected Gaussian distributions (62%, 13%, and 38% probability, respectively, according to a KS test), indicating that our error estimate for the flux is at worst an overestimate.

A procedure similar to that used for determining the uncertainty in spectral indices was used to estimate the global mean uncertainty in the FES-derived magnitude. Using a trial value for the uncertainty, we generated the normalized error distribution for pairs of adjacent measurements separated by less than 5 hours, looking for a value that would give a variance equal to 1. The normalized error distribution for $\Delta V = 0.08$ mag had variance equal to one and was consistent (97% probability according to a KS test) with a Gaussian distribution centered on zero. It is also commensurate with previous estimates ($\Delta V \sim 0.07$ mag) of the accuracy of the FES (Holm & Crabb 1979; Barylak et al. 1984). However, the few large, apparently non-Gaussian excursions, could seriously compromise the value of the data, thus an unbiased method was devised to improve the data quality so they could be used in time-series analysis.

First, the 5000 Å data were paired up, with phases locked to the 96 min sampling at shorter wavelengths (to aid in correlation analysis). Next, the flux differences (ΔF_i) and averages ($\langle F \rangle_i$) were computed for each (i^{th}) pair. While the data for most pairs were within a few percent, five had $\Delta F_i / \langle F \rangle_i > 10\%$. These five pairs were excluded on the basis of their large internal dispersions. The fractional errors on the remaining 75 points were reduced from 8% to $\lesssim 3\%$ (measured from the internal dispersions ΔF_i), at the cost of reducing the sampling by a factor of two. However, this is not an important loss, since the original 5000 Å sampling was at least twice as frequent as that in any other band.

2.1.1.2 Results

2.1.1.2.a Ultraviolet and Optical Light Curves

During the monitoring campaign PKS 2155–304 increased in intensity by a factor of 2 over the month to roughly its historical maximum brightness. The light curves for the full month and for the central period are shown in Fig. 2.2. During the intensive monitoring, the UV flux varied by ~30% in several distinct flares that are well-sampled apart from a possible dip during the 7-hour gap on 11 November. The width of these rapid flares is roughly half a day; if we define an exponential variability timescale as $t_{var} = (d \ln F/dt)^{-1}$, then values for these flares are less than 2 days. Such fast UV variations have been detected previously in PKS 2155–304 itself and in Mkn 421, while slightly longer and/or lower amplitude flares have been seen in another three (3C 279, OI 158, and OD 26; Edelson 1992). Flux doubling in time intervals of days or even hours was found during the recent IUE campaigns on 3C 279 and OJ 287 (Sections 2.2 and 2.3); the flux errors are however rather large. The UV flares of PKS 2155–304 show no discernible asymmetry in time according to a dI/I test (Wagner & Witzel 1992). The depth of the dip during 12 November is unclear. The low SWP point comes from a very short exposure of only 13 minutes and no corresponding dip is seen in the LWP light curve, so the SWP point should be considered uncertain.

Based on the rapid flaring seen during the intensive monitoring, it appears

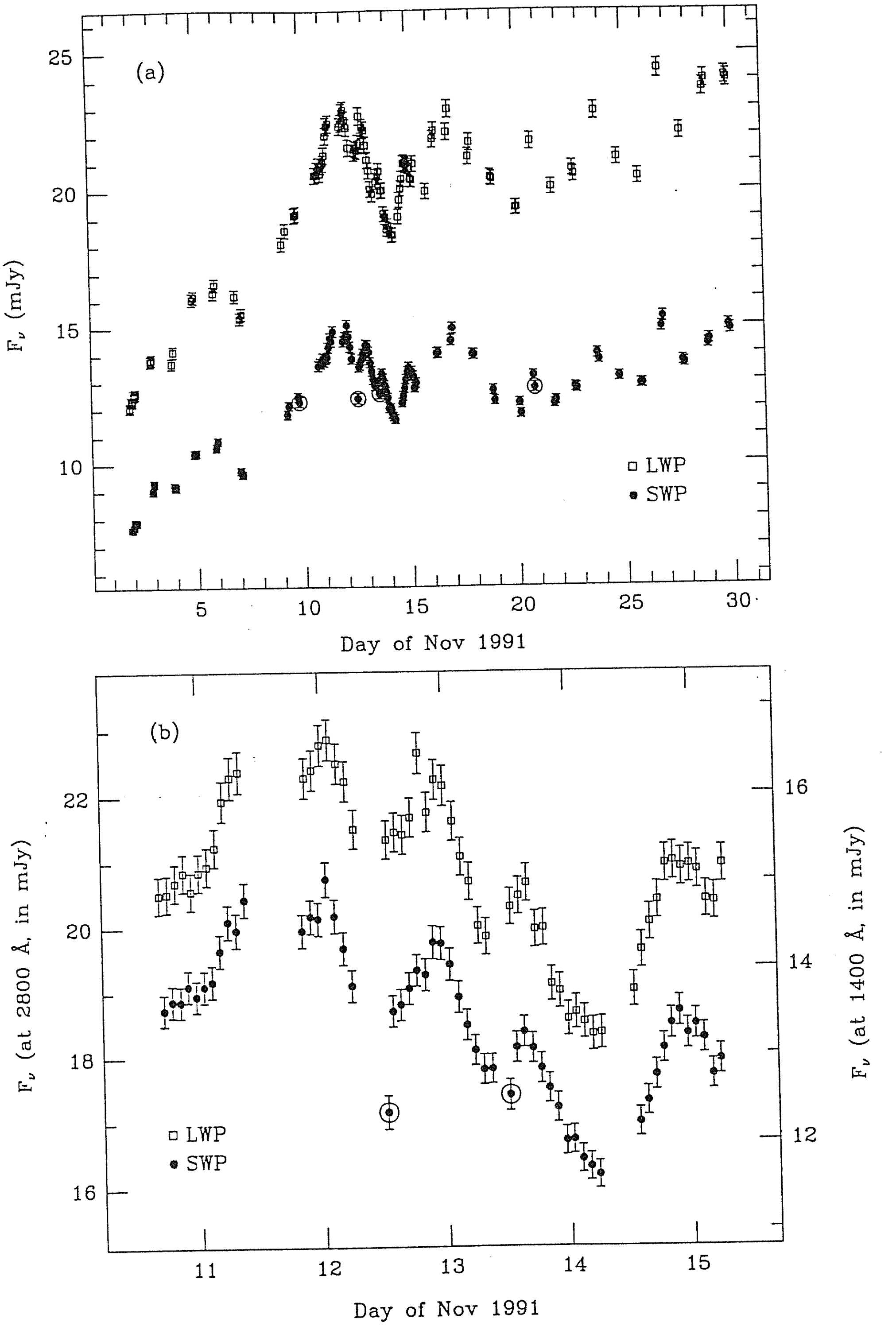

FIG. 2.2 — Ultraviolet light curves of PKS 2155-304. *(a)* The full month-long light curve, with fitted LWP fluxes at 2800 Å (*open squares*) and SWP fluxes at 1400 Å (*filled circles*) on the same scale. The four SWP fluxes that are uncertain due to anomalously short exposure times are circled. *(b)* Expanded view of the intensive monitoring period, during which IUE observations were nearly continuous. The LWP scale is at left, the SWP scale at right.

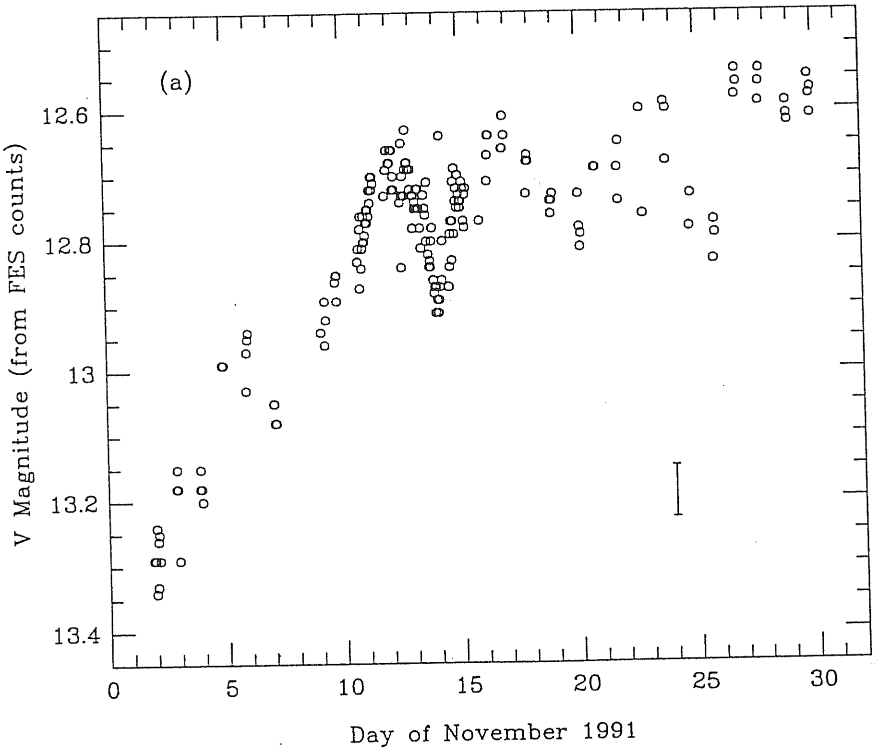

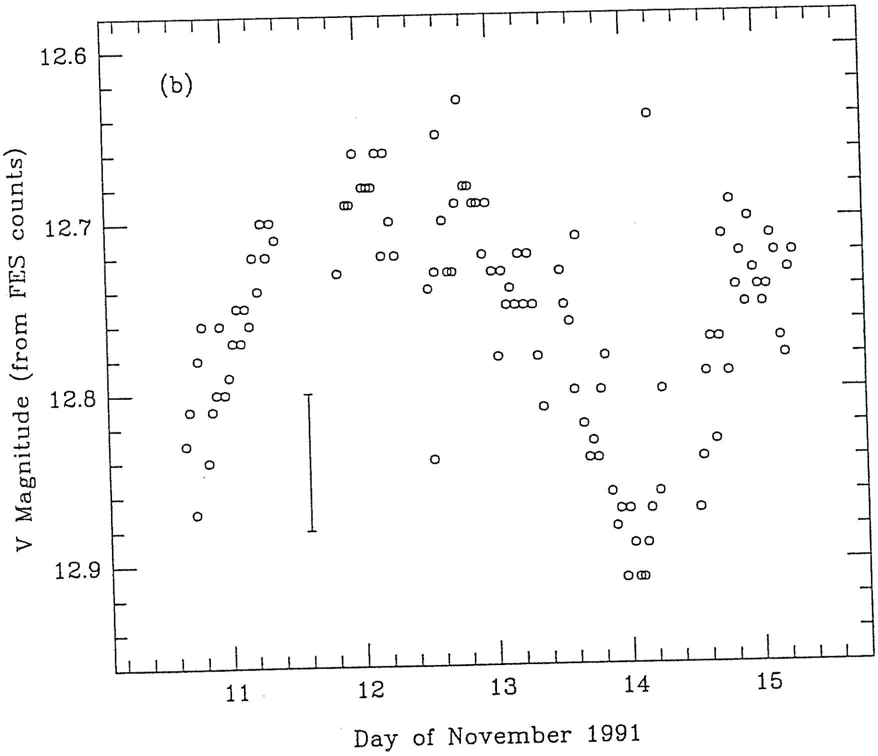

FIG. 2.3 — Optical light curves deduced from the IUE FES monitor for *(a)* the full month and *(b)* the intensive monitoring period. Typical error bars of ~ 0.08 mag are shown in each panel.

we probably failed to sample the fastest-timescale flares during the rest of the month, although the overall doubling of the flux is well-sampled. The fractional variability is comparable for the SWP and LWP bands: both light curves show a doubling of flux, and in both bands the variance is about 15% of the mean flux. This is in contrast to the historical trends in other blazars, where long-term IUE monitoring indicates the SWP flux is more variable than the LWP flux (Edelson 1992).

The FES light curve, shown in Fig. 2.3, shows the same trends as the UV light curves, on both long and short timescales, although the larger error bars mean the variations are less well defined. Although the light curve is given as V-magnitude (from the algorithm used to convert FES counts to optical magnitudes; Perez & Loomis 1991), the FES sensitivity is slightly bluer than the V-band. To test the correlation of the SWP, LWP, and FES fluxes we resorted here to the Discrete Correlation Function method (DCF; Edelson & Krolik 1988). The DCF is analogous to the classical correlation function (which requires evenly sampled data), except that it can work with unevenly sampled data. It works as follows: first, the two unevenly sampled light curves, $x(t_i)$ and $y(t_j)$, are normalized to zero mean and unit dispersion:

$$x_i{}' = \frac{x(t_i) - \langle x \rangle}{\sigma_x}, \tag{2.1a}$$

and

$$y_j{}' = \frac{y(t_j) - \langle y \rangle}{\sigma_y}, \tag{2.1b}$$

where $\langle x \rangle$ and σ_x are the mean and standard deviation measured for the light curve $x(t_i)$. Then, for each pair of points, $x_i{}'$ and $y_j{}'$, the time lag Δt_{ij} and unbinned DCF ($UDCF$) are computed:

$$\Delta t_{ij} = t_i - t_j, \tag{2.2a}$$

and

$$UDCF_{ij} = x_i{}' \times y_j{}'. \tag{2.2b}$$

The $UDCF$s are then binned in bins of width τ, such that for all pairs with

$$T_{lag} - \tau/2 < \Delta t_{ij} \leq T_{lag} + \tau/2, \tag{2.3a}$$

the following is computed:

$$DCF(T_{lag}) = \frac{1}{N} \sum UDCF_{ij}. \tag{2.3b}$$

The result is the autocorrelation function when the input light curves are the same ($x_i = y_i$), and the cross-correlation function when they are different. As a final step, the best estimate of the lag is made with a three-point parabolic fit to the point with maximum correlation and the two adjacent points.

The SWP, LWP, and FES light curves are all highly correlated, as shown in the DCFs for SWP versus LWP and SWP versus FES (Fig. 2.4). The peaks of both DCFs are at zero lag, with an upper limit of $\lesssim 0.1$ days, but both cross-correlation functions are asymmetric, in the sense of the short-wavelength emission leading the longer wavelength emission. These are not necessarily contradictory; see interpretation in § 2.1.1.3.

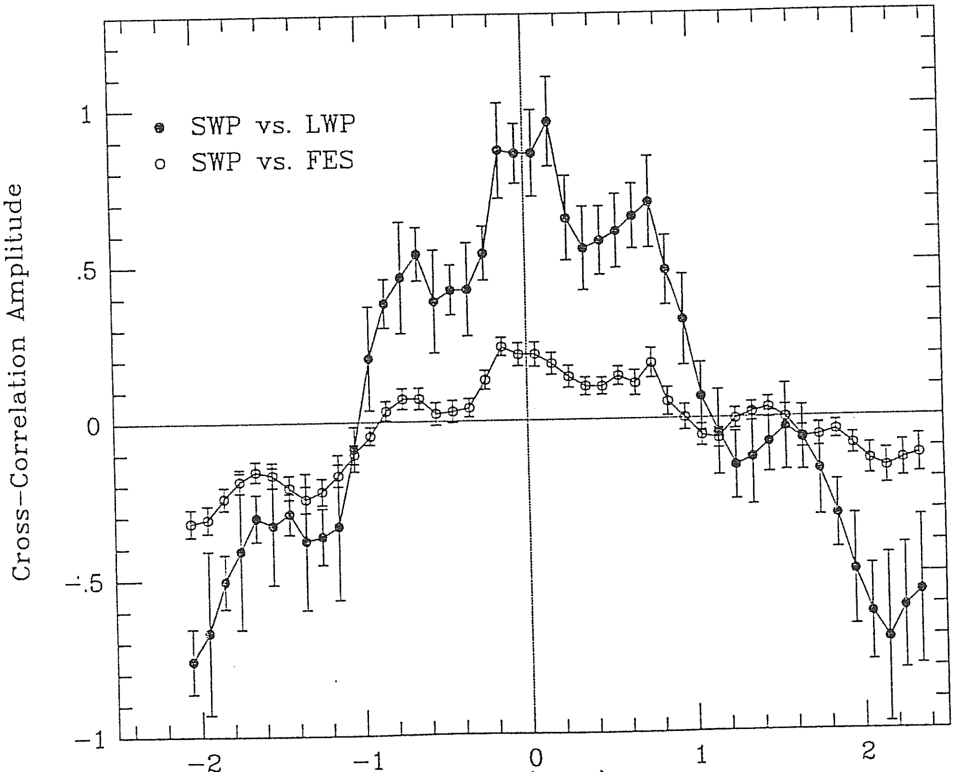

FIG. 2.4 — Discrete cross-correlations between SWP flux and longer-wavelength flux for the intensive monitoring period. (*filled circles*) SWP flux at 1400 Å versus LWP flux at 2800 Å; (*open circles*) SWP versus FES flux.

The autocorrelation functions of the SWP, LWP, and FES light curves are shown in Fig. 2.5.

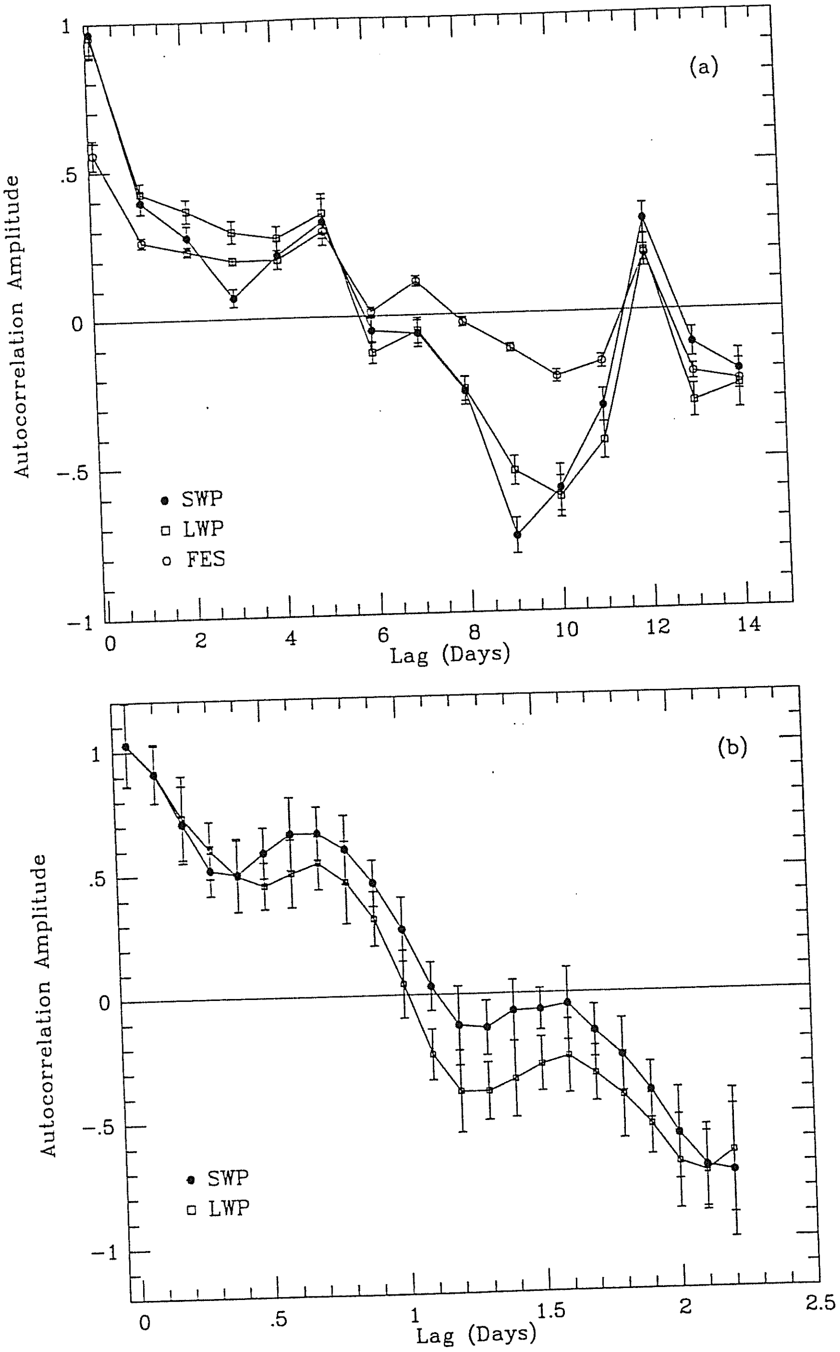

FIG. 2.5 — Discrete auto-correlation functions for SWP flux at 1400 Å *filled circles*), LWP flux at 2800 Å(*open squares*), and FES flux (*open circles*). *(a)* Calculated for the full 30-day data set, which is probably undersampled. *(b)* Calculated for the 4.6-day intensive monitoring period only.

The SWP and LWP give similar results, while the FES amplitude is generally smaller because the relative errors are larger (for the SWP and LWP, the behavior of the autocorrelation functions suggests the estimates of flux errors were about right). On long timescales, the autocorrelation functions suggest smooth "red" power spectra, with relatively more power on longer timescales. However, on shorter timescales (using the data from the well-sampled, 4.6-day intensive monitoring) they are modulated with a period of ~0.7 days. This quasi-periodic behavior, which will be discussed in detail in Section 2.1.2, can be seen going through five cycles in the light curves (Fig. 2.2b), despite the gap at 11.5 November.

2.1.1.2.b Ultraviolet Spectral Variability

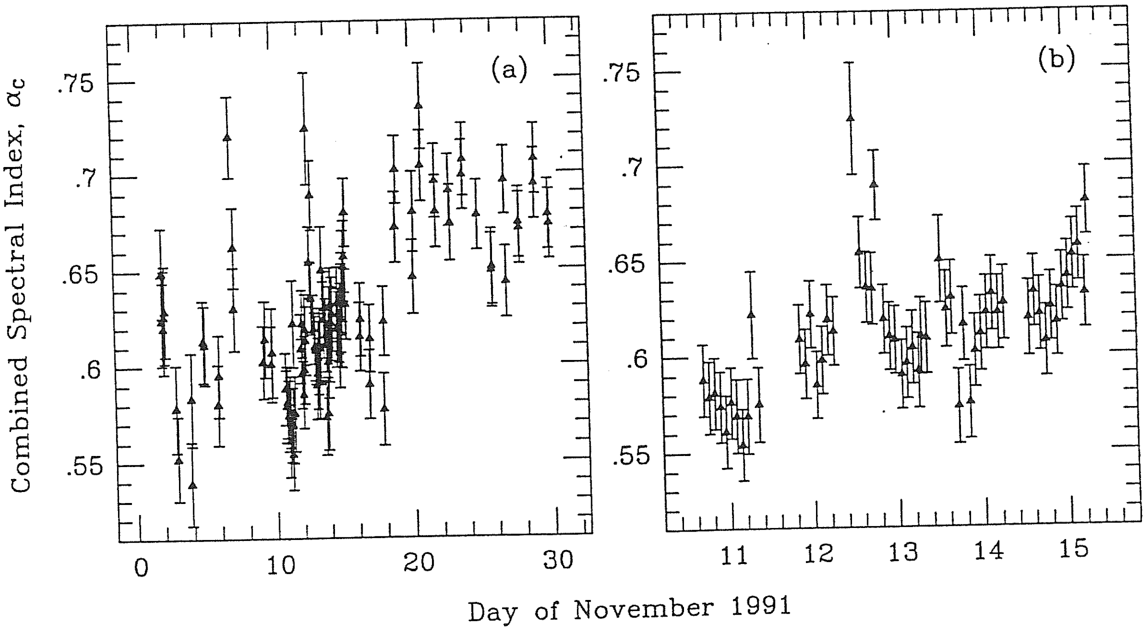

FIG. 2.6 — Variability of the combined spectral index *(a)* over the full month and *(b)* during the intensive monitoring period.

A key point in the interpretation of the continuum emission from PKS 2155–304 is the relationship between variability in intensity and spectral shape.

Previous monitoring has suggested that the spectral index varies little during flares in intensity, but this observation was always restricted to grossly undersampled light curves. The present campaign, with its improved sampling, should be more sensitive to related variations in flux and spectral index. The variation of spectral index throughout the run is shown in Fig. 2.6. According to the chi-squared statistics, the model of constant spectral shape can be ruled out: $\chi^2_\nu = 4.68$ for the combined spectral index. This is also seen in the SWP camera alone, where $\chi^2_\nu = 1.94$ ($P(\chi^2_\nu) = 5.9 \times 10^{-8}$) for a constant fit to α_{SWP} (the variation in the LWP spectral index is not significant, $\chi^2_\nu = 0.98$, because of the larger errors due to the low S/N below 2400 Å).

Plausible physical processes causing intensity variability, such as acceleration of radiating particles near a shock, predict accompanying changes in the spectrum of the emitted radiation. For example, electron acceleration would cause spectral hardening with increasing intensity. Thus one might expect flux and spectral index to be inversely correlated. Such correlations have been found previously for Mkn 421 (Ulrich et al. 1984) and OJ 287 (Maraschi et al. 1986a), although these studies referred to data taken over much longer time intervals. In the present case, a non-parametric Spearman Rank-Order Correlation test suggests an inverse correlation between F_{1400} and α_{SWP} ($P = 9.2 \times 10^{-3}$ of occurring by chance for the full data set; $P = 0.07$ for the intensive monitoring period only), but not between F_{2800} and α_{LWP} ($P = 0.87$ and $P = 0.76$ for full and intensive periods, respectively) or F_{2000} and α_C ($P = 0.41$ and $P = 0.19$ for full and intensive periods, respectively). Fig. 2.7a shows the scatter plot of the last of these, with filled circles indicating data from the intensive monitoring period.

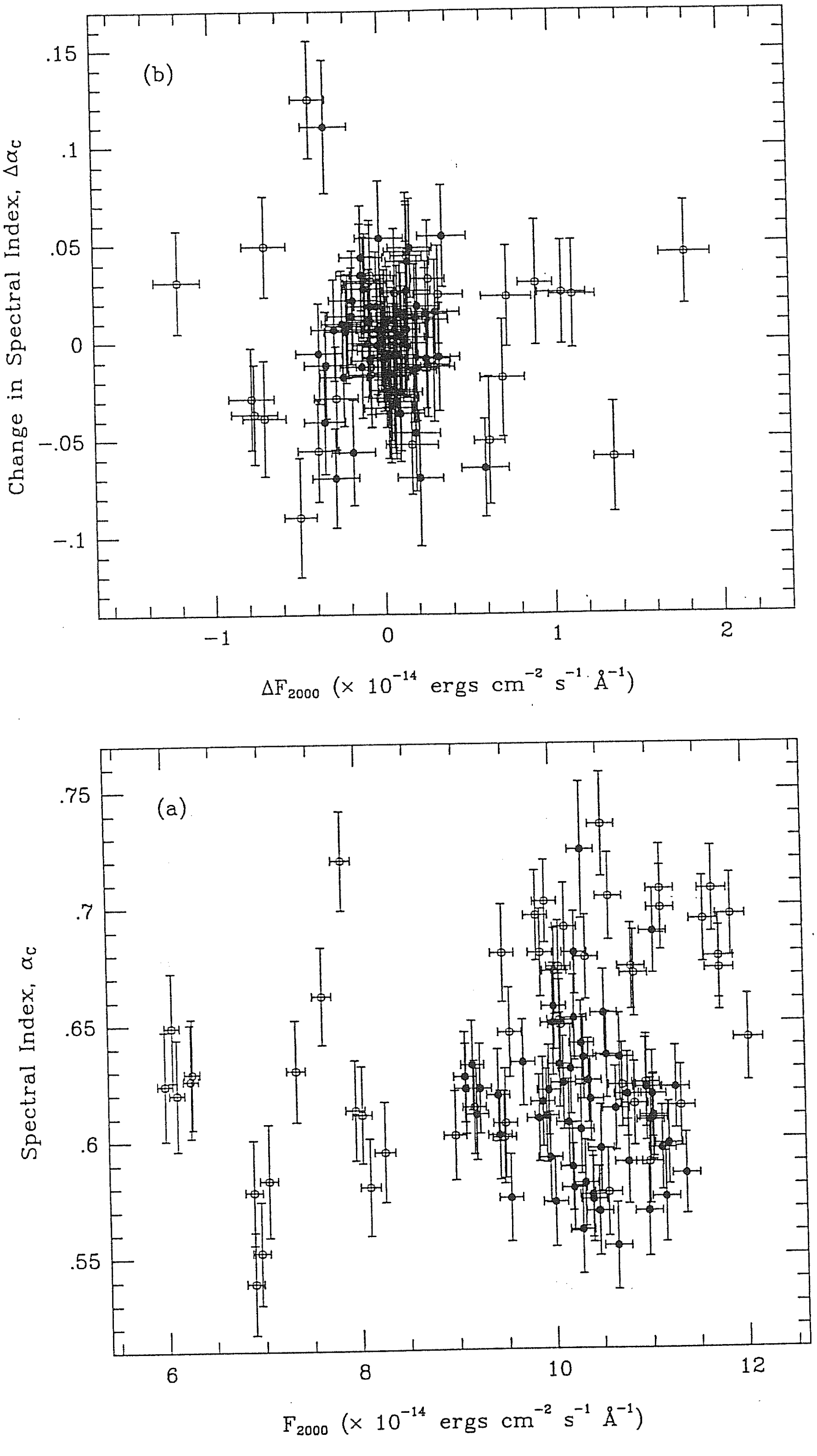

FIG. 2.7 — Ultraviolet flux versus spectral index. *(a)* F_{2000} versus α_C for the full month *(open circles)* and for the intensive monitoring period *(filled circles)*. *(b)* ΔF_{2000} versus $\Delta\alpha_C$ for the full month *(open circles)* and for the intensive monitoring period *(filled circles)*.

Previous authors found no correlation between flux and spectral index for PKS 2155–304, but did find a correlation between ΔF and $\Delta\alpha$, where the change is measured between pairs of spectra taken close in time (Maraschi et al. 1986a; Urry et al. 1988; Edelson 1992). In the present instance, in contrast, change in spectral index and change in flux are not strongly correlated; Fig. 2.7b shows the change in spectral index versus the change in flux for the combined SWP-LWP spectral fits. The probability of correlation between $\Delta\alpha$ and ΔF for the intensive monitoring period (measured from adjacent data points) is significant only for the lower-quality LWP data ($P > 99.9\%$). For the full data stream, using the differences between daily averages, $\Delta\alpha$ and ΔF are marginally anti-correlated for the SWP data ($\sim$ 96.7%). In neither case are the combined SWP-LWP data correlated or anti-correlated. We conclude that there is no significant direct correlation between instantaneous spectral shape and intensity, or changes thereof, in the IUE data.

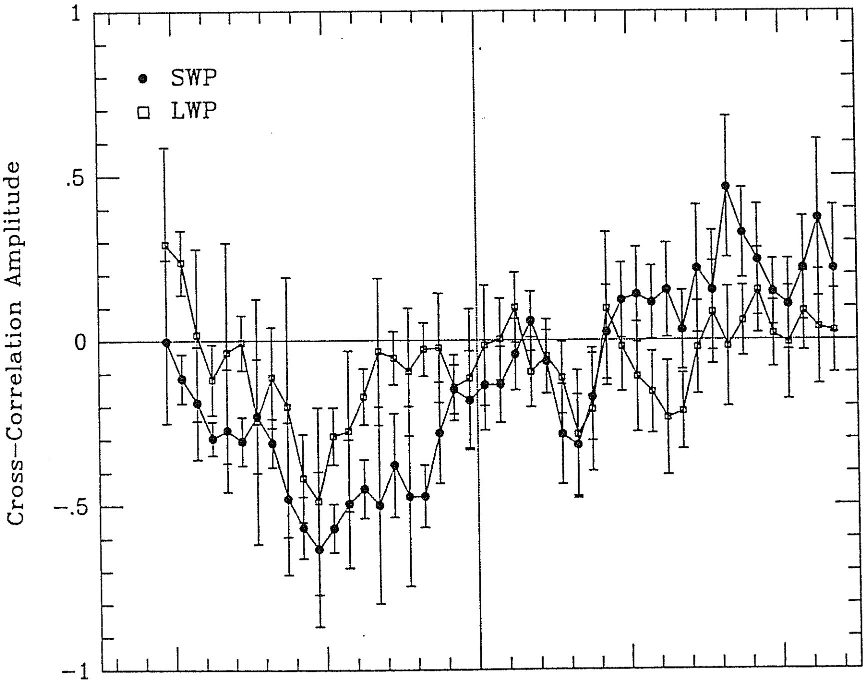

FIG. 2.8 — Discrete cross-correlation of spectral index versus intensity for the intensive monitoring period. (*filled circles*) F_{1400} vs. α_{SWP}; (*open squares*) F_{2800} vs. α_{LWP}.

Given the importance of understanding spectral variability, we applied the DCF, usually used to investigate flux-flux correlations, to the cross-correlation between flux and spectral index for the intensive monitoring period, where the light curve is well-sampled. The results are shown in Fig. 2.8 for the SWP and LWP fits (which track each other well). There is clearly structure in this DCF. The negative lag means that changes in the spectral index precede changes in the intensity, and the negative correlation amplitude means that spectral hardening (decreasing α) is associated with increasing intensity. Thus, there appears to be some kind of inverse correlation between spectral index and intensity, but with a lag of one to two days.

2.1.1.2.c Ultraviolet Spectral Shape

The spectral shape in the UV band depends critically on the dereddening correction. When no correction is applied, the LWP spectral indices are systematically higher than the SWP spectral indices (e.g. Edelson 1992). This implies flattening of the spectrum toward shorter wavelengths; that is, a "concave-up" shape in ν-F_ν space, in contrast to the overall "concave-down" shape of the radio through soft-X-ray spectrum. The excess at long wavelengths due to inclusion of starlight is not strong ($\lesssim 3\%$, see Section 1.2), as the host galaxy for PKS 2155–304 is too faint ($V \sim 16.5$, Falomo et al. 1991; Falomo et al. 1993b) relative to the nuclear point source. The spectral curvature goes away, however, when a dereddening correction with $E(B-V) = 0.034$ mag is applied (if we fit the entire ensemble of combined SWP-LWP spectra to a power-law model leaving the dereddening correction as a free parameter, chi-squared is minimized for this value). Fig. 2.9 shows the distributions of SWP and LWP spectral indices for three assumed values of $E(B-V)$: 0.0 mag, 0.034 mag, and 0.05 mag. With no correction, the LWP spectra are steeper; with $E(B-V) = 0.05$ mag, the SWP spectra are steeper; and $E(B-V) = 0.034$ mag is roughly the value at which the SWP and LWP spectral indices agree best. Thus, although the amount of reddening is generally uncertain, depending on the assumed gas-to-dust ratio, which has a large uncertainty, the assumption that the UV spectrum is either a flat power-law or concave-down would indicate a minimum reddening of $E(B-V) \sim 0.03$ mag.

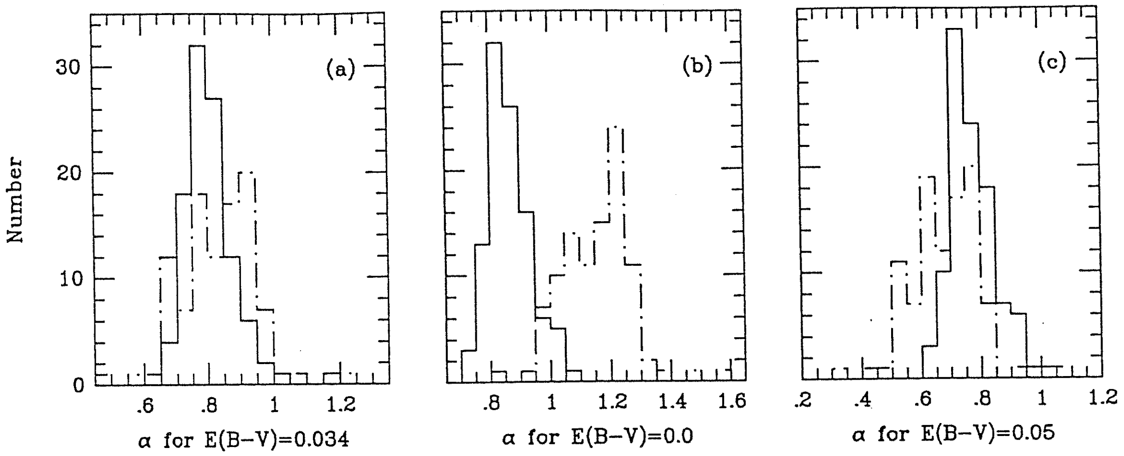

FIG. 2.9 — Histograms of spectral index distributions for SWP *(solid line)* and LWP *(dotted-dashed line)*. *(a)* Fits presented in Table A.1, corrected for reddening using $E(B-V) = 0.034$ mag; *(b)* raw data, not corrected for reddening; *(c)* fits after correction with $E(B-V) = 0.05$ mag.

Taking the reddening into account, then, there is no evidence for spectral curvature in the UV band. The flatness of the UV spectral index ($\alpha < 1$) means that peak of the luminosity emitted from this BL Lac object is in the far-UV, as noted by previous authors. PKS 2155–304 is one of the few extragalactic objects detected in the Rosat WFC survey (Pounds et al. 1993), and by the Extreme Ultraviolet Explorer (EUVE; Malina & Bowyer 1992), indicating that its EUV luminosity must be considerable.

2.1.1.3 Discussion

Throughout our month-long observing campaign the UV and optical flux of PKS 2155–304 increased by a factor of two. The light curves are far from smooth, however, with rapid lower-amplitude events superimposed. During the intensive monitoring period in the middle of the month, there are a number of well-sampled, large-amplitude ($\sim 30\%$) variations which appear to have a quasi-periodic timescale of ~ 0.7 days. Whether this periodicity is real requires a longer data train with equal or better sampling. The exponential timescales associated with the most rapid events are a few days or less; the actual time in which flux was seen to double was approximately 10 days. Similar fast, intraday variability, including the appearance of quasi-periodicity, has been seen in optical observations of BL Lac objects (Quirrenbach et al. 1991). Such short timescales are consistent with the predictions of the standard relativistic jet models for BL Lac objects (see Section 2.1.3).

The spectral variability observed is intriguing, and not easily interpreted. The fluxes within both IUE bands and the optical flux deduced from the FES are all well correlated with no discernible lags on timescales $\gtrsim 3$ hours. The cross-correlation functions are asymmetric, however, in the sense that short-wavelength emission leads the long. This may indicate that the emitting volumes are not significantly different across the UV band, but that radiative losses are sufficiently energy dependent that the short-wavelength flux decays faster than the long-wavelength flux.

The overall amplitude of variability is roughly the same in the short- and long-wavelength IUE bands, but the UV spectral shape does vary significantly during the campaign. Comparing Figs. 2.6 and 2.7, we can see that the relation between intensity and spectral shape is not simple. While the source flux doubled in the first ten days, the spectral index increased briefly and then returned to roughly its initial level. In the latter half of the month, while the source intensity remained high, the spectral index steepened. During the intensive monitoring period, the flux-spectral index relationship is similarly complicated.

Spectral variability is a strong diagnostic of any emission process. The general sense of the variation in PKS 2155–304 is that the spectrum hardens with increasing intensity, as expected for nonthermal processes where increases (decreases) result from acceleration (radiative losses) of the non-thermal electron population. The apparent temporal lag (~1 day) between change in spectral shape and change in intensity (Fig. 2.8) is more difficult to interpret.

Specifically, Celotti et al. (1991) consider the variability characteristics of a range of jet models, assuming that an increase in emissivity is triggered by a signal traveling along the jet, without affecting the local particle spectra. In this case it is possible to produce UV variability with very small spectral changes. Correlated variability the different energies is deeply discussed in Section 2.1.3.

2.1.2 MULTI-WAVELENGTH ANALYSIS

The simultaneous X-ray, UV, optical, IR, and radio monitoring data from the multi-wavelength 1991 November campaign are used here to test and constrain models of continuum emission from the BL Lac object PKS 2155–304. The frequent and regularly spaced sampling of the high energy data gives an unprecedented opportunity of rigorously apply correlation methods and to determine lags among the light curves and possible periodicities.

The multi-wavelength variability data are shown altogether in Fig. 2.10. Light curves covering the entire 30-day time span for seven UV-optical-IR bands and four radio bands are given in Fig. 2.10a. Data from the intensive satellite monitoring period (November 10.7–15.3), covering observing bands centered on 24 Å (PSPC), 1400 Å (SWP), 2800 Å (LWP) and 5000 Å (FES), are given in Fig. 2.10b.

Normalized variability amplitudes (NVA) are computed by taking all of the N data points in a given waveband and time span, and taking the ratio of the standard deviation over the mean. A crude measure of the error on each estimate is given by $NVA/\sqrt{N-1}$. These data are tabulated in Table 2.1, for a number of different observing bands and time spans.

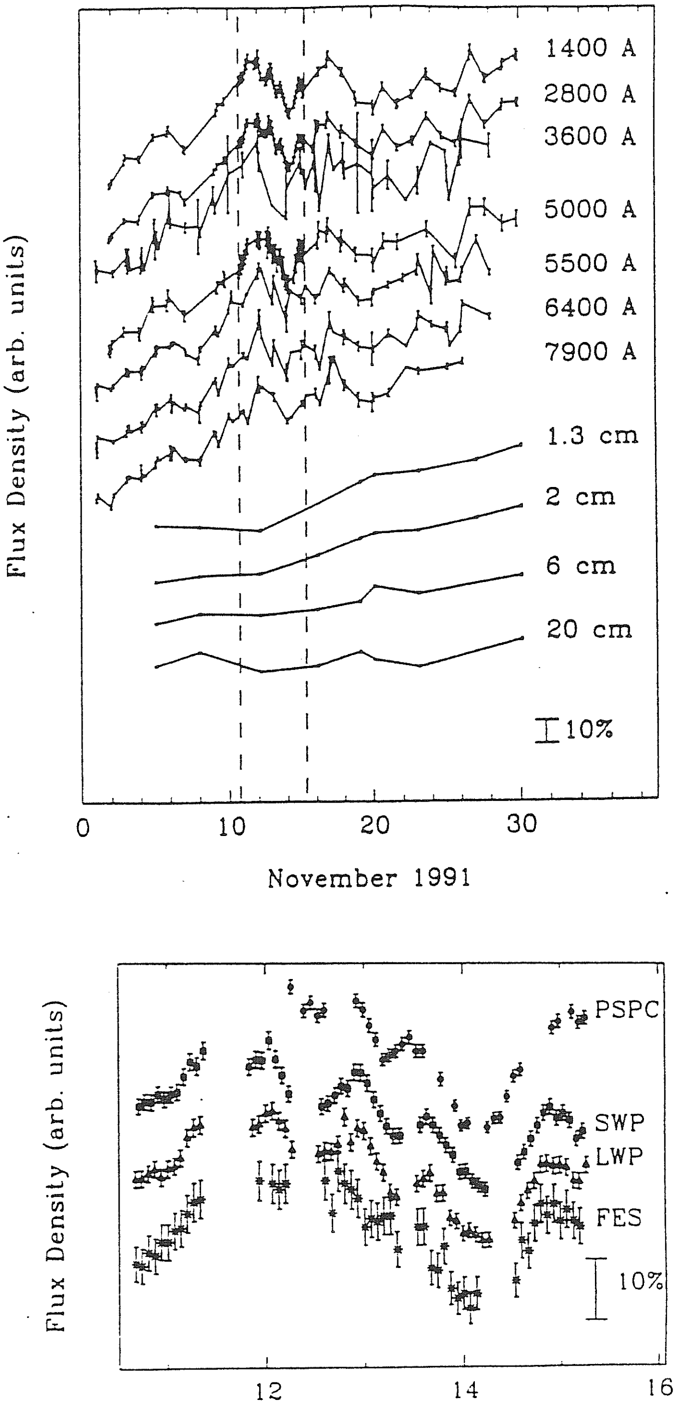

FIG. 2.10 — Multi-wavelength light curves. The data for the entire 30-day observing period in seven UV, optical, IR bands and four radio bands are given in Figure 2.10a. The dotted lines mark the intensive satellite monitoring period (1991 Nov 10.7–15.2). Light curves from this period, covering four observing bands centered on 24 Å, 1400 Å, 2800 Å and 5000 Å, are given in Figure 2.10b.

TABLE 2.1

NORMALIZED VARIABILITY AMPLITUDES IN DIFFERENT WAVEBANDS AND TIME SPANS

Waveband	Total		Intensive		non-Intensive		Second Half	
(Å)	*NVA* (%)	*N*	*NVA* (%)	*N*	*NVA* (%)	*N*	*NVA* (%)	*N*
24	7.3 ± 1.3	33	7.3 ± 1.3	33				
1400	13.6 ± 1.4	98	5.4 ± 0.9	36	18.4 ± 2.8	45	7.5 ± 1.4	28
2800	14.3 ± 1.4	99	5.7 ± 0.9	39	20.0 ± 3.0	45	7.0 ± 1.5	23
3600	19.1 ± 2.6	54	9.0 ± 4.5	5	19.8 ± 3.0	46	8.1 ± 1.9	19
4400	17.8 ± 2.2	68	6.0 ± 2.7	6	18.2 ± 2.4	60	5.6 ± 1.3	20
5000	17.9 ± 2.0	84	6.0 ± 1.0	34	20.7 ± 3.5	36	6.9 ± 1.6	19
5500	18.2 ± 2.1	78	7.1 ± 2.5	9	19.1 ± 2.4	64	5.9 ± 1.3	23
6400	18.1 ± 2.2	66	6.0 ± 2.2	8	19.1 ± 2.6	54	5.8 ± 1.3	20
7900	18.5 ± 2.3	64	6.6 ± 2.5	8	20.1 ± 2.8	52	5.4 ± 1.3	19
12500	8.1 ± 2.3	13					7.2 ± 2.4	10
16500	6.5 ± 1.9	13					6.1 ± 2.0	10
22000	7.2 ± 2.1	13					6.4 ± 2.1	10
1.3×10^8	14.8 ± 5.6	8			13.6 ± 5.5	7		
2.0×10^8	12.1 ± 4.3	9			11.7 ± 4.4	8		
3.5×10^8	8.9 ± 3.2	9			9.0 ± 3.4	8		
6.1×10^8	7.1 ± 2.7	8			7.2 ± 3.0	7		
2.0×10^9	4.7 ± 1.8	8			4.5 ± 1.8	7		

Perhaps the most striking point in Table 2.1 is that the variability amplitudes appear to stay constant from X-ray through IR wavelengths, and then decline markedly to longer radio wavelengths. While this analysis is somewhat complicated by the fact that the different bands were observed over different timescales, a quantitative comparison can be made by restricting the analysis to bands and time spans in which the coverage is similar. For instance, during the period when both IUE and Rosat were observing PKS 2155–304 (November 12.2–15.1), all of the X-ray through optical bands showed a similar level of variability (~6.5%). During the second half of the campaign (November

16–31, the only period with good IR coverage), the entire UV through IR variability was again consistent with a single value of $NVA \approx 6.5\%$. Finally, restricting the analysis to those wavebands that spanned the entire month-long campaign and excluding data from the intensively sampled period (which could bias the amplitude of a well-sampled band relative to a poorly sampled one), the UV-optical data are again consistent with a single value ($NVA \approx 19\%$), but in the radio, the level of variability decreases monotonically with wavelength, from 13.6% at 1.3 cm to 4.5% at 20 cm over the entire month.

2.1.2.1 Time-Series Analysis

The first observational result of this campaign is that the variations in the different bands (except the radio) were all clearly correlated. The variations were sufficiently rapid that only the quasi-continuous data from the intensive monitoring period were sampled fast enough to allow a detailed measurement of the correlation properties. For that reason, the correlation between the Rosat 24 Å and IUE 1400 Å variations is examined in detail in § 2.1.2.1.a,b,c,d. The rest of the intensively sampled data are analysed in § 2.1.2.1.f, and the optical through radio variations are discussed in § 2.1.2.1.g. Finally, the issue of possible periodicities in the data is discussed in § 2.1.2.1.h.

In order to make quantitative estimates of the degree of correlation and the lag between variations at different wavelengths, four methods are applied to the relatively well-sampled 24 Å and 1400 Å data: the Discrete Correlation Function (already described in § 2.1.1.2.a), a modification of the mean variance technique (§ 2.1.2.1.b), the χ^2 minimization technique (§ 2.1.2.1.c), and the maximum entropy method (§ 2.1.2.1.d). The results are summarized and compared in § 2.1.2.1.e. In the following, a maximum (or, for the MMD and χ^2 method, a minimum) at positive lags means that the shorter wavelength variations lead those at longer wavelengths.

2.1.2.1.a Discrete Correlation Function

This method is described in Section 2.1 (§ 2.1.1.2.a). The 24 Å–1400 Å cross-correlation function is shown in Fig. 2.11. The highest point in the cross-correlation is at −1.80 hr, but it also shows a clear, double-peaked structure, with the other peak of almost equal strength at +3.88 hr. This type of problem is often seen in the DCF, and it appears to be related to the fact that the measured function is a convolution of the lag with an autocorrelation function of non-zero width. PKS 2155–304 (like most AGN) appears to have a steep fluctuation power density spectrum (Tagliaferri et al. 1991), with significant power on time scales longer than the few days probed in the intensive sampling. This leads to a wide autocorrelation function, so the cross-correlation function is also very wide with a broad, flat peak, and thus is relatively insensitive to the exact value of the lag. To be conservative, we adopt the mean of the two peak values (+1.04 hr) as the best estimate of the lag.

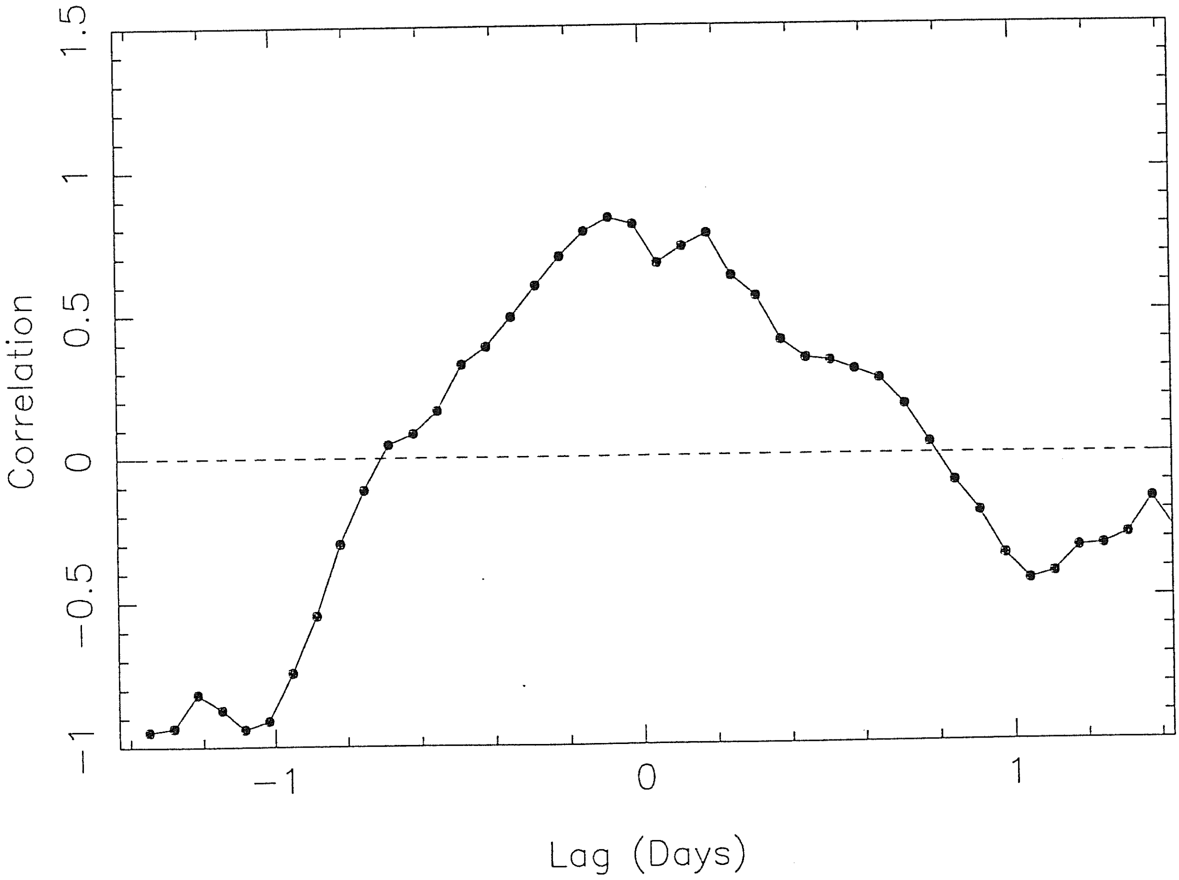

FIG. 2.11 — Discrete correlation function between 24 Å and 1400 Å.

At zero lag, the DCF is equivalent to the standard correlation coefficient (i.e. $DCF(T_{lag} = 0) = r$), for which the significance can be simply calculated. These data can then be used to determine directly the probability that the data are in fact truly correlated. The values of r at zero lag and the associated false-alarm probability (p_0) are given in Table 2.2

TABLE 2.2
CORRELATIONS AND LAGS

Wavebands (Å)	$r_S(0)$	$N(0)$	$p(0)$	χ^2 Min. Lag (hr)	MMD Lag (hr)	MEM Lag (hr)	DCF Lag (hr)
24 – 1400	0.79	22	$< 10^{-4}$	$+2.28^{+1.25}_{-0.60}$	$+2.84^{+1.75}_{-1.73}$	2.4	$-1.80^{+4.60}_{-0.68}$
1400 – 2800	0.93	51	$< 10^{-4}$	$-0.48^{+0.84}_{-0.96}$	$+0.20^{+2.13}_{-2.07}$	0.0	$+0.48^{+1.99}_{-2.57}$
2800 – 5000	0.84	48	$< 10^{-4}$	$-0.96^{+1.20}_{-1.92}$	$-0.31^{+10.87}_{-9.91}$		$-2.76^{+5.99}_{-4.93}$

This provides quantitative confirmation of what is probably obvious from examination of Fig. 2.10, namely, that the UV-X-ray correlation is highly significant ($p_0 < 10^{-4}$).

However, this prescription cannot be used for non-zero lags, and systematic effects do not allow the DCF to measure meaningful errors across the entire function directly from the data, as was originally suggested by Edelson & Krolik (1988). Their error bars were measured by assuming that the *UDCF* points are independent, while in fact they are dominated by systematic effects introduced by the particular sampling pattern. In the case of evenly sampled observations, such as the UV monitoring of NGC 5548 (Clavel et al. 1991), the errors are overestimated, while for unevenly sampled light curves (e.g. Edelson et al. 1990), the errors are clearly underestimated. Because the errors on the points are not reliable, and in any event, the goal of correlation analysis is generally to measure the errors on the lag, not on the value of the correlation function at a given lag (which the DCF does not directly provide), another method must be used to estimate the errors.

Therefore, Monte Carlo simulations are used to estimate the error on the lag and determine if it is significantly different from zero, as follows: first, identical synthetic 24 Å and 1400 Å light curves are produced with the same statistical characteristics as the observed ones. A fluctuation power density spectrum with a power-law slope of $P(f) \propto f^{-2}$ (where $P(f)$ is the fluctuation power at temporal frequency f) is assumed. Although the interruptions make this data set unsuitable for measuring the slope of the power density spectrum, previous X-ray measurements by Tagliaferri et al. (1991) indicate a slope of about –2. Next, the variability amplitudes are normalized to those observed (7.3% for the 24 Å data and 5.4% for the 1400 Å data). Then, the synthetic data are sampled at the same times as the observed data, and Gaussian noise added at the measured noise level (1% for the 24 Å data and 1.5% for the 1400 Å data). The cross-correlation is then derived, and the best estimate of the lag is measured, in the same fashion as the observed data. This process is repeated to produce 10,000 independent tests, and the confidence range is taken to be that containing 90% of the test lags.

These simulations yielded a 90% confidence interval of –6.66 hr to +3.74 hr. Only about half the test runs yielded lags outside of the range ±1.04, indicating that the lag measured by the DCF was not significantly different from zero.

2.1.2.1.b Modified Mean Deviation Technique

The second method used in this study is a modification of the mean variance method introduced by Hufnagel & Bregman (1992). It assumes that the two light curves are actually realizations of the same process, but shifted in time and flux level. Thus, it cannot be used to estimate the significance of the correlation between wavelengths.

This Modified Mean Deviation (MMD) method works as follows: First, the two unevenly sampled light curves, $x(t_i)$ and $y(t_j)$, are normalized to zero mean and unit dispersion, to yield x_i' and y_j', as above. Then, for each pair, the lag Δt_{ij} and flux difference ΔF_{ij} are computed:

$$\Delta t_{ij} = t_i - t_j, \tag{2.4a}$$

and

$$\Delta F_{ij} = x_i' - y_j'. \tag{2.4b}$$

The ΔF_{ij}'s are then grouped into ranges of Δt_{ij} such that for all of the N pairs with

$$T_{lag} - \tau/2 < \Delta t_{ij} \leq T_{lag} + \tau/2, \tag{2.5a}$$

the following are computed:

$$\langle \Delta F \rangle = \frac{1}{N} \sum \Delta F_{ij}, \tag{2.5b}$$

and

$$MMD(T_{lag}) = \sigma_{\Delta F} = \sqrt{\frac{1}{N} \sum (\Delta F_{ij} - \langle \Delta F \rangle)^2}\ . \tag{2.5c}$$

Finally, as with the DCF, the best estimate of the lag is made with a parabolic fit. The results are shown in Fig. 2.12.

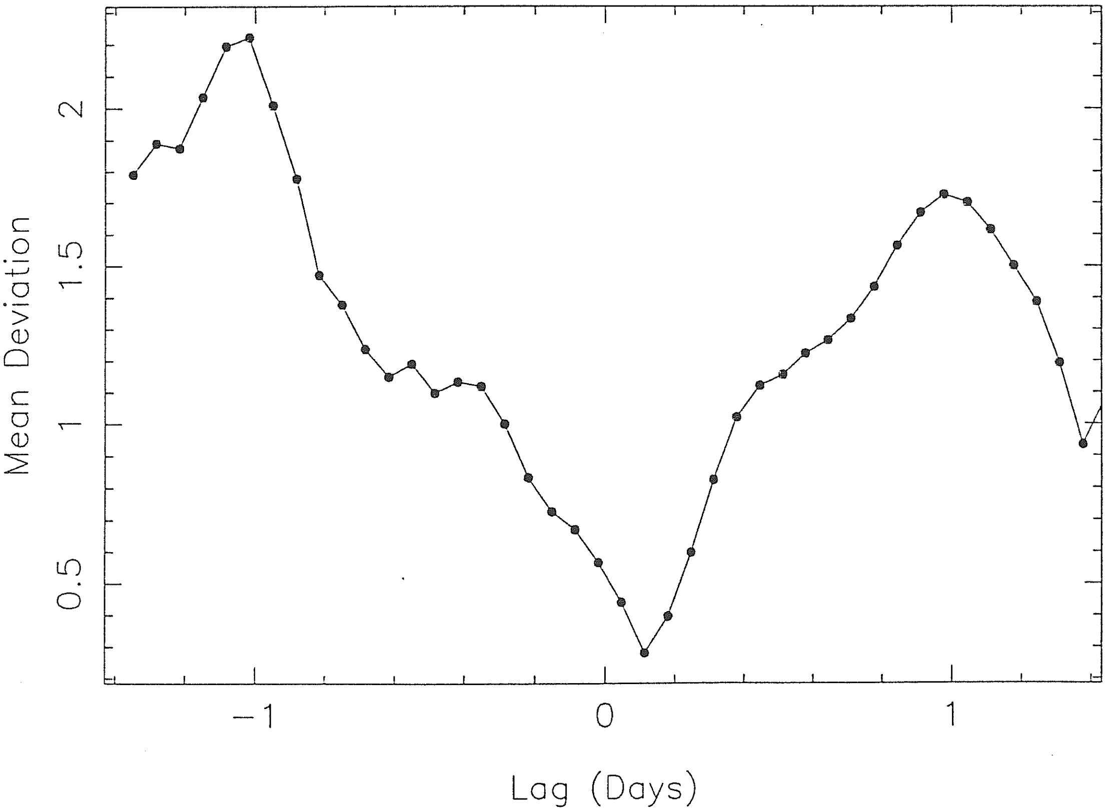

FIG. 2.12 — MMD analysis between 24 Å and 1400 Å.

There is no "double-peak" seen with the MMD method. Errors on the lag are estimated in the same fashion as with the DCF. The best estimate of the lag is +2.84 hr, and the 90% confidence interval is −6.22 hr to +6.21 hr. Thus, the simulations show that the lag measured by the MMD method is not significantly different than zero.

2.1.2.1.c χ^2 *Minimization Technique*

The third method is an adaptation of a technique developed for the analysis of time delays in the light curves of the gravitational lens 0957+561. Like the MMD technique, this method assumes that the light curves have the same underlying correlation properties, so it cannot be used to test the strength or significance of the correlation. In principle, it allows analytic estimation of the errors on the lag. Details are given in Press et al. (1992).

As before, the data are normalized to zero mean and unit variance. Then, the one point estimate of the structure function, v_{ij}, is calculated for all pairs of points,

$$\Delta t_{ij} = |t_i - t_j|, \tag{2.6a}$$

and

$$v_{ij} = \frac{1}{2}(x_i' - x_j')^2 - \frac{1}{2}\epsilon_i^2 - \frac{1}{2}\epsilon_j^2, \tag{2.6b}$$

where ϵ_i is the fractional error on the measurement, x_i'. The structure function, of the form, $V(\tau) = b\,|\tau|^\gamma$, is fitted after binning the v_{ij}s into equal size bins. Since the analysis assumes that the structure functions are identical for all light curves, the parameters used in the time delay analysis are the average of the fitted parameters. These structure function fit parameters for the different light curves are in fact very similar, and in any event, the time delay measurement is insensitive to the values assumed.

The two light curves are combined to form a single light curve, assuming a flux ratio and time delay. The statistical properties of this joint light curve are compared with those of the individual light curves by calculating the generalized χ^2 statistic, defined as

$$\chi^2 = \sum x_i' A(\Delta t_{ij}) x_j', \tag{2.7}$$

where $A(\Delta t_{ij})$ is the inverse of the total covariance matrix,

$$A(\Delta t_{ij}) = \left[\sigma^2 - V(\Delta t_{ij}) - \frac{1}{2}(1 - \delta_{ij})(\epsilon_i^2 + \epsilon_j^2)\right]^{-1}, \tag{2.8}$$

and where σ^2 is the unknown population variance of $x(t)$. By taking the limit, $\sigma^2 \to \infty$, the dependence on the population variance is removed. When the generalized χ^2 is minimized, the assumed time delay and flux ratio yield maximum likelihood estimates of the true time delay and flux ratio. In other words, when the assumed time delay and flux ratio approximate the true delay and ratio, the joint light curve should exhibit the same correlation properties as the individual light curves, provided that the original assumption, that the two light curves are drawn from the same parent light curve, is correct.

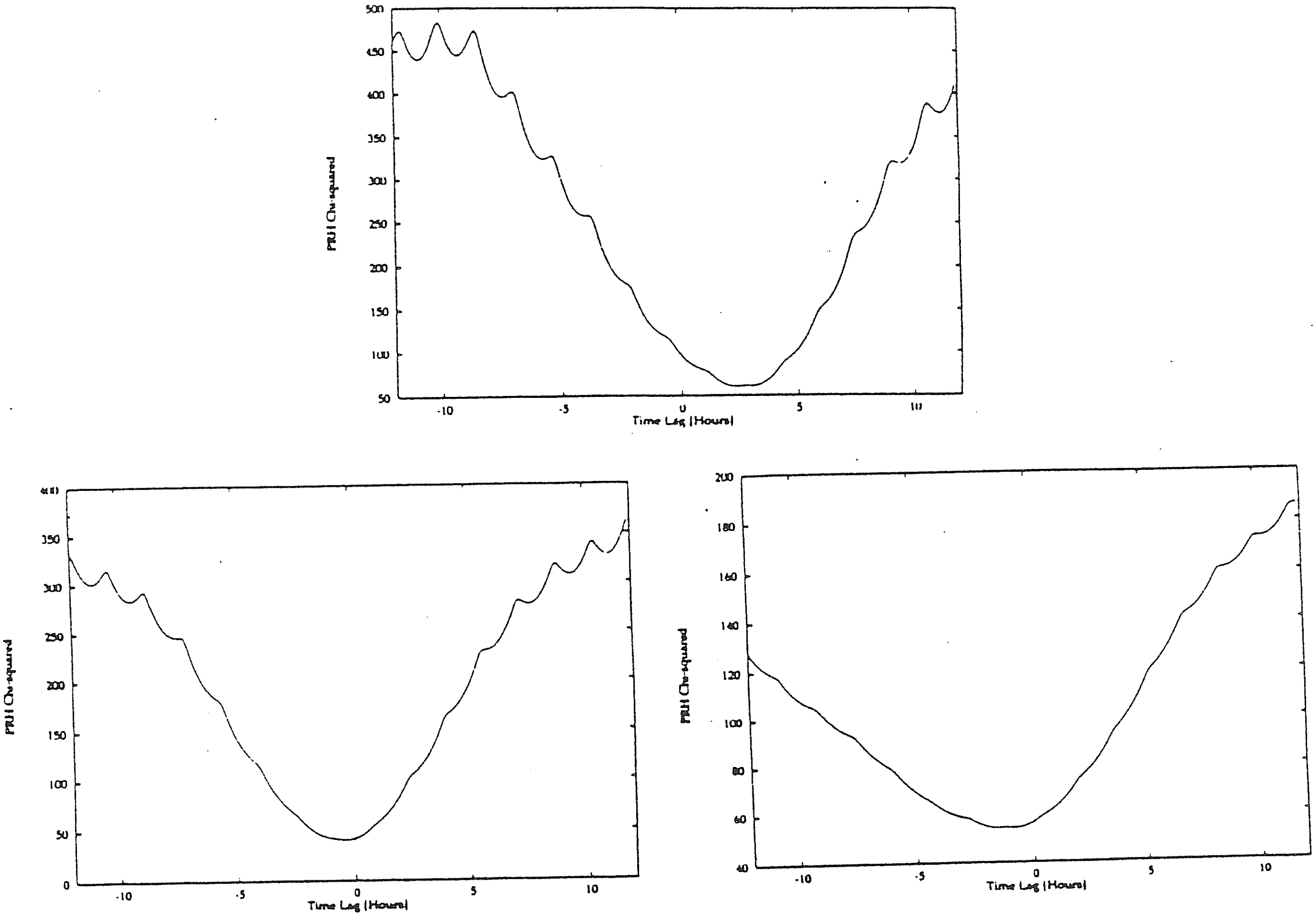

FIG. 2.13 — χ^2 analysis between 24 Å and 1400 Å (top panel), 1400 Å and 2800 Å (bottom left panel), 2800 Å and 5000 Å (bottom right panel).

Since this statistic is not a true χ^2 statistic (Press et al. 1992), the confidence intervals are determined by Monte Carlo simulation, as before. The resulting plot of χ^2 as a function of delay is presented in Fig. 2.13. The best estimate of the lag is +2.28 hr, and the 90% confidence interval is +1.68 hr to +3.53 hr, in the sense that the X-rays lead the UV. The simulations show that the lag measured with the χ^2 method is significantly different from zero at the $\sim 5\sigma$ level. Thus, for this problem, the χ^2 method is more powerful than the DCF or MMD methods. No significant lag can be measured between the other bands.

2.1.2.1.d Maximum Entropy Technique

The final method used to estimate the lag was the maximum entropy method (MEM). MEM tries to find both a "smooth" X-ray light curve that fits the 24 Å data points and "smooth" transfer functions that, when convolved with the X-ray light curve, gives a light curve that fits the 1400 Å points. In this approach, the 1400 Å light curve is modeled as a linear convolution of the X-ray light curve with a transfer function. The transfer function then gives the time delay distribution of the UV variations with respect to the X-ray variations. Details of the method, used previously to measure transfer functions between line and continuum variations of Seyfert 1 galaxies, may be found in Horne et al. (1991) and Krolik et al. (1991).

The MEM reconstructions were performed of transfer functions obtained for the 1400 Å, 2800 Å and 5000 Å light curves measured with respect to the 24 Å light curve (unlike the previous methods, MEM permits simultaneous analysis of more than two light curves). A two-parameter family of satisfactory solutions is examined to fit the data with reduced χ^2 values of 1.0 to 0.5. In all of these solutions, the peak of the 1400 Å transfer function occurs at a delay of ~2.5 hr. The transfer function has a full width at half maximum of 2.5–7.5 hr. This range indicates that the width of the transfer function is not tightly constrained by these data. No attempt is made to quantitatively estimate the errors on the MEM results with Monte Carlo simulations.

2.1.2.1.e Summary, Comparisons and Caveats

The results of the 24 Å–1400 Å correlation analyses are summarized in the first line of Table 2.2. Note that the errors refer to 90% confidence intervals. The DCF (the only method tested that is sensitive to the strength of the correlation) confirms that all of the light curves are strongly correlated. The χ^2 method found that the lag of ~2–3 hr is significant at the $\sim 5\sigma$ level. The other three methods yield similar values for the lag, but the significance is lower ($\sim 1.5\sigma$). Thus, for this experiment, the χ^2 method proved to be the most powerful. However, no one method is best in all cases, and another approach may prove more useful under different circumstances.

An unfortunate defect of this data set is the presence of gaps in the otherwise even sampling. In particular, gaps occur in the 24 Å coverage around November 12.8 and 14.8, just prior to two of the three local maxima in the 1400 Å light curve (although the minima in both light curves are well defined). The MEM fit introduces unobserved X-ray flares in the 24 Å data gaps in order to produce the observed maxima in the 1400 Å light curve while retaining rather broad transfer functions. The other methods must also effectively do this as well.

The data near the end of the experiment appear to diverge, with the 1400 Å fluxes declining from a maximum while the 24 Å flux is rising. MEM makes a rather strained fit to this difficult section by means of a flare in the data gap around November 14.8 and a dip between the two 24 Å measurements around November 15.05. This suggests that the true relationship between the X-ray and UV variations could be more complicated than a simple linear convolution, and that while the light curves are strongly correlated on short timescales, they may diverge when timescales longer than the ~3 days sampled in the intensive period are probed.

Such behavior may indicate that there is a hierarchy of size and time scales, in which case the measured lag could depend on the length of the monitoring campaign. For instance, consider what would happen if the same process operates in two regions of different size, with the larger region having larger amplitude variations, longer lags and longer variability timescales. Then, if one monitored for only a short time, one would only be sensitive to the small, rapid variations from the smaller region, and the shorter lag would be measured. However, if one monitored for long times, the larger amplitude variations would dominate, and the larger lag would be found. In both cases the direction of the lag is the same if both regions emit by the same process. Thus, this experiment gives greater confidence in the sign of the lag (which indicates whether the X-rays or UV lead) than its magnitude.

This is the first measurement of the temporal correlation between X-ray and lower-energy variations from any BL Lac object, and the first indication that X-ray variations precede those at lower-energies. This has very important implications for emission models, as discussed in Section 2.1.3.

2.1.2.1.f Correlations Measured with the Intensively Sampled IUE Data

The intensively sampled 1400 Å–2800 Å and 2800 Å–5000 Å correlations were analysed in a fashion identical to the 24 Å–1400 Å correlations. These results are presented in lines 2 and 3 of Table 2.1 and in Figs. 2.4 (DCF, § 2.1.1.2.a) and 2.14 (MMD). For the correlations involving only IUE data (1400 Å–2800 Å and 2800 Å–5000 Å), slightly longer timescales are covered, and the Monte Carlo simulations assumed errors of 1.5% at 1400 Å and 2800 Å and 3% at 5000 Å, and *NVA* of 6.2%, 5.7% and 6.0% at 1400 Å, 2800 Å and 5000 Å, respectively.

Again, the DCF confirms that all of the light curves are strongly correlated (see also Section 2.1.1). For both the 1400 Å–2800 Å and 2800 Å–5000 Å correlations, all the methods yield results consistent with no lag, within limits of $\lesssim$ 1–2 hr in the most constraining analysis (the χ^2 technique).

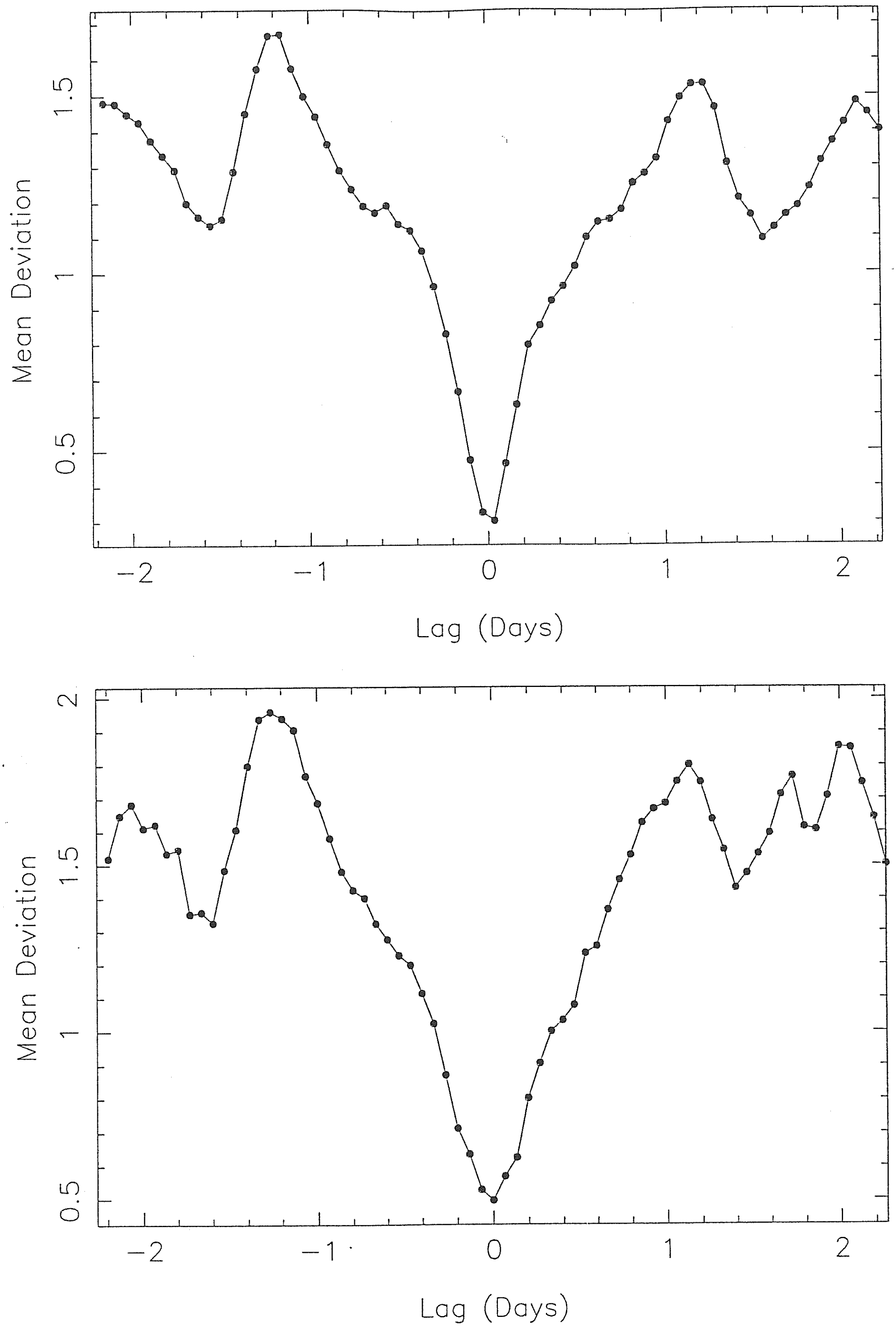

FIG. 2.14 — MMD analysis of UV-optical correlations in the intensively sampled data. The 1400–2800 Å correlation is on the top and the 2800–5000 Å correlation is on the bottom.

2.1.2.1.g Lower-Frequency Correlations

Extending these results to lower frequencies and longer timescales is more difficult. This is not because there are not enough data. With $N \approx 65$ in a number of optical bands, there are actually more data than the $N = 35$ to 50 points used in the UV-X-ray analyses. Rather, the problem is that the lower frequency data lack the homogeneity and relatively even sampling of the intensive satellite monitoring. The ground-based data in any given band consist of observations made with many different telescopes, detectors, calibration sources and reduction techniques (see Courvoisier et al. 1994 for a detailed discussion of these data). Although each of the data sets contributing to this large database may be internally consistent, systematic differences between different observer's data could greatly affect the result. Since there is no obvious, reliable way to weight these data or estimate errors by Monte Carlo simulation, only qualitative analyses are given.

Visual inspection of the month-long light curves (Fig. 2.10) suggests a correlation throughout the UV-optical-IR regime. All of the UV-optical data appear strongly correlated, with no significant evidence for a lag greater than the typical sampling limit of ~1 day. The IR data have even poorer sampling, with only 8–13 points, but again appear to closely follow the trend in the high-frequency data.

The sparsely sampled radio data do not show this correlation at zero lag, however. The radio data can crudely be described as staying roughly constant for the first half of the campaign and then rising somewhat in the second half. The rise appears to occur later and become progressively weaker as one goes from 1.3 cm to longer wavelengths, with very weak variability and no obvious trend at the longest wavelength band sampled, 20 cm. The long-term optical-UV light curve rises in the first 10 days of the campaign and remains at a high level for the last 20 days. It does appear that the radio variations could be related to but lagging the optical-UV by ~5–10 days, with shorter delays and stronger correlations at the shorter radio wavelengths. Unfortunately, the lack of mm/sub-mm data make it impossible to track the lag and tell with certainty if this behavior is connected to the variations seen at higher energies.

2.1.2.1.h Periodicity Analysis

Detection of a periodic component to the variations would be of great importance, arguing against beaming and for a more isotropic emission source, such as an orbiting source or a hot spot on a disk. The autocorrelation functions derived from the IUE observations by means of the DCF method appear to have shoulders at ~0.7–0.8 days (Section 2.1.1, Fig. 2.5). However, as mentioned previously, errors generated by the DCF are not meaningful, so the significance of any potential periodicity cannot be accessed by examination of the autocorrelation function alone. Therefore, a procedure designed specifically to detect periodicity in the presence of noise is here employed.

There are two general types of statistical methods which have been used to search for periodicities. The first and most widespread uses Fourier techniques to measure the power spectrum (e.g. Bracewell 1986), and as such is not directly applicable to these unevenly sampled data (for example, directly transforming the DCF autocorrelation function would yield a highly corrupted power spectrum). The second method, folding the data on test periods, can be applied to unevenly sampled data, and is also more sensitive to non-sinusoidal pulse shapes that might be seen in AGN.

The epoch-folding Q^2-statistic of Daves et al. (1989) is used. This method, which has already been used to test for periodicities in AGN (e.g. Done et al. 1992), is well suited for detecting periodic modulation in the presence of both erratic variability and measurement noise. It tests the hypothesis that there is no periodic signal with a given period: first, the N data points are folded on a trial period and binned by phase. For the i^{th} of M phase bins, the mean x_i and sample variance ${\sigma_i}^2$ are computed, as is the overall mean, $\langle x \rangle$. Then, the Q^2 statistic is computed,

$$Q^2 = \sum_{i=1}^{M} \frac{(x_i - \langle x \rangle)^2}{{\sigma_i}^2}. \tag{2.9}$$

Q^2 is distributed similarly to the χ^2 statistic. The false-alarm probability (the confidence with which one can reject the null hypothesis) can be determined from

$$L = \frac{(N-M)Q^2}{(M-1)(N-1)-Q^2}, \tag{2.10}$$

where L has an F distribution with $(M-1)$ and $(N-1)$ degrees of freedom.

The intensively sampled 24 Å, 1400 Å, 2800 Å and 5000 Å light curves are sampled fairly regularly (but with interruptions totaling about 1/3 of the time) for 2.3 to 4.5 days. This test has been done for these four data sets and the results are plotted in Fig. 2.15 (the sampling frequency and homogeneity of the ground-based data are insufficient for meaningful periodicity analysis).

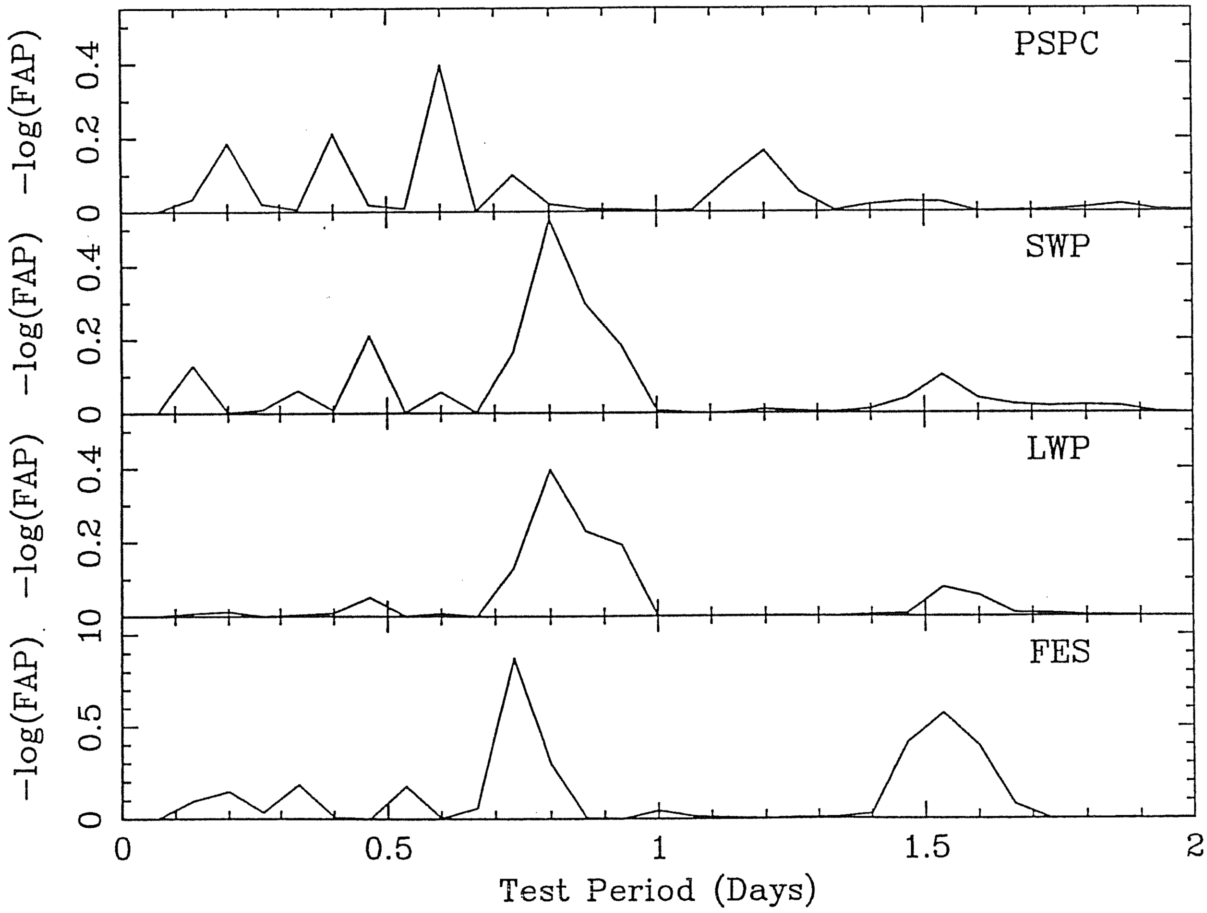

FIG. 2.15 — Results of the epoch-folding tests for the 24 Å, 1400 Å and 2800 Å data. The ordinate is the log of the inverse of the false-alarm probability (the confidence level).

For the three UV-X-ray light curves, the confidence level at which one can reject the hypothesis that the source is periodic is $p_0 = 30\%$ to 50%, while for the most significant case, the 5000 Å data, the confidence level is $p_0 = 13\%$. These are not statistically significant.

An alternate, non-statistical approach is to time the maxima and minima in the light curves. Application of this technique to the 1400 Å light curve, for instance, shows four clear maxima (at November 11.97–12.10, 12.90–12.97, 13.57–13.70 and 14.83–14.96) and three clear minima (at November 12.23–12.57, 13.30–13.37, and 14.23–14.56; the large gap at November 11.37–11.83 makes it impossible to determine if and when any earlier changes of direction occurred). Because the data have such high S/N, the times of these minima and maxima are fairly well defined. There is no single periodic function consistent with all these times. For instance, a 0.8 day periodicity is consistent with the first three maxima, but would predict a peak at ~November 14.50, when the source is actually in a minimum.

There are two possible reasons why the IUE autocorrelation functions showed features which are not confirmed by more rigorous analyses. First, the IUE data were subjected to ~0.2–0.3 day interruptions by Earth occultation at the same time each day. The average span of uninterrupted observations was 0.7–0.8 day, resulting in a window function with a spike at this timescale. Since AGN show strong variability over many timescales, the poor window function can irretrievably alias variability power to this particular time scale.

Second, signals with red power spectra frequently show spurious periodicities on timescales that are an appreciable fraction (~1/3) of the length of the data stream because there are too few large-amplitude components at low frequencies to achieve the Gaussian behavior of the central limit theorem. During the intensive IUE monitoring period of 10.7–15.2 November, the source was actually observed only about 2/3 of the time, with other sources being observed during the remaining time, so the effective period was 4.5 days × 2/3 = 3 days. Thus, timescales of order ~1 day are suspect. There is no compelling evidence for periodic behavior in these data. A more firm conclusion could be achieved only if there were 10 or 20 periods (so that the central limit theorem would indeed apply).

These results do not support the hypothesis that the variations in PKS 2155–304 have a "quasi-periodic oscillator" (or QPO) character similar to that seen in X-ray binaries (e.g. van der Klis 1989). In QPOs, the fundamental temporal frequency of the periodicity is not fixed at a single, constant value. Instead, it wanders slowly around a mean value. However, for these sources, the apparent temporal frequency of the periodicity does remain approximately stationary over a small number (< 10) of cycles. This would produce an apparently sharp and detectable periodicity, which was not seen. Of course, the possibility of QPO cannot be completely eliminated, since one could always posit changes in the peak temporal frequency which would be too rapid to detect, or a fundamental temporal frequency that is too low to detect in this finite data train. However, these data give no positive evidence of such QPO behavior.

Furthermore, this period is not present in extensive, well-sampled optical data taken in 1988 (Carini & Miller 1992), which means, since we now know the optical and UV are closely related, that any periodicity, if real, is transitory. Only a longer run of intensive monitoring can clearly confirm or refute the stability of this periodicity.

2.1.3 MODELS FOR VARIABILITY

2.1.3.1 Synchrotron Emission within an Inhomogeneous Jet

The time-averaged radio through X-ray spectral energy distribution of PKS 2155–304 is shown in Fig. 2.16. The IR through X-ray data were taken on November 14.75–15.30, and the radio data were taken at November 16.1.

The spectral energy distribution is very smooth, at least over the wavebands observed in this experiment, rising monotonically in νF_ν from 20 cm (where the mean spectral index is $\langle\alpha\rangle = +0.01; S_\nu \propto \nu^\alpha$) to 1400 Å (where

$\langle\alpha\rangle = -0.79$). The X-rays (with $\langle\alpha\rangle = -1.65$) show no sign of the flattening that would be expected from Compton scattering. The γ-ray upper limit ($1.3 \cdot 10^{-7}$ ph s^{-1} cm^{-2} at energy > 100 MeV) determined non-simultaneously (October 1992) by EGRET is also reported.

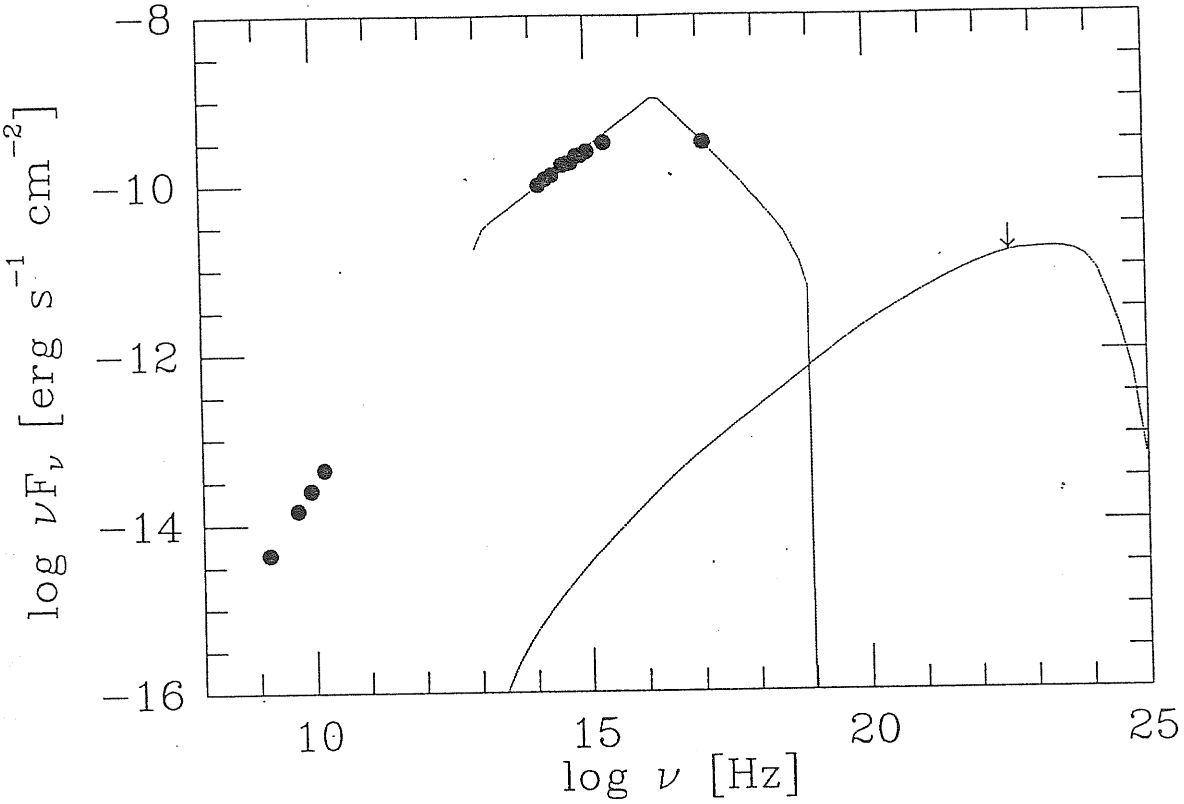

FIG. 2.16 — Spectral energy distribution of PKS 2155–304. The synchrotron model of GMT is overimposed on the data (dotted line).

The 30% change in intensity occurring over a day (for example, around 13–14 November 1991) at optical, UV and X–ray frequencies corresponds to a total variation $\Delta L/\Delta t \sim 4 \times 10^{41}$ ergs s^{-2} (for $z = 0.116$, assuming $H_0 = 50$ km s^{-1} Mpc^{-1} and isotropic emission), which is a factor of 2 above the fiducial limit for Eddington-limited accretion with efficiency $\eta = 0.1$ (Fabian 1979; see also § I.d). Thus the flaring would in fact have exceeded the limit, suggesting relativistic beaming is present.

This strongly favors the interpretation of the emission in PKS 2155–304 through a radiating jet. In the jet models, the low-frequency spectrum (up to the optical-UV band) is attributed to synchrotron radiation from relativistic electrons, while, depending on the specific assumptions about the physical quantities in the jet, either synchrotron emission or Compton scattering could produce the X-rays.

The first issue that can be clearly addressed with these data is whether the soft-X-ray emission seen with Rosat can be produced by the Compton upscattering of lower-energy photons. If a single homogeneous source of relativistic electrons provides the lower-energy seed photons (via the synchrotron process) which are then upscattered (i.e. the SSC process), then the X-ray variations should occur either after or at the same time as lower-energy variations. Thus, the simplest SSC model cannot account for the soft-X-ray emission (in the 0.2–2 keV band) since it *leads* the lower energy variations.

Consider further if the seed photons derived from some independent source. If the relativistic electrons responsible for upscattering these photons to soft-X-ray energies were the same as those which produce the radio through UV synchrotron spectrum, the Compton radiation should have roughly the same spectral slope as the longer wavelengths ($\alpha = +0.01$ to -0.79). However, it is much steeper in the X-rays ($\alpha = -1.65$) than in any lower frequency band (see Fig. 2.16 and Brinkmann et al. 1994), arguing against this hypothesis.

However, these data do not address the importance of Compton scattering at energies higher than those probed by Rosat (>1 keV). In particular, Compton scattering is often invoked to explain the high-energy γ-rays from blazars (see Section 2.3), a conclusion that is not contradicted by these results, and suggested by the EGRET upper limit. Finally, it should also be kept in mind that PKS 2155–304 is an X-ray-selected BL Lac, the class for which synchrotron emission is thought to be most dominant.

The spectral continuity (Fig. 2.16) and synchronous variations (within a few hours) at IR through UV frequencies are easily interpreted as a consequence of the synchrotron process, acting at those energies. The strong

X-ray-UV correlation, when combined with the fact that the X-rays lead the UV, argues that the X-rays would also be produced by direct synchrotron emission. This would require that the electron energy distribution extend to higher energies than would be necessary to produce only the radio through UV spectral energy distribution. This means that the maximum electron energy would have to increase by an order of magnitude, for a fixed magnetic field strength.

Another general constraint derives from the absence of strong X-ray spectral variability (e.g. Brinkmann et al. 1994). Reasonable estimates of the lifetimes for the X-ray emitting electrons are very short (e.g. ~0.01 sec). Since the UV and X-ray light curves are so similar, the temporal behavior must be dominated by the energy input mechanism in essentially one region, with frequency-dependent geometry playing a secondary role. That is, the electrons would need to be continually re-accelerated in situ, because any electron distribution derived from a single injection would quickly steepen, producing significant spectral changes.

Finally, the 2–3 hr lead of the X-rays with respect to the lower frequencies is much shorter than the fastest variations seen in any band. If the variability timescales are related to size of the emitting regions, the short lag could be caused by Doppler foreshortening and phase effects in the direction of motion of the plasma or perturbation and/or to a flattened geometry (e.g. a shock front in a jet oriented towards us, see § 2.1.3.2.).

In the context of the inhomogeneous jet model (Marscher 1980; GMT, see § I.d), an increase in the flow of energy down the jet would lead to a flare seen first at higher and later at lower frequencies. The observation that the X-rays lead the longer wavelengths suggests that the innermost synchrotron-producing region is radiating at X-ray or higher energies, and qualitatively conforms with expectations.

However, this model has difficulties explaining both the magnitude of the UV-X-ray lag and the lack of spectral variability. To estimate the range of physical conditions required by this model, the broad-band spectral energy distribution of PKS 2155–304 (Fig. 2.16), was fitted with the relativistic jet model described in GMT (see also Section 1.4). A bulk relativistic velocity of $\Gamma \sim 5$ was assumed. In this model, the jet starts with a dimension of 3×10^{13} cm and extends with parabolic shape to 3×10^{16}cm, which is the dominant region for emission above 10^{13} Hz. At lower frequencies, the emission is self-absorbed and the jet structure is assumed to change to a conical shape (not included in the fit shown). The magnetic field at the core of the jet is $B \approx 3000$ G, corresponding to a maximum electron energy of $\gamma \approx 5000$.

This implies that the high energy electrons emitting in the X-rays will have very short radiative lifetimes ($t_{1/2} \approx 0.01$ sec). As mentioned earlier, the electrons responsible for the X-ray variations cannot also produce the UV variations unless they are re-accelerated. Likewise, if a shock traveling down the jet is responsible for the variations, it would have to travel $\sim 10^{16}$ cm to reach the UV emitting region. This corresponds to a light travel time of $\sim$4 days. Extremely large relativistic corrections would be needed to make this compatible with the observed lag of 2–3 hr.

Furthermore, Celotti et al. (1991) computed simulated light curves that would be expected in such a model, approximating the propagation of a shock wave in the jet by a schematic perturbation of given size and amplitude moving at constant speed (but without making relativistic corrections to the timescales). They predicted strong spectral variability, with the X-ray variations being much stronger than those at lower energies. The observed lack of spectral variability in the X-rays and similarity between the different waveband light curves argue further against the specific model described above.

However, it should be kept in mind that this argument is valid only above the spectral break, while for this object, the break falls close to the Rosat band. Indeed, GINGA observations of PKS 2155–304 show that the spectrum continues smoothly to higher energies, and there is evidence for spectral variability at these higher energies (Sembay et al. 1992).

2.1.3.2 Emission from a Shock Front

As mentioned in 2.1.3.1, the short UV-X-ray lag argues for flattened geometry.

As shown by Marscher & Gear (1985), a shock front in a relativistic jet would produce both a flattened geometry as well as the particle acceleration and magnetic field amplification required to produce synchrotron flares. Such shock waves would presumably be caused by the non-stationary energy input responsible for the variations.

Since the distance traveled behind the shock front by a relativistic electron before suffering radiative losses would depend on energy, the thickness of the emission region would decrease with increasing frequency. This would naturally produce the X-ray-UV lag, and account for its being shorter than the variability timescales. Furthermore, simulated light curves published by Marscher et al. (1992) bear some qualitative resemblance to the observed light curves, with similar shapes at high frequencies and a small but significant time delay toward lower frequencies, although this is difficult to quantify. Finally, the radio data show a spectral flattening throughout the flux rise, which is qualitatively consistent with the Compton loss stage of the shock (Marscher & Gear 1985). However, shock fronts alone cannot solve all the problems with the relativistic jet model, since spectral variability would still inevitably be expected, and invoking a shock front introduces even more free parameters for these already poorly constrained data.

2.1.3.3 The Accretion Disk Model

Wandel & Urry (1991) proposed that the UV continuum of PKS 2155–304 could be thermal emission from an accretion disk. There is evidence that emission from an accretion flow contributes to the UV spectra of Seyfert 1s. This includes the success of disk models in reproducing their spectra (e.g. Malkan & Sargent 1982) and the observed anticorrelation between the degree of variability and luminosity (e.g. Edelson et al. 1990).

However, the observation that BL Lacs vary much more rapidly than even the lowest luminosity Seyfert 1s (Edelson et al. 1991), and as a group show a positive correlation between luminosity and variability amplitude (Edelson 1992), pose severe problems for the model of thermal UV emission from BL Lacs. Also, the linear polarization of PKS 2155–304 has been observed to increase toward shorter wavelengths in previous optical observations (Smith & Sitko 1991), this campaign (Smith et al. 1992; Courvoisier et al. 1994), and UV observations with *HST* (Allen et al. 1993). Emission from an accretion disk would be expected to show the opposite behavior.

Furthermore, one would expect the *shape* of the IR through UV spectral energy distribution to vary with time, since the UV emission would be dominated by the accretion disk, while another component (presumably with different variability behavior) would have to produce the optical-IR emission. Such a predicted hardening of the optical-UV spectral energy distribution as the flux level increases has been observed in Seyfert 1 galaxies and quasars (Cutri et al. 1985; Edelson et al. 1990). Contrarily, the shape of the spectral energy distribution of PKS 2155–304 remained very stable as the flux varied, with multi-wavelength flux ratios such as F_{1400}/F_{5000} remaining fixed to $\sim$10% while the overall flux level changed by a factor of two. This argues that the optical-UV spectral energy distribution is a single emission component, not the combination of components called for in the accretion disk model (see also Introduction, § I.b).

Finally, one would expect a measurable *lag* between the UV and optical bands, because the higher energy emission would be produced at smaller radii. In the model of Wandel & Urry (1991), the 1400 Å flux is produced at a radius of $\sim 2 \times 10^{15}$ cm (20 lt–hr), while the 5000 Å flux comes from a distance of $\sim 7 \times 10^{15}$ cm (70 lt–hr). However, the 1400 Å–5000 Å correlation analyses show no evidence for a lag, with an upper limit of a few hours. Thus, the accretion disk model would require the disturbance to propagate at $\gg 10c$. This discrepancy is too large to be accounted for by relatively minor effects such as possible non-axisymmetry and inhomogeneities in the disk. While monitoring of the Seyfert galaxy NGC 5548 has also failed to measure a 1400 Å–2800 Å lag, that experiment had much lower temporal resolution (4 days), and the propagation speed was limited to only $\gtrsim 0.1c$. The above arguments rule out the accretion disk model for PKS 2155–304.

2.1.3.4 Gravitational Micro-Lensing

Specific candidates for micro-lensing (see § I.d) have been suggested for some of the radio-selected BL Lac objects on the basis of their variability characteristics (Stickel et al. 1991).

If the size of the emitting region is independent of wavelength, the variability will be achromatic, as is approximately the case with the IUE data for PKS 2155–304. It is required that a foreground galaxy be closely aligned with PKS 2155–304, so that the line of sight intersects a large number of densely packed stars. Rapid ($t_{var} \ll 1$ year) variations could be caused by the relative motion of the background quasar and a foreground star cluster (Stickel et al. 1988; Schneider & Weiss 1987) but require the relative source/lens velocities to be extremely high, such as the superluminal motion that results from an aligned relativistic jet.

If the size of the emission volume is independent of wavelength, then the variability timescales would also be independent of wavelength. The result that the X-rays lead the UV by 2–3 hr can be understood if the X-rays arise in a smaller region. Then, one would expect that the UV light curve should be smoother than the X-ray light curve (because the lensing star will have a longer crossing time and possibly weaker amplification). This means that the autocorrelation function of the UV light curve would be wider than the X-ray autocorrelation function. Unfortunately, given the gaps and the short length of the data train, as well as the differences in the sampling patterns, the UV and X-ray light curves cannot be used to quantitatively test this prediction.

Calculations of the amplification pattern due to micro-lensing that include the macro-lensing shear can even produce a quasi-periodic signal (Wambsganss et al. 1990). Minor spectral changes could be explained by intrinsic effects in the jet, while the bulk of the variations could be due to micro-lensing.

2.1.3.5 Periodicity

The possible periodicity at $\sim 15 - 20$ hours is one of the most intriguing yet ultimately frustrating results of the present campaign. We lack enough data to be confident of its reality. During our observations, PKS 2155–304 was in a particularly bright state, as was the BL Lac object OJ 287 when a possible periodicity was detected in its optical light curve (Carrasco et al. 1985). It is clearly important to obtain longer, high-quality light curves of PKS 2155–304 in a bright state.

Meanwhile, keeping in mind the uncertainties, we explored what such a period, if real, might mean. One possible origin of a periodicity is orbital motion. The nearest stable orbit around a black hole is at a few ($n \gtrsim 3$) Schwarzschild radii, where $R_S = 2GM_{BH}/c^2$. Using Kepler's law and ignoring relativistic effects, the central black hole mass is related to the orbital period, T, by $M_{BH} = Tc^3/(4\sqrt{2}\pi n^{3/2}G)$. If the UV emission is not relativistically beamed, then $M_{BH} < 1.3 \times 10^8\ M_{\odot}$. Relativistic beaming would shorten the observed timescale relative to the true timescale, and so would allow higher masses in this simple limit.

In the context of a relativistic jet picture, the periodicity can be explained if the production of the jet is closely coupled to the orbital dynamics. For example, Camenzind & Krockenberger (1992) considered jets that are magnetically collimated winds emanating from the inner edge of an accretion disk. In this model, spiraling motion of plasma bubbles moving along magnetic field lines in the jet causes quasi-periodic fluctuations in observed intensity simply as a result of a smooth variation in the Doppler factor. The rotation period of the escaping plasma bubbles is initially the Keplerian period of the inner disk, increasing beyond the Alfven point, R_A, as $(R/R_A)^2$, where R is the perpendicular distance of the bubble from the jet axis. The bubbles become collimated and are observed at $R > R_A$. The observed period will be shorter by the factor $(1 - \beta \cos\theta)$, where θ is the inclination of the jet, due to a relativistic projection effect.

The estimate of the Lorentz factor and of the viewing angle for PKS 2155–304 based on the GMT model (§ 2.1.3.1) give $\Gamma \sim 5$ and $\theta \lesssim 1/\Gamma \sim 10^{\circ}$, so that the observed period of 0.7 days corresponds to a true period of 1.7×10^6 seconds. For $R/R_A \sim 10$ (Camenzind & Krockenberger 1992), the Keplerian period at $5R_S$ is then 1.7×10^4 seconds, and the black hole mass is $1.8 \times 10^7\ M_{\odot}$.

2.2 Simultaneous UV, Optical and Radio Monitoring of the BL Lac OJ 287

OJ 287 (z = 0.306) is one of the best studied flat-spectrum radio sources across the whole electromagnetic spectrum. Recent observations are reported at radio (Gabuzda & Sitko 1994), mm and sub-mm (Gear et al. 1994), near-IR-optical (Falomo et al. 1993d; Takalo et al. 1994) and X-ray (Rosat, Boller et al. 1992) wavelengths. An upper limit of $1.9 \cdot 10^{-7}$ ph s^{-1} cm^{-2} (E>100 MeV) for the γ-ray emission was determined by EGRET (Fichtel et al. 1994). The object was observed previously in the X-rays both by EXOSAT (Sambruna et al. 1994) and *Einstein* (Madejski & Schwartz 1988).

The presence of strong beaming of the energy outflow along the observing direction is suggested by the large core-to-extended radio emission ratio and by the detection of superluminal motions (R>3.5 and $\beta_{app} = 6.4$ respectively, Ghisellini et al. 1993, and references therein).

Large optical magnitude variations ($\Delta m_V \simeq 3$) were reported by Carini et al. (1992), who monitored the source between 1979 and 1989, finding a microvariability of ~0.03 mag/hr. A peak in the optical flux ($m_V = 12.92$) was found by Haarala et al. in January 1983 (IAUC 3764).

At the UV frequencies, OJ 287 is the most variable blazar after 3C 446 (Edelson 1992). Its activity peaked in April 1983 when a big flare was detected at optical and UV wavelengths (Maraschi et al. 1986a; Carini et al. 1992; Moles et al. 1984). The historical optical light curve suggests that outbursts may occur with a 11.6 period (Sillanpää et al. 1988; Kidger et al. 1992; Takalo 1994). Since the last remarkable flare was detected in 1983, observations during 1994 are of crucial importance. We present here simultaneous UV, optical and radio observations performed in several places during one of the faintest ever recorded states of the source.

2.2.1 Observations and Data Analysis

IUE observed OJ 287 on 1993 March 15–20 (4.3 days) within a broad-band microvariability intensive monitoring program. No simultaneous Rosat observations were organized since the objects is too faint for X-ray time-series analysis.

The target was in an extremely weak state (in some cases below the limit of detectability), then only the LWP camera was exposed. Each line-by-line image file was displayed and carefully examined. All of the 23 images exhibit underexposed spectra, however some signal is visible in a large fraction of them (see in Table 2.3 the journal of observations).

TABLE 2.3
JOURNAL OF IUE OBSERVATIONS OF OJ 287

IUE Image (1)	Exp. Time[a] (2)	Date (3)	F_λ^b (4)
LWP 25099	50	1993 Mar 16.03	0.127 ± 0.023^c
LWP 25106	45	16.66	0.099 ± 0.021
LWP 25108	44	16.79	0.191 ± 0.049
LWP 25112	50	17.04	0.164 ± 0.023
LWP 25114	50	17.21	0.106 ± 0.021
LWP 25119	50	17.65	0.132 ± 0.021
LWP 25126	50	18.07	0.121 ± 0.018
LWP 25140	50	19.06	0.162 ± 0.025
LWP 25149	50	19.65	0.129 ± 0.043
LWP 25151	50	19.79	0.129 ± 0.034
LWP 25156	50	20.06	0.132 ± 0.018

[a] In minutes

[b] Integrated and averaged GEX extracted spectral flux at 2650 Å (units are 10^{-14} erg s^{-1} $cm^{-2}$$\text{Å}^{-1}$)

[c] Errors represent 1σ statistical uncertainties

The IUE spectra have been extracted with the GEX procedure (modifying the threshold of signal extraction from r.m.s./2 to r.m.s./3 in order to recover very low signal, see Section 1.2, § 1.2.2.3) and with the Optimal Extraction. Calibration to flux units has been performed after Cassatella et al. (1988). The resulting GEX extracted spectra are given in Appendix B. For both sets of extracted spectra the signal was integrated and averaged in the wavelength region 2600–2700 Å, where the instrumental sensitivity is maximal and the scattered light due to the IUE baffle anomaly is minor (Rodriguez Pascual & Fernley 1993). The associated uncertainty was evaluated as described in § 1.2.2.3. Comparing the results of the two extractions (Fig. 2.17), no systematic difference is seen between them and an agreement within ~20% is found, which is comparable to the intrinsic flux uncertainties.

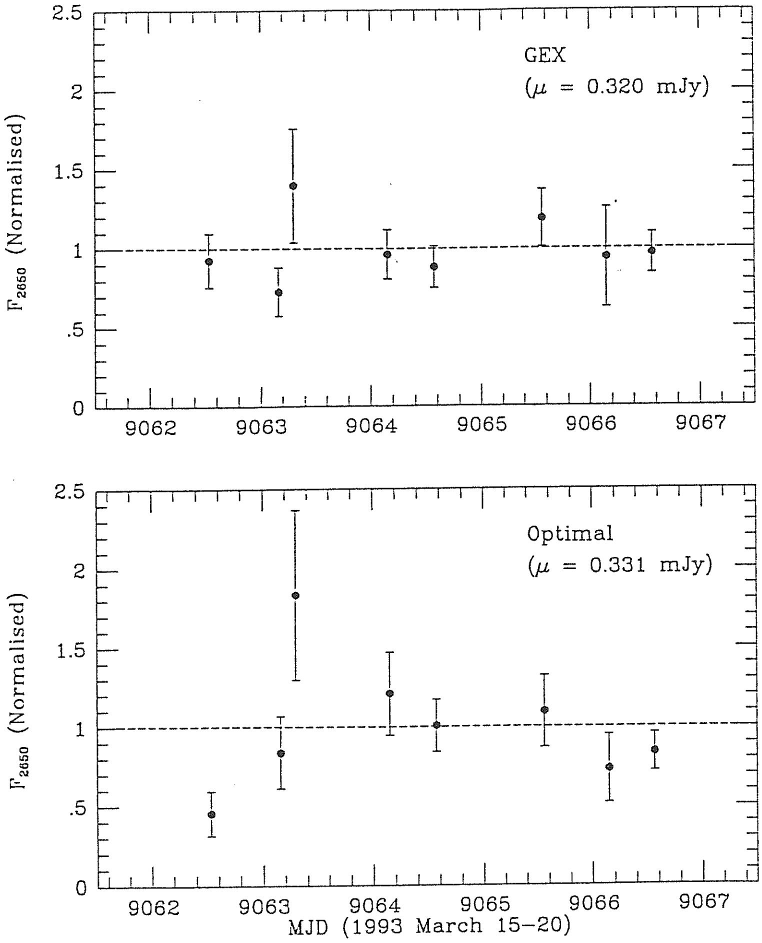

FIG. 2.17 — Light curves obtained from GEX and Optimal extractions of IUE spectra.

We generally noted a fair correspondence between image luminosity and level of GEX extracted signal, whereas the Optimal method in two cases fails in extracting flux from well exposed images. Thus we tend to confirm that GEX is slightly more reliable than Optimal for faint IUE spectra. Due to the low quality of the data and to the large flux errors no spectral fit was attempted to the data. In Fig. 2.18a the GEX light curve normalized to the average <F(2650 Å)> = (0.32 ± 0.06) mJy is reported.

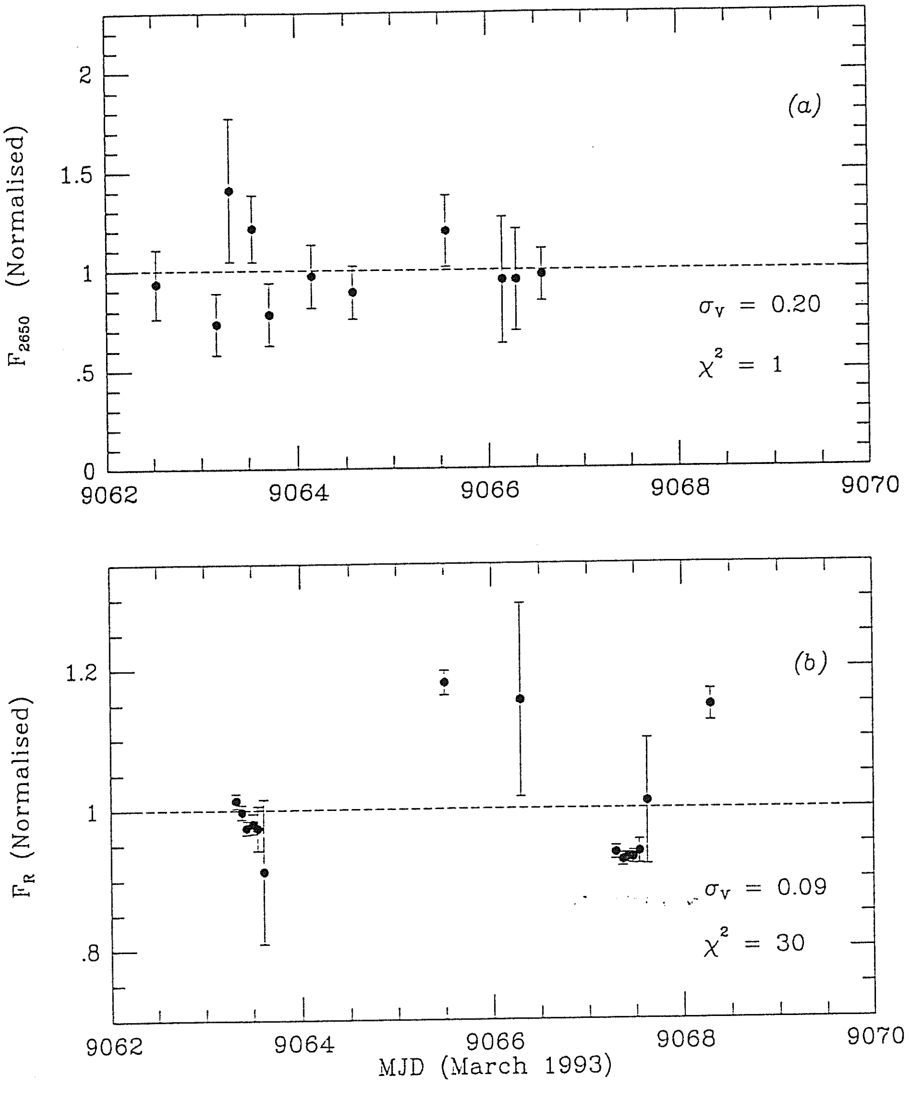

FIG. 2.18 — Light curves of OJ 287 normalised to the average: *(a)* UV (2650 Å); *(b)* optical R band. The variability indices and χ^2 values calculated as in Edelson (1992) are also reported.

Relative photometry with the R filter was obtained nearly simultaneously to IUE at the Landessternwarte Heidelberg (see Fig. 2.18b). Radio data at 37 Ghz were obtained in March 1993 at the Metsähovi Radio Research Station (Finland; see Fig. 2.19). Optical and radio observations have been already shortly described and discussed in Sillanpää et al. (1994).

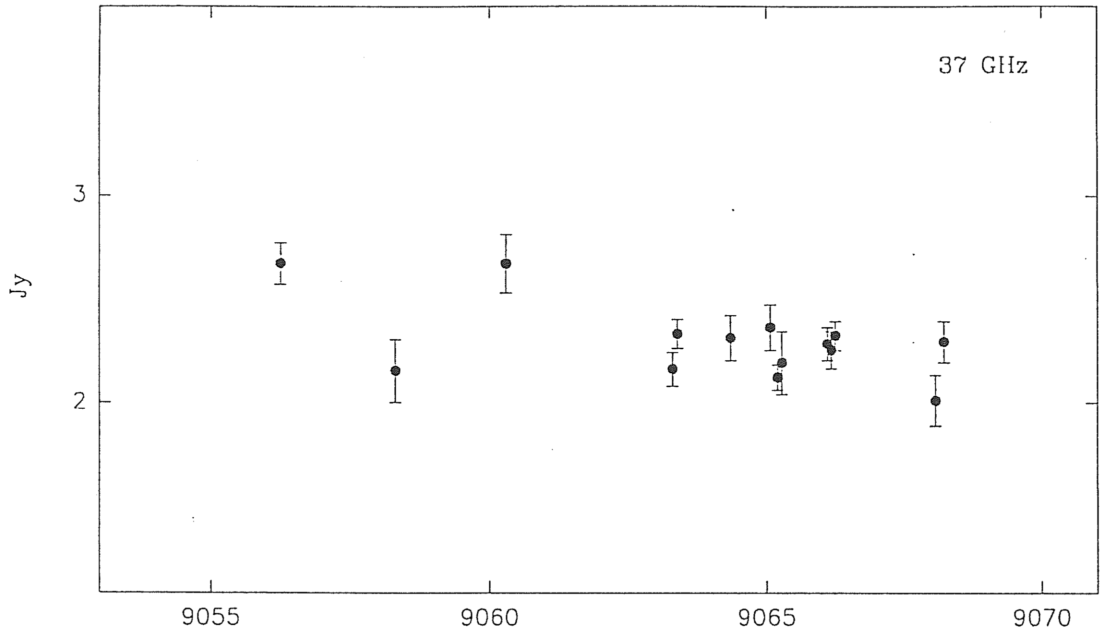

FIG. 2.19 — Radio light curve at 37 GHz (March 1993).

2.2.2 Discussion

In the UV band it is difficult to detect variability, since the errors are large ($\chi^2 = 1$). The indication of a flux variation of $\gtrsim 90\%$ in ~3 hours is present in the light curve at MJD = 9063.3 with a 2σ significance. Variability is much more significant in the optical range; but the variability index σ_V (which does not depend on errors, see Edelson 1992) is approximately equal or lower than that found in the UV. The radio flux at 37 GHz decreases by 30 % in ~ 2 weeks, but it appears to be constant (~2.2 Jy) during the UV monitoring time.

Although the time coverage of optical and UV data is not regular and not strictly simultaneous, the light curves present a similar trend in the temporal fractions of common observation and appear correlated without any apparent lag. The data are however too scarce and unevenly sampled to attempt a rigorous correlation analysis.

The object has been observed several times with the LWP and LWR cameras of IUE before our 1993 exposures. The historical light curve at 2650 Å, based on IUESIPS extracted archival spectra, is shown in Fig. 2.20 together with the average flux obtained in March 1993. A general decrease seems to characterize the UV emission of OJ 287 in the IUE life period, with occasional flares of even a factor of 20 larger than the flux detected during the present monitoring.

Based on the periodical 11.6 yr variability, an outburst is predicted for next July/August 1994. Recently, observations at mm, submm and optical wavelengths showed indeed an increasing trend with respect to March 1993 (IAUC 5909, 5913, 5944, 5971). Therefore, UV observations in the second half of 1994 would be of vital importance.

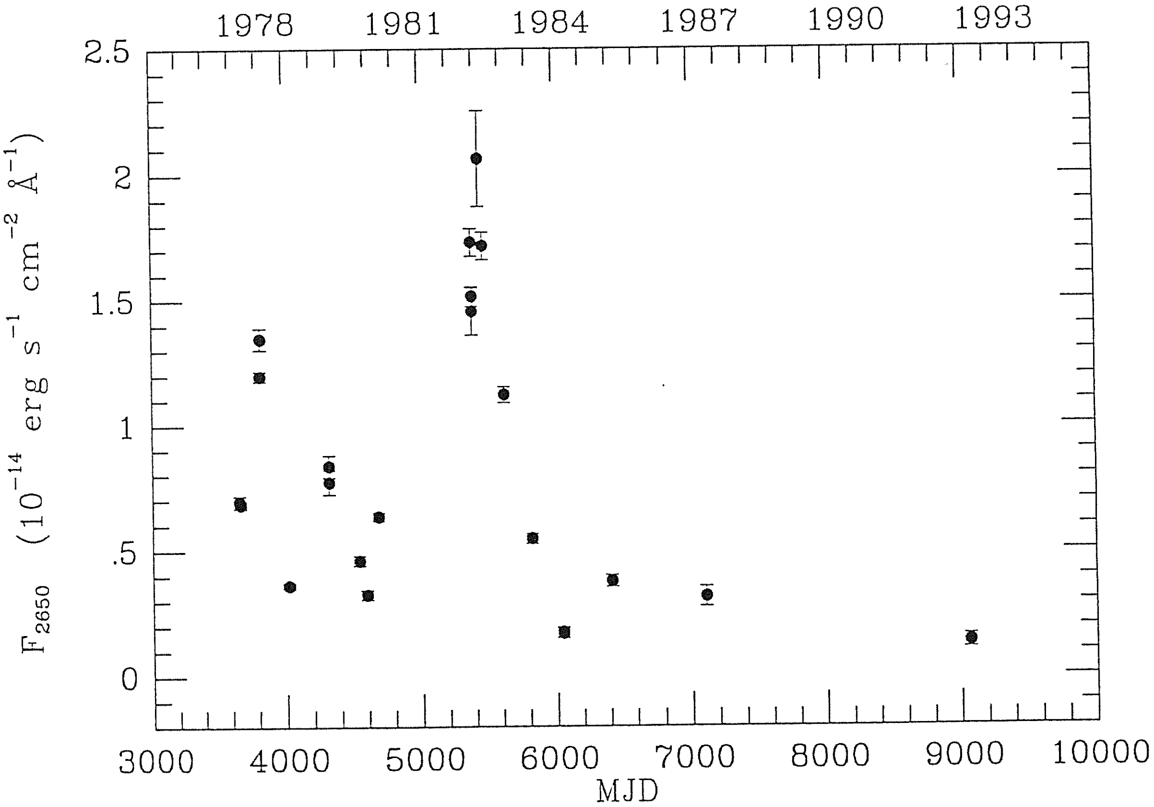

FIG. 2.20 — Historical IUE light curve of OJ 287.

2.3 The 1992/1993 Multi-Wavelength Campaign on 3C 279. The Radio-to-Gamma-Ray Energy Distribution in Low State

In 1992/1993, a large observational campaign was organized to obtain simultaneous data at all available wavelengths, from radio to γ-rays, on 3C 279, which at the time was the brightest extragalactic γ-ray source observed. The observing dates (December 1992–January 1993) were chosen to allow simultaneous observation by three spacecrafts — IUE, Rosat and CGRO — and from ground-based observatories.

Since γ-ray variability on timescale of days had been detected previously in 3C 279 (Kniffen et al. 1993), the program aimed at studying the correlation of variability in different frequency bands within a 20 day time interval. However, the source was found to be in a quiescent or "low" state in γ-ray emission: COMPTEL obtained an upper limit while the sensitivity of the EGRET instrument was barely sufficient to derive an average flux value over the entire period. Nevertheless, due to the excellent wavelength coverage resulting from the contributions of the numerous observers, we could derive a good multi-frequency spectrum for the quiescent state (Fig. 2.22). The full data set will be presented in separate papers devoted respectively to the coordinated VLBI (Wehrle et al. 1994), radio-to-optical (Grandi et al. 1994), and UV-to-X-ray observations (Urry et al. 1994a). In § 2.3.2 the 1993 energy distribution is compared with that observed in June 1991, the epoch of the highest measured γ-ray flux, and the results are discussed in Section § 2.3.3.

2.3.1 Observations

2.3.1.1 γ-rays

The EGRET instrument onboard CGRO observed 3C 279 with good sensitivity (7 degrees off-axis) from 1992 December 22 to 1993 January 12. The summed data for the entire 3-week observation were analysed, as were 3 separate 1-week intervals. 3C 279 was not detected at the $\geq 4\sigma$ level (the minimum used by the EGRET Team) in any of the 4 analyses. However, in each of them, a weak source (3.5σ for the summed data, $\sim 3\sigma$ for the separate weeks) appeared to be present at a position consistent with that of 3C 279. The integral flux for a source at the true position of 3C 279 is $(1.2 \pm 0.4) \times 10^{-7}$ ph s^{-1} cm^{-2} above 100 MeV, averaged over the entire 3-week observation. This value, reported in Table 2.4, was converted to the appropriate units assuming a photon index of $\Gamma = 2$. It should be kept in mind that the detection is marginal.

The COMPTEL instrument did not detect the source but provided 2σ upper limits of 4.7, 7.6, 3.4, and 1.2 $\times 10^{-5}$ ph s^{-1} cm^{-2} in the energy bands of 0.75–1, 1–3, 3–10, and 10–30 MeV respectively. Only the most stringent limit, adjacent to the EGRET sensitivity range, is reported in Table 2.4; conversion to flux assumed a photon spectral index of $\Gamma = 2$.

2.3.1.2 X-rays

Rosat PSPC observations were arranged to cover the whole period (1992 December 27–1993 January 15) with one observation per day plus more intensive coverage (24 observations) between January 2–5, 1993. Throughout the observations, the spectra are well fitted by a simple absorbed power-law model, with a column density in close agreement with the galactic $N_{\rm H}$ measured by Elvis et al. (1989). We use here the average spectrum obtained during the latter period. The derived photon spectral index and column density are respectively $\Gamma_X = 1.91 \pm 0.07$ and $N_H = 2.35 \pm 0.18 \times 10^{20}$ cm^{-2}. The 1 keV flux is reported in Table 2.4. No large amplitude (> 15 % r.m.s.) variability is seen in the Rosat data neither within the intensive nor within the extended monitoring periods.

2.3.1.3 Ultraviolet

Fourteen spectra were obtained with IUE between 25 December and 12 January 1993: ten exposures in the LWP camera and four exposures in the SWP camera (see Table 2.5). All of them had poor S/N. Both the GEX ("relaxed"

TABLE 2.4
3C 279 MULTIFREQUENCY DATA

Observers	Instrument	Date	n[a]	log ν	flux(Jy)	σ[b]
Hartman	GRO/EGRET (0.1-5 GeV)	92 Dec 22-93 Jan 12	1	22.38	8.12×10^{-11}	2.7×10^{-11}
Collmar	GRO/COMPTEL (10-30 MeV)	92 Dec 22-93 Jan 12	1	21.62	6.96×10^{-9}	upp. lim
Fink & Thomas	ROSAT/PSPC (0.1-2.4 keV)	93 Jan 2-5	1	17.38	1.02×10^{-6}	0.02×10^{-6}
Maraschi & Urry	IUE/SWP (1600-1650 Å)	93 Jan 2-5	2	15.27	0.99×10^{-4}	0.34×10^{-4}
	IUE/LWP (2600-2700 Å)	93 Jan 2-5	4	15.05	2.92×10^{-4}	0.31×10^{-4}
Bailyn & Méndez	CTIO (0.9 m)	93 Jan 3-6	4	14.83	5.02×10^{-4}	$^{+0.37\times10^{-4}}_{-0.77\times10^{-4}}$
	(B,V,R,I)	93 Jan 3-6	4	14.73	7.59×10^{-4}	$^{+0.90\times10^{-4}}_{-0.97\times10^{-4}}$
		93 Jan 3-6	4	14.67	1.05×10^{-3}	$^{+0.12\times10^{-3}}_{-0.14\times10^{-3}}$
		93 Jan 3-6	4	14.58	1.58×10^{-3}	$^{+2.30\times10^{-4}}_{-2.30\times10^{-4}}$
Wagner & Bock	LSW Heidelberg Tel. (R)	93 Jan 1-6	5	14.67	1.04×10^{-3}	$^{+0.20\times10^{-3}}_{-0.17\times10^{-3}}$
Glass	1.9-m Sutherland Tel.	93 Jan 12	1	14.40	2.61×10^{-3}	0.22×10^{-3}
	(JHK)	93 Jan 12	1	14.25	4.72×10^{-3}	0.17×10^{-3}
		93 Jan 12	1	14.15	7.98×10^{-3}	0.22×10^{-3}
Mc Hardy et al.	JCMT	93 Jan 14	1	11.57	5.20	0.30
	(0.8,1.1,2.0 mm)	92 Dec 30-93 Jan 14	2	11.43	7.75	0.63
		92 Dec 29-93 Jan 14	2	11.18	8.50	0.5
Steppe & Reuter	IRAM	93 Jan 1-7	4	11.36	6.85	0.35
	(90,230 GHz)	93 Jan 1-8	6	10.95	15.80	0.33
Teräsranta	Metsähovi Radio Stat.	93 Jan 4-9	3	10.57	17.92	$^{+1.17}_{-0.73}$
	(22,37 GHz)	93 Jan 2-9	6	10.34	15.56	0.18
Aller & Aller	Michigan Radio Tel.	93 Jan 1	1	10.16	13.87	0.12
	(4.8,8.0,14.5 GHz)	93 Jan 1-7	2	9.90	12.25	0.13
		93 Jan 3	1	9.68	10.42	0.27

[a] Number of observations used to compute the average flux

[b] 1σ uncertainty. In case of suspected variability, the reported values correspond to the difference between the maximum and minimum observed flux

TABLE 2.5

JOURNAL OF IUE OBSERVATIONS OF 3C 279

IUE Image (1)	Exp. Time[a] (2)	Date (3)	F_G^b (4)	F_O^b ($\times 10^{-14}$ erg s^{-1} cm^{-2}Å^{-1}) (5)
LWP 24540[c]	180	1992 Dec 19.75	–	0.068 ± 0.011[d]
LWP 24597	130	26.60	0.055 ± 0.015	0.091 ± 0.021
LWP 24607	115	27.61	0.147 ± 0.022	0.175 ± 0.021
LWP 24616	156	29.43	0.065 ± 0.007	0.114 ± 0.012
LWP 24640[e]	150	31.74	0.115 ± 0.018	0.139 ± 0.014
LWP 24652	360	1993 Jan 02.66	0.088 ± 0.006	0.143 ± 0.009
SWP 46649[f]	220	02.91	–	–
SWP 46653	600	03.34	0.065 ± 0.036	0.177 ± 0.045
LWP 24656	360	03.76	0.127 ± 0.010	0.130 ± 0.008
SWP 46657	660	04.32	0.070 ± 0.027	0.104 ± 0.042
LWP 24661	360	04.79	0.152 ± 0.014	0.171 ± 0.010
SWP 46662[g]	820	05.33	–	0.087 ± 0.056
LWP 24665	315	05.82	0.078 ± 0.010	0.108 ± 0.016
LWP 24699[h]	150	10.07	0.185 ± 0.021	–

[a] In minutes

[b] Integrated and averaged GEX (Col. 4) and Optimal (Col. 5) extracted spectral fluxes at 1625 Å (SWP) or at 2650 Å (LWP)

[c] The GEX extracted flux is consistent with zero in the selected interval

[d] Errors represent 1σ statistical uncertainties

[e] A narrow luminous feature at ~2655 Å was discarded during the analysis

[f] Underexposed spectrum

[g] In the selected interval no signal is present in the GEX spectrum

[h] The Optimal extraction is not available for this image

version, see § 1.2.2.3) and Optimal extractions were applied; among the GEX extracted spectra, only SWP 46649 seems to be definitely underexposed and unusable. The flux distributions have been calibrated with the curves provided by Bohlin et al. (1990, SWP) and Cassatella et al. (1988, LWP). To the SWP spectra a correction of 2% per year during 6 years was applied to take into account the yearly sensitivity degradation of the SWP camera. No sensitivity degradation correction has been applied to the LWP spectra. The GEX extracted spectra are given in Appendix C.

To optimise the S/N, the flux was integrated and averaged on both series of GEX and Optimal spectra in the interval 1600–1650 Å for SWP and 2600–2700 Å for LWP. In Table 2.5 are reported the integral fluxes in the selected regions divided by the wavelength interval. The flux uncertainties are calculated as in § 1.2.2.3.

A systematic difference between the two IUE spectra extraction methods was found of ~65% for SWP spectra and of ~30% for LWP ones. Such difference cannot be completely accounted for by the calibration and photometric errors (note however that the intrinsic errors are rather large). Therefore, we used in the construction of the overall radio-to-γ-ray spectrum the average values between the results of GEX and Optimal. In Fig. 2.21 both resulting light curves at 2650 Å are shown, which exhibit a similar increasing trend, apart from the systematic flux offset.

A more detailed and complete description and discussion of the IUE campaign data will be given by Urry et al. (1994a), and some preliminary results are discussed in § 2.3.3.1. Here we use average fluxes in short- and long-wavelength bands derived from the spectra obtained in the period between January 2–5 (4 LWP and 2 SWP, see Table 2.5), simultaneous to the intensive coverage with Rosat. The fluxes reported in Table 2.4 have been dereddened with $E(B-V) = 0.015$.

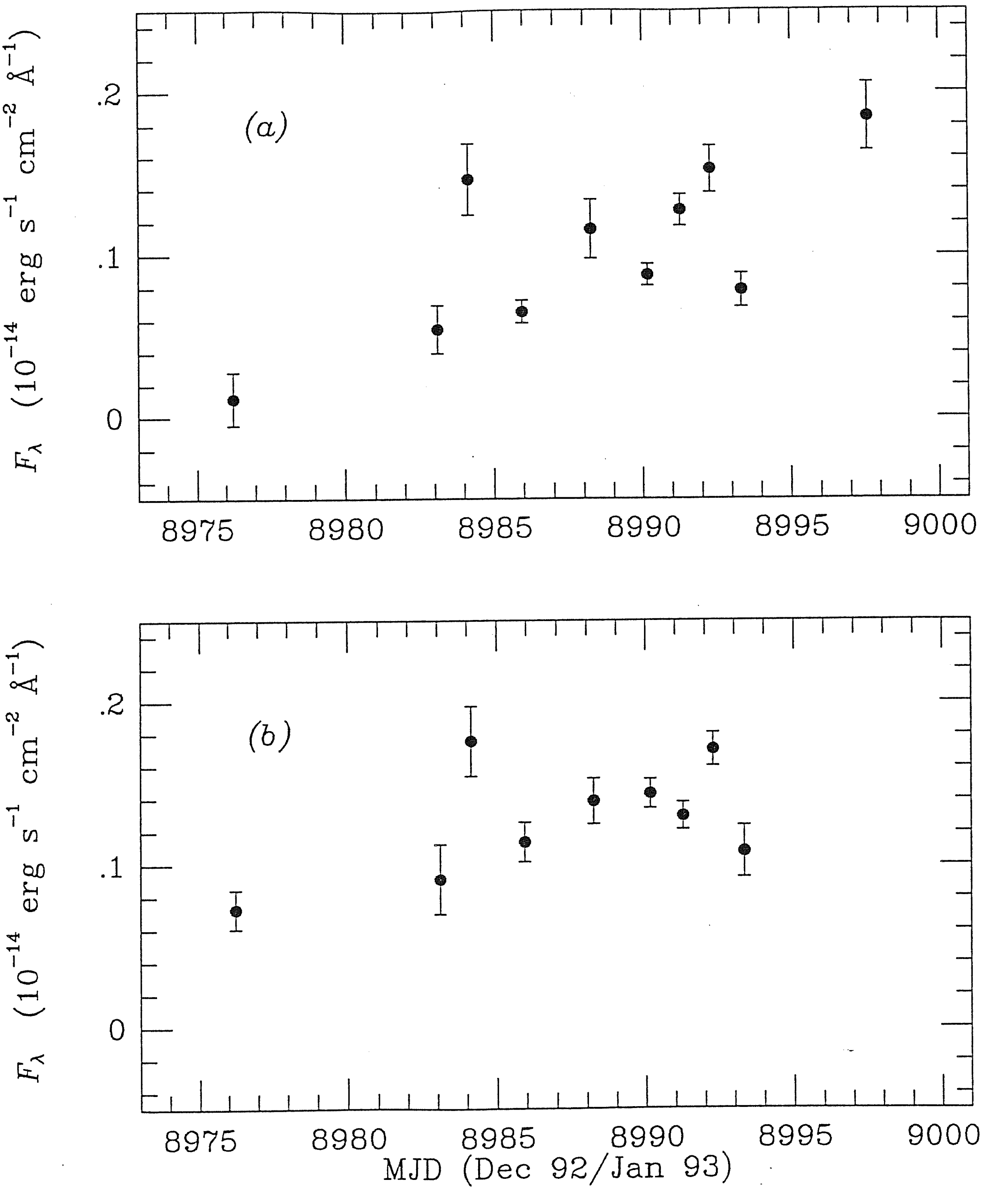

FIG. 2.21 — Light curves at 2650 Å derived from *(a)* GEX extracted spectra; *(b)* Optimal extracted spectra.

2.3.1.4 Ground-Based Observations

The ground-based observations involved many telescopes and observers at various dates; they will be described extensively elsewhere (Grandi et al. 1994). The best temporal sampling occurred at the beginning of January when all the space-based instruments and most of the ground-based telescopes could simultaneously (within less than a day) observe the source. Bad weather prevented only the JCMT mm and near-IR wavelengths from being strictly simultaneous with the spacecraft observations (see Table 2.4). In order to construct the broad-band energy distribution of 3C 279, we therefore used in each waveband average flux values of the observations performed in the time intervals specified in Table 2.4.

2.3.2 Comparison of the 1992/1993 and 1991 Energy Distributions

The energy distribution of 3C 279 derived from this campaign is shown in Fig. 2.22, together with that measured in June 1991 when the maximum γ-ray flux was observed (from references listed below and in Hartman et al. 1993).

Data for the bright state of June 1991 were obtained by M. Aller (4.8, 8.0, 14.5 GHz), H. Teräsranta (22, 37 GHz) and I. McHardy (mm, sub-mm and IR wavelengths). Optical, UV, X-ray and γ-ray fluxes were taken from the literature (Takalo et al. 1992; Bonnell et al. 1994; Makino et al. 1992; Hermsen et al. 1993; Kniffen et al. 1993). With the exception of the optical data, all the observations were conducted while the CGRO satellite was pointing at the source (16–28 June 1991) or close to that period (the radio (22 GHz) and UV observations were obtained respectively before (June 7) and after (July 29) the γ-ray measurements). The nearest published BVRI magnitudes (used in Fig. 2.22) date from 6 February 1991.

Comparing the December 1992/January 1993 and June 1991 energy distributions, it is striking that in 1993 the source was much fainter than in 1991 at all frequencies above 10^{14} Hz, while at lower frequencies there are only small differences between the two states. Data taken when 3C 279 was between flaring and quiescent states indicate that the emission from 10^{14} to 10^{23} Hz probably varies in a correlated fashion, at least on timescales of months (Grandi et al. 1994).

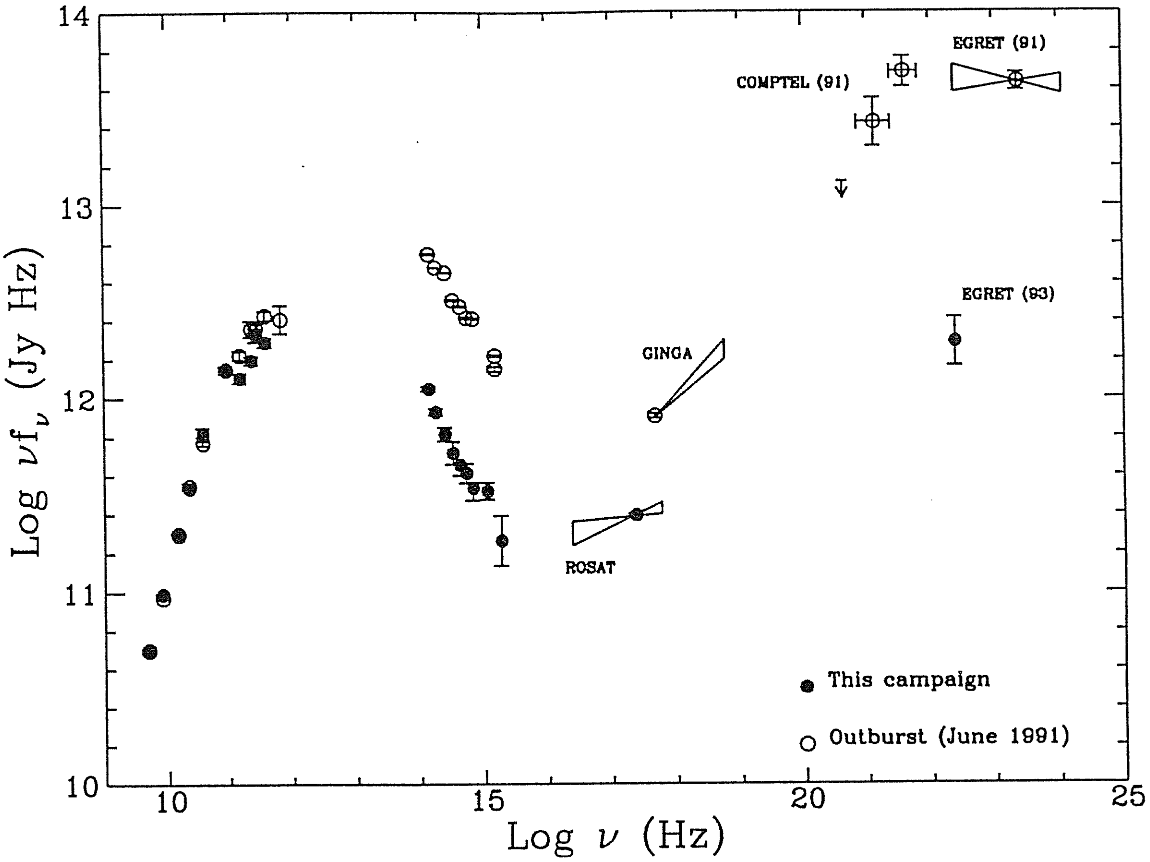

FIG. 2.22 — The radio-to-γ-ray energy distribution of 3C 279 as derived from the quasi simultaneous observations in Dec 1992–Jan 1993 (*filled dots*). Data referring to June 1991, mostly taken from the literature, are shown for comparison (*open dots*). The Comptel upper limit refers to the 1991 observation.

In the near-IR through UV wavelength region, the spectral shape varies, being softer in the fainter state. This result was derived also within the UV band alone (see § 2.3.3.2). The ratios between the high state and low state fluxes are 6.5 at 3×10^{14} Hz and 11 at 10^{15} Hz.

At X- and γ-ray frequencies, the 1991:1992–93 flux ratios are 3 at 4.8×10^{17} Hz (2 keV) and 20 at 2.4×10^{22} Hz (100 MeV). The Rosat spectrum is significantly softer than the GINGA spectrum, consistently with the spectral softening seen at other wavelengths, but because the energy bands overlap only marginally, we cannot exclude that the change in spectral shape depends on wavelength rather than time. Unfortunately, no information on the spectral shape in the γ-ray band can be derived for the quiescent state, since the detection was marginal for EGRET, and COMPTEL provided only an upper limit.

Finally, the ratio between the integrated γ-ray flux and the integrated flux in all the other observation bands varied substantially between the two epochs, the luminosity in γ-rays being comparable to that in other frequency bands in the low state, while in the brightest state the γ-ray luminosity exceeded that in other bands by a factor of 10.

2.3.3 Discussion

2.3.3.1 UV Continuum and Lyman-α Emission Line

An general brightening is seen in the UV along the monitoring time with variations of a factor ~2 in a weak. Short-term variability determines several flares overimposed on such long-term increase (Fig. 2.21). The short-wavelength signal is too poor and undersampled to allow independent conclusions.

At the three epochs when both SWP and LWP spectra were available, we fitted the 1200–3000 Å spectral flux distributions to a power-law using a standard χ^2 procedure ($F_\lambda \propto \lambda^{-\alpha_\lambda}$). The results are given in Table 2.6 in terms of the energy index α_ν (see § 2.1.1.1.e). Our fitting procedure yields confidence intervals at the 90% probability level for the fitted parameters, so that the error bars on the right and on the left of each best fit value can be different. Here is listed the highest one.

TABLE 2.6

FITTED PARAMETERS FOR MERGED SPECTRA

IUE Images	GEX			Optimal		
	α_ν^a	F_λ^b	$\chi^2/d.o.f.$	α_ν^a	F_λ^b	$\chi^2/d.o.f.$
SWP46653 + LWP24656	3.00 ± 0.60^c	0.072 ± 0.011	1.06	1.66 ± 0.26	0.144 ± 0.008	0.24
SWP46657 + LWP24661	2.45 ± 0.40	0.123 ± 0.009	1.38	2.10 ± 0.31	0.146 ± 0.008	1.57
SWP46662 + LWP24665	2.15 ± 0.89	0.077 ± 0.017	2.64	1.86 ± 0.46	0.125 ± 0.011	4.45

[a] Fitted energy index

[b] Fitted flux at 2000 Å (in units of 10^{-14} erg s^{-1} $cm^{-2}Å^{-1}$)

[c] Errors are 90% uncertainties deduced from the fitting procedure

The Optimal spectra appear slightly harder than the corresponding combined GEX spectra, which is related to the larger difference of the two extractions at higher far-UV energies.

On the SWP spectra a feature is visible at ~1870 Å ascribable to the redshifted Lyman-α emission line near the nucleus ($z = 0.538$). In the coadded spectrum resulting from the weighted mean of the 3 GEX spectra (Fig. 2.23a) the line intensity is $2.3 \cdot 10^{-14}$ erg s^{-1} cm^{-2}, whereas in the coadded Optimal spectrum it is ~50% brighter. The equivalent width is $W_\lambda \sim 50$ Å in the first case and 24 Å in the second.

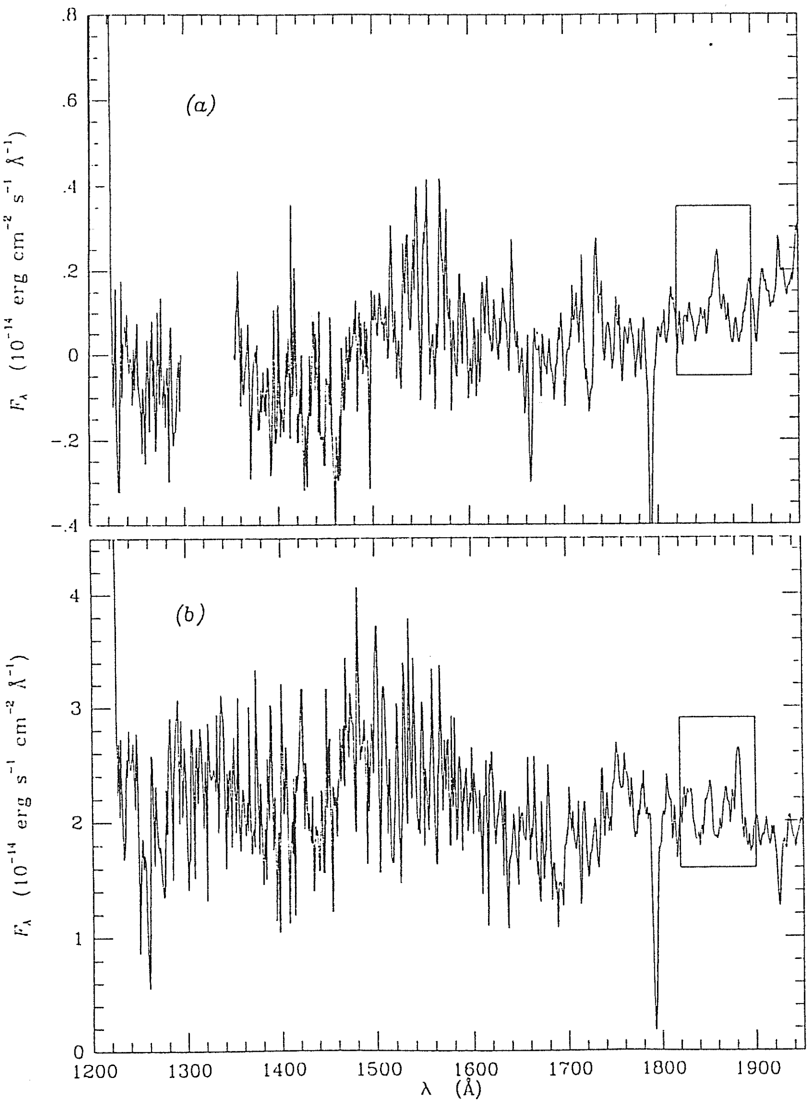

FIG. 2.23 — *(a)* Coadded SWP spectrum; *(b)* archival coadded SWP spectrum. The boxes circumscribe the Lyman-α emission line at ~1870 Å.

2.3.3.2 Comparison with Previous IUE Observations

The object has been observed several times with IUE before our 1992/3 exposures. In Table 2.7 are reported the results of archival observations of 3C 279 collected from the literature. Using these data and including the fluxes of the present monitoring (Table 2.6), we obtained light and spectral index curves spanning ~6 years (Fig. 2.24). The archival fluxes are averagely about a factor of 17 higher than those of the present campaign, indicating that during the last monitoring the source was in a very low emission state. There is indication of a softening spectrum with fading emission. A statistically marginal evidence for a long-term monotonic anticorrelation between UV flux and spectral slope is also found by Bonnell et al. (1994) based on data spanning from 1988 to 1991; and by Schrader et al. (1994) in the optical-UV domain.

TABLE 2.7
HISTORICAL LIGHT CURVE OF 3C 279

Image Numbers	Date	α_ν^a	F_ν^b (mJy)	Refs.[c]
SWP33864 + LWP13566	1988 Jul 06	1.68	2.67	1
SWP33865 + LWP13567	1988 Jul 06	1.39	2.80	1
SWP35443 + LWP14933	1989 Jan 29	1.53	1.25	1
SWP36420 + LWP15677	1989 Jun 09	1.81	1.57	1
SWP40489 + LWP19492	1990 Dec 30	1.81	1.69	1
SWP42132 + LWP20891	1991 Jul 27	–	1.12	2
SWP44806 + LWP23207	1992 May 29	1.77	2.24	3

[a] Energy index over the range 1200–3000 Å
[b] Fitted flux at 2000 Å
[c] REFERENCES: (1) E92. (2) Bonnell et al. (1994). (3) Schrader et al. (1994)

Two IUESIPS extracted SWP spectra (33864 and 33865) available on the IUE

ULDA archive have been coadded in order to improve their S/N (Fig. 2.23b). A broad feature ($W_\lambda \sim 3.5$ Å) centered at ~ 1870 Å is visible, which we ascribe to Lyman-α emission near the nucleus. The intensity of the line is $6.75 \cdot 10^{-14}$ erg s^{-1} cm^{-2}, which is only a factor $\sim$2 higher than found from our observations. This implies that the line emission varies in a correlated way with the continuum, but with smaller amplitude.

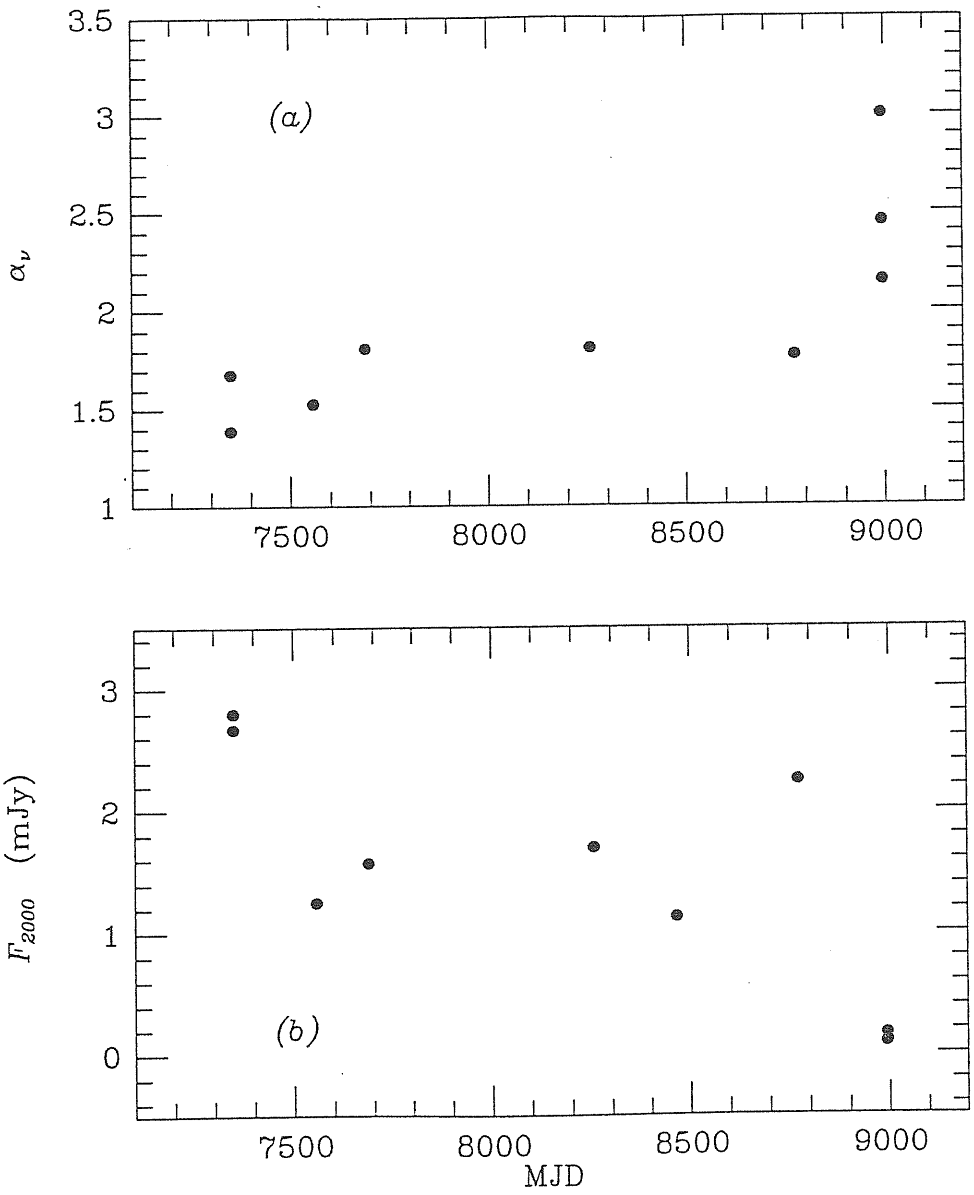

FIG. 2.24 — Fit parameters for archival and recent UV spectral observations: *(a)* energy index; *(b)* flux at 2000 Å.

2.3.3.3 The Broad-Band Energy Distribution

At both epochs the broad-band energy distribution of 3C 279 in the νF_ν represention (Fig. 2.22) is rising in the radio through mm band, falling in the IR through UV band, and rising again in the X-ray band. From the available, admittedly incomplete, wavelength coverage, the spectral energy distribution of 3C 279 appears to consist of two broad components, with peaks in the mm-IR range (where there is an unfortunate gap in our current observing capabilities) and in the 10 MeV–1 GeV range. The γ-ray spectrum for the brightest state is flat in νF_ν, while there is no spectral information for the low state; however, since in all bands above 10^{14} Hz the energy distribution for the low state is softer than for the high state, this is likely to be true also in the γ-ray band.

The first broad spectral component is commonly interpreted as synchrotron radiation by high energy electrons in a relativistic jet, which is self-absorbed at centimeter wavelengths. The second, shorter-wavelength component has been interpreted as IC-scattered radiation by the same population of relativistic electrons responsible for the synchrotron emission.

The seed photons to be upscattered could be the synchrotron photons themselves, as in the SSC model (Maraschi et al. 1992; Bloom & Marscher 1993), or photons external to the jet. These may derive from an accretion disk (Dermer et al. 1992; Dermer & Schlickeiser 1993) and could possibly be isotropized by scattering in a hot intercloud medium and/or may be emitted by the broad-line region itself (Blandford 1993; Sikora et al. 1994). The relative importance of the two types of seed photons (synchrotron or external), estimated on the basis of observed quantities, depends on a high power of the beaming factor ($\sim \delta^5$; Sikora et al. 1994). However in neither case is it easy to reproduce accurately the observed energy distributions with a simple homogeneous model; multiple components or an inhomogeneous jet are required.

In the case of the simplest SSC model, the most important photons for upscattering are those at the peak of the synchrotron emission (i.e., 10^{13-14} Hz).

The similarity of the spectral shape of the synchrotron and IC components suggests that these photons are upscattered to the γ-ray band (10^{22-23} Hz), which requires a relatively high electron Lorentz factor, $\gamma \sim 10^4$, and a rather low magnetic field $B = 0.3(\frac{\gamma}{10^4})^{-2}\delta^{-1}$ Gauss.

External seed photons, even if isotropic in the rest frame of the AGN, would appear blue-shifted and therefore enhanced in the jet frame. The typical frequency of accretion disk or broad-line photons as seen from the jet would be in the EUV-soft-X-ray band, thus providing an IC γ-ray component peaking at higher energies than in the case of the SSC mechanism (for the same mean electron Lorentz factor) and/or allowing for higher values of the magnetic field (e.g. MGC).

With regard to variability, a general property of the SSC model is that, when the electron distribution decreases in number and/or average square energy, the synchrotron luminosity decreases proportionally, while the IC (γ-ray) luminosity decreases quadratically (e.g. MGC).

If instead the photon energy density as seen in the jet frame is dominated by external photons, when the electron spectrum varies, the synchrotron and IC emission components will both scale proportionally, unless the external photon field varies at the same time and in the same sense as the electron spectrum.

The energy distributions of 3C 279 in high and low state are qualitatively consistent with the SSC model, since the γ-ray luminosity, assumed to be representative of the IC luminosity, varies more than the synchrotron luminosity, peaking presumably in the far-IR range. However one can still salvage the external photon models fairly naturally by postulating that the synchrotron decrease is caused by a change in the *bulk* Lorentz factor of the radiating electrons. In that case, the external photon field *as seen by the relativistic electrons* also decreases, and if at the same time the spectrum of relativistic electrons in the jet decreases, the resulting variation of the γ-ray flux is larger than that of the synchrotron one. A decrease of δ by a factor of 2 would account for the observed variation in the broad-band energy distribution of

3C 279.

It is interesting to recall that a steepening of the electron distribution is a natural consequence of a diminishing strength of a shock, while a flattening of the electron spectrum is expected if a shock gets stronger or a new shock forms (Schneider & Kirk 1989). Moreover the evolution of a relativistic shock may offer a physical framework, whereby the relativistic amplification factor for the observed flux (more complicated than a simple Doppler correction, Lind & Blandford 1985, Celotti et al. 1991) could be related to the shock strength. Thus shocks in a jet can qualitatively explain the observed variation in L_γ/L_{bol}. If external photons dominate the IC mechanism the shock front should accelerate or slow down substantially when getting respectively stronger or weaker.

2.4 Remarks

We have presented the results of simultaneous multi-frequency observations of three blazar sources, which are representative examples of the radio-weak BL Lacs (PKS 2155–304), radio-strong BL lacs (OJ 287) and OVV (3C 279).

Similarly to the case of 3C 279, also for PKS 0521–365 (Section 1.4) it was concluded that the spectral energy distribution should be produced by the SSC mechanism. A comparison, indicates that the overall energy distribution of PKS 0521–365 above the self-absorbed part of the synchrotron spectrum, resembles that of 3C 279 in low state, i.e., the radio, IR, optical, UV, X-ray and γ-ray fluxes have similar ratios in the two objects. Since the beaming factor in PKS 0521–365 is nearly frequency independent, and assuming that the *intrinsic* flux ratios are the same in every blazar, we deduce the indication that also for 3C 279 the Doppler beaming factor could be constant along the jet, though all beaming indicators suggest that, contrary to the case of PKS 0521–365, its viewing angle is small and the Doppler boosting is large. An analogous indication can be seen comparing the spectral energy distributions of PKS 0537–441 and 3C 279 (see Maraschi et al. 1993).

This similarity in spectral shape, despite the difference in viewing angle, suggests that for some objects, the entire spectrum, from radio to γ-rays, could be produced by plasma moving with nearly constant Lorentz factor, i.e., independent of distance from the nucleus.

Both for PKS 2155–304 and 3C 279 we find that the synchrotron process from a relativistic jet is likely responsible for the emission, though the location of the synchrotron component peak is different: it is seen in the IR ($\sim 10^{13}$ Hz) region in 3C 279 (Fig. 2.22) and "blue-shifted" to the EUV (unobservable) band in PKS 2155–304 (see Fig. 2.16). This different behaviour typically distinguishes RW and RS sources as already noted in this thesis (see Introduction and Chapter 1).

The spectral rise seen in the X-rays for 3C 279 indicates the appearance of a second component, formed through the IC process, which accounts also for the large γ-ray output. Our 1991 spectral energy distribution for PKS 2155–

304 does not extend thus far in energy, since EGRET observations are lacking. A subsequent EGRET determination of an upper limit for the GeV emission indicates that it should be much more modest than in 3C 279. Our theoretical prediction (see Fig. 2.16) shows that its contribution should be more important, though still not dominant, at TeV energies.

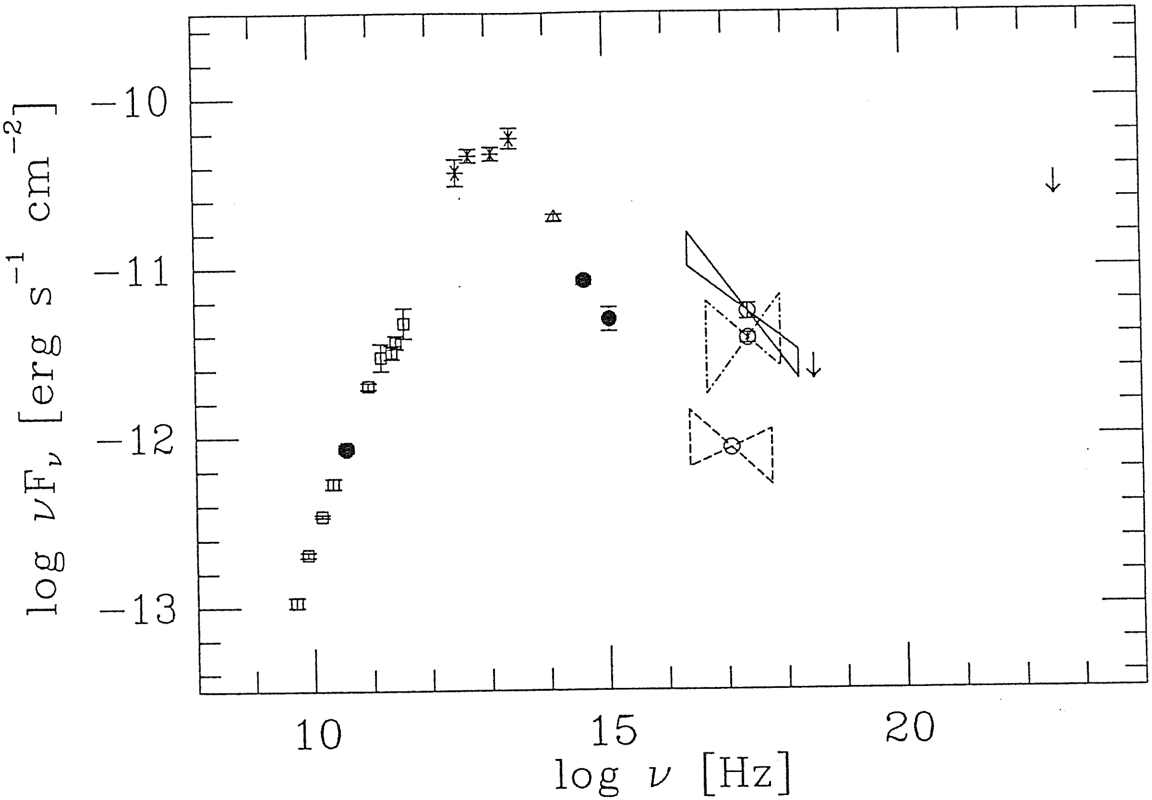

FIG. 2.25 — Spectral energy distribution of OJ 287. Simultaneous data are represented by equal symbols: *open squares*, Gear et al. (1994); *filled dots*, 1993 March campaign (§ 2.2); *stars*, Impey & Neugebauer (1988, IRAS); *open triangle*, Bersanelli et al. (1992). The X-ray data (represented by the 90% confidence ranges for the spectral fits) are from Sambruna et al. (1994, EXOSAT, *solid line*); Madejski & Schwartz (1988, *Einstein, dashed-dotted line*); Boller et al. (1994, Rosat, *dashed line*). Two upper limits are also added at hard-X- and γ-ray energies, from GINGA (Ohashi 1989) and from EGRET (Fichtel et al. 1994) respectively.

For OJ 287 we do not have high energy data and constructed an overall energy distribution (Fig. 2.25) with non simultaneous data derived from the literature. The radio-to-UV data suggest the presence of a synchrotron component peaking in the far-IR. A rising toward higher frequencies is suggested by the slope of the *Einstein* spectrum, but the EXOSAT one, which also covers a medium energy range, is quite steep. The high energy upper limits do not exclude a second hard component, but the rather large errors affecting the X-ray data and the lack of simultaneity with fluxes at lower frequencies prevent a description of the continuum in terms of the models (note that the EXOSAT flux at 1 keV is about a factor 10 above the extrapolation from the optical-UV data). The radio-to-UV spectral energy distribution of OJ 287 is similar to that of 3C 279, which is a diagnostic of a similar degree of beaming in the two objects.

In the UV range, small but significant spectral variability is detected both for PKS 2155–304 and 3C 279, though not clearly correlated with the flux variations. For PKS 2155–304 such weak flux-spectral shape correlation has been already noted in previous occasions (Maraschi et al. 1986a; Urry et al. 1988), whereas the long-term behaviour of 3C 279 indicates that there is a clear anticorrelation (Fig. 2.24) in the sense that the spectrum flattens when the source brightens. No comparison can be made with the present observations of OJ 287 due to the lack of spectral information. This anticorrelation, though consistent with the nonthermal acceleration processes expected in relativistic plasmas, is hardly seen in blazars and much better observed in Seyferts (see § 2.1.3.3).

Summary and Future Work

The issue of explaining the broad-band spectral properties of blazars and their relation with the source geometry and with the continuum emission processes have been addressed through the analysis of both single-epoch and repeated multi-wavelength observations. The former yielded information on the overall spectral shape and then on the implied emission mechanism (Sections 1.2, 1.4), the latter allowed to study correlated variability at different frequencies, and correlated flux and spectral variability (Chapter 2). In Section 1.1 we particularly concentrated on the UV continua of IUE observed blazars, whose spectral properties were studied from a statistical point of view. The most important findings of this work are:

1) The average UV spectral index of blazars is ~1, which implies that the energy emitted per unit frequency is nearly constant over the examined wavelength range (1200–3000 Å); a segregation seems to be present within the blazar class according to the radio properties: OVV objects have significantly steeper spectra than radio-weak BL Lacs. The radio-strong BL Lacs represent a "transition" group, being characterized by an intermediate average spectral index.

2) The dominant emission mechanism in blazars is SSC within a relativistic jet, which gives rise to a double peaked radio-to-γ-ray energy spectrum: the first peak is located at IR frequencies in radio-strong objects and optical-UV frequencies in radio-weak ones and is ascribed to synchrotron radiation. The second peak is formed through IC upscattering of relativistic electrons off synchrotron photons and is generally situated at GeV or TeV frequencies in radio-strong and radio-weak objects respectively.

3) In the best monitored BL Lac, PKS 2155–304, the optical, UV and soft-X-ray light curves are well correlated with no measurable lag between the optical and UV, and a lag of 2–3 hr between the X-ray and UV emission.

This indicates on one hand that the optical-UV emission cannot be produced by an accretion disk and, on the other hand, since the UV-X-ray lag is much less than the variability timescale, a progressive shock along the jet is responsible for flux variations at high energies. Moreover, the X-rays lead the UV emission, thus they can not be produced through IC, but presumably by the same process (synchrotron radiation) which produces the UV.

Some open problems concerning the structure and emission of blazars will be the matter of further research. Particularly, observational programs on some of the targets presented and studied in this thesis were devised, and partially realized, including IUE scheduling.

An intensive IUE monitoring of PKS 2155–304 was conducted in May 15–25, 1994. Simultaneous CGRO, ASCA, Rosat (HRI and WFC), EUVE, optical, IR and radio observations were organized with the aim of studying multi-frequency variability. The IUE campaign should improve the previous 1991 monitoring (see Section 2.1) by reducing temporal gaps and extending the sampling period in order to: *a)* investigate the stability of the UV-X-ray correlation over longer timescales and better measure the lag; *b)* obtain well-sampled UV light curves long enough to study the power spectrum in the frequency interval around the suggested period of ~0.7 days; the confirmation at a reliable confidence level of the presence of a period would be unprecedented for an AGN, after the rejection of the reality of the 12,000 seconds period in the Seyfert galaxy NGC 6814 (Madejski et al. 1994); *c)* investigate possible radio-UV correlations on short timescales. The UV brightness of the object was possibly higher than found in 1991 November, but the complete and detailed results of the campaign are not yet available (Urry et al. 1994b).

IUE observations of 3C 279 coordinated with the CGRO pointing to the source field were made in 1993 December. Due to the IUE baffle anomaly, which causes contamination in LWP exposures from solar scattered light, only SWP spectra were taken, which will help in studying the Lyman-α line emission, in addition to the 1200–2000 Å continuum, which was in a some brighter state than detected in 1992 December/1993 January.

The object is indeed brightening in the optical band. Harvanek & Stocke (IAUC 5978) reported an average magnitude $m_V = 14.6$ in April 1994, to compare with $m_V = 15.5$ in December 1993 and $m_V = 16.1$ in December 1992.

Two recent observing proposals have been submitted to IUE, coordinated with other instruments. The first one (ESA), coordinated with CGRO, is aimed to the study of UV-γ-ray correlation in seven γ-ray emitters including 3C 279 and PKS 0521–365. The second (NASA) is a project of year-long IUE observation of 3C 279 for correlation with studies at other wavelengths. Extensive monitoring is foreseen during a complete year (2 observations per month) and intensive observing is requested during the CGRO pointing period, which will be on 1994 December. In this way, variability timescales from few hours to one year will be probed. The observed variations in L_γ / L_{UV} and Lyman-α will determine the origin of the seed UV photons that are Compton-scattered to γ-ray energies. This proposal includes also the quasar 3C 273, which should be observed by IUE in conjunction with an intensive Rosat campaign. Both sources will be observed also by ASCA and ground-based coverage at optical through radio wavelengths will be organised. Together with ongoing VLBI observations, these data allow determination of bulk velocity, viewing angle and physical parameters of the relativistic jet.

The BL Lac OJ 287 was selected for a broad-band microvariability study program, due to its known large optical and UV flares (see results of the radio, optical and IUE campaign in Section 2.2). The possible periodic nature of the optical-UV variability, which is ascribed to a binary supermassive black hole system (Sillanpää et al. 1988; Kidger et al. 1992), leads to the prediction of an imminent outburst. The recent optical, mm and sub-mm observations (IAUC 5909, 5913, 5944, 5971, 5990) show that the object steadily brightened from 1993 December to 1994 April, which can suggest that the rise to maximum has initiated. The source will be therefore proposed as a Target of Opportunity for IUE observations next autumn, as soon as optical observations will confirm the flux increase. Furthermore, the object will be included in a Target of

Opportunity program for the soon flying Infrared Space Observatory (ISO).

Great interest has been recently raised by the X-ray-selected BL Lac Mkn 421 due to its γ-ray behaviour. This is the only X-ray-selected blazar seen at γ-ray energies by EGRET, and the unique blazar detected at TeV energies (due to its proximity, see § 1.4.4). The object underwent an extraordinarily strong and rapid outburst in 1994 May 15, when it was observed by Whipple, reaching a flux of $(1.87 \pm 0.34)\cdot 10^{-10}$ ph s^{-1} cm^{-2} at the energy threshold of 250 GeV, which is comparable to the flux from the Crab Nebula at this energy (IAUC 5996). A simultaneous ASCA observation yielded a very high X-ray flux as well in the 2–10 keV energy range. An IUE SWP spectrum taken on 1994 June 1 (Fig. S.1) is at the same flux level of the previous March 1993 observations. It exhibits an unusual absorption feature at ~1525 Å, whose nature is not clear.

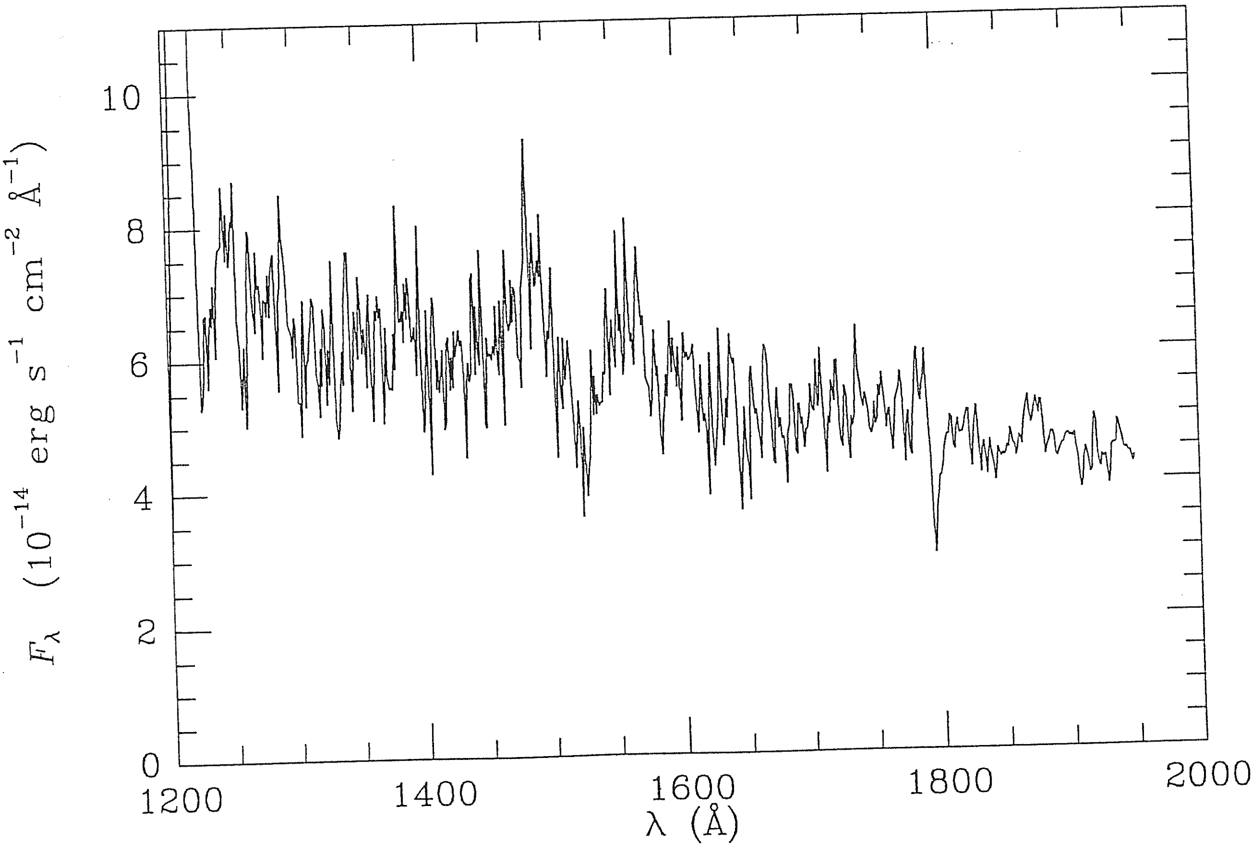

FIG. S.1 — IUE spectrum of Mkn 421 taken on June 1, 1994 (SWP 50964).

The feature appears transitory from comparison with the spectra of the March 1993 campaign, when the source was monitored alternately with OJ 287. The analysis and interpretation of the data from this IUE intensive monitoring are still in progress (Edelson et al. 1994b); preliminary results of simultaneous CCD optical observations taken at La Palma and Heidelberg, radio observations at Metsähovi and UBVRI photopolarimetry at Crimea were presented by Sillanpää et al. (1994). Here is presented the UV light curve at 1650 Å (Fig. S.2), resulting from the analysis of the IUE spectra extracted with the SWET procedure. An intense short-term variability is seen, though the overall variation along the monitoring time is modest. The dip visible at ~ 17.5 March is quite remarkable: it is unlikely to be spurious since it is seen also on the GEX extracted spectrum; moreover, it was detected by both IUE cameras. This sudden UV flux drop, together with the variability behaviour noted in the γ-rays makes Mkn 421 a representative source among BL Lacs, and an extremely interesting object both for observational and theoretical programs on rapid, large amplitude blazar variability.

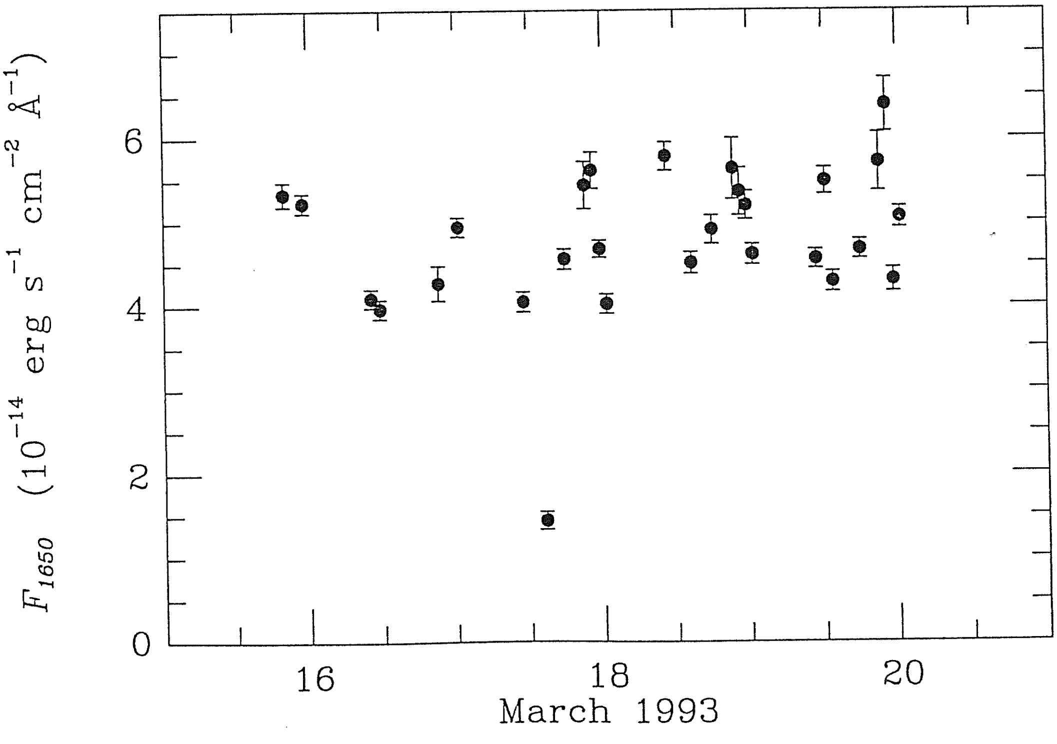

FIG. S.2 — IUE light curve at 1650 Å of Mkn 421.

This research has made use of the graphics package Super Mongo by R. Lupton and P. Monger and of the NASA/IPAC Extragalactic Database (NED) which is operated by the Jet Propulsion Laboratory, Caltech, under contract with the National Aeronautics and Space Administration.

Appendix A

Fit Parameters for PKS 2155–304

In this Appendix are reported the tables with the fit parameters of the dereddened spectra of PKS 2155–304 from the 1991 November IUE campaign (see Section 2.1). Table A.1 contains the power-law fit results on the single SWP and LWP spectra; in Table A.2 are given the fit parameters for the pairs of merged SWP-LWP spectra.

TABLE A.1

POWER-LAW FITS TO DEREDDENED SPECTRA

IUE Image	Observation Midpoint (UT) (Day of Nov 91)	F_{1400}	$\sigma_{F_{1400}}$	Spectral Index		
		($\times 10^{-14}$ erg cm^{-2} s^{-1} Å^{-1})		α_{SWP}	$\sigma_{\alpha_{SWP}}$	χ^2_ν
SWP 42969	1.87912	11.68	0.16	0.88	0.06	3.92
SWP 42970	1.94888	11.82	0.16	0.86	0.06	3.40
SWP 42971	2.01254	12.09	0.17	0.78	0.06	3.71
SWP 42972	2.07773	12.06	0.17	0.96	0.06	3.71
SWP 42979	2.86603	13.78	0.19	0.86	0.05	2.99
SWP 42980	2.93207	14.23	0.19	0.74	0.05	4.75
SWP 42995	3.87643	14.09	0.19	0.76	0.05	3.72
SWP 42996	3.94092	14.00	0.20	0.88	0.06	3.21
SWP 43008	4.86099	15.89	0.21	0.77	0.05	3.57
SWP 43009	4.93195	15.94	0.21	0.77	0.05	3.78
SWP 43017	5.87164	16.24	0.22	0.85	0.05	3.53
SWP 43018	5.94727	16.58	0.22	0.74	0.05	3.84
SWP 43025	7.00403	14.91	0.20	0.79	0.05	5.20
SWP 43026	7.07547	14.70	0.20	0.89	0.05	3.95
SWP 43040	9.19641	18.02	0.24	0.73	0.05	3.85
SWP 43041	9.27063	18.50	0.25	0.71	0.05	3.33
SWP 43047	9.71866	18.99	0.25	0.77	0.05	3.75
SWP 43048[a]	9.77417	18.71	0.26	0.89	0.06	3.83
SWP 43054	10.70386	20.71	0.27	0.69	0.04	4.01
SWP 43055	10.77008	20.86	0.28	0.68	0.05	4.11
SWP 43056	10.83871	20.85	0.28	0.76	0.05	3.36
SWP 43057	10.90527	21.13	0.28	0.75	0.05	3.78
SWP 43058	10.97137	20.95	0.28	0.74	0.05	3.59
SWP 43059	11.03726	21.12	0.28	0.72	0.04	4.20
SWP 43060	11.10294	21.21	0.28	0.76	0.05	3.13

TABLE A.1 (continued)

IUE Image	Observation Midpoint (UT) (Day of Nov 91)	F_{1400}	$\sigma_{F_{1400}}$	Spectral Index		
		($\times 10^{-14}$ erg cm^{-2} s^{-1} Å^{-1})		α_{SWP}	$\sigma_{\alpha_{SWP}}$	χ^2_ν
SWP 43061	11.16980	21.75	0.29	0.71	0.04	3.69
SWP 43062	11.23703	22.26	0.30	0.75	0.05	3.44
SWP 43063	11.30371	22.11	0.30	0.68	0.06	4.10
SWP 43064	11.37048	22.65	0.30	0.75	0.05	4.23
SWP 43065	11.83447	22.09	0.29	0.73	0.04	4.02
SWP 43066	11.90454	22.34	0.30	0.73	0.05	3.85
SWP 43067	11.96689	22.30	0.29	0.78	0.04	2.89
SWP 43068	12.03357	23.00	0.30	0.72	0.04	4.57
SWP 43069	12.10080	22.35	0.30	0.77	0.04	4.02
SWP 43070	12.16840	21.78	0.29	0.82	0.05	3.38
SWP 43071	12.23428	21.12	0.28	0.81	0.05	3.67
SWP 43073[a]	12.51471	18.89	0.29	1.02	0.09	2.95
SWP 43074	12.56787	20.67	0.27	0.76	0.05	3.88
SWP 43075	12.63367	20.78	0.28	0.78	0.05	4.20
SWP 43076	12.70255	21.07	0.28	0.78	0.05	3.84
SWP 43077	12.76688	21.39	0.28	0.78	0.04	3.62
SWP 43078	12.83356	21.31	0.28	0.80	0.04	3.68
SWP 43079	12.89929	21.88	0.29	0.80	0.04	3.14
SWP 43080	12.96588	21.86	0.29	0.82	0.04	3.90
SWP 43081	13.03345	21.49	0.29	0.86	0.05	4.17
SWP 43082	13.10092	20.91	0.28	0.81	0.05	3.70
SWP 43083	13.16806	20.42	0.27	0.84	0.05	3.69
SWP 43084	13.23126	19.97	0.27	0.76	0.05	4.00
SWP 43085	13.29907	19.63	0.26	0.84	0.05	3.67
SWP 43086	13.36594	19.64	0.26	0.76	0.04	4.39
SWP 43088[a]	13.50720	19.18	0.27	0.94	0.06	3.50

TABLE A.1 (continued)

IUE Image	Observation Midpoint (UT) (Day of Nov 91)	F_{1400}	$\sigma_{F_{1400}}$	Spectral Index		χ^2_ν
		($\times10^{-14}$ erg cm^{-2} s^{-1} Å^{-1})		α_{SWP}	$\sigma_{\alpha_{SWP}}$	
SWP 43089	13.56894	20.02	0.27	0.77	0.05	3.65
SWP 43090	13.63153	20.30	0.27	0.72	0.05	4.34
SWP 43091	13.69809	20.01	0.27	0.83	0.05	4.35
SWP 43092	13.76599	19.65	0.26	0.81	0.05	3.70
SWP 43093	13.83084	19.30	0.26	0.76	0.05	3.08
SWP 43094	13.89709	18.96	0.25	0.74	0.05	3.21
SWP 43095	13.96570	18.38	0.25	0.74	0.05	3.86
SWP 43096	14.03030	18.40	0.25	0.76	0.05	3.68
SWP 43097	14.09653	18.06	0.24	0.78	0.05	3.57
SWP 43098	14.16336	17.92	0.24	0.80	0.05	3.76
SWP 43099	14.23135	17.78	0.24	0.83	0.05	3.51
SWP 43101	14.56296	18.70	0.25	0.77	0.05	4.20
SWP 43102	14.62903	19.07	0.25	0.80	0.05	4.06
SWP 43103	14.69815	19.52	0.26	0.85	0.05	3.62
SWP 43104	14.76279	19.99	0.27	0.85	0.05	3.59
SWP 43105	14.82904	20.43	0.27	0.82	0.05	3.72
SWP 43106	14.89505	20.65	0.27	0.77	0.04	3.70
SWP 43107	14.96176	20.25	0.27	0.82	0.05	3.43
SWP 43108	15.02841	20.42	0.27	0.73	0.04	3.59
SWP 43109	15.09451	20.17	0.27	0.73	0.04	3.99
SWP 43110	15.16229	19.53	0.26	0.79	0.05	3.82
SWP 43111	15.22717	19.79	0.26	0.81	0.05	4.81
SWP 43114	16.20871	21.42	0.28	0.81	0.04	3.96
SWP 43115	16.26831	21.46	0.29	0.83	0.05	4.10
SWP 43121	16.86020	22.14	0.29	0.73	0.04	3.61
SWP 43122	16.92563	22.82	0.30	0.67	0.04	3.81

TABLE A.1 (continued)

IUE Image	Observation Midpoint (UT) (Day of Nov 91)	F_{1400}	$\sigma_{F_{1400}}$	Spectral Index		
		($\times 10^{-14}$ erg cm^{-2} s^{-1} Å^{-1})		α_{SWP}	$\sigma_{\alpha_{SWP}}$	χ^2_ν
SWP 43135	17.86005	21.37	0.28	0.78	0.05	3.73
SWP 43136	17.92896	21.36	0.28	0.74	0.04	3.60
SWP 43145	18.83432	19.35	0.26	0.85	0.05	3.27
SWP 43146	18.90332	18.77	0.25	0.92	0.05	4.07
SWP 43157	20.05450	18.63	0.25	0.85	0.05	3.30
SWP 43158	20.11401	18.00	0.25	0.94	0.06	2.80
SWP 43164	20.71451	20.13	0.27	0.87	0.05	3.65
SWP 43165[a]	20.77444	19.46	0.27	0.96	0.06	4.01
SWP 43174	21.69171	18.56	0.25	0.94	0.05	3.91
SWP 43175	21.76627	18.74	0.25	0.93	0.05	3.58
SWP 43184	22.68073	19.48	0.26	0.81	0.05	3.75
SWP 43185	22.74625	19.40	0.26	0.83	0.05	3.76
SWP 43192	23.70206	21.34	0.28	0.82	0.04	4.28
SWP 43193	23.76813	21.03	0.28	0.90	0.05	3.51
SWP 43211[b]	24.70337	20.04	0.27	0.78	0.05	3.76
SWP 43220	25.69824	19.64	0.26	0.82	0.05	3.39
SWP 43221	25.76685	19.65	0.26	0.80	0.05	3.58
SWP 43230	26.69736	22.84	0.30	0.79	0.04	3.96
SWP 43231	26.76675	23.40	0.31	0.84	0.05	3.38
SWP 43236	27.69647	20.94	0.28	0.81	0.04	3.94
SWP 43237	27.76450	20.83	0.28	0.89	0.05	3.16
SWP 43246	28.87381	21.91	0.29	0.91	0.05	4.23
SWP 43247	28.93491	22.14	0.29	0.87	0.05	3.70
SWP 43260	29.84335	22.93	0.30	0.73	0.04	4.27
SWP 43261	29.90997	22.70	0.30	0.83	0.05	4.12

TABLE A.1 (continued)

IUE Image	Observation Midpoint (UT) (Day of Nov 91)	F_{2800}	$\sigma_{F_{2800}}$	Spectral Index		χ^2_ν
		($\times10^{-14}$ erg cm^{-2} s^{-1} Å^{-1})		α_{LWP}	$\sigma_{\alpha_{LWP}}$	
LWP 21607	1.84244	4.62	0.07	0.70	0.14	1.78
LWP 21608	1.91510	4.72	0.07	0.93	0.14	2.38
LWP 21609	1.97968	4.71	0.07	0.97	0.16	2.20
LWP 21610	2.04449	4.80	0.07	0.94	0.16	2.15
LWP 21611	2.10934	4.82	0.07	0.74	0.15	1.95
LWP 21616	2.83383	5.28	0.08	0.59	0.15	2.26
LWP 21617	2.89771	5.30	0.08	0.93	0.15	2.07
LWP 21625	3.84235	5.24	0.08	0.49	0.15	2.40
LWP 21626	3.91318	5.41	0.08	0.69	0.14	2.56
LWP 21636	4.82599	6.15	0.09	0.99	0.13	2.04
LWP 21637	4.89694	6.18	0.09	0.96	0.14	2.37
LWP 21644	5.83676	6.24	0.09	0.76	0.13	2.36
LWP 21645	5.91180	6.35	0.09	0.74	0.13	2.05
LWP 21652	6.82202	6.19	0.09	0.78	0.13	2.39
LWP 21653	7.03946	5.87	0.08	0.68	0.13	2.12
LWP 21654	7.11139	5.93	0.08	0.88	0.14	2.02
LWP 21667	9.04929	6.92	0.10	0.85	0.12	2.40
LWP 21668	9.23254	7.10	0.10	1.16	0.12	2.54
LWP 21673	9.68405	7.31	0.10	0.85	0.12	2.38
LWP 21674	9.75076	7.33	0.10	0.89	0.12	2.52
LWP 21683	10.67126	7.85	0.11	0.90	0.12	2.81
LWP 21684	10.73682	7.85	0.11	0.75	0.11	1.75
LWP 21685	10.80591	7.92	0.11	0.85	0.12	2.29
LWP 21686	10.87241	7.98	0.11	0.91	0.11	2.31
LWP 21687	10.93814	7.87	0.11	0.65	0.12	1.98

TABLE A.1 (continued)

IUE Image	Observation Midpoint (UT) (Day of Nov 91)	F_{2800}	$\sigma_{F_{2800}}$	Spectral Index		
		($\times 10^{-14}$ erg cm^{-2} s^{-1} Å^{-1})		α_{LWP}	$\sigma_{\alpha_{LWP}}$	χ^2_ν
LWP 21688	11.00476	7.98	0.11	0.82	0.11	2.49
LWP 21689	11.07086	8.01	0.11	0.77	0.11	2.56
LWP 21690	11.13641	8.12	0.11	0.72	0.11	2.38
LWP 21691	11.20306	8.39	0.12	0.90	0.12	2.41
LWP 21692	11.26898	8.53	0.12	0.75	0.14	2.29
LWP 21693	11.33670	8.56	0.12	0.69	0.13	2.50
LWP 21696	11.87045	8.53	0.12	0.71	0.11	2.73
LWP 21697	11.93353	8.57	0.12	0.64	0.11	1.94
LWP 21698	12.00150	8.72	0.12	0.77	0.11	2.50
LWP 21699	12.06717	8.75	0.12	0.66	0.10	3.07
LWP 21700	12.13443	8.61	0.12	0.80	0.11	2.69
LWP 21701	12.20102	8.51	0.12	0.97	0.11	2.69
LWP 21702	12.26740	8.23	0.11	0.77	0.11	2.51
LWP 21704	12.53397	8.16	0.11	0.66	0.11	3.05
LWP 21705	12.60086	8.21	0.11	0.88	0.11	2.26
LWP 21706	12.66708	8.19	0.11	0.75	0.11	2.37
LWP 21707	12.73361	8.29	0.11	0.84	0.11	2.66
LWP 21708	12.79990	8.67	0.11	1.24	0.11	4.10
LWP 21709	12.86646	8.32	0.11	0.79	0.11	2.43
LWP 21710	12.93216	8.51	0.12	0.84	0.10	2.32
LWP 21711	13.00006	8.48	0.12	0.96	0.11	2.39
LWP 21712	13.06924	8.27	0.11	0.93	0.11	2.50
LWP 21713	13.13214	8.06	0.11	0.78	0.11	2.39
LWP 21714	13.19809	7.92	0.11	0.90	0.11	2.44
LWP 21715	13.26642	7.66	0.11	0.68	0.12	2.44

TABLE A.1 (continued)

IUE Image	Observation Midpoint (UT) (Day of Nov 91)	F_{2800}	$\sigma_{F_{2800}}$	Spectral Index		
		($\times10^{-14}$ erg cm^{-2} s^{-1} Å^{-1})		α_{LWP}	$\sigma_{\alpha_{LWP}}$	χ^2_ν
LWP 21716	13.33105	7.59	0.11	0.79	0.12	2.56
LWP 21717	13.53159	7.77	0.11	0.88	0.12	2.65
LWP 21718	13.59872	7.83	0.11	0.69	0.11	2.26
LWP 21719	13.66470	7.91	0.11	0.86	0.12	2.38
LWP 21720	13.73138	7.64	0.11	0.77	0.12	2.53
LWP 21721	13.79739	7.65	0.11	0.89	0.11	2.57
LWP 21722	13.86356	7.32	0.10	0.69	0.11	2.37
LWP 21723	13.93060	7.27	0.10	0.90	0.12	2.95
LWP 21724	13.99689	7.11	0.10	0.71	0.11	2.38
LWP 21725	14.06299	7.15	0.10	0.93	0.12	2.98
LWP 21726	14.12988	7.09	0.10	0.92	0.12	2.14
LWP 21727	14.19751	7.02	0.10	0.78	0.12	2.16
LWP 21728	14.26501	7.03	0.10	0.70	0.11	2.42
LWP 21730	14.52951	7.28	0.10	0.90	0.12	2.40
LWP 21731	14.59549	7.51	0.10	0.78	0.12	2.83
LWP 21732	14.66269	7.67	0.11	0.90	0.12	2.43
LWP 21733	14.72964	7.80	0.11	0.83	0.12	2.12
LWP 21734	14.79572	8.02	0.11	0.91	0.11	2.76
LWP 21735	14.86139	8.03	0.11	0.76	0.11	2.44
LWP 21736	14.92819	7.99	0.11	0.91	0.11	2.46
LWP 21737	14.99469	8.01	0.11	0.94	0.11	2.58
LWP 21738	15.06076	7.98	0.11	0.80	0.11	2.58
LWP 21739	15.12793	7.81	0.11	0.77	0.11	2.40
LWP 21740	15.19437	7.80	0.11	0.86	0.11	2.46
LWP 21741	15.26242	8.01	0.11	1.00	0.10	2.72

TABLE A.1 (continued)

IUE Image	Observation Midpoint (UT) (Day of Nov 91)	F_{2800}	$\sigma_{F_{2800}}$	Spectral Index		
		($\times 10^{-14}$ erg cm^{-2} s^{-1} Å^{-1})		α_{LWP}	$\sigma_{\alpha_{LWP}}$	χ^2_ν
LWP 21744	15.82483	7.63	0.11	0.88	0.12	2.40
LWP 21747	16.17667	8.35	0.11	0.91	0.11	2.56
LWP 21748	16.24106	8.46	0.12	0.82	0.11	2.40
LWP 21755	16.82968	8.45	0.12	0.77	0.11	2.65
LWP 21756	16.89108	8.76	0.12	0.96	0.11	2.11
LWP 21768	17.82776	8.11	0.11	0.80	0.11	2.28
LWP 21769	17.89197	8.31	0.11	0.77	0.11	1.92
LWP 21777	18.86792	7.83	0.11	0.90	0.11	2.31
LWP 21778	18.93918	7.81	0.10	0.72	0.07	2.64
LWP 21786	20.02225	7.41	0.10	1.07	0.12	2.14
LWP 21787	20.08722	7.41	0.10	0.83	0.11	2.24
LWP 21793	20.74850	8.33	0.11	0.85	0.11	2.54
LWP 21799	21.72665	7.69	0.11	0.95	0.12	1.76
LWP 21810	22.71548	7.95	0.11	0.91	0.11	2.11
LWP 21811	22.77560	7.87	0.11	0.84	0.12	2.27
LWP 21828	23.73749	8.75	0.12	0.91	0.11	2.28
LWP 21837[b]	24.76144	8.10	0.11	0.93	0.10	2.70
LWP 21847	25.73145	7.83	0.11	0.88	0.12	2.64
LWP 21856	26.73236	9.33	0.13	0.84	0.11	2.80
LWP 21864	27.73346	8.45	0.12	0.94	0.11	2.22
LWP 21877	28.84067	9.06	0.12	0.92	0.11	2.54
LWP 21878	28.90332	9.18	0.12	0.92	0.11	2.25
LWP 21888	29.87552	9.22	0.13	0.67	0.11	2.62
LWP 21889	29.94113	9.18	0.13	0.86	0.11	2.43

[a] Unusually short exposure time

[b] Interrupted exposure

TABLE A.2
POWER-LAW FITS TO MERGED SWP-LWP SPECTRA

Spectral Pair Image Numbers		Observation Midpoint (UT)	F_{2000}	$\sigma_{F_{2000}}$	Spectral Index		
SWP	LWP	(Day of Nov 91)	($\times 10^{-14}$ ergs cm^{-2} s^{-1} Å^{-1})		α_C	σ_{α_C}	χ^2_ν
42969	21607	1.86078	5.99	0.08	0.62	0.02	0.83
42970	21608	1.93201	6.06	0.08	0.65	0.02	0.88
42971	21609	1.99609	6.11	0.08	0.62	0.02	0.82
42972	21610	2.06110	6.25	0.08	0.63	0.02	1.00
42972	21611	2.09354	6.27	0.08	0.63	0.02	0.94
42979	21616	2.84991	6.89	0.09	0.58	0.02	0.83
42980	21617	2.91489	6.96	0.09	0.55	0.02	1.04
42995	21625	3.85938	6.90	0.09	0.54	0.02	0.91
42996	21626	3.92706	7.05	0.09	0.58	0.02	0.92
43008	21636	4.84351	7.95	0.10	0.61	0.02	0.88
43009	21637	4.91443	8.02	0.10	0.61	0.02	0.95
43017	21644	5.85419	8.10	0.10	0.58	0.02	1.90
43018	21645	5.92953	8.26	0.11	0.59	0.02	0.87
43025	21652	6.91302	7.84	0.10	0.72	0.02	1.07
43026	21653	7.05746	7.34	0.09	0.63	0.02	3.95
43026	21654	7.09344	7.62	0.10	0.66	0.02	0.90
43040	21667	9.12286	8.98	0.12	0.60	0.02	0.96
43041	21668	9.25159	9.17	0.12	0.61	0.02	0.99
43047	21673	9.70135	9.48	0.12	0.60	0.02	0.93
43048	21674	9.76245	9.49	0.12	0.61	0.02	1.01
43054	21683	10.68756	10.19	0.13	0.59	0.02	1.09
43055	21684	10.75345	10.20	0.13	0.58	0.02	0.83
43056	21685	10.82233	10.32	0.13	0.58	0.02	0.90
43057	21686	10.88885	10.41	0.13	0.57	0.02	0.98
43058	21687	10.95477	10.29	0.13	0.56	0.02	0.86
43059	21688	11.02100	10.40	0.13	0.58	0.02	0.96

TABLE A.2 (continued)

Spectral Pair Image Numbers SWP	LWP	Observation Midpoint (UT) (Day of Nov 91)	F_{2000} ($\times 10^{-14}$ ergs cm^{-2} s^{-1} Å^{-1})	$\sigma_{F_{2000}}$ ($\times 10^{-14}$ ergs cm^{-2} s^{-1} Å^{-1})	Spectral Index α_C	σ_{α_C}	χ^2_ν
43060	21689	11.08691	10.47	0.13	0.57	0.02	0.90
43061	21690	11.15311	10.65	0.14	0.55	0.02	0.94
43062	21691	11.22003	10.97	0.14	0.57	0.02	0.97
43063	21692	11.28635	10.96	0.14	0.62	0.02	0.90
43064	21693	11.35358	11.15	0.14	0.58	0.02	0.95
43065	21696	11.85248	11.03	0.14	0.61	0.02	1.01
43066	21697	11.91904	11.12	0.14	0.60	0.02	0.85
43067	21698	11.98419	11.26	0.14	0.62	0.02	0.86
43068	21699	12.05035	11.37	0.15	0.59	0.02	1.17
43069	21700	12.11761	11.19	0.14	0.60	0.02	1.06
43070	21701	12.18469	11.02	0.14	0.62	0.02	1.02
43071	21702	12.25085	10.64	0.14	0.61	0.02	0.96
43073	21704	12.52435	10.32	0.14	0.72	0.03	0.93
43074	21705	12.58435	10.53	0.14	0.65	0.02	0.89
43075	21706	12.65039	10.56	0.14	0.64	0.02	0.96
43076	21707	12.71811	10.69	0.14	0.64	0.02	1.00
43077	21708	12.78345	11.05	0.14	0.69	0.02	1.33
43078	21709	12.85004	10.77	0.14	0.62	0.02	0.96
43079	21710	12.91574	11.03	0.14	0.61	0.02	0.90
43080	21711	12.98297	11.00	0.14	0.61	0.02	1.03
43081	21712	13.05136	10.77	0.14	0.59	0.02	1.06
43082	21713	13.11655	10.49	0.13	0.60	0.02	0.96
43083	21714	13.18307	10.29	0.13	0.60	0.02	0.98
43084	21715	13.24884	9.95	0.13	0.59	0.02	0.98
43085	21715	13.28275	9.92	0.13	0.61	0.02	0.95
43086	21716	13.34851	9.84	0.13	0.61	0.02	1.05

TABLE A.2 (continued)

Spectral Pair Image Numbers		Observation Midpoint (UT)	F_{2000}	$\sigma_{F_{2000}}$	Spectral Index		χ^2_ν
SWP	LWP	(Day of Nov 91)	($\times 10^{-14}$ ergs cm^{-2} s^{-1} Å^{-1})		α_C	σ_{α_C}	
43088	21717	13.51941	10.00	0.13	0.65	0.02	1.00
43089	21718	13.58383	10.11	0.13	0.62	0.02	0.88
43090	21719	13.64813	10.18	0.13	0.63	0.02	1.01
43091	21720	13.71472	10.00	0.13	0.57	0.02	1.14
43092	21721	13.78168	9.88	0.13	0.62	0.02	0.95
43093	21722	13.84720	9.54	0.12	0.58	0.02	0.86
43094	21723	13.91385	9.43	0.12	0.60	0.02	1.00
43095	21724	13.98129	9.20	0.12	0.61	0.02	0.94
43096	21725	14.04663	9.23	0.12	0.62	0.02	1.05
43097	21726	14.11322	9.16	0.12	0.63	0.02	0.88
43098	21727	14.18042	9.09	0.12	0.62	0.02	0.92
43099	21728	14.24817	9.08	0.12	0.63	0.02	0.94
43101	21730	14.54623	9.42	0.12	0.62	0.02	1.01
43102	21731	14.61224	9.68	0.12	0.63	0.02	1.00
43103	21732	14.68042	9.95	0.13	0.62	0.02	0.98
43104	21733	14.74622	10.16	0.13	0.61	0.02	0.97
43105	21734	14.81238	10.37	0.13	0.62	0.02	1.07
43106	21735	14.87823	10.39	0.13	0.62	0.02	0.94
43107	21736	14.94498	10.32	0.13	0.63	0.02	0.96
43108	21737	15.01154	10.30	0.13	0.64	0.02	0.95
43109	21738	15.07764	10.23	0.13	0.65	0.02	0.97
43110	21739	15.14511	10.01	0.13	0.66	0.02	0.92
43111	21740	15.21075	10.07	0.13	0.63	0.02	1.12
43111	21741	15.24481	10.24	0.13	0.68	0.02	1.18
43114	21747	16.19269	10.84	0.14	0.62	0.02	1.08
43115	21748	16.25470	10.95	0.14	0.62	0.02	1.02

TABLE A.2 (continued)

Spectral Pair Image Numbers		Observation Midpoint (UT)	F_{2000}	$\sigma_{F_{2000}}$	Spectral Index		
SWP	LWP	(Day of Nov 91)	($\times 10^{-14}$ ergs cm^{-2} s^{-1} Å^{-1})		α_C	σ_{α_C}	χ^2_ν
43121	21755	16.84494	10.98	0.14	0.59	0.02	0.97
43122	21756	16.90836	11.32	0.14	0.61	0.02	0.92
43135	21768	17.84390	10.56	0.14	0.58	0.02	0.91
43136	21769	17.91046	10.72	0.14	0.62	0.02	0.80
43145	21777	18.85114	10.03	0.13	0.67	0.02	0.91
43146	21778	18.92126	9.93	0.13	0.70	0.02	1.03
43157	21786	20.03839	9.55	0.12	0.65	0.02	0.90
43158	21787	20.10062	9.48	0.12	0.68	0.02	0.82
43164	21793	20.73151	10.60	0.14	0.70	0.02	0.94
43165	21793	20.76147	10.54	0.14	0.74	0.02	0.96
43174	21799	21.70917	9.84	0.13	0.70	0.02	0.89
43175	21799	21.74646	9.88	0.13	0.68	0.02	0.92
43184	21810	22.69812	10.14	0.13	0.69	0.02	0.90
43185	21811	22.76093	10.07	0.13	0.67	0.02	0.93
43192	21828	23.71979	11.13	0.14	0.70	0.02	0.98
43193	21828	23.75281	11.13	0.14	0.71	0.02	0.91
43211	21837	24.73242	10.36	0.13	0.68	0.02	1.01
43220	21847	25.71484	10.08	0.13	0.65	0.02	0.98
43221	21847	25.74915	10.07	0.13	0.65	0.02	1.00
43230	21856	26.71484	11.86	0.15	0.70	0.02	1.00
43231	21856	26.74957	12.03	0.15	0.64	0.02	1.03
43236	21864	27.71497	10.82	0.14	0.67	0.02	0.95
43237	21864	27.74896	10.85	0.14	0.67	0.02	0.89
43246	21877	28.85724	11.58	0.15	0.69	0.02	1.02
43247	21878	28.91913	11.67	0.15	0.71	0.02	0.92
43260	21888	29.85944	11.74	0.15	0.68	0.02	1.00
43261	21889	29.92554	11.74	0.15	0.67	0.02	1.00

Appendix B

IUE Spectra of OJ 287

In this Appendix are presented the GEX extracted spectra from the IUE observing campaign of 1993 March 15–20 on the BL Lac object OJ 287 (see Section 2.2 for data analysis and discussion). Flux units are 10^{-14} erg^{-1} s^{-1} cm^{-2} Å^{-1}.

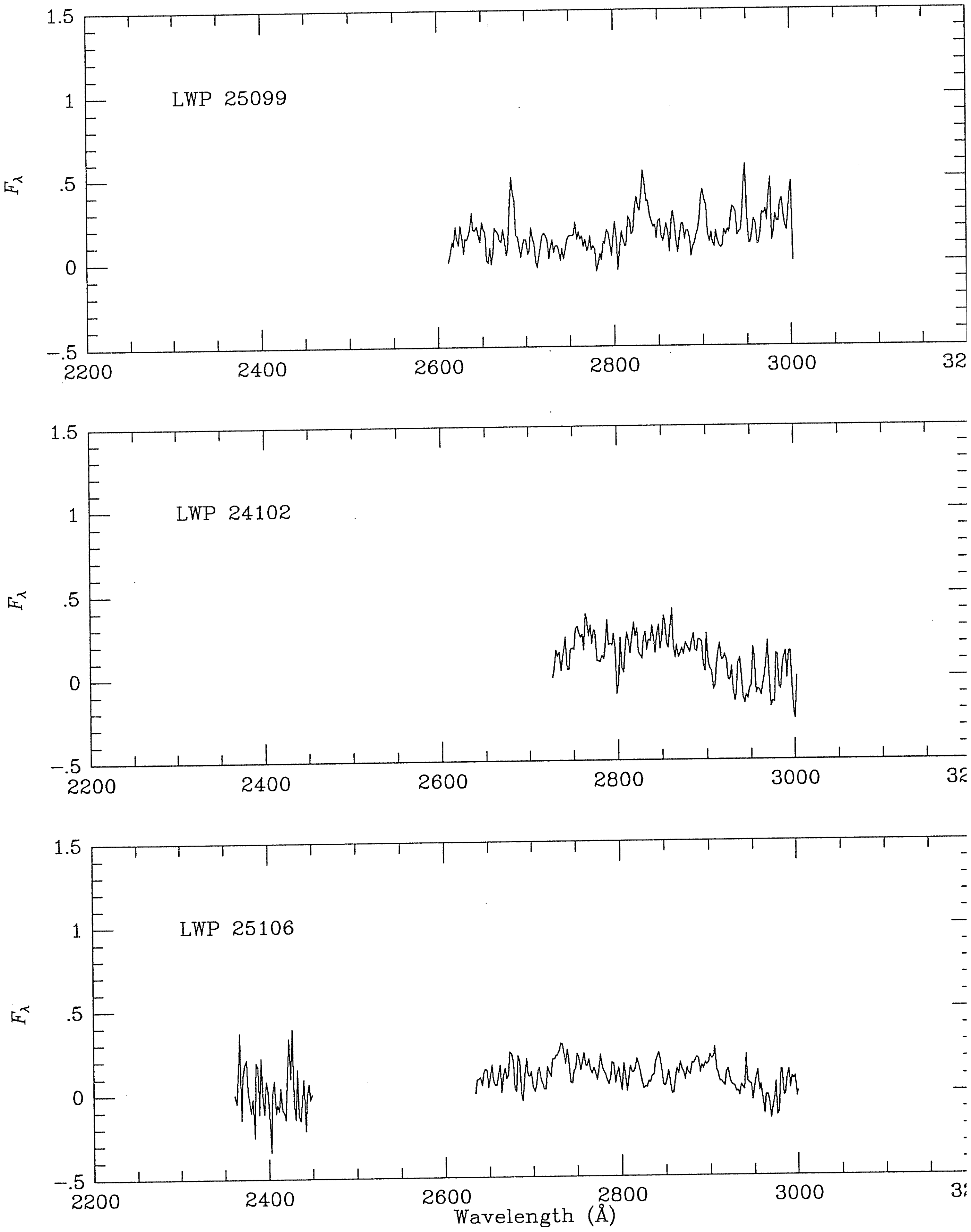
LWP 25099
LWP 24102
LWP 25106
F_λ
1.5
1
.5
0
−.5
2200
2400
2600
2800
3000
32
Wavelength (Å)

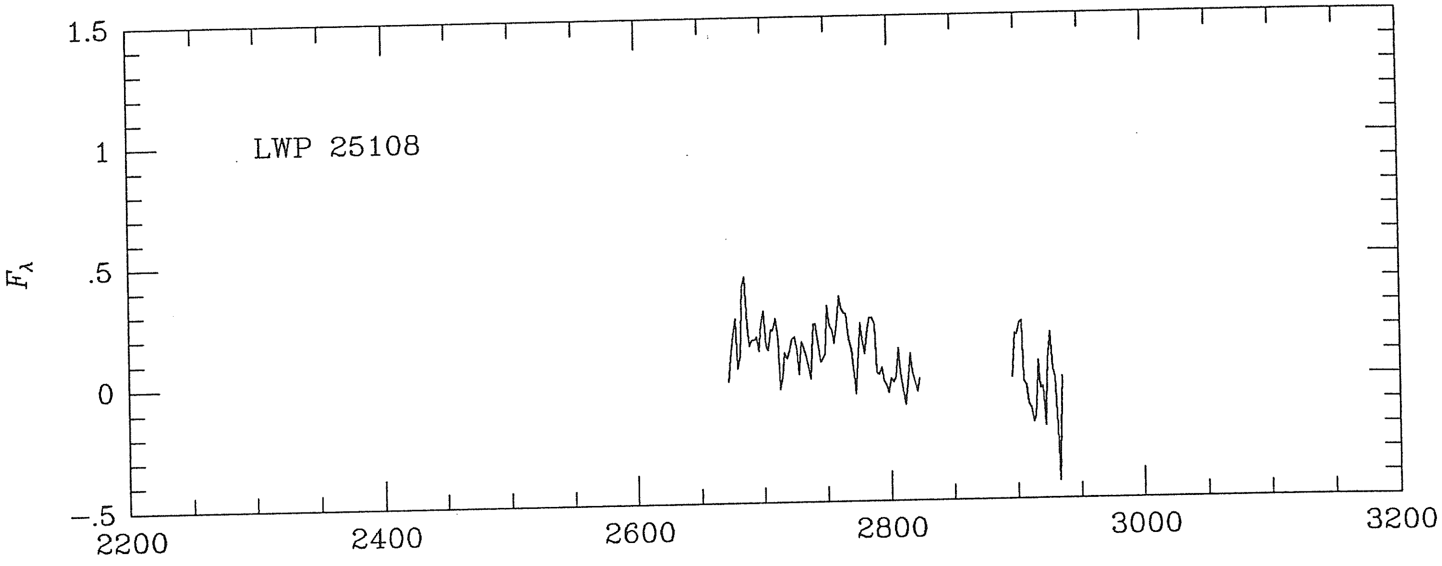
LWP 25108
F_λ
1.5
1
.5
0
−.5
2200
2400
2600
2800
3000
3200

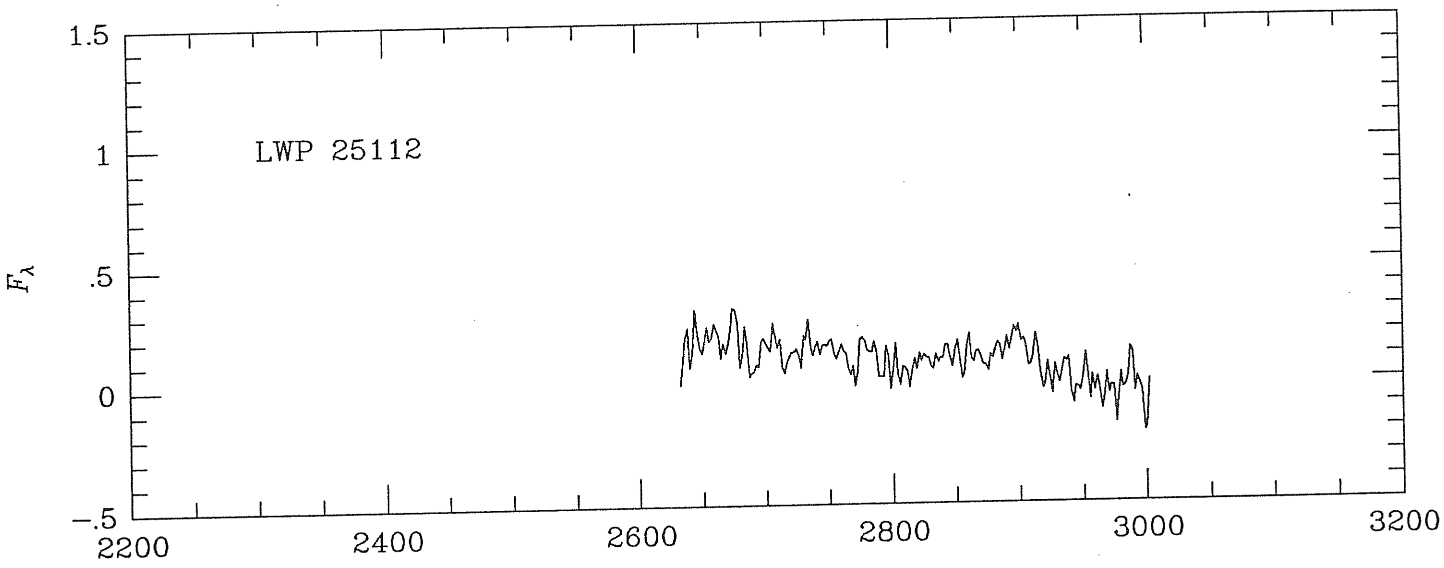
LWP 25112
F_λ
1.5
1
.5
0
−.5
2200
2400
2600
2800
3000
3200

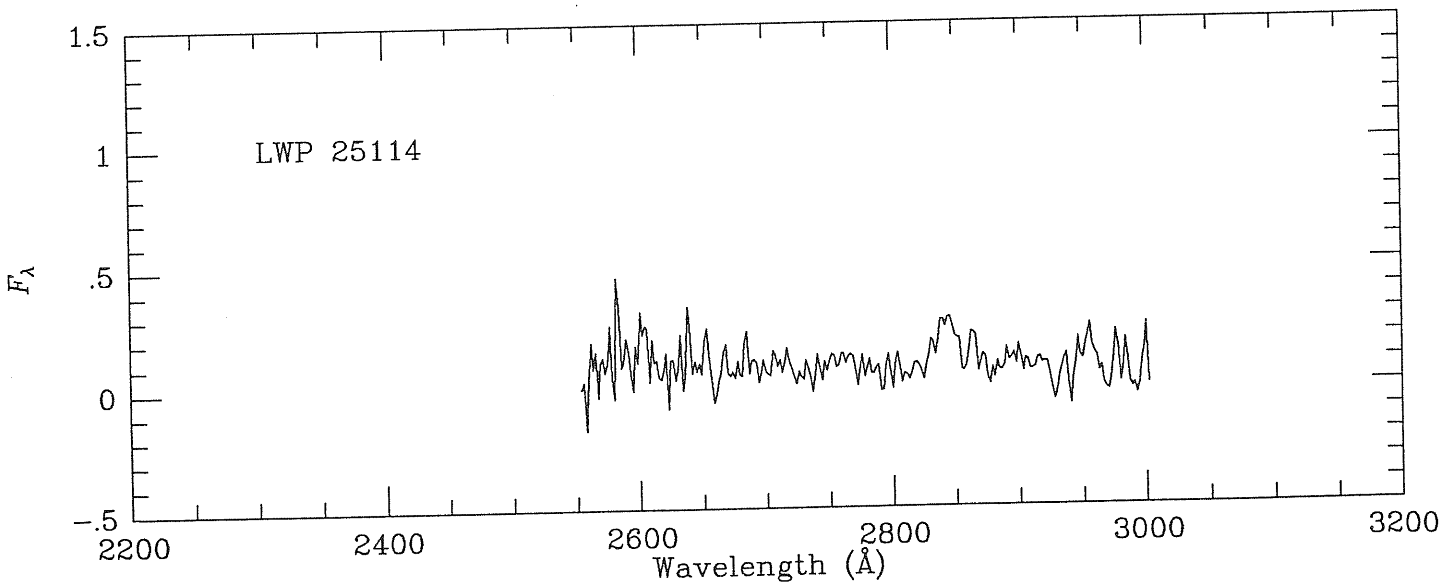
LWP 25114
F_λ
1.5
1
.5
0
−.5
2200
2400
2600
2800
3000
3200
Wavelength (Å)

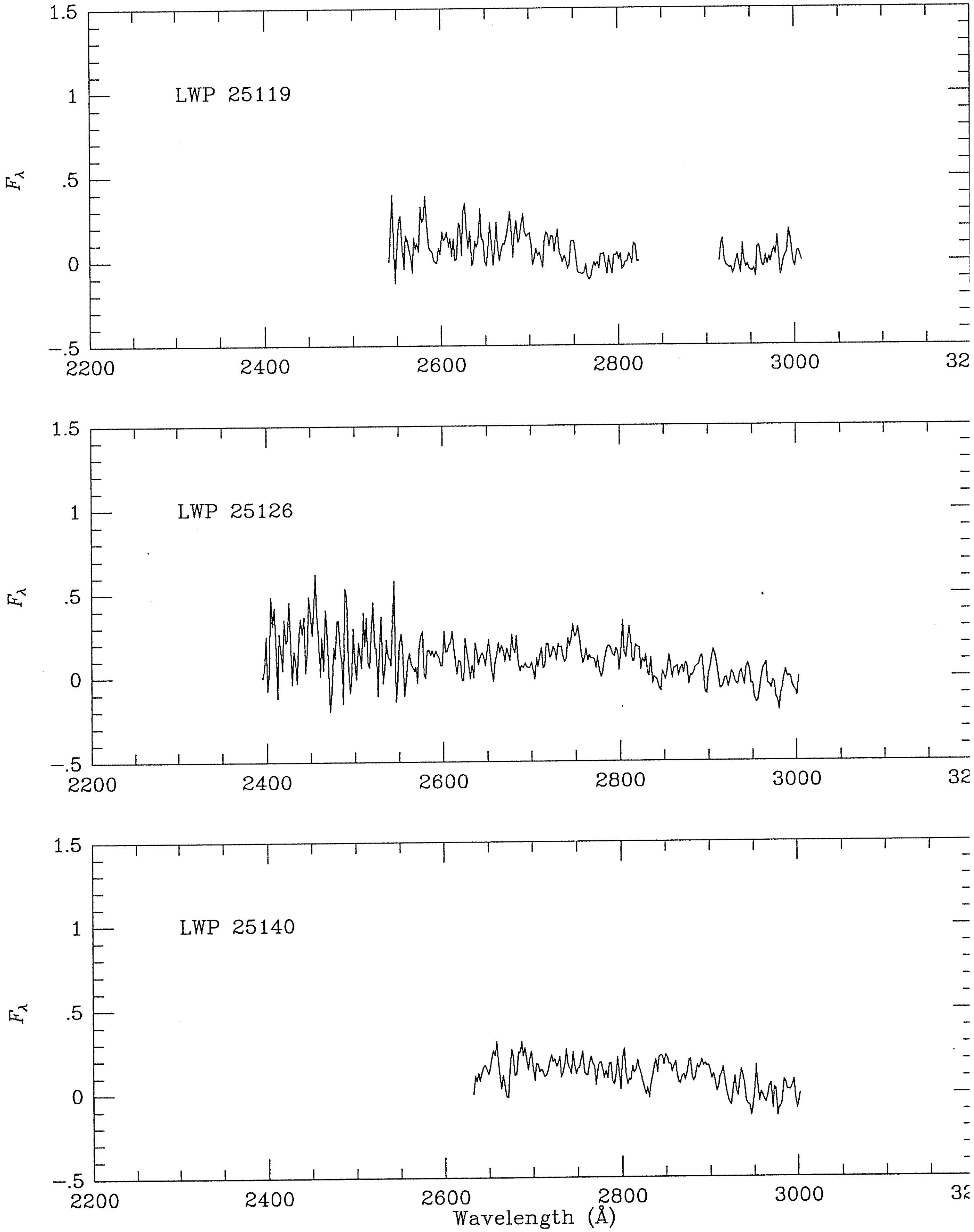
LWP 25119
LWP 25126
LWP 25140
F_λ
1.5
1
.5
0
−.5
2200
2400
2600
2800
3000
32
Wavelength (Å)

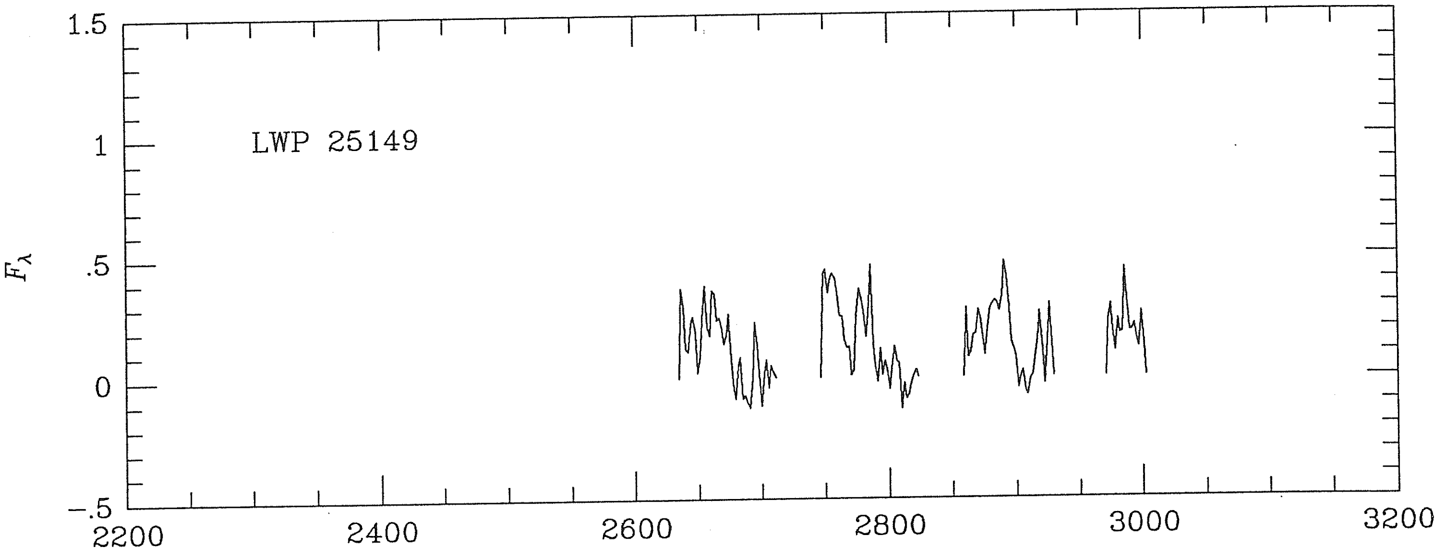
LWP 25149
F_λ
1.5
1
.5
0
−.5
2200
2400
2600
2800
3000
3200

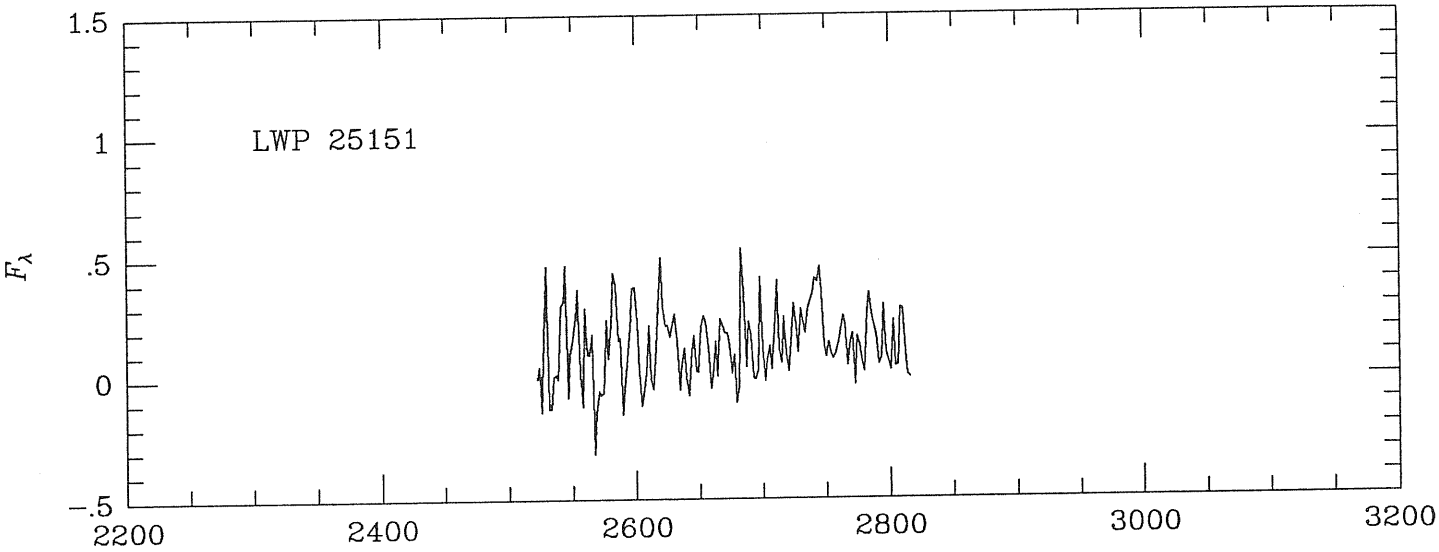
LWP 25151
F_λ
1.5
1
.5
0
−.5
2200
2400
2600
2800
3000
3200

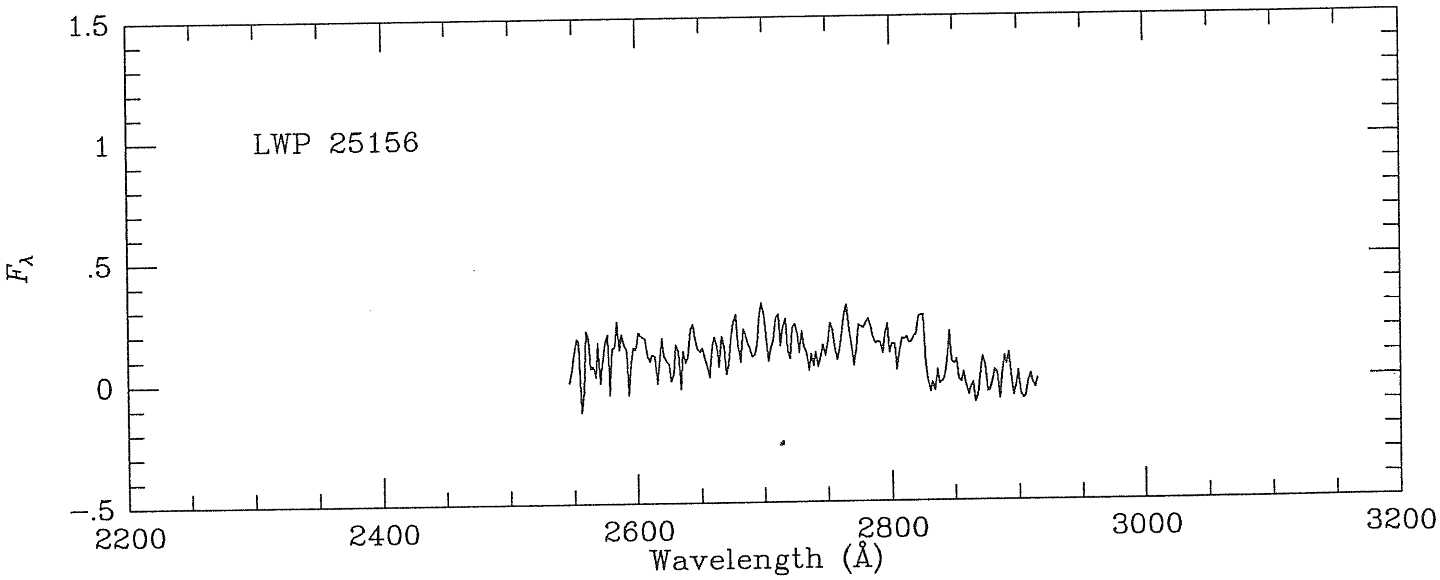
LWP 25156
F_λ
1.5
1
.5
0
−.5
2200
2400
2600
2800
3000
3200
Wavelength (Å)

Appendix C

IUE Spectra of 3C 279

In this Appendix are presented the GEX extracted spectra from the IUE observing campaign of 1992 December/1993 January on the OVV 3C 279 (see Section 2.3 for data analysis and discussion). Flux units are 10^{-14} erg^{-1} s^{-1} cm^{-2} Å^{-1}.

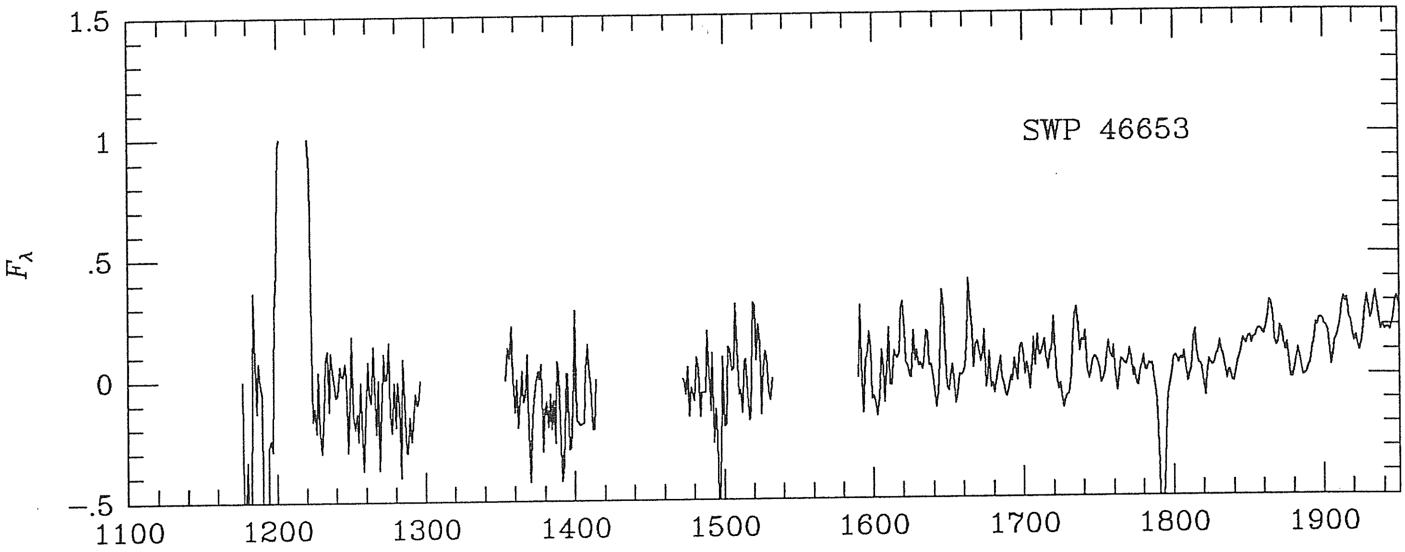
SWP 46653
F_λ
1.5
1
.5
0
−.5
1100
1200
1300
1400
1500
1600
1700
1800
1900

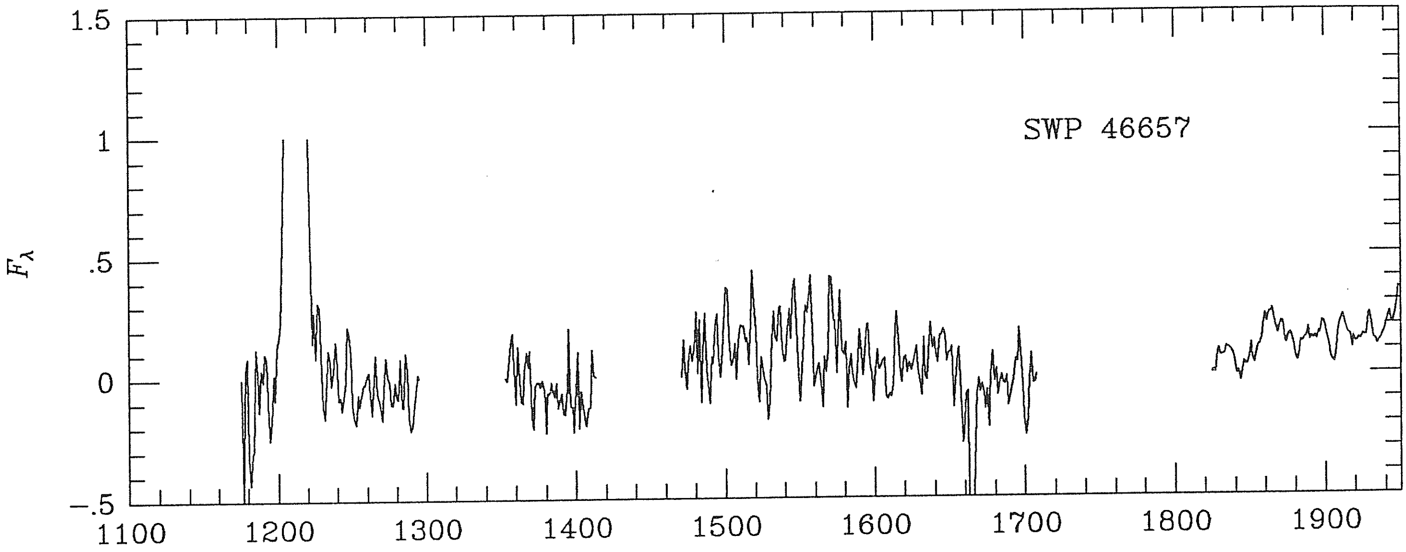
SWP 46657
F_λ
1.5
1
.5
0
−.5
1100
1200
1300
1400
1500
1600
1700
1800
1900

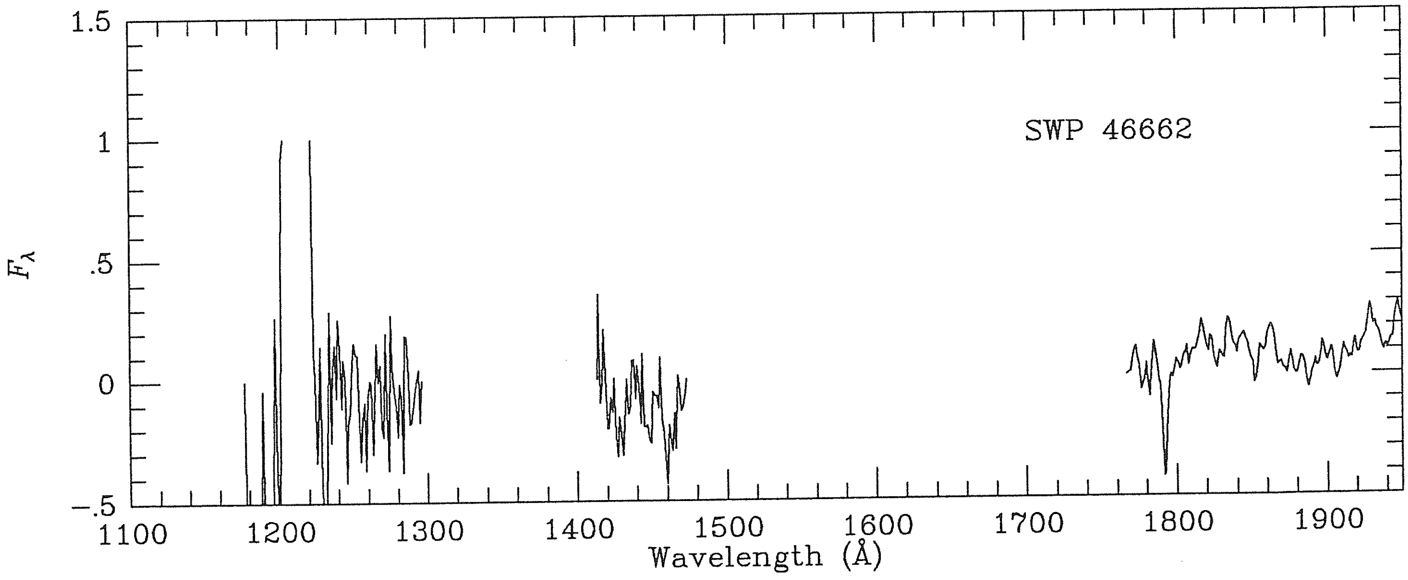
SWP 46662
F_λ
1.5
1
.5
0
−.5
1100
1200
1300
1400
1500
1600
1700
1800
1900
Wavelength (Å)

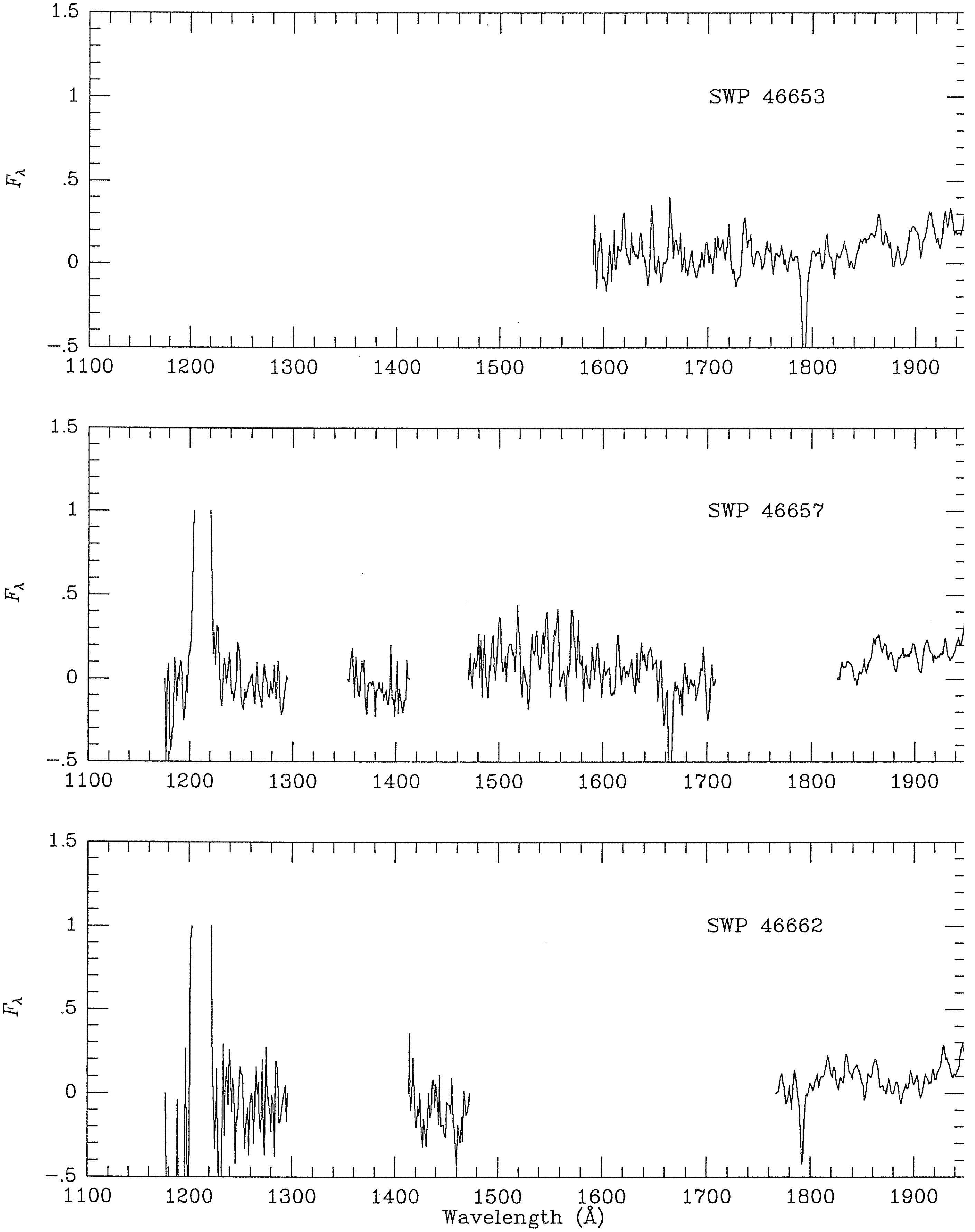
SWP 46653
SWP 46657
SWP 46662
F_λ
1.5
1
.5
0
−.5
1100
1200
1300
1400
1500
1600
1700
1800
1900
Wavelength (Å)

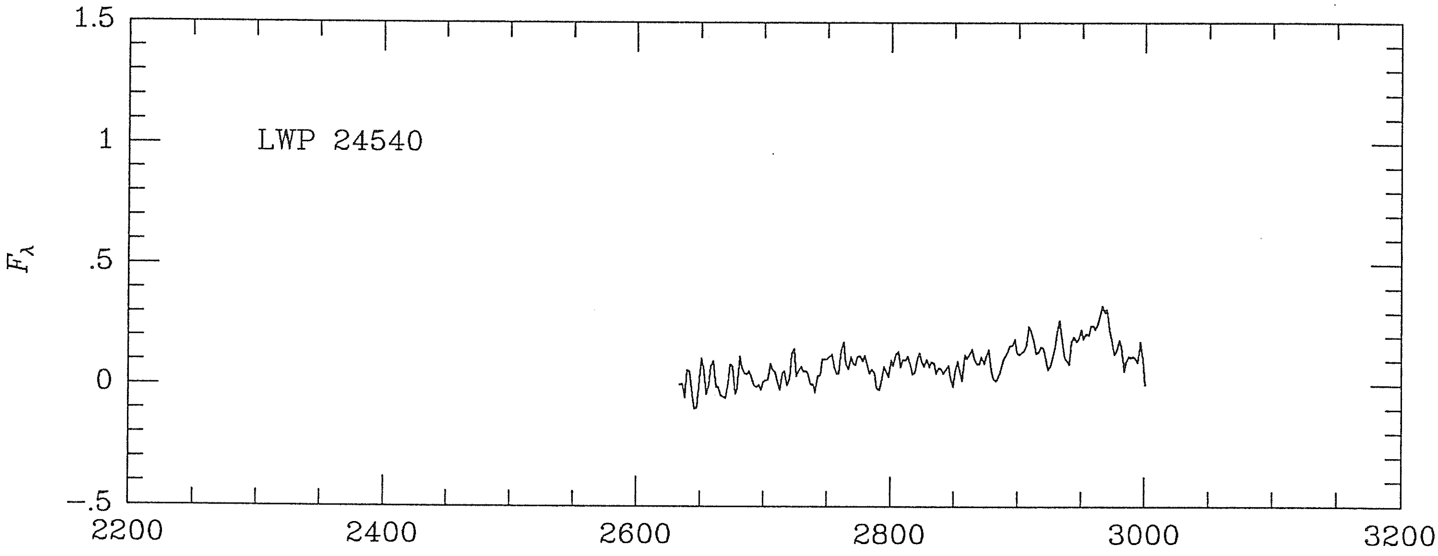
LWP 24540
F_λ
1.5
1
.5
0
−.5
2200
2400
2600
2800
3000
3200

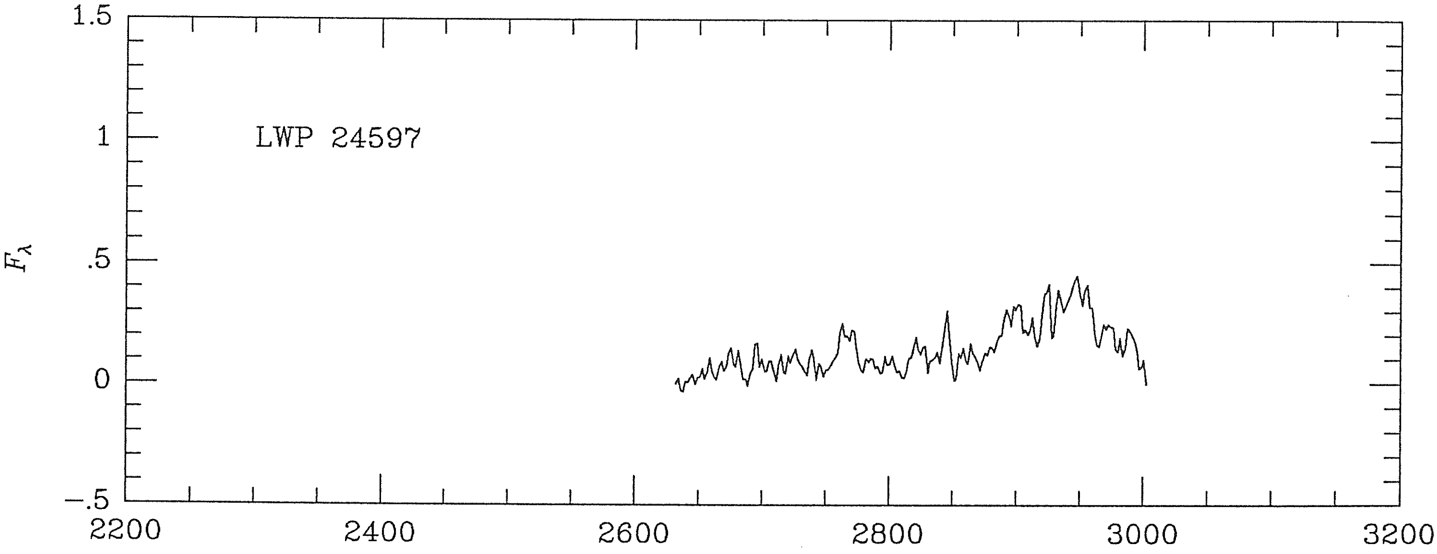
LWP 24597
F_λ
1.5
1
.5
0
−.5
2200
2400
2600
2800
3000
3200

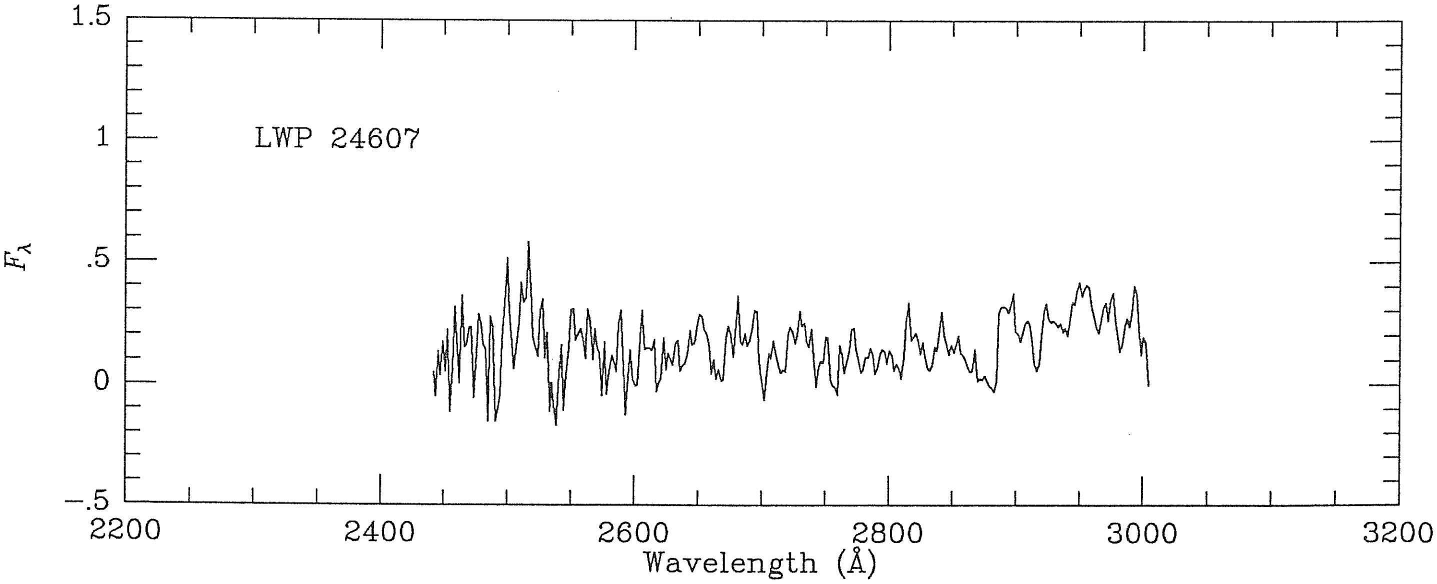
LWP 24607
F_λ
1.5
1
.5
0
−.5
2200
2400
2600
2800
3000
3200
Wavelength (Å)

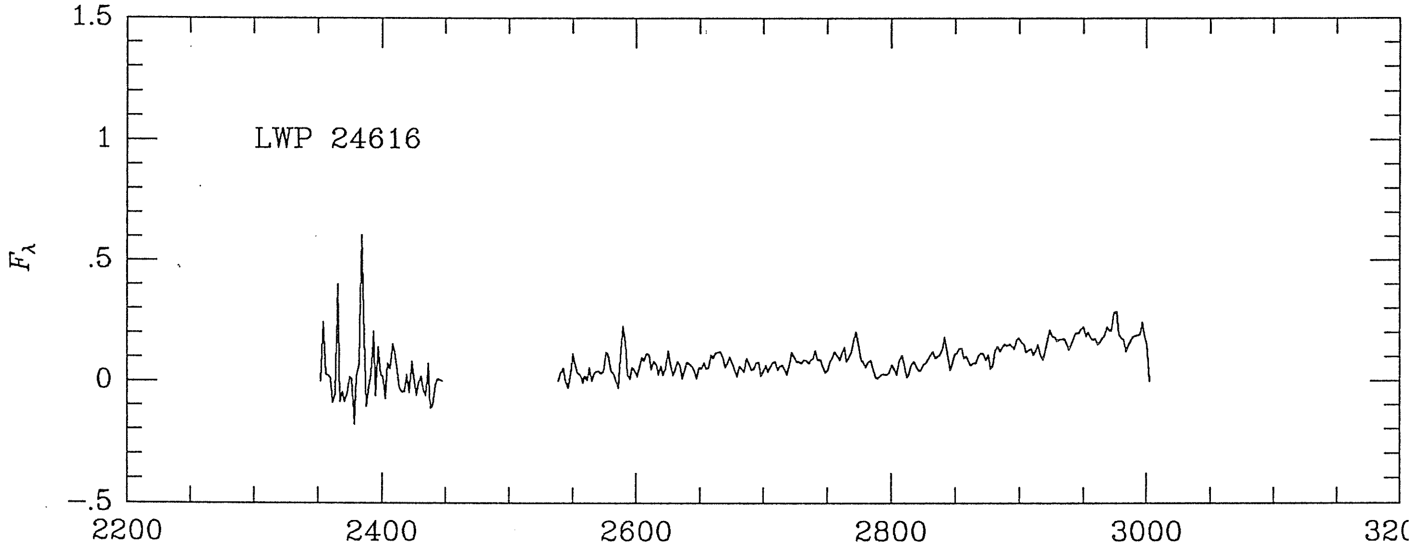
LWP 24616
F_λ
1.5
1
.5
0
−.5
2200
2400
2600
2800
3000
320

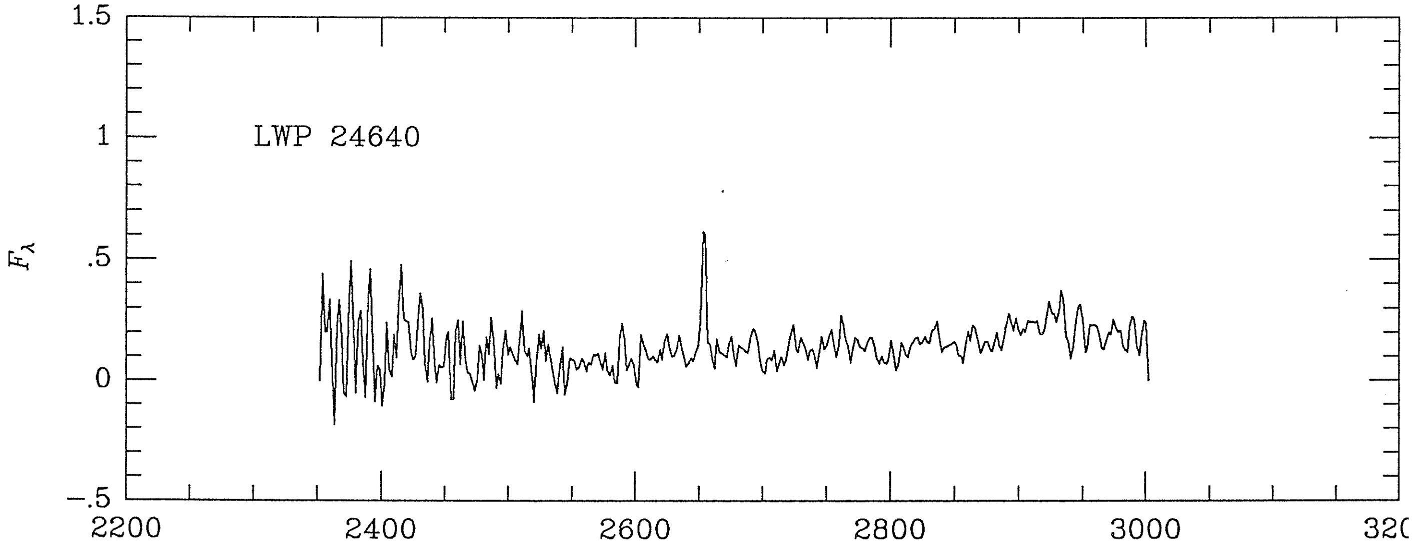
LWP 24640
F_λ
1.5
1
.5
0
−.5
2200
2400
2600
2800
3000
320

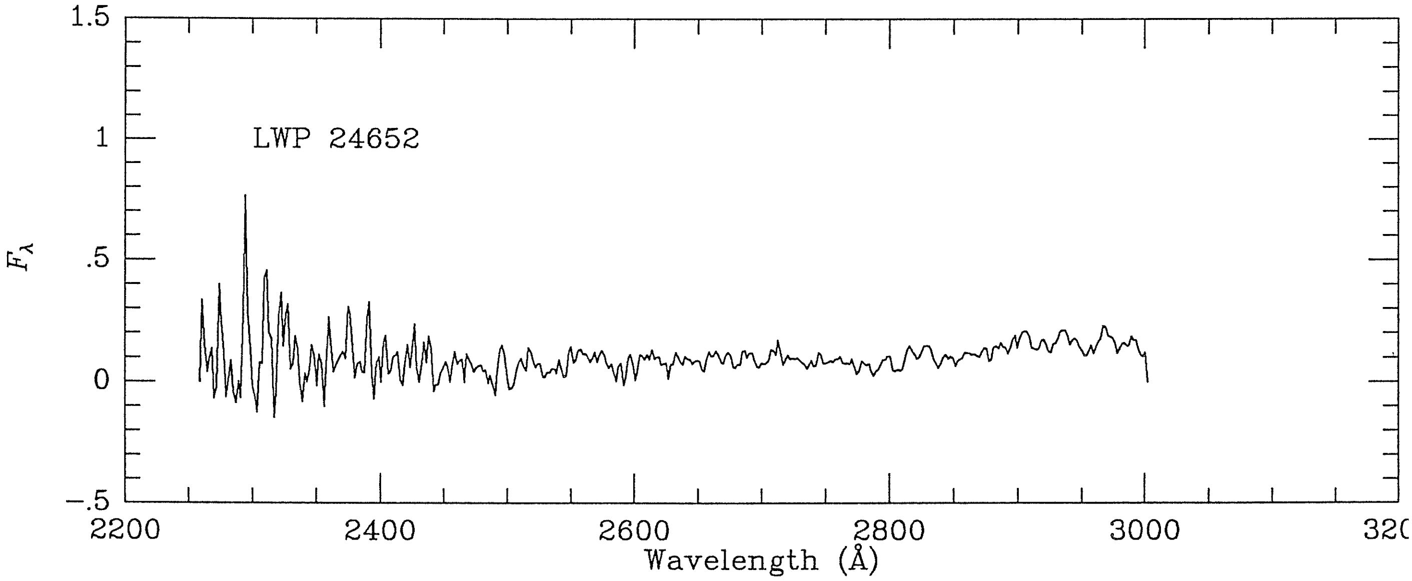
LWP 24652
F_λ
1.5
1
.5
0
−.5
2200
2400
2600
2800
3000
320
Wavelength (Å)

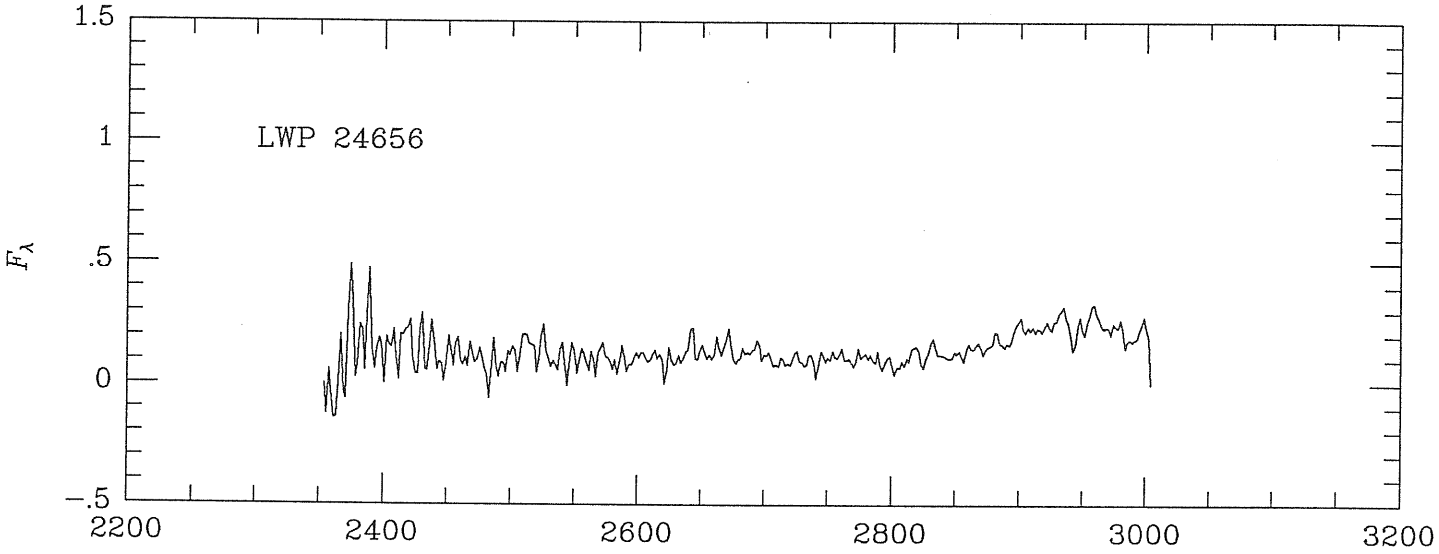
LWP 24656
F_λ
1.5
1
.5
0
−.5
2200
2400
2600
2800
3000
3200

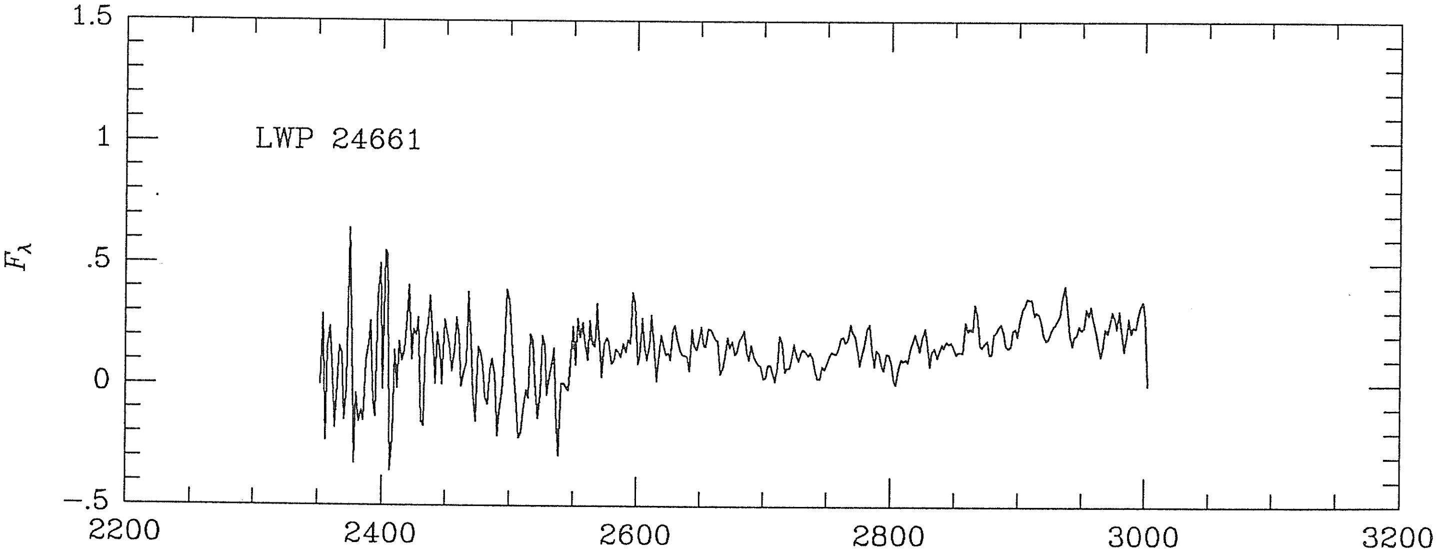
LWP 24661
F_λ
1.5
1
.5
0
−.5
2200
2400
2600
2800
3000
3200

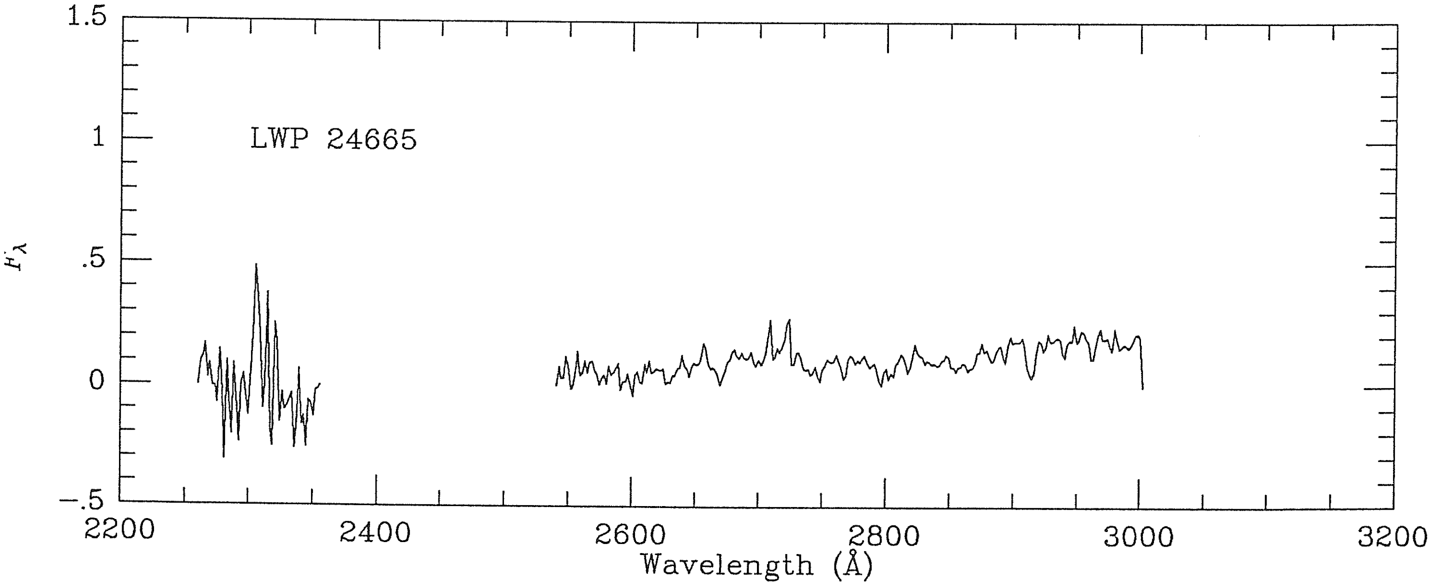
LWP 24665
F_λ
1.5
1
.5
0
−.5
2200
2400
2600
2800
3000
3200
Wavelength (Å)

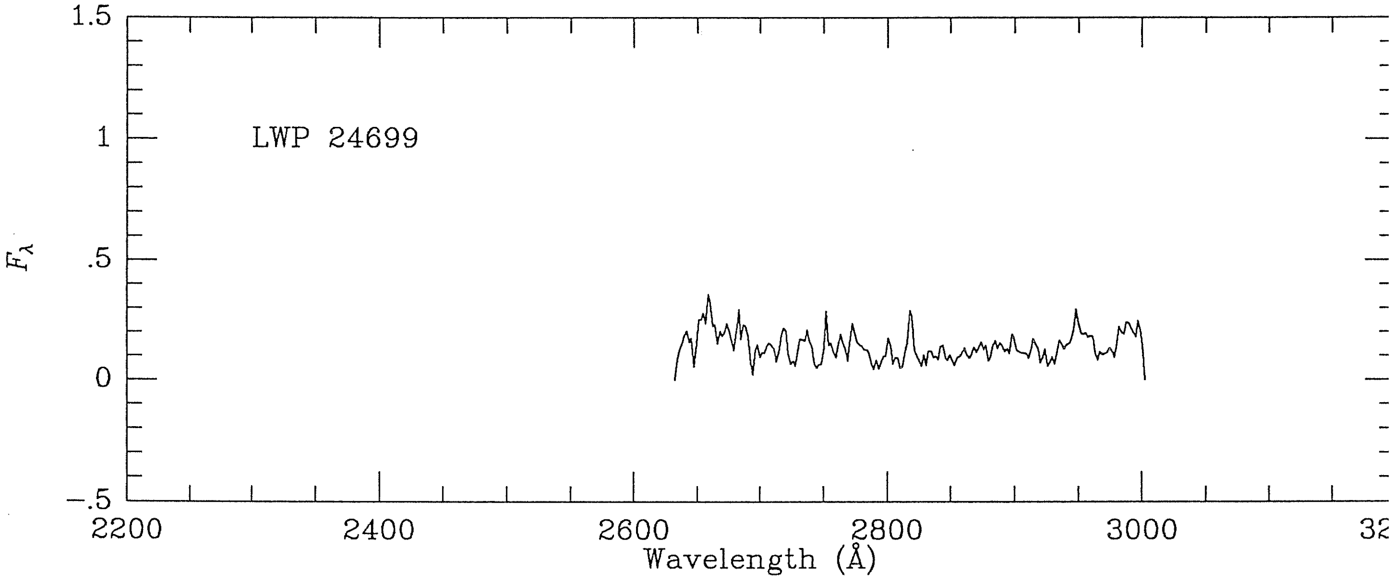
LWP 24699
1.5
1
.5
0
−.5
F_λ
2200
2400
2600
2800
3000
32
Wavelength (Å)

References

Allen, R. G., Smith, P. S., Angel, J. R. P., Miller, B. W., Anderson, S. F., & Margon, B. 1993, ApJ, 403, 610

Angel, J. R. P., & Stockman, H. S. 1980, ARA&A, 18, 321

Antonucci, R. R. J., & Ulvestad, J. S. 1985, ApJ, 294, 158

Arimoto, N., & Yoshii, Y. 1987, A&A, 173, 23

Baldwin, J. A., & Stone, R. P. S. 1984, MNRAS, 206, 241

Ballard, K. R., Mead, A. R. G., Brand, P. W. J. L., & Hough, J. H. 1990, MNRAS, 243, 640

Barylak, M., Wasatonic, R., & Imhoff, C. 1984, ESA IUE Newsletter, 20, 201

Bersanelli, M., Bouchet, P., & Falomo, R. 1991, A&A, 252, 854

Bersanelli, M., Bouchet, P., Falomo, R., & Tanzi, E. G. 1992, AJ, 104, 28

Bevington, P. R. 1969, Data Reduction and Error Analysis for the Physical Sciences, (New York: McGraw-Hill), p. 169

Blandford, R. D., & Rees, M. J. 1978, in Pittsburgh Conference on BL Lac Objects, ed. A. M. Wolfe, (U. of Pittsburgh), p. 328

Blandford, R. D. 1993, in 1st Compton Gamma-Ray Observatory Symposium, AIP Conference Proc. 280, ed. M. Friedlander, N. Gehrels, and D.J. Macomb (New York: American Institute of Physics), p. 533

Blecha, A., et al. 1994, in IAU Symp. 159, Multi-Wavelength Continuum Emission of AGN, ed. T. J.-L. Courvoisier and A. Blecha (Dordrecht: Kluwer), p. 319

Bloom, S. D., & Marscher, A. P., 1993, in Compton Gamma-Ray Observatory, AIP Conference Proc., 280, ed. M. Friedlander, N. Gehrels, and D.J. Macomb (New York: American Institute of Physics), p. 578

Boggess, F. A., et al. 1978, Nature, 275, 372

Bohlin, R. C., & Holm, A. V. 1980, NASA IUE Newsletter, 10, 37

Bohlin, R. C. 1988, NASA IUE Newsletter, 35, 141

Bohlin, R. C., & Grillmair, C. J. 1988, ApJS, 68, 487

Bohlin, R. C., Harris, A. W., Holm, A. V., & Gry, C. 1990, ApJS, 73, 413

Boller, T., Meurs, E. J. A., Brinkmann, W., Fink, H. H., Zimmermann, U., & Adorf, H.-M. 1992, A&A, 261, 57

Bolton, J. G., Shimmins, A. J., & Merkelijn, J. 1968, AuJP, 21, 81

Bonnell, J. T., Vestrand, W. T., & Stacy, J. G. 1994, ApJ, 420, 545

Bracewell, R. N. 1986, The Fourier Transform and its Applications, 2d ed. (McGraw-Hill: New York)

Bregman, J. N., Maraschi, L., & Urry, M. C. 1987, in Scientific Accomplishments of IUE, ed. Y. Kondo (Dordrecht: Reidel), p. 685

Bregman, J. N. 1990, Astron. Astrophys. Rev., 2, 125

Bregman, J. N. 1994, in IAU Symp. 159, Multi-Wavelength Continuum Emission of AGN, ed. T. J.-L. Courvoisier and A. Blecha (Dordrecht: Kluwer), p. 5

Brinkmann, W., et al. 1994, A&A, in press

Brown, L. M. J., et al. 1989, ApJ, 340, 129

Browne, I. W. A. 1989, in BL Lac Objects, ed. L. Maraschi, T. Maccacaro and M.-H. Ulrich, Lecture Notes in Physics, 334 (Springer Verlag: Berlin), p. 401

Bruhweiler, F. C., Boggess, A., Norman, D. J., Grady, C. A., Urry, C. M., & Kondo, Y. 1993, ApJ, 409, 199

Brunner, H., Lamer, G., Worrall, D. M., & Staubert, R. 1994, A&A, in press

Camenzind, M., & Krockenberger, M. 1992, A&A, 255, 59

Canizares, C. R., & Kruper, J. S. 1984, ApJ, 278, L99

Cardelli, J. A., Clayton, G. C., & Mathis, J. S. 1989, ApJ, 345, 245

Carini, M. T., & Miller, H. R. 1992, ApJ, 385, 482

Carini, M. T., Miller, H. R., Noble, J.C., & Goodrich, B.D. 1992, AJ, 104, 15

Carrasco, L., Dultzin-Hacyan, D., & Cruz-Gonzalez, I. 1985, Nature, 314, 146

Cassatella, A., Lloyd, C., & Gonzalez-Riestra, R. 1988, ESA IUE Newsletter, 31, 13

Cayatte, V., & Sol, H. 1987, A&A, 171, 25

Celotti, A., Maraschi, L. & Treves, A. 1991, ApJ, 337, 403

Celotti, A., Maraschi, L., Ghisellini, G., Caccianiga, A., & Maccacaro, T. 1993, ApJ, 416, 118

Chiappetti, L. 1992, Changes in IUE Data Reduction, IFCTR IUE Reduction Software Note (Milano)

Cimatti, A., di Serego Alighieri, A., Fosbury, R. A. E., Salvati, M., & Taylor, D. 1993, MNRAS, 264, 421

Clavel, J., et al. 1991, ApJ, 366, 64

Clavel, J. 1994, in IAU Symp. 159, Multi-Wavelength Continuum Emission of AGN, ed. T. J.-L. Courvoisier and A. Blecha (Dordrecht: Kluwer), p. 131

Cohen, M. & Unwin, S. 1981, in IAU Symp. 97, Extragalactic Radio Sources, ed. D. Heeschen & C. Wade (Reidel: Dordrecht), p. 345

Condon, J.J., Hicks, P.D., & Jauncey, D.L. 1977, AJ, 82, 692

Courvoisier, T. J.-L., & Paltani, S. 1992, IUE-ULDA Access Guide No. 4, ESA SP 1153 A & B

Courvoisier, T. J.-L., et al. 1994, submitted

Crenshaw, M. D., Bruegman, O. W., & Norman, D. J. 1990, PASP, 102, 463

Cruz-Gonzalez, I., & Huchra, J. P. 1984, AJ, 89, 441

Cutri, R. M., Wisniewski, W. Z., Rieke, G. H., & Lebofsky, M. J. 1985, ApJ, 296, 423

Danziger, I. J., Fosbury, R. A. E., Goss, W. M., & Ekers, R. D. 1979, MNRAS, 188, 415

Danziger, I. J., Bergeron, J., Fosbury, R. A. E., Maraschi, L., Tanzi, E. G., & Treves, A. 1983, MNRAS, 203, 565

Daves, S., et al. 1990, MNRAS, 244, 93

De Jager, O. C., Stecker, F. W., & Salamon, M. H. 1994, Nature, 369, 294

Dermer, C. D., Schlickeiser, R., & Mastichiadis, A. 1992, A&A, 256, L27

Dermer, C. D., & Schlickeiser, R. 1993, ApJ, 416, 458

Dondi, L., & Ghisellini, G. 1994, in preparation

Done, C., et al. 1992, ApJ, 400, 138

Doxsey, R. E., McClintock, J. E., Petro, L., Remillard, R., & Schwartz, D. A. 1981, BAAS, 13, 558

Doxsey, R. E., et al. 1983, ApJ, 264, L43

Edelson, R. A., & Malkan, M. A. 1987, ApJ, 323, 516

Edelson, R. A., & Krolik, J. H. 1988, ApJ, 333, 646

Edelson, R. A., Krolik, J. H., & Pike, G. 1990, ApJ, 359, 86

Edelson, R. A., et al. 1991, ApJ, 372, L9

Edelson, R. A., Pike, G. F., Saken, J. M., Kinney, A., & Shull, J. M. 1992, ApJS, 83, 1 (E92)

Edelson, R. A. 1992, ApJ, 401, 516

Edelson, R. A. 1994, in IAU Symp. 159, Multi-Wavelength Continuum Emission of AGN, ed. T. J.-L. Courvoisier and A. Blecha (Dordrecht: Kluwer), p. 113

Edelson, R. A., et al. 1994a, ApJ, in press

Edelson, R. A., et al. 1994b, in preparation

Eggen, O. J. 1970, ApJ, 159, L95

Elvis, M., Lockman, F. J., & Wilkes, B. J. 1989, AJ, 97, 777

Elvis, M., Plummer, D., Schachter, J., & Fabbiano, G. 1992, ApJS, 80, 257

Fabian, A. C. 1979, Proc. Roy. Soc., 366, 449

Falomo, R., Maraschi, L., Tanzi, E. G., & Treves, A. 1987, ApJ, 318, L39

Falomo, R., Bouchet, P., Maraschi, L., Tanzi, E. G., & Treves, A. 1988, ApJ, 335, 122

Falomo, R., Bouchet, P., Maraschi, L., Tanzi, E. G., & Treves, A. 1989, ApJ, 345, 148

Falomo, R., & Treves, A. 1990, PASP, 102, 1120

Falomo, R., & Tanzi, E. G. 1991, AJ, 102, 1294

Falomo, R. 1991, AJ, 102, 1991

Falomo, R., Giraud, E., Maraschi, L., Melnick, J., Tanzi, E. G., & Treves, A. 1991, ApJ, 380, L67

Falomo, R., Treves, A., Chiappetti, L., Maraschi, L., Pian, E., & Tanzi, E. G. 1993a, ApJ, 402, 532

Falomo, R., Pesce, J. E., & Treves, A. 1993b, ApJ, 411, L63

Falomo, R., Pesce, J. E., & Treves, A. 1993c, AJ, 105, 2031

Falomo, R., Bersanelli, M., Bouchet, P., & Tanzi, E. G. 1993d, AJ, 106, 11

Falomo, R., Pian, E., Scarpa, R., & Treves, A. 1994a, in IAU Symp. 159, Multi-Wavelength Continuum Emission of AGN, ed. T. J.-L. Courvoisier and A. Blecha (Dordrecht: Kluwer), p. 17

Falomo, R., Scarpa, R., & Bersanelli, M. 1994b, ApJS, 93, in press

Falomo, R., Pesce, J. E., & Treves, A. 1994c, ApJL, submitted

Falomo, R. 1994, in preparation

Feigelson, E. D., et al. 1986, ApJ, 302, 337

Fichtel, C. E., et al. 1994, ApJS, in press

Filippenko, A. V., Djorgovski, S., Spinrad, H., & Sargent, W. L. W. 1986, AJ, 91, 49

Gabuzda, D. C., Cawthorne, T. V., Roberts, D.H ., & Wardle, J. F. C. 1992, ApJ, 388, 40

Gabuzda, D. C., & Sitko, M. L. 1994, AJ, 107, 884

Garilli, B., & Maccagni, D. 1990, A&A, 229, 88

Gear, W. K., et al. 1994, MNRAS, 267, 167

George, I. M. 1988, Ph.D. thesis, University of Leicester

George, I. M., Warwick, R. S., & Bromage, G. E. 1988, MNRAS, 232, 793

Ghisellini, G., Maraschi, L., & Treves, A. 1985, A&A, 146, 204 (GMT)

Ghisellini, G., Maraschi, L., Tanzi, E. G., & Treves, A. 1986, ApJ, 310, 317 (GMTT)

Ghisellini, G., & Maraschi, L. 1989, ApJ, 340, 181

Ghisellini, G., Padovani, P., Celotti, A., & Maraschi, L. 1993, ApJ, 407, 65

Giommi, P., et al. 1990, ApJ, 356, 432

Giommi, P., Ansari, S. G., & Micol, A. 1994, in IAU Symp. 159, Multi-Wavelength Continuum Emission of AGN, ed. T. J.-L. Courvoisier and A. Blecha (Dordrecht: Kluwer), p. 506

Grandi, P., et al. 1994, in preparation

Green, R. F., Schmidt, M., & Liebert, J. 1986, ApJS, 61, 305

Griffiths, R. E., Tapia, S., Briel, U., & Chaisson, L. 1979, ApJ, 234, 810

Halpern, J. P., Chen, V. S., Madejski, G. M., & Chanan, G. A. 1991, AJ, 101, 818

Hartman, R. C., et al. 1993, in Proc. 2nd Compton Symp., Maryland, in press

Hermsen, W., et al. 1993, A&AS, 97, 97

Hewitt, A., & Burbidge, G. 1987, ApJS, 63, 1

Hewitt, A., & Burbidge, G. 1989, ApJS, 69, 1

Holm, A. V., & Crabb, W. G. 1979, NASA IUE Newsletter, 7, 40

Horne, K., Welsh, W., & Peterson, B. 1991, ApJ, 367, L5

Hufnagel, B., & Bregman, J. 1992, ApJ, 386, 473

Hutter, D. J., & Mufson, S. L. 1986, ApJ, 301, 50

Impey, C. D., & Neugebauer, G. 1988, AJ, 95, 307

Impey, C. D., & Tapia, S. 1988, ApJ, 333, 666

Impey, C. D., & Tapia, S. 1990, ApJ, 354, 124

Impey, C. D., Lawrence, C. R., & Tapia, S. 1991, ApJ, 375, 46

Jannuzi, B. T. 1994, in IAU Symp. 159, Multi-Wavelength Continuum Emission of AGN, ed. T. J.-L. Courvoisier and A. Blecha (Dordrecht: Kluwer), p. 470

Keel, W. C., 1986, ApJ, 302, 296

Kidger, M. R. 1988, PASP, 100, 1248

Kidger, M., Takalo, L. O., Sillanpää, A. 1992, A&A, 264, 32

Kinman, T. D. 1976, ApJ, 205, 1

Kinney, A. L., Bohlin, R. C., Blades, J. C., & York, D. G. 1991a, ApJS, 75, 645

Kinney, A. L., Bohlin, R. C., & Neill, J. D. 1991b, PASP, 694, 103

Knapp, G. R., & Patten, B. M. 1991, AJ, 101, 1609

Kniffen, D. A., et al. 1993, ApJ, 411, 133

Kollgaard, R. I. 1994, Vistas in Astronomy, in press

Königl, A. 1981, ApJ, 243, 700

Königl, A. 1989, in BL Lac Objects, ed. L. Maraschi, T. Maccacaro and M.-H. Ulrich, Lecture Notes in Physics, 334 (Springer Verlag: Berlin), p. 321

Krichbaum, T. P., Standke, K. J., Graham, D. A., Witzel, A., Schalinski, C. J., & Zensus, J. A. 1994, in IAU Symp. 159, Multi-Wavelength Continuum Emission of AGN, ed. T. J.-L. Courvoisier and A. Blecha (Dordrecht: Kluwer), p. 187

Krolik, J. H., et al. 1991, ApJ, 371, 541

Kurfess, J. D. 1994, in IAU Symp. 159, Multi-Wavelength Continuum Emission of AGN, ed. T. J.-L. Courvoisier and A. Blecha (Dordrecht: Kluwer), p. 39

Landau, R., et al. 1986, ApJ, 308, 78

Lanzetta, K. M., Turnshek, D. A., & Sandoval, J. 1993, ApJS, 84, 109

Ledden, J. E., & O'Dell, S. L. 1985, ApJ, 298, 630

Lind, K. R., & Blandford, R. D. 1985, ApJ, 295, 358

Macchetto, F., et al. 1991, ApJ, 369, L55

Madau, P., Ghisellini, G., & Persic, M. 1987, MNRAS, 224, 257

Madejski, G. M., & Schwartz, D. A. 1983, ApJ, 275, 467

Madejski, G. M.1985, Ph.D. Thesis, Harvard University

Madejski, G. M., & Schwartz, D. A. 1988, ApJ, 330, 776

Madejski, G. M., et al. 1994, in IAU Symp. 159, Multi-Wavelength Continuum Emission of AGN, ed. T. J.-L. Courvoisier and A. Blecha (Dordrecht: Kluwer), p. 127

Makino, K., et al. 1992, in The International Symposium on Neutrino Astrophysics, Takayama, Kamioka, Japan, October 19–22

Malina, R. F., & Bowyer, C. S. 1992, EUVE Newsletter, Vol. 2, No. 6

Malkan, M. A., & Sargent, W. L. W. 1982, ApJ, 254, 22

Maraschi, L., Tagliaferri, G., Tanzi, E. G., & Treves, A. 1986a, ApJ, 304, 637

Maraschi, L., Ghisellini, G., Tanzi, E. G., & Treves, A. 1986b, ApJ, 310, 325

Maraschi, L., Blades, J. C., Calanchi, C., Tanzi, E. G., & Treves, A. 1988, ApJ, 333, 660

Maraschi, L. 1992, in Variability of Blazars, ed. E. Valtaoja & M. Valtonen (Cambridge Univ. Press), p. 447

Maraschi, L., Ghisellini, G., & Celotti, A. 1992, ApJ, 397, L5

Maraschi, L., Ghisellini, G., & Boccasile, A. 1993, Proc. Physics of AGNs, Cambrige, in press

Maraschi, L., Ghisellini, G., & Celotti, A. 1994a, in IAU Symp. 159, Multi-Wavelength Continuum Emission of AGN, ed. T. J.-L. Courvoisier and A. Blecha (Dordrecht: Kluwer), p. 221 (MCG)

Maraschi, L., et al. 1994b, ApJL, in press

Maraschi, L., Ciapi, A., Fossati, G., Tagliaferri, G., & Treves, A. 1994c, ApJ, submitted

Maraschi, L., Fossati, G., Tagliaferri, G., & Treves, A. 1994d, submitted

Marscher, A. P., Marshall, F. E., Mushotzky, R. F., Dent, W. A., Balonek, T. J., & Hartman, R. F. 1979, ApJ, 233, 498

Marscher, A. P. 1980, ApJ, 235, 386

Marscher, A. P., & Gear, W. K. 1985, ApJ, 298, 114

Marscher, A. P., Gear, W. K., & Travis, J. P. 1992, in Variability of Blazars, ed. E. Valtaoja & M. Valtonen (Cambridge Univ. Press), p. 85

Marscher, A. P., & Bloom, S. D. 1994, in Compton Gamma-Ray Observatory, AIP Conference Proc., ed. C.E. Fichtel, N. Gehrels and J.P. Norris (New York: American Institute of Physics)

Massaro, E., Nesci, R., Perola, G. C., Lorenzetti, D., & Spinoglio, L. 1994, in IAU Symp. 159, Multi-Wavelength Continuum Emission of AGN, ed. T. J.-L. Courvoisier and A. Blecha (Dordrecht: Kluwer), p. 400

Miller, H. R., Carini, M. T., Gaston, B. J., & Hutter, D. J. 1988, in A Decade of UV Astronomy with the IUE satellite, Proc. of Celebratory Symp. held at GSFC, Greenbelt, Maryland, ESA SP-281, p. 303

Moles, M., Garcia-Pelayo, J., & Masegosa, J. 1984, MNRAS, 211, 621

Moore, R. L., & Stockman, H. S. 1981, ApJ, 243, 60

Moore, R. L., & Stockman, H. S. 1984, ApJ, 279, 465

Morini, M., et al. 1986, ApJ, 306, L71

Mufson, S. L., Hutter, D. J., Kondo, Y., Urry, C. M., & Wisniewski, W. Z. 1990, ApJ, 354, 116

Netzer, H., et al. 1994, ApJ, submitted

Ohashi, T. 1989, in BL Lac Objects, ed. L. Maraschi, T. Maccacaro and M.-H. Ulrich, Lecture Notes in Physics, 334 (Springer Verlag: Berlin), p. 296

Ostriker, J. P., & Vietri, M. 1985, Nature, 318, 446

Ostriker, J. P., & Vietri, M. 1990, Nature, 344, 45

Owen, F. N., Helfand, D. J., & Spangler, S. R. 1981, ApJ, 250, L55

Padovani, P., & Urry, C. M. 1990, ApJ, 356, 75

Paltani, S., & Courvoisier, T. J.-L. 1994, A&A, in press

Perez, M., & Loomis, C. 1991, Record of the Meeting of the International Ultraviolet Explorer User's Committee, (CSC/TM–91/6142), p. I-3

Pian, E. 1992, Magister Philosophiae Thesis, International School for Advanced Studies (Trieste)

Pian, E., & Treves, A. 1993, ApJ, 416, 130

Pian, E., Falomo, R., Scarpa, R. & Treves, A. 1994a, ApJ, in press

Pian, E., et al. 1994b, Advances in Space Research, submitted

Pian, E., Falomo, R., Ghisellini, G., Maraschi, L., Sambruna, R. M., Scarpa, R., & Treves, A. 1994c, ApJ, submitted

Pica, A. J., Pollock, J. T., Smith, A. G., Leacock, R. J., Edwards, P. L., & Scott, R. L. 1980, AJ, 85, 1442

Pica, A. J., & Smith, A. G. 1983, ApJ, 272, 11

Pica, A. J., Smith, A. G., Webb, J. R., Leacock, R. J., Clements, S., & Gombola, P. P. 1988, AJ, 96, 1215

Piccinotti, G., Mushotzky, R. F., Boldt, E. A., Holt, S. S., Marshall, F. E., Serlemitsos, P. J., & Shafer, R. A. 1982, AJ, 253, 485

Pounds, K. A., et al. 1993, MNRAS, 260, 77

Press, W., Rybicki, G., & Hewitt, J. 1992, ApJ, 385, 404

Preston, R. A., et al. 1989, AJ, 98, 1

Punch, M., et al. 1992, Nature, 358, 477

Quirrenbach, A., Witzel, A., Krichbaum, T. P., Hummel, A., Alberdi, A., & Schalinski, C. 1989, Nature, 337, 442

Quirrenbach, A., et al. 1991, ApJ, 372, L71

Rees, M. J. 1990, ARA&A, 22, 471

Rieke, G. H., & Lebofsky, M. 1985, ApJ, 288, 618

Rodriguez Pascual, P., & Fernley, J. 1993, ESA IUE Newsletter, 43, 15

Sambruna, R. M., Barr, P., Giommi, P., Maraschi, L., Tagliaferri, G., & Treves, A. 1994, ApJ, in press

Sanders, D. B., Phinney, E. S., Neugebauer, G., Soifer, B. T., & Matthews, K. 1989, ApJ, 347, 29

Savage, A., Bolton, J. G., Wright, A. E. 1977, MNRAS, 179, 135

Scarpa, R., Falomo, R., & Pian, E. 1994, A&A, submitted

Schmidt, M., & Green, R. F. 1983, ApJ, 269, 352

Schneider, P., & Weiss, A. 1987, A&A, 171, 49

Schneider, P., & Kirk, J. G. 1989, A&A, 217, 344

Schrader, C. R., et al. 1994, AJ, 107, 904

Schwartz, D. A., Doxsey, R. E., Griffiths, R. E., Johnston, M. D., & Schwarz, J. 1979, ApJ, 229, L53

Seaton, M. J. 1979, MNRAS, 187, 73p

Sembay, S., Warwick, R. S., Urry, C. M., Sokoloski, J., George, I. M., Makino, F., & Ohashi, T. 1993, ApJ, 404, 112

Shen, B. S. P., Usher, P. D., & Barrett, J. W. 1972, ApJ, 171, 457

Shlosman, I., Begelman, M. C., & Frank, J. 1990, Nature, 345, 679

Shull, J. M., & Van Steenberg, M. E. 1985, ApJ, 294, 599

Sikora, M., Begelman, M. C., & Rees, M. J. 1993, in Compton Gamma-Ray Observatory, AIP proceedings 280, ed. M. Friedlander, N. Gehrels & D. J. Macomb (New York: AIP), p. 598

Sikora, M. 1994, ApJS, 90, 923

Sikora, M., Begelman, M. C., & Rees, M. J. 1994, ApJ, 421, 153

Sillanpää, A., Haarala, S., Valtonen, M. J., Sundelius, B., & Byrd, G. G. 1988, ApJ, 325, 628

Sillanpää, A., et al. 1994, in IAU Symp. 159, Multi-Wavelength Continuum Emission of AGN, ed. T. J.-L. Courvoisier and A. Blecha (Dordrecht: Kluwer), p. 404

Smith, P. S., & Sitko, M. L. 1991, ApJ, 383, 580

Smith, P. S., Hall, P. B., Allen, R. G., & Sitko, M. L. 1992, ApJ, 400, 115

Smith, P. S., Allen, R. G., & Angel, J. R. P. 1993, ApJ, 415, L83

Snyder, W. A., et al. 1980, ApJ, L11

Sparks, W. B., Biretta, J. A., & Macchetto, F. 1994, ApJS, 90, 909

Stark, A. A., Gammie, C. F., Wilson, R. W., Bally, J., Linke, R. A., Heiles, C., & Hurwitz, M. 1992, ApJS, 79, 77

Stecker, F. W., De Jager, O. C., & Salamon, M. H. 1992, ApJ, 390, L49

Stickel, M., Fried, J. W., & Kühr, H. 1988, A&A, 191, L16

Stickel, M., Padovani, P., Urry, C.M., Fried, J.W., & Kühr, H. 1991, ApJ, 374, 431

Stocke, J. T., Morris, S. L., Gioia, I., Maccacaro, T., Schild, R. E., & Wolter, A. 1990, ApJ, 348, 141

Stone, R. P. S. 1977, ApJ, 218, 767

Stull, M. A., 1972, AJ, 77, 13

Tagliaferri, G., Stella, L., Maraschi, L., Treves, A., & Celotti, A. 1991, ApJ, 380, 78

Takalo, L. O. 1992, in Variability of Blazars, ed. E. Valtaoja and M. Valtonen (Cambridge Univ. Press), p. 300

Takalo, L. O., et al. 1992, A&AS, 94, 37

Takalo, L. O., Sillanpää, A., Nilsson, K., Kidger, M., & De Diego, J.A. 1994, A&AS, 104, 115

Takalo, L.O. 1994, in IAU Symp. 159, Multi-Wavelength Continuum Emission of AGN, ed. T. J.-L. Courvoisier and A. Blecha (Dordrecht: Kluwer), p. 409

Teays, T., & Garhart, M. 1990, NASA IUE Newsletter, 41, 94

Thompson, D. J., Djorgovski, S., & De Carvalho, R. 1990, PASP, 102, 1235

Thompson, D. J., et al. 1994, in IAU Symp. 159, Multi-Wavelength Continuum Emission of AGN, ed. T. J.-L. Courvoisier and A. Blecha (Dordrecht: Kluwer), p. 49

Treves, A., et al. 1989, ApJ, 341, 733

Treves, A., & Girardi, E. 1990, in Variability of Active Galaxies, ed. W. J. Duschl, S. J. Wagner, and M. Camenzind, Lecture Notes in Physics, 377 (Springer Verlag: Berlin), p. 175

Treves, A., Belloni, T., Falomo, R., Fink, H. H., Maraschi, L., Sambruna, R. M., Tagliaferri, G., & Zimmermann, H. U. 1993, ApJ, 406, 447

Treves, A., et al. 1994, ApJ, submitted

Ulmer, M. P., Brown, R. L., Schwartz, D. A., Patterson, J., & Cruddace, R. G. 1983, ApJ, 270, L1

Ulrich, M.-H., et al. 1981, A&A, 103, L1

Ulrich, M.-H., Hackney, K. R. H., Hackney, R. L., & Kondo, Y. 1984, ApJ, 276, 466

Ulrich, M.-H. 1989, in BL Lac Objects, ed. L. Maraschi, T. Maccacaro and M.-H. Ulrich, Lecture Notes in Physics, 334 (Springer Verlag: Berlin), p. 45

Ulrich, M.-H. 1990, in Variability of Active Galaxies, ed. W. J. Duschl, S. J. Wagner, and M. Camenzind, Lecture Notes in Physics, 377 (Springer Verlag: Berlin), p. 249

Urry, C. M., & Mushotzky, R. F. 1982, ApJ, 253, 38

Urry, C. M., Kondo, Y., Hackney, K. R. H., & Hackney, R. L. 1988, ApJ, 330, 791

Urry, C. M., & Reichert, G. 1988, NASA IUE Newsletter, 34, 96

Urry, C. M., et al. 1993, ApJ, 411, 614

Urry, C. M., & Padovani, P. 1993, in The Physics of Active Galaxies, Proc. of the First Stromlo Symposium, Canberra, in press

Urry, C. M., et al. 1994a, in preparation

Urry, C. M., et al. 1994b, in preparation

Valtaoja, E. 1994, in IAU Symp. 159, Multi-Wavelength Continuum Emission of AGN, ed. T. J.-L. Courvoisier and A. Blecha (Dordrecht: Kluwer), p. 145

Van der Klis, M. 1989, ARA&A, 27, 517

Veron-Cetty, M. P., & Veron, P. 1989, ESO Scientific Rep. N.7

Wagner, S., & Witzel, A. 1992, in Extragalactic Radio Sources, ed. J. Roland, H. Sol, and G. Pelletier, (Cambridge: Cambridge Univ. Press), p. 59

Wall, J. V., Danziger, I. J., Pettini, M., Warwick, R. S., & Wamsteker, W. 1986, MNRAS, 219, 23P

Walter, R., & Courvoisier, T. J.-L. 1991, A&A, 250, 312

Wambsganss, J., Paczynski, B., & Katz, N. 1990, ApJ, 352, 407

Wandel, A., & Urry, C. M. 1991, ApJ, 367, 78

Wehrle, A., et al. 1994, in preparation

Wills, D., & Wills, B. J. 1974, ApJ, 190, 271

Wills, D., & Wills, B. J. 1976, ApJS, 31, 143

Woltjer, L., & Setti, G. 1982, in Astrophysical Cosmology, Pont. Acad. Sci. Scripta Varia, 48, ed. H. A. Brück, G. V. Coyne, and M. S. Longair, p. 293

Worrall, D. M., et al. 1986, ApJ, 303, 589

Worrall, D. M., & Wilkes, B. J. 1990, ApJ, 360, 396

Yee, H. K. C., & Oke, J. B. 1978, ApJ, 226, 753

Zensus, J. A. 1989, in BL Lac Objects, ed. L. Maraschi, T. Maccacaro and M.-H. Ulrich, Lecture Notes in Physics, 334 (Springer Verlag: Berlin), p. 3